UNIVERSITY OF CALIFORNIA

Los Angeles

Energetic Electron Losses Driven by Whistler-Mode Waves in the Inner Magnetosphere: ELFIN observations and theoretical models

A dissertation submitted in partial satisfaction
of the requirements for the degree
Doctor of Philosophy in Geophysics and Space Physics

by

Ethan Tsai

2024

© Copyright by
Ethan Tsai
2024

ABSTRACT OF THE DISSERTATION

Energetic Electron Losses Driven by
Whistler-Mode Waves in the Inner Magnetosphere:
ELFIN observations and theoretical models

by

Ethan Tsai
Doctor of Philosophy in Geophysics and Space Physics
University of California, Los Angeles, 2024
Professor Vassilis Angelopoulos, Chair

Resonant interactions between energetic radiation belt electrons and equatorially-generated whistler-mode waves are widely studied because they yield either electron acceleration or precipitation – where electrons are scattered and lost into the Earth's atmosphere – both of which are fundamental to space weather forecasting, which is an increasingly relevant challenge as society scales up its reliance on space technologies. This dissertation investigates the mechanisms that govern the effectiveness of electron losses from Earth's radiation belts driven by whistler-mode waves using novel electron precipitation measurements from the ELFIN CubeSats. A culmination of innovative engineering efforts and a refactored satellite operations program has allowed ELFIN to obtain over 12,500 high-quality, low-altitude electron measurements of the radiation belts. These measurements are uniquely capable of resolving the bounce loss cone, allowing us to probe the physics that drive electron precipitation in great detail. We first present a test particle simulation that directly compares ELFIN-measured electron precipitation with equatorial electron and wave measurements by the THEMIS and MMS spacecraft during magnetic conjunctions, confirming the importance of mid-high latitude wave-power. Next, we demonstrate that test particle simulations combined with an empirical wave amplitude model adequately approximate statistical ELFIN

observations at the dawn, day, and dusk MLT sectors, but they significantly underestimate relativistic (> 500 keV) electron losses on the nightside. To resolve this discrepancy, we additionally use quasi-linear diffusion simulation methods to find that considering wave obliquity, wave frequency, and plasma density together are required to recover the energetic portion (> 100 keV) of precipitating electron spectra without overestimating the loss contributions from the quasi-linear regime (~ 100 keV). We conclude by presenting the ranges of wave and plasma characteristics necessary for the incorporation of accurately modeled electron loss rates into modern radiation belt models. This unlocks the potential to remotely sense equatorial wave properties using electron precipitation measurements, but also calls for future *in situ* satellite experiments to more deeply understand the interconnected role of energetic electron losses in atmospheric, ionospheric, and magnetospheric dynamics.

The dissertation of Ethan Tsai is approved.

Anton Artemev

Jacob Bortnik

Hao Cao

Marco CM Velli

Xiaojia Zhang

Vassilis Angelopoulos, Committee Chair

University of California, Los Angeles

2024

"Strive not to be a success

but rather to be of value."

– Albert Einstein

Table of Contents

List of Figures . . . . . **x**

List of Tables . . . . . **xiii**

Acknowledgments . . . . . **xiv**

Curriculum Vitae . . . . . **xvi**

1 Introduction **1**

1.1 Executive Summary 5

1.2 Scientific Background 8

1.2.1 Electrons in the Radiation Belt 8

1.2.2 Whistler-mode Waves 12

1.2.3 Wave-Particle Interactions 13

1.2.4 Beyond Quasi-Linear Theory 17

1.3 Review of Past Work 19

1.3.1 Observational Studies 20

1.3.2 Statistical Studies 22

1.3.3 Theoretical Work 22

1.4 Thesis Organization 24

2 The ELFIN Mission and its Operations **26**

2.1 Introduction 26

2.2 Technical Overview 31

2.2.1 Avionics 35

2.3 Refactor 2.0 . . . 45
2.3.1 Key Concepts . . . 45
2.3.2 Rules, Assumptions and Overall Philosophy . . . 50
2.3.3 The Downlink Completeness Table (DCT) . . . 53
2.3.4 Autohban . . . 54
2.4 Reflection and Lessons Learned . . . 56
2.5 Electron Precipitation Studies Enabled by ELFIN . . . 58
2.6 Summary . . . 62

3 Test Particle Simulations . . . 63
3.1 Introduction . . . 63
3.2 Derivation of Equations of Motion . . . 64
3.2.1 Basic Simulation Setup . . . 64
3.2.2 Adiabatic Invariant I_x . . . 65
3.2.3 Full Hamiltonian . . . 67
3.2.4 Dimensionless Variables . . . 68
3.2.5 Equations of Motion . . . 70
3.3 Simulation Implementation . . . 71
3.3.1 System Parameters . . . 71
3.3.2 Julia . . . 72
3.3.3 Phase Bunching/Trapping . . . 74
3.4 Model Parameters . . . 76
3.4.1 Wave Amplitude and Modulation . . . 77
3.4.2 Empirical Wave Amplitude . . . 80
3.4.3 Wave Frequency and Wave Normal Angle . . . 82

3.5 Summary . . . 84

4 Simulation Validation using In Situ Measurements . . . 86

4.1 Introduction . . . 86

4.2 Observations . . . 88

4.2.1 Datasets . . . 88

4.2.2 Conjunction Event #1 . . . 89

4.2.3 Conjunction Event #2 . . . 91

4.3 Simulation Results . . . 95

4.3.1 Conjunction Event #1 . . . 96

4.3.2 Conjunction Event #2 . . . 101

4.4 Discussion . . . 103

5 Investigating Whistler-Mode Wave Intensity Along Field Lines . . . 107

5.1 Introduction . . . 107

5.2 Data Sets . . . 110

5.3 Simulation of Wave-Particle Interactions . . . 113

5.4 Precipitation Events . . . 114

5.5 Statistical Results . . . 120

5.6 Discussion . . . 123

6 Explaining Nightside Relativistic Electron Precipitation . . . 126

6.1 Introduction . . . 126

6.2 Data Sets . . . 129

6.3 Simulation . . . 131

6.3.1 Quasi-linear Diffusion Code . . . 132

6.3.2 Wave Frequency and Obliquity Models . . . 133
6.4 Data-model Comparison . . . 135
6.4.1 Role of Plasma Density . . . 135
6.4.2 Role of Wave Frequency . . . 138
6.4.3 Role of Wave Obliquity . . . 139
6.4.4 Combined Results . . . 141
6.5 Conclusion . . . 145

7 Summary and Future Work . . . 147
7.1 Research Summary . . . 147
7.2 Future Work . . . 150
7.2.1 Determining Key Wave Characteristics on the Dayside . . . 150
7.2.2 Remote Sensing of Chorus Waves Properties . . . 150
7.2.3 Future In Situ Electron Precipitation Measurements . . . 152

A Acronyms . . . 154
A.1 Chapter 1 . . . 154
A.2 Chapter 2 . . . 155

B Derivations . . . 158
B.1 Derivation of I_x . . . 158
B.2 Derivation of Full Hamiltonian . . . 160

List of Figures

1.1 Radiation Belt Schematic 4

1.2 Wave Particle Interactions and Measurement Schema 7

1.3 Resonant Diffusion Surfaces 15

1.4 Minimum Energy Resonance Curves 16

1.5 Electron Trajectories for Nonlinear Wave Particle Interactions 19

2.1 ELFIN EM/FM Test Flowchart 28

2.2 ELFIN Lifetime Science Downlink Efficiency 30

2.3 ELFIN Expanded View 32

2.4 Photos of ELFIN Flight Model 34

2.5 ELFIN Avionics Block Diagram 35

2.6 Command/Data Protocol 37

2.7 ELFIN Ground Block Diagram 44

2.8 Planner Summary Page 46

2.9 Planner Rules Flowchart 51

3.1 System Parameters 72

3.2 Progression of Particle Tracing Efficiency 73

3.3 Nonlinear Wave Particle Interactions 77

3.4 Electron Trajectories with Wave Damping 79

3.5 Electron Trajectories with Short Wave Packets 80

3.6 Modified Empirical Wave Model 81

4.1 THEMIS Data for Conjunction #1 90

4.2 THEMIS Data for Conjunction #1 . . . 91
4.3 ELFIN Data for Conjunction #1 . . . 92
4.4 Magnetic Footprint of Conjunction #2 . . . 93
4.5 MMS Data for Conjunction #2 . . . 94
4.6 ELFIN Data for Conjunction #2 . . . 95
4.7 THEMIS PSD Fits . . . 97
4.8 THEMIS Waveburst Detail . . . 97
4.9 Test Particle Trajectories as a Function of $\delta\lambda_2$ . . . 98
4.10 Observation/Model Comparison for Conjunction #1 . . . 100
4.11 MMS PSD Fits . . . 102
4.12 Observation/Model Comparison for Conjunction #2 as a function of $\delta\lambda_2$ . . . 103
4.13 Observation/Model Comparison for Conjunction #2 as a Function of Wave Modulation . . . 104

5.1 Example precipitating to trapped flux ratio from ELFIN data . . . 112
5.2 Comparisons of Dayside Case Studies . . . 115
5.3 Comparisons of Nightside Case Studies . . . 116
5.4 Statistical comparison between modelled and observed j_{prec}/j_{trap} . . . 119
5.5 ELFIN statistical coverage . . . 122

6.1 ELFIN Nightside REP Examples . . . 130
6.2 ELFIN Statistical Distributions . . . 131
6.3 Plasma Density Effects on Energetic Electron Precipitation . . . 136
6.4 Comparing Effects of Wave Frequency Models on Energetic Electron Precipitation 138
6.5 Comparing Effects of Wave Obliquity Models on Energetic Electron Precipitation 140
6.6 Comparing Various Combinations of Wave/Plasma Modifications . . . 142

6.7 Summary of Modifications 143

7.1 Future Mission Concept 152

List of Tables

2.1 ELFIN Radiation Belt Observation Rate 29

5.1 Parameters of 12 events selected for case study 111

Acknowledgments

This dissertation would not have been possible without the countless people I have had the privilege of calling my peers, friends, and family. First and most importantly is Prof. Vassilis Angelopoulos, who has given me countless opportunities to prove myself while always pushing me towards success. The last decade spent in your lab seems to have flown by in a blink of an eye. Anton, your electric enthusiasm, well-honed wisdom, and quick-witted humor have been guiding me since 2017 (I think you have reached the strong diffusion limit with the ratio of your willingness to mentor students to the depths of your subject matter expertise nearly reaching one!). Prof. Xiao-Jia, thank you for the many times you have helped me with IDL (you helped me overcome my fear of IDL, which is truly an accomplishment!). Prof. Jacob Bortnik, your AOS250B class really ignited my curiosity for this field (I also appreciate your insistence on accounting for oblique waves in every single one of my SPARTHRB talks!). Finally, thank you to Prof. Ray Walker for the generous time you spent preparing me for my oral exam.

I also have so many awesome ELFINers to thank for everything I have learned and for making ELFIN what it is today. Without a doubt, satellite operations turned out to be much harder than any of us ever anticipated, but we somehow managed to turn ELFIN into one of the most successful scientific CubeSat missions ever. I wanted to acknowledge the great sacrifices of the 3 generations of incredibly dedicated operation leads (Chen and Erica, Kelly and Suyash, Izzy and JTam) as well as the core members of our talented software dev team (Austin, Akhil, Jason, Sharvani, Graham, Chanel, James) that were critical when the going got tough. Special thanks to Sophie for fixing ELFIN ADCS and taking on so many different responsibilities throughout your time here, including interim PM-ship as I write this dissertation. My predecessors, Chris Shaffer and Lydia Bingley, did such a wonderful job guiding the many ELFINers – too many to properly acknowledge here – in designing, developing, and building the little CubeSats that could. Of course, none of this would be possible without the incredible staff/grad students that made ELFIN possible: Ryan Caron, Pat Cruce, Max Chung, Colin Wilkins, Kathryn Rowe, Eric Grimes, Emmanuel Masongsong, Jonathan Green, Shiyu Xia, Chris Liu; each of you has played a pivotal role in shaping my skills both as an engineer and as a technical manager. I am forever grateful and deeply honored to have had the

opportunity to work with you all.

Finally, this endeavor could not have been possible without the people who shaped me throughout my life. Li Lin, my childhood violin teacher, imbued me with focused discipline and sharp attention to detail. Mr. Woosnam, my high school physics teacher, was the first to empower me to think logically for myself. My loving parents and caring brother have been unwaveringly cheering me on and financially supporting me, despite mostly being clueless about what I actually do. I am also very lucky to have Auntie Ingrid, Uncle Steven, Jennifer, and Sherman in close proximity, who have literally housed me in times of need, cared for me when I was sick, watered my plants when I was away, and fed me continuously all year. This thesis is not about my success, but rather about how it takes a village.

-Ethan Tsai

Final Defense on January 5th, 2024

Chapter 2 is adapted from "Tsai, E., et al. (2024), ELFIN Mission Operations and ADCS Design." to be submitted to the Journal of Spacecraft and Rockets. A preprint can be found at doi: 10.31224/3487.

Chapter 4 is adapted from "Tsai, E., Artemyev A. V., Zhang, X.-J., Angelopoulos, V. (2022), Relativistic electron precipitation driven by non-linear resonance with whistler-mode waves, J. Geophys. Res., 127, e2022JA030338. doi: 10.1029/2022JA030338."

Chapter 5 is adapted from "Tsai, E., Artemyev, A., Angelopoulos, V., Zhang, X.-J. (2023). Investigating whistler-mode wave intensity along field lines using electron precipitation measurements. Journal of Geophysical Research: Space Physics, 128, e2023JA031578. doi: 10.1029/2023JA031578."

Chapter 6 is adapted from "Tsai, E., Artemyev, A. V., Ma, Q., Mourenas, D., Agapitov, O., Zhang, X.-J., Angelopoulos, V. (2023). Key factors determining nightside energetic electron losses driven by whistler-mode waves." submitted to Journal of Geophysical Research: Space Physics and currently under review as of this submission. A preprint can be found at doi: 10.22541/au.170216582.29158404/v1.

I acknowledge funding support from NASA grants 80NSSC20K1507, NNX14AN68G, and NAS5-02099, as well as NSF grants AGS-1242918 and AGS-2019950.

Curriculum Vitae

2013-2017	B.S. in Physics, UCLA
2014-2016	ADCS Lead, NASA+NSF ELFIN Mission, UCLA
2015-2017	NASA Space Grant Scholarship
2017-2022	Project Manager, NASA+NSF ELFIN Mission, UCLA
2019-2022	M.S. in Geophysics and Space Physics, UCLA
2019-Present	Graduate Student Researcher, UCLA
2020-2023	NASA FINESST Scholar

Publications

1. **Tsai, E.**, et al. (2024). ELFIN Mission Operations and ADCS Design. Journal of Spacecraft and Rockets. doi: 10.31224/3487, to be submitted.
2. Bashir, M., Artemyev, A., Zhang, XJ., Angelopoulos, V., **Tsai, E.**, et al. (2024). First direct observations of relativistic electron precipitation driven by the combined scattering of whistler and EMIC waves. Geophysical Research: Space Physics. doi: 10.22541/essoar.169111414.40123177/v1, in review.
3. **Tsai, E.**, Artemyev, A., Ma, Q., Mourenas, D., Agapitov, O., Zhang, X.-J., & Angelopoulos, V. (2024). Key factors determining nightside energetic electron losses driven by whistler-mode waves. Journal of Geophysical Research: Space Physics. doi: 10.22541/au.170216582.29158404/v1, in review.
4. Wilkins, C., Angelopoulos, V., Runov, A., Artemyev, A., Zhang, X.-J., Liu, J., & **Tsai, E.** (2023). Statistical Characteristics of the Electron Isotropy Boundary. Journal of Geophysical Research: Space Physics, 128. doi: 10.1029/2023JA031774
5. **Tsai, E.**, Artemyev, A., Angelopoulos, V., & Zhang, X.-J. (2023). Investigating whistler-mode wave intensity along field lines using electron precipitation measurements. Journal of Geophysical Research: Space Physics, 128. doi: 10.1029/2023JA031578
6. Angelopoulos, V., Zhang, XJ., Artemyev, A.V., Mourenas, D., **Tsai, E.**, et al. (2023). Energetic Electron Precipitation Driven by Electromagnetic Ion Cyclotron Waves from ELFIN's Low Altitude Perspective. Space Sci Rev 219, 37. doi: 10.1007/s11214-023-00984-w
7. Zhang, X.-J., Angelopoulos, V., Artemyev, A., Mourenas, D., Agapitov, O., **Tsai, E.**, et al. (2023). Temporal scales of electron precipitation driven by whistler-mode waves. Journal of Geophysical Research: Space Physics, 128. doi: 10.1029/2022JA031087
8. Shi, X., Zhang, X.-J., Artemyev, A., Angelopoulos, V., Hartinger, M. D., **Tsai, E.**, et al. (2022). On the role of ULF waves in the spatial and temporal periodicity of energetic electron precipitation. Journal of Geophysical Research: Space Physics, 127. doi: 10.1029/2022JA030932

9. Shen, Y., Artemyev, A. V., Ma, Q., Zhang, X.-J., Mourenas, D., **Tsai, E.**, Wilkins, C., Wu, J., Angelopoulos, V. (2022). Inner belt wisp precipitation measured by ELFIN: Regimes of energetic electron scattering by VLF transmitter waves. Journal of Geophysical Research: Space Physics, 127. doi: 10.1029/2022JA030968

10. Artemyev, A. V., Angelopoulos, V., Zhang, X.-J., Runov, A., Petrukovich, A., Nakamura, R., **Tsai, E.**, Wilkins, C. (2022). Thinning of the magnetotail current sheet inferred from low-altitude observations of energetic electrons. Journal of Geophysical Research: Space Physics, 127. doi: 10.1029/2022JA030705

11. Grach, V. S., Artemyev, A. V., Demekhov, A. G., Zhang, X.-J., Bortnik, J., Angelopoulos, V., Nakamura, R., **Tsai, E.**, Wilkins, C., Roberts, O. W. (2022). Relativistic electron precipitation by EMIC waves: Importance of nonlinear resonant effects. Geophysical Research Letters, 49. doi: 10.1029/2022GL099994

12. Shen, Y., Artemyev, A. V., Zhang, X.-J., Angelopoulos, V., Vasko, I. Y., Turner, D. L., **Tsai, E.**, et al. (2022), Tens to hundreds of keV electron precipitation driven by kinetic Alfvén waves during an electron injection. Journal of Geophysical Research: Space Physics, 127. doi: 10.1029/2022JA030360

13. Artemyev, A. V., Zhang, X.-J., Zou, Y., Mourenas, D., Angelopoulos, V., Vainchtein, D., **Tsai, E.**, et al. (2022), On the nature of intense sub-relativistic electron precipitation. Journal of Geophysical Research: Space Physics, 127. doi: 10.1029/2022JA030571

14. Mourenas D., Zhang, X.-J., Nunn, D., Artemyev, A. V., Angelopoulos, V., **Tsai, E.**, Wilkins, C. (2022), Short Chorus Wave Packets: Generation within Chorus Elements, Statistics, and Consequences on Energetic Electron Precipitation, Journal of Geophysical Research: Space Physics, 127. doi: 10.1029/2022JA030310

15. **Tsai, E.**, Artemyev A. V., Zhang, X.-J., Angelopoulos, V. (2022), Relativistic electron precipitation driven by non-linear resonance with whistler-mode waves, J. Geophys. Res., 127. doi: 10.1029/2022JA030338

16. Zhang, X.-J., Angelopoulos, V., Mourenas, D., Artemyev, A. V., **Tsai, E.**, Wilkins, C. (2022), Characteristics of Electron Microburst Precipitation based on High-Resolution ELFIN Measurements, J. Geophys. Res., 127. doi: 10.1029/2022JA030509

17. Zhang, XJ., Artemyev, A., Angelopoulos, V. **Tsai, E.**, et al. (2022) Superfast precipitation of energetic electrons in the radiation belts of the Earth. Nat. Comm. 13, 1611. doi: 10.1038/s41467-022-29291-8

18. Chen. L., Zhang, X.-J., Artemyev, A. V., Angelopoulos, V., **Tsai, E.**, Wilkins, C., Horne, R. (2022), Ducted Chorus waves Cause Sub-Relativistic and Relativistic Electron Microbursts. Geophys. Res. Lett., 49. doi: 10.1029/2021GL097559

19. Mourenas, D., Artemyev, A. V., Zhang, X.-J., Angelopoulos, V., **Tsai, E.**, Wilkins, C. (2021), Electron Lifetimes and Diffusion Rates inferred from ELFIN Measurements at Low Altitude: First Results., J. Geophys. Res., 126. doi: 10.1029/2021JA029757

20. Artemyev, A. V., Demekhov, A. G., Zhang, X.-J., Angelopoulos, V., Mourenas, D., Fedorenko, Y. V., Manninen, J., **Tsai, E.**, et al. (2021), Role of ducting in relativistic electron loss by whistler-mode wave scattering. J. Geophys. Res., 126. doi: 10.1029/2021JA029851

21. Angelopoulos, V., **Tsai, E.**, et al. (2020), The ELFIN Mission. Space Sci Rev 216, 103, doi: 10.1007/s11214-020-00721-7

22. **Tsai, E.** A. V. Artemyev, V. Angelopoulos. (2017), Ion motion in a polarized current sheet., Phys. Plasmas, 24 (1): 012908. doi: 10.1063/1.4975017

CHAPTER 1

Introduction

Earth's magnetic field traps energetic particles into massive toroidal regions where electrons traveling at relativistic velocities are so dynamic that they can vary by five orders of magnitude on timescales that span from days to minutes (Horne et al., 2007). These regions, called the radiation belts, exhibit emergent behavior that is governed by the interaction of diverse plasma populations (i.e., of varying densities, temperatures, and species) and plasma waves (i.e., electrostatic, electromagnetic, and electron/ion scale waves) all constrained by the geomagnetic field. In particular, there remain many open questions regarding the nature of electron energization and losses, the behavior of which is currently impossible to predict during some of the most active types of magnetospheric phenomena: geomagnetic storms and substorms. What determines charged particle dynamics in the radiation belts is the confluence of particles sourced from the solar wind and outer magnetosphere interacting with a variety of plasma waves within Earth's inner magnetosphere. Energetic ion motion is largely controlled by the geomagnetic field configuration and Ultra-Low-Frequency (ULF; < 1 Hz) dynamics, while the smaller and more magnetized energetic electrons are mostly affected by electromagnetic waves within the Extremely Low Frequency (ELF) and Very Low Frequency (VLF) ranges ($10 - 10^4$ Hz) (Lyons and Williams, 1984). One of the most prevalent type of VLF wave, the whistler-mode wave, plays a large role in both accelerating electrons and removing electrons from Earth's radiation belts (Burtis and Helliwell, 1969; Li et al., 2009; Santolík et al., 2003; Storey, 1953; Tsurutani and Smith, 1974), and will be discussed in great detail in Section 1.2.2. Both of these processes are important to understand and quantify: losses have a wider implication in atmospheric chemistry, ionospheric modeling, and further coupling with the magnetosphere (Millan and Thorne, 2007; Thorne

et al., 2021), while acceleration often yields highly energetic "killer electrons" that are an important space weather proxy (Horne et al., 2013; Thorne et al., 2013).

These highly energetic electrons traveling around in near-Earth space can cause significant damage to satellites, leading to malfunctions and shorter operational lifetimes. In fact, during the 2003 Halloween storm, the radiation belts completely drained and reformed significantly closer to Earth where most satellites were orbiting (Looper et al., 2005). Later modeling showed that whistler-mode waves were necessary to generate this near-Earth super-relativistic band of up to 3 MeV electrons (Shprits et al., 2006b). As a result, $\sim$ 10% of all operational satellites (47 out of 450) reported malfunctions, 10 satellites lost operational service for multiple days, and one reported a total loss (Barbieri and Mahmot, 2004; Cannon et al., 2013). At the same time, astronauts onboard the International Space Station were required to shelter inside the more shielded Russian Orbital Segment to protect themselves against dangerous radiation levels, while GNSS failures, communications blackouts, and rerouted flights caused hundreds of millions of dollars in combined economic losses (Xue et al., 2023).

Ultimately, the waves that drive these electrons are themselves also driven by the solar wind's density, speed, and B_z. While a strong statistical relationship between these upstream conditions and the intensification of relativistic electrons has been established (Li et al., 2015b), a deeper understanding of the physical processes is necessary in order to accurately predict the time, location (latitude/longitude), and intensity of flux increases. This will enable us to adjust our physics-based or neural-network based models to perform a high fidelity assimilative reconstruction and prediction of space weather, just like we currently do with state-of-the-art atmospheric weather prediction (Clare et al., 2021; Lam et al., 2023).

Therefore, our motivation is to develop a more comprehensive understanding of the impact of whistler-mode waves on radiation belt electrons to then better forecast how geomagnetic storms unfold. Many electron acceleration processes have been measured *in situ* across a multitude of space weather observatories launched by multiple international space agencies. Although almost all of these wave and particle measurements are made equatorially

(where much of the source and interaction regions are between electrons and whistler-mode waves, see Santolík et al., 2009), much uncertainty still surrounds the concepts of wave growth, wave propagation, and origins of wave characteristics; therefore, the predictability of whistler-mode wave interactions with electrons is still quite nebulous.

For electrons trapped in and bouncing along Earth's dipolar magnetic field, resonant interactions with waves occupy a wide range of latitudes, making it difficult to evaluate the characteristics with only near-equatorial measurements. Near-equatorial electron populations – the most stably trapped electrons with large perpendicular velocities – are captured well and provide detailed insight into the nature of electron acceleration (Li et al., 2014b; Thorne et al., 2013). However, losses are attributed to mostly field-aligned electron populations, the dynamics of which are poorly captured by near-equatorial missions (with the exception of specially designed experiments exemplified in Kasahara et al., 2018a). Low-altitude spacecraft then provide a more promising alternative for quantification of electron losses (Li et al., 2013; Ni et al., 2014).

Before the launch of the Electron Losses and Fields INvestgiation (ELFIN) mission in 2018 (Angelopoulos et al., 2020), there had yet to be high-resolution measurements of electron precipitation (i.e., electron losses caused by electrons impacting Earth's atmosphere) contextualized with measurements of the electrons trapped in near-Earth space. ELFIN is the key enabling technology of this dissertation, and its challenging road to success is discussed in Chapter 2. The mission consists of two CubeSats in circular polar low earth orbit (LEO), each identically equipped with an energetic particle detector for electrons. These mini spacecraft were built and operated by my team of undergraduate students and staff engineers at UCLA, and, over its 4-year orbital lifetime, made key measurements necessary to quantify the electron losses, in particular, those caused by whistler-mode waves, to understand the full extent of the impact of whistler-mode waves in Earth's magnetosphere.

Fig. 1.1 shows a schematic cut-out of Earth's radiation belts, which is traditionally viewed as two discrete toroids filled with highly energetic electrons and ions that both bounce up and down (i.e., from pole to pole) and drift azimuthally (i.e., east/west around Earth

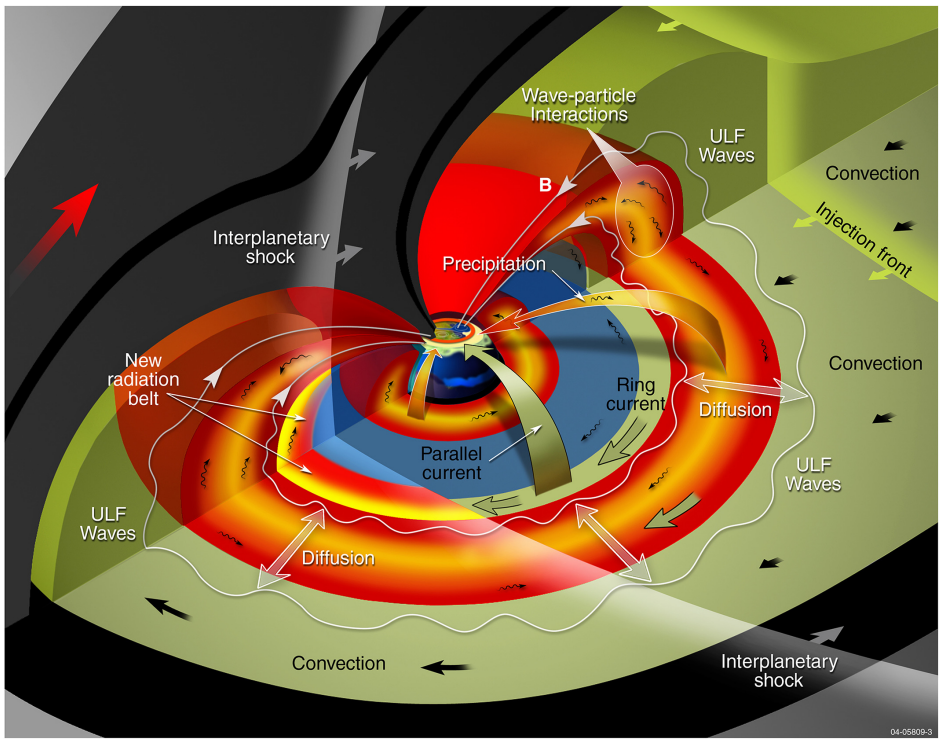


Figure 1.1: Schematic of some of the physical processes that contribute to the dynamicism of Earth's radiation belts (from Fig 5 in (Mauk et al., 2013))

for electrons/ions respectively) in a quasi-stable manner. This diagram highlights some of the most important magnetospheric structures along with the processes that govern the lifetimes of electrons in the radiation belt. The source of electrons is usually plasma injections from the magnetotail (i.e., on the nightside or on the right of the plot). Charged particle interactions with ULF, ELF, and VLF waves drive radial diffusion and local scattering, each causing acceleration and loss (Shprits et al., 2008a,b). One of the key loss mechanisms is precipitation, which occurs when particles reach the collisional ionosphere and are often correlated with various types of aurora (Thorne et al., 2010). The range of pitch angles (angle between velocity and the background magnetic field) corresponding to precipitation to the ionosphere (i.e., the loss cone angle) is very narrow at the equator (less than few degrees), but grows large when following the field line to low altitudes. As a result, precipitation and associated losses are reliably measured only at low altitudes (i.e., high latitudes along the field line), which is not where most spacecraft in NASA's fleet of heliophysics observatories are located. The Japan Aerospace Exploration Agency (JAXA) Exploration of energization

and Radiation in Geospace (ERG) mission (narrow pitch-angle resolution that can resolve the loss cone, see Kasahara et al., 2018a) and the NOAA POES mission (low altitude polar orbit with perpendicular and parallel look directions, see Evans and Greer, 2004; Green, 2013) can measure precipitating particles, but they lack the appropriate energy range or pitch-angle resolution to cleanly and simultaneously resolve precipitating and trapped particles throughout the outer radiation belt range (10 keV to 1 MeV, and above). The ELFIN mission is therefore the key technology that has enabled, for the first time, the investigation of electron losses in great detail. In my dissertation, we will use statistical, numerical, and analytical methods to build a complete picture of how whistler-mode waves can drive the electron precipitation that ELFIN observes.

1.1 Executive Summary

Since the 1960s, theoretical work has firmly established that resonant electron interactions with whistler-mode waves waves represent an important mechanism for both electron acceleration in addition to pitch-angle scattering and subsequent loss to the atmosphere (Andronov and Trakhtengerts, 1964; Kennel and Petschek, 1966; Lyons et al., 1972). Such scattering has been considered to be a major driver of electron losses, see, e.g. pulsating auroras (10s of keV; see, e.g., Kasahara et al., 2018a; Nishimura et al., 2010), diffuse auroras (keV to tens of keV; see, e.g., Ni et al., 2016; Nishimura et al., 2020; Thorne et al., 2010), and even energetic losses beyonds 100s of keV (see, e.g., Blake and O'Brien, 2016; Breneman et al., 2017; O'Brien et al., 2004; Shumko et al., 2018; Thorne et al., 2005). This dissertation examines the key elements that influence the higher energy range of electron precipitation (energetic ($>$ 100 keV) and relativistic ($>$ 500 keV) electrons). It particularly focuses on electron resonant scattering by very intense coherent waves that may resonate nonlinearly with electrons, either accelerating electrons to very high energies, rapidly scattering them, or both. This type of precipitation is essential for the dynamics of Earth's outer radiation belt, serves as a significant space weather proxy (Horne et al., 2013), and must be included in radiation belt flux models to better understand not only the dynamics of the radiation belt, but

also its effects on climate and atmospheric chemistry. In contrast to lower-energy electron losses, higher-energy precipitation can penetrate deep into the thermosphere/mesosphere (Xu et al., 2020); when fluxes are sufficiently high this can contribute to ozone depletion (Lam et al., 2010; Thorne, 1980; Turunen et al., 2016). Section 1.2 will provide an overview of the scientific context concerning outer radiation belt electrons and how they interact with whistler-mode waves.

All global radiation belt models today only incorporate quasi-linear diffusion effects from whistler-mode waves based on empirical models of averaged wave intensity. Such models are typically limited to diffusive losses of electrons up to $\sim$ 500 keV, primarily due to the lack of proper characterization and parameterization of nonlinear effects but also because of the lack of mid-latitude observations of wave activity; the latter being most important for effective scattering of $>$ 500 keV electrons (see discussion in Lorentzen et al., 2001). This same issue has also been implicated in microbursts (ultra fast intense precipitation that lasts $\sim$ 100 ms) as well – where measurement time resolution is often insufficient – making the prediction of electron losses via whistler-mode waves quite challenging. Incorporating relativistic electron losses into models requires characterizing each factor that may play a potential role, which has been historically difficult because previous missions lacked the pitch-angle/energy resolution/range to resolve the finer details of these energetic electron losses. Prior work is detailed in Section 1.3.

To address these phenomena comprehensively, low-altitude observations of both precipitating and trapped particle populations are necessary. Rapid measurements of both populations yield the ratio of precipitating-to-trapped fluxes, which uniquely requires a spacecraft with an Attitude Determination and Control Subsystem (ADCS) capable of keeping the spacecraft stably spinning with spin axis normal to the orbital plane. Additionally, data must be acquired as a function of activity and MLT in order to statistically ascertain the effects of wave-particle interaction. This cannot be achieved with a single (let alone dozens) of balloon flight(s) or sub-orbital rocket flight(s), but instead requires long-lived LEO satellites with a significant throughput of high-quality measurements. This is precisely what the

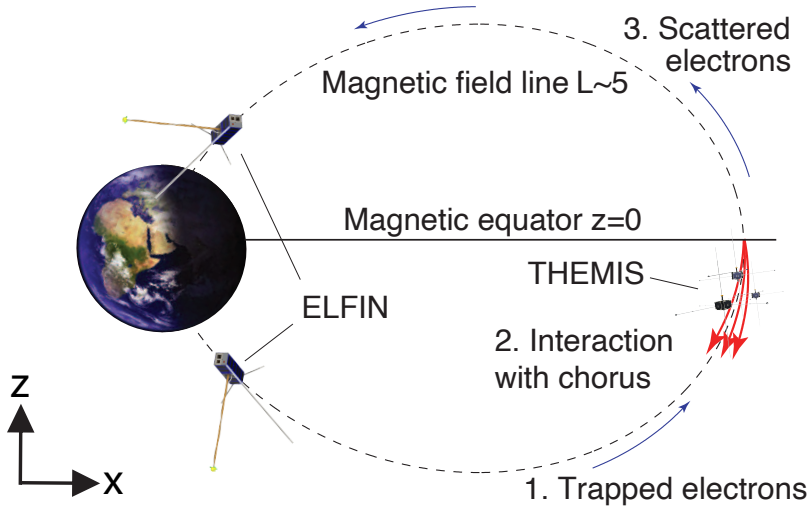


Figure 1.2: A diagram showing equatorial wave-particle interaction and conjugate measurements of waves (e.g., by THEMIS) and scattered electrons by ELFIN before they become lost.

Electron Losses and Fields INvestigation (ELFIN) mission sought to achieve, and Chapter 2 details the challenges we overcame to achieve mission success. More than just long-term *in situ* observations, the many ELFIN observations led to opportunities to perform case studies with equatorial spacecraft (and ground stations) during magnetic conjunctions to verify theory. An example of this is illustrated in Fig. 1.2 showing equatorial measurements by the THEMIS spacecraft near the source region (source of particles, waves, and thus wave-particle interactions) while the low-altitude, polar-orbiting ELFIN CubeSats are able to measure the resulting electron losses into the ionosphere. Using large-ensemble test-particle simulations, detailed in Chapter 3, we examine two such conjunction case studies – one with THEMIS, the other with MMS – which will be detailed in Chapter 4. MLT examination of the scattering efficiency as a function of energy is also required to be compared against models of wave power for future incorporation into radiation belt models and will be discussed in great detail throughout Chapters 5 and 6. Our goals in this thesis are to answer three major questions:

1. Can we accurately infer equatorially-measured wave activity from precipitation measurements at conjugate points in the ionosphere?

   We will use a test particle simulation with large particle ensembles, reasonable as-

sumptions of wave-power distribution along the magnetic field line, and realistic wave modulation properties to examine how whistler-mode driven precipitation can resonate and efficiently precipitate electrons between 100 keV and 1 MeV. Simulation parameters and initial conditions are based on equatorial measurements and the resulting precipitation will be compared with conjugate ELFIN observations for validation.

2. Can current statistically-averaged empirical wave-power models explain ELFIN-observed electron precipitation rates? If not, where do they fall apart?
   After validation, the same test particle simulation will now be used with a statistically averaged empirical wave-power model (Agapitov et al., 2018). We will compare modeled precipitation with statistically averaged precipitation bursts observed by ELFIN. The discrepancy will elucidate whether or not a simple empirical wave intensity model can adequately describe electron precipitation in the 100 keV to 1 MeV range across a variety of L-shells and MLT sectors.

3. What key aspects of resonant wave-particle interactions affect relativistic electron precipitation efficiency?
   If incorporating empirical wave amplitude data is not enough to explain statistically averaged in situ ELFIN relativistic electron precipitation measurements, we will investigate adding modifications to our simulations. ELFIN measurements will confirm which additions are realistic and necessary, allowing for more confident incorporation of various physics into radiation belt modeling.

1.2 Scientific Background

1.2.1 Electrons in the Radiation Belt

Observed first by Sputnik-2 (Vernov and Chudakov, 1960) (and subsequently by Explorer-1, despite being first reported in Van Allen and Frank, 1959), the Van Allen radiation belts are prominent features within the inner magnetosphere of Earth that are composed of high-

energy charged particles that are trapped in a quasi-stable magnetic bottle configuration formed by Earth's mostly-dipolar magnetic field. These trapped particles typically form two toroids surrounding Earth, with the more stable inner belt somewhere between 0.2-2 Earth radii ($L \in [1.2, 3]$, or 1000-12000 km) above Earth's surface and the more dynamic outer belt somewhere between 2-6 Earth radii ($L \in [3, 7]$, or 13000-40000 km) (Ganushkina et al., 2011). Measurements from early spacecraft missions already showed that the inner belt is primarily composed of multi-MeV protons, up to 1-2 GeV, the outer belt is home to a dynamic population of electrons between tens of keV to 10 MeV, and the "slot region" separating the two belts is usually devoid of energetic particles. For reference, the proton and electron rest masses are 931 MeV c^{-2} and 511 keV c^{-2}, respectively, meaning these radiation belt particles are relativistic, often traveling near the speed of light. While the inner belt is relatively stable, the outer electron belt is in continuous flux, changing with timescales that span between tens of milliseconds and multiple days. In fact, the outer belt can cycle from fully empty to fully filled of relativistic electrons, changing energetic electron fluxes by several orders of magnitude within hours. This makes the study of electrons in the outer radiation belt simultaneously interesting and challenging, since both electron enhancements and depletions are governed by such an intricate balance of interdependent processes. These processes are depicted in Fig. 1.1 and include radial transport, wave particle interactions, and other magnetospheric processes that can change the global magnetic field configuration. The complex relationship between these processes, driven by a dynamic solar wind and influenced by pre-storm magnetospheric conditions, ultimately renders it difficult to predict whether the outer radiation belt will be enhanced, depleted, or relatively unchanged during storm times.

One particularly important reason for striving to understand radiation belt dynamics is that the mechanisms that accelerate electrons to relativistic energies – named "killer electrons" for their ability to severely damage satellites or shorten their operational lifespans (Horne et al., 2007) – are not yet fully understood and accounted for in modern radiation belt models. A local acceleration process requires the presence of "seed electrons": electrons on

the order of tens of keV often carried in by substorm injections or enhanced global convection from the magnetotail. These seed electrons not only serve as the population of electrons that get accelerated, but also generate a type of electromagnetic wave – the whistler-mode wave – that actually accelerates the electrons. As these electrons are convected earthward, they encounter stronger magnetic fields and, due to conservation of the first adiabatic invariant (magnetic moment), the electrons' perpendicular energy increases, leading to a temperature anisotropy where the perpendicular temperature (relative to the magnetic field) of the electron population is greater than the parallel temperature. This anisotropic electron population is unstable and provides the free energy necessary for the generation and growth of whistler-mode waves (Kennel, 1966; Sagdeev and Shafranov, 1961). These whistlers, in turn, resonantly interact with electrons, potentially accelerating them up to relativistic energies (Baker, 1998). Properties of these waves are discussed in the following section (Section 1.2.2) and the specifics of their interaction with electrons are discussed in Section 1.2.3.

While the thermal population of injected electrons generate electromagnetic waves and waves can reciprocate by accelerating the energetic "tail" of the injected electron population, the density of such energetic electrons is so low that they do not affect the electric and magnetic fields that govern their overall motion; this means that we can treat them as true test particles. More formally, waves provide energy transfer from the core anisotropic population – which generates and amplifies waves – to a small energetic population of electrons. Electron magnetization by a strong geomagnetic magnetic field, combined with the negligible electron contribution to the field deformation, allows us to define three adiabatic invariants which govern the quasi-periodic motions of electrons in the radiation belts. These invariants are quantities that remain approximately constant as long as the magnetic field varies at a rate much slower than the associated quasi-period. The first adiabatic invariant is the magnetic moment $\mu = \frac{mv_\perp^2}{2B}$, derived from the gyromotion of a charged particle in a magnetic field and, for tens of keV electrons and $B \sim 100$ nT, have a typical period of $\sim 10^{-4}$ seconds. This adiabatic invariant is violated when magnetic fields change at similar (or faster) timescales, leading to energy and pitch-angle variations, which have a significant

impact on the lifetimes of the electron (lifetime is the typical time electrons spend in the radiation belt before precipitating into the ionosphere). This is precisely what happens with whistler-mode waves, which have frequencies in the kHz range and will be discussed further in Section 1.2.2. The second adiabatic invariant relates to the particle's motion along magnetic field lines between mirror points and is given by the integral $J = \int v_{||}\, dl$ where $v_{||}$ is the velocity parallel to the magnetic field line, and dl is the differential element along the field line. For tens of keV electrons, the bounce period is on the order of ~ 1 second. The third adiabatic invariant involves the drift of a charged particle around the Earth, which takes $\sim 10^5$ s for 10 keV electrons, and is related to the magnetic flux Φ enclosed by the drift path $\Phi = \oint A \cdot dl$ where A is the scalar potential. This last invariant is generally less important for the purpose of our study, where we will be studying single wave particle interactions and subsequent associated losses.

Related to the second adiabatic invariant is the concept of the loss cone, which is defined by a specific range of pitch angles at which the mirror point is sufficiently low enough in altitude such that particles impact the atmosphere rather than magnetically reflecting back. This process of electron precipitation can modify the ionosphere (via further ionization or conductivity changes), chemically change the atmosphere (via ozone depletion (Turunen et al., 2016)), and cause aurora (photoemissions from electron collisions with the air), while permanently removing the loss cone electrons from the radiation belts within a single bounce period (although a significant fraction can backscatter, reflecting back into trapped trajectories within the radiation belts via Coulomb scattering, see Marshall and Bortnik, 2018). Particles with pitch angles lower than the critical loss cone angle $\alpha_{lc} = \sin^{-1}\sqrt{\frac{B_0}{B_m}}$, where B_0 is the equatorial magnetic field strength and B_m is the field strength at the mirror point (typically defined at 100 km along the magnetic field line), are defined as locally precipitating, while particles with pitch angles outside α_{lc} remain trapped and continue their bouncing motion between the poles and drift around Earth. Electron precipitation is one of two primary radiation belt loss mechanisms, so studying mechanisms which drive electrons into the loss cone is critical for predicting outer electron belt lifetimes and understanding downstream

effects within both the atmosphere and ionosphere.

1.2.2 Whistler-mode Waves

Throughout the collisionless plasma of Earth's magnetosphere, energy transport is naturally mediated by a variety of plasma waves. These waves are generated due to the natural formation of unstable particle populations and are some of the primary drivers of electron diffusion and precipitation in the radiation belts. There is a wide variety of waves in the magnetosphere, but for this thesis, we focus on whistler-mode waves. Among them, there are two main populations: plasmaspheric hiss – an incoherent broadband wave confined within the plasmasphere, primarily responsible for emptying the slot region (Lyons and Thorne, 1973) – and equatorially-generated chorus, the primary focus of our study. For the latter, the source region is usually at a distance of $L \sim 5 - 10$, where transversely anisotropic injected suprathermal electrons can generate whistler-mode waves via cyclotron resonance. As a result, the frequency of whistler-mode chorus is inherently tied to the electron gyrofrequency f_{ce}, such that $f \in 0.1 - 0.8 f_{ce}$, with a gap at $0.5 f_{ce}$ separating the emissions into lower band ($0.1 f_{ce} < f < 0.5 f_{ce}$) and upper band ($0.5 f_{ce} < f < 0.8 f_{ce}$) chorus (Tsurutani and Smith, 1974).

In addition to wave power (i.e., the amount of energy transported by the wave), waves have two defining characteristics: their wavevector and frequency (i.e., their spatial and temporal variation rates). The dispersion relation relates these with a single equation that yields valuable information about the phase and group velocities which characterize wave propagation. For example, a standard electromagnetic plane wave propagating in a vacuum has a linear dispersion relation with $\omega = ck$, meaning that both the phase ($\frac{\omega}{k}$) and group ($\frac{d\omega}{dk}$) velocities are equal to the speed of light c. However, when an electromagnetic wave travels in a plasma, the properties change significantly because the plasma can interact with the wave fields. In the case of electrostatic waves, the conductivity (σ) is a scalar and motion is simply parallel to the wave propagation. In magnetized plasmas, however, the Lorentz force comes into play and the conductivity becomes a tensor $J = \overleftrightarrow{\sigma} E$, resulting in a current that is the

vector sum of E and $v \times B$. This added complexity is captured in the dispersion for whistler-mode waves in cold magnetized plasmas which primarily depends on two parameters: how much plasma there is (plasma density determining the plasma frequency ω_{pe}) and how strong the magnetic field is (captured by the electron gyrofrequency Ω_{ce}). This is represented by the simplified dispersion relation for field-aligned whistler-mode waves (Stix, 1962):

$$\frac{c^2k^2}{\omega^2} = 1 + \frac{\omega_{pe}^2}{\omega(\Omega_{ce} + \omega)} \tag{1.1}$$

where $\omega_{pe}^2 = \frac{4\pi N_e e^2}{4\pi m_e}$ and $\Omega_{ce} = \frac{eB_0}{m_e c}$, and N_e is the electron density of the plasma, and B_0 is the local magnetic field.

1.2.3 Wave-Particle Interactions

Both theoretical (Lyons and Williams, 1984; Schulz and Lanzerotti, 1974) and observational (Millan and Baker, 2012; Millan and Thorne, 2007; Thorne et al., 2021) studies have shown that whistler-mode waves interact with electrons. Since whistler-mode waves are electron scale waves, their circular polarization matches the electron cyclotron rotation resulting in right-handed circularly polarized waves. When the waves are Doppler-shifted (i.e., electron parallel velocity is modified) such that the electron gyrofrequency can resonate with the wave frequency in the electron rest frame, energy is transferred between waves and electrons. This resonance condition is defined by:

$$\omega - k_{\|} v_{\|} = n\Omega_{ce}, \quad n = 0, \pm 1, \pm 2, ... \tag{1.2}$$

where $k_{\|}$ is the component of the wave vector parallel to the ambient magnetic field B_0 and $\Omega_{ce} = |\frac{eB_0}{\gamma m_e c}|$ is the relativistic angular electron gyrofrequency. Landau resonance occurs at the zeroth order resonance ($n = 0$), which describes when electrons travel along the ambient magnetic field with wave parallel phase speed, allowing for significant and continuous energy exchange in the parallel direction. The case of $n = 1$ describes first-order cyclotron resonance: when the phase velocity of the wave is Doppler-shifted upwards enough to equal

$\Omega_{ce}/k_\parallel$, which happens for $k_\parallel v_\parallel < 0$ (i.e., the electron is ramming head on into the wave helix). When this happens, the electron "feels" an electric field vector (perpendicular to B) that is rotating at the gyrofrequency and resonance is achieved. Although first-order resonance is significantly more effective at changing electron pitch angles than the Landau resonance, both of these processes are most effective in the equatorial inner magnetosphere at accelerating or scattering < 100 keV electrons. Higher order resonance ($|n| > 1$) is less important for field-aligned waves, but can become significantly more effective with more oblique waves, because the effective wave amplitude is proportional to $J_n(k_\perp v_\perp/\Omega_{ce})$ and for higher n the argument of Bessel function J should be sufficiently large ($k_\perp$ should be large, i.e., wave should be sufficiently oblique) as $J_n(0) \to 0$ for $n \neq 0$ (Shklyar and Matsumoto, 2009). Note that the resonant energy $E_r \propto v_\parallel^2$ scales with the resonant number as $\sim n^2$, and so, if the waves are oblique enough to provide a finite amplitude at large n, these waves can then resonantly scatter electrons of much higher energy (Artemyev et al., 2016; Bortnik et al., 2011). The derivation of oblique interactions is further discussed in Section 3.4.3 and its effects are demonstrated in Section 6.4.3.

These resonant interactions lead to diffusion in both the electron's pitch angle and energy, amplifying or damping waves in the process. Such diffusion smooths the gradients of the electron distribution function along so-called "diffusion curves" (Lyons and Williams, 1984):

$$\left(v_\parallel - \frac{\omega}{k_\parallel}\right)^2 + v_\perp^2 = \text{const} \tag{1.3}$$

The diffusion curves define a diffusion surface by which the phase space density gradient determines the preferential direction of diffusion. To determine the net energy and pitch-angle diffusion direction, one must analyze the particle diffusion direction in relation to the constant energy curves in velocity space. If the isotropization in the phase space density along the diffusion curves is in the direction such that the net phase space density transport results in energy loss, then the waves will grow. Conversely, if the transport results in energy gain, the waves will be damped.

Electrons at the equator exhibit more particle fluxes at 90° (i.e., electrons are mostly

trapped and moving perpendicular to the magnetic field, forming a more "pancake"-shaped distribution) (Gannon et al., 2007; Shi et al., 2016). Fig. 1.3 shows that for electrons with lower energy, the pancake shape of the gradient in phase space density rapidly transports electrons to a lower pitch angle and energy, therefore moving electrons toward the loss cone (i.e., towards the deficit in phase space density). Such transport results in electron energy loss, which, in turn, supports wave growth. Thus, this low-energy diffusion predominantly causes net wave growth and electron pitch-angle scattering into the loss cone. At higher energies, however, electrons remain in resonance and can interact with the wave only at higher pitch angles, so diffusion tends to go in the opposite direction, locally accelerating electrons. Thus, diffusion at high energies predominantly causes overall wave damping and electron acceleration. These diffusion curves demonstrate the two regimes of wave particle interaction that can lead to both pitch-angle scattering, predominantly at low energies, and acceleration (energy scattering), predominantly at high energies (Bortnik and Thorne, 2007).

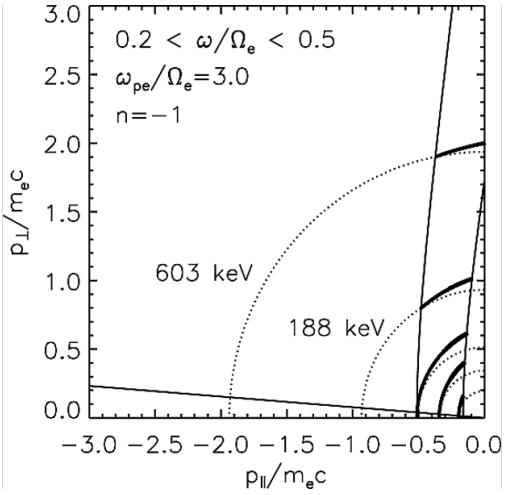


Figure 1.3: This is Figure 3 from (Horne and Thorne, 2003). The cyclotron resonant ellipses (solid) and resonant diffusion surfaces (bold) are shown for a band of equatorial lower band whistler-mode waves when $L = 4.5$. Also shown are constant energy surfaces (dotted) at 10, 29, 63, 188, and 603 keV. The narrow equatorial loss-cone at $L = 4.5$ is shown as a straight line.

The electron energy required to resonate with these waves is defined by the minimum resonance energy, which is primarily a function of when the local magnetic field (via the electron gyrofrequency) allows for the first resonance condition to be satisfied:

$$\gamma \cdot \omega - \frac{k(\lambda) \cdot p_{\parallel}(\lambda, E, \alpha_{lc})}{m_e} = \Omega_{ce}(\lambda) \tag{1.4}$$

This equation adds the relativistic correction factor $\gamma(E) = 1 + \frac{E}{m_e c^2}$ to Eq. 1.2 and also

explicitly shows the parameters for each term, especially magnetic latitude λ (analog of the field-aligned coordinate for the dipole magnetic field). The dispersion relation, combined with a plasma density model (Denton et al., 2005), provides the wavenumber k

$$\omega = \frac{\Omega_{ce}}{1 + (\frac{\omega_{pe}}{kc})^2} \rightarrow k(\lambda) = \frac{\Omega_{ce,eq}\omega_p \cos^{-5/2}\lambda}{c\sqrt{\frac{\Omega_{ce}(\lambda)}{\omega} - 1}} \tag{1.5}$$

where $\omega_{pe} = \Omega_{ce,eq}\omega_p \cos^{-5/2}\lambda$, and ω_p determines the equatorial plasma density $\omega_{pe,eq}/\Omega_{ce,eq}$.

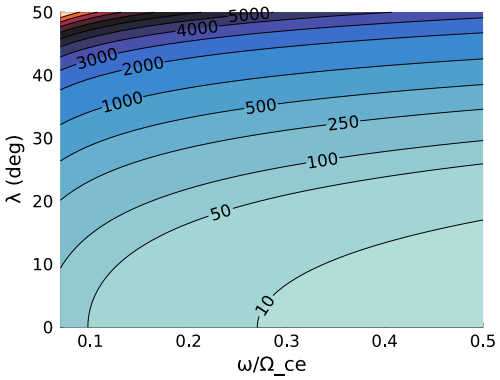


Figure 1.4: Minimum energy required to resonate with waves at $L = 5$, $\omega_p = \omega_{pe,eq}/\Omega_{ce,eq} = 5$.

Because the loss cone angle changes as a function of L shell, we can then plot the minimum resonance energy as a function of latitude for a given L shell, seen in Fig. 1.4.

This does not rely on the wave amplitude, and, purely based on the resonance condition, allows for waves to interact with even relativistic electrons should those waves be able to reach $> 30°$ in latitude. The effectiveness of this wave-particle interaction, however, depends greatly on other parameters – such as wave amplitude or electron phase space density. To reach $> 30°$ in latitude wave rays generally need to be trapped within localized, field-aligned density perturbations that guide whistler-mode waves to much higher latitudes while avoiding damping (Helliwell, 1965; Karpman and Kaufman, 1982; Pasmanik and Trakhtengerts, 2005; Streltsov and Bengtson, 2020). Ray tracing simulations and spacecraft observations have both confirmed that even weak density perturbations can result in ducting (Chen et al., 2021b; Hanzelka and Santolík, 2022, 2019; Hosseini et al., 2021; Shen et al., 2021; Yearby et al., 2011), while more effective ducting can cause waves that propagate all the way to the ground (Demekhov et al., 2017; Martinez-Calderon et al., 2016, 2020; Titova et al., 2017).

1.2.4 Beyond Quasi-Linear Theory

Due to how much smaller wave fields are compared to Earth's background dipolar field in the inner magnetosphere – $\delta B/B_0 \sim \mathcal{O}(10^{-4})$ – wave particle interactions in the radiation belts are often treated with perturbation theory (Andronov and Trakhtengerts, 1964; Drummond and Pines, 1962; Kennel and Petschek, 1966; Vedenov et al., 1962). This approach assumes that electrons move in a dipole field and experience the Lorentz force $F_w(r,p) = eE_w + ep \times B_w/m_e c\gamma$ of wave fields $E_w(r)$, $B_w(r)$ that can be estimated as $F_w(r_0,p_0)$ with electron coordinates r_0 and momentum p_0 given by unperturbed ($F_w = 0$) orbits in a dipole field. This approximation of unperturbed trajectories forms the basis of quasi-linear theory for wave-particle interactions (Kennel and Engelmann, 1966). The description of small amplitude waves is generally based on the concept of a random phase (turbulent) ensemble of plane waves (i.e., waves with $E_w, B_w = E_w(\phi), B_w(\phi)$) with wave-vectors centered around $k = \partial\phi/\partial r$ and wave frequencies centered around $\omega = -\partial\phi/\partial t$ that are connected by the linear dispersion relation $\omega = \omega(k)$ (Stix, 1962). As they are periodic functions of phase ϕ, the wave fields $E_w(\phi), B_w(\phi)$ quickly oscillate with randomized phases that have no net effect on particles everywhere (because $\langle E_w(\phi)\rangle_\phi = 0$, $\langle B_w(\phi)\rangle_\phi = 0$) unless they satisfy the resonance condition, where $\dot{\phi} = 0$ and wave fields remain constant within a some fragment of particle trajectory.

This condition takes the form $\dot{\phi} = (\partial\phi/\partial \boldsymbol{r})\dot{\boldsymbol{r}} + \partial\phi/\partial t = \boldsymbol{k}\cdot\boldsymbol{r} - \omega = 0$, and, in a strong background magnetic field, it can be rewritten as $k_\parallel p_\parallel/m_e\gamma + k_\perp p_\perp/m_e\gamma - \omega = 0$, where the transverse electron momentum is the fast gyrating function $p_\perp = \bar{p}_\perp \sin\theta$ and $\dot{\theta} = \Omega_{ce}/\gamma = eB_0/m_e c\gamma$ is the electron gyrofrequency. The standard approach is to expand periodic wave fields $\sim \sin\phi$ into Bessel functions, $\sin\phi = \sum_n J_n(k_\perp \bar{p}_\perp/m_e\gamma\Omega_{ce})\sin\phi_n$ with $\dot{\phi}_n = k_\parallel p_\parallel/m_e\gamma + n\Omega_{ce}/\gamma - \omega$, and consider each resonance (each n) separately. As mentioned above, higher order resonances (i.e., $|n| \gg 1$) are possible, but require wave obliquity (i.e., $\hat{k} \neq \hat{B}$) to become relevant (Albert, 2017; Artemyev et al., 2013; Mourenas et al., 2012b; Shklyar and Matsumoto, 2009). For only moderate obliquity, when higher-order resonances start to appear, the rapid falloff of the Bessel function amplitude (at small argument $\sim k_\perp$)

with order number guarantees that only the first order resonance will dominate. Thus, applying first order cyclotron resonance is sufficient for modeling quasi-parallel ($k_{\parallel} \gg k_{\perp}$) propagating whistler-mode waves.

Using quasi-linear theory, the electron only "feels" a perturbing wave force at resonance $\dot{\phi}_n = 0$ for unperturbed electron orbits, r_0 and p_0, although its impact depends on the initial phase, ϕ_n, which is defined far from resonance. Averaging over a large ensemble of initial phases (equivalently, averaging over a large ensemble of resonant electrons with the same energy and pitch angle but different phases) results in zero mean impact and nonzero (finite) dispersion. Thus, quasi-linear theory describes diffusion of electrons in energy and pitch-angle space driven by multiple resonances with whistler-mode waves (Kennel and Engelmann, 1966; Lerche, 1968). Various numerical models can evaluate electron flux dynamics due to this fairly simple diffusion premise (Horne et al., 2005; Li et al., 2014a; Thorne et al., 2013).

Quasi-linear theory relies on the wave amplitude being weak enough to keep the electron orbit unperturbed ($|B_w| \ll B_0$). However, bounce oscillations are controlled by a much weaker mirror force $\sim \bar{p}_{\perp}(\partial B_0/\partial r_{\parallel})/m_e\Omega_{ce}$ that can be comparable to (or even smaller than) the wave force $\sim |B_w|$ (see Bell, 1984; Nunn, 1971). Quasi-linear theory breaks down when this condition is met (see more precise criterion in Omura et al., 2008), and modeling with unperturbed electron orbits is no longer sufficient. Accounting for the wave field is now required when calculating r, p. This regime is characterized as nonlinear (Albert et al., 2013), and intense high-amplitude whistler-mode waves have often been observed in this nonlinear region before (Cattell et al., 2008; Cully et al., 2008; Wilson et al., 2011).

Nonlinear wave particle interactions can take the form of either phase bunching or phase trapping Bortnik et al. (2008), as shown in Fig. 1.5. Phase bunching is characterized by small but finite mean decrease in pitch angle and energy, inducing faster electron drift in the energy/pitch-angle space, while phase trapping refers to non-local transport to much higher energy and pitch angles. While most nonlinear interactions take the form of phase bunching, overall phase space density conservation dictates that the collective nonlinear effects are actually non-diffusive. In a system without loss mechanisms, multiple resonant

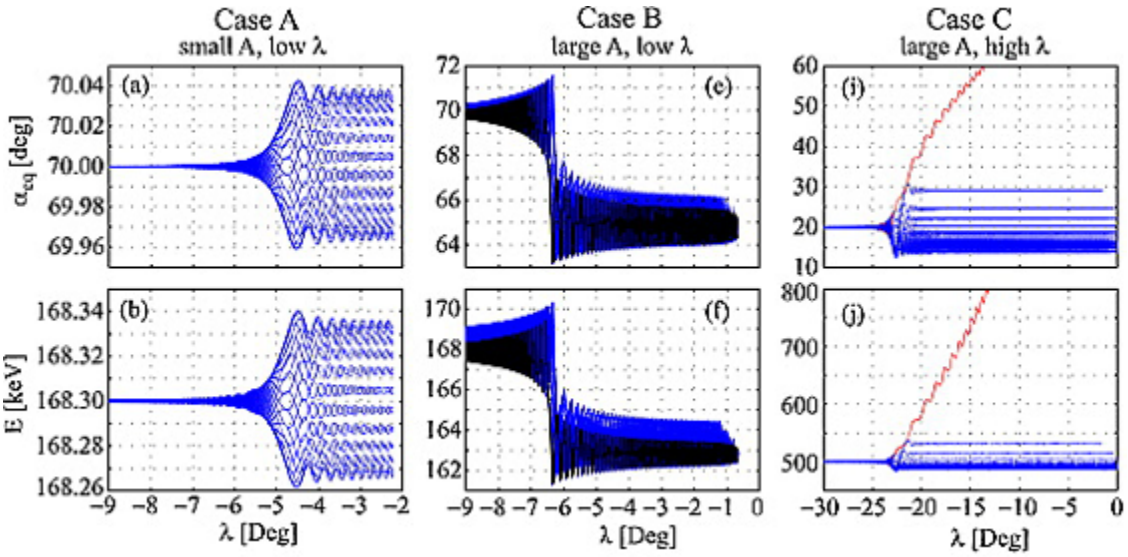


Figure 1.5: From Figure 2 in Bortnik et al. (2008), we see quasi-linear diffusion with low amplitudes resulting in random spread for case A; phase bunching in case B with large amplitude waves resulting in a mean decrease in pitch angle and energy; and phase trapping in case C, resulting in a large jump in both energy and pitch angle.

interactions will just generate more extreme diffusive-like mixing in velocity space (Artemyev et al., 2022b). However, on short time intervals (e.g. during bursty precipitation), nonlinear effects can preferentially scatter electrons into the loss cone, therefore having great potential to quickly drain the radiation belts.

1.3 Review of Past Work

The ramifications of whistler-mode waves interacting with electrons in the inner magnetosphere have several knock-on effects in a wide set of disciplines. Studying these mechanisms in geospace can help quantify these contributions towards auroral, ionospheric, magnetospheric, and atmospheric physics, but also has implications for defense applications and wave-particle interactions beyond Earth. As such, there has already been a wide body of work spanning the gamut of observational, statistical, and theoretical studies, upon which the thesis presented here will build upon.

1.3.1 Observational Studies

Although ionospheric electron precipitation driven by wave-particle resonant interactions has been covered by over 60 years of investigations (see review literature in Li and Hudson (2019); Millan and Thorne (2007); Thorne et al. (2021)), we will focus here only on the most relevant recent results. Studies of conjunctions between low-altitude POES and near-equatorial RBSP missions have shown an increase in precipitating electrons strongly correlated with whistler-mode waves (Li et al., 2013; Ni et al., 2014). Furthermore, whistler-mode wave activity is correlated with auroral intensity (Nishimura et al., 2010). This was verified with ERG, which is able to directly and simultaneously measure electrons scattered into the loss cone with whistler-mode wave activity (Kasahara et al., 2018a). Correlation of wave intensity with pulsating aurora has been shown in Hosokawa et al. (2020) using ERG and PWING (study of dynamical variation of Particles and Waves in the INner magnetosphere using Ground-based network observations) ground networks, while correlated high energy microbursts were shown by simultaneous particle and wave measurements from ERG in Miyoshi et al. (2020). Correlating ERG with EISCAT (European Incoherent Scatter Scientific Association) measurements, they were able to show that these microbursts were able to deposit energy deep into the mesophere (Miyoshi et al., 2020). In fact, ELFIN measurements of microbursts show that they are well correlated with whistler-mode waves (Zhang et al., 2022a) and are likely caused by ducted waves (Chen et al., 2022). These results demonstrate the strong connection between < 10 keV (aurora) to 1 MeV (relativistic microbursts) precipitation and whistler-mode waves, and provide a basis for further investigation of correlations between wave (and background plasma) characteristics and ELFIN's electron precipitating spectra.

The dynamics of electrons are significantly influenced by whistlers even beyond Earth. Plasma wave measurements from Voyager have shown various phenomena occurring in all the gas giants (Jupiter, Saturn, Uranus, and Neptune) involving whistler-mode waves (Kurth, 1992). Whistler-mode wave resonant interaction with electrons controls the dynamics of the planetary radiation belts (Li et al., 2021; Menietti et al., 2021; Thorne et al., 2013),

the relaxation of unstable electron populations in magnetic reconnection regions (Kitamura et al., 2022; Le Contel et al., 2016b; Wang et al., 2022; Zhang et al., 2019b; Zhong et al., 2022), the dynamics of energetic electrons in interplanetary shocks (Davis et al., 2021; Wilson et al., 2013) and Earth's bow shock (Amano et al., 2020; Oka et al., 2019; Shi et al., 2020), the scattering and isotropization of solar wind electrons (Cattell et al., 2020; Cattell and Vo, 2021; Tong et al., 2019), and the dynamics of energetic electrons in solar flares (Filatov and Melnikov, 2017; Melnikov and Filatov, 2020). Near the Sun, these interactions are likely responsible for the halo formation of strahl electrons (Micera et al., 2020) and cause "horns" in velocity space due to resonant scattering of strahl electrons with oblique whistlers in solar flares Roberg-Clark et al. (2019). Thus, we are interested in quantifying how different variables contribute to the scattering and energizing electrons, especially where the common quasi-linear treatment is often insufficient.

The many past observations of wave-particle interactions between electrons and whistler-mode waves highlight two key challenges: (1) electron precipitation occurs over a wide spatial and temporal range and (2) it is currently impossible to observe the full evolution of whistler-mode waves and their interactions with electrons even in the confines of Earth's magnetosphere. While whistler-mode waves interact with electrons primarily below 100 keV in the linear regime, a wealth of studies have shown that the energetic electron range (up to 1 MeV) is also very important. However, spacecraft measurements mostly only show correlation between whistler-mode wave and these related electron phenomena, both within and beyond Earth's magnetosphere, and only quantification in more limited scenarios. ELFIN was designed to resolve this range well, and we first demonstrate this capability by utilizing conjunctions with equatorial spacecraft to test if wave-particle interaction theory can accurately reproduce the energetic electron precipitation measured at its conjugate near-ionospheric footprint. Chapter 4, with related ELFIN papers (Chen et al., 2022; Tsai et al., 2022; Zhang et al., 2022b), constitute some of the first direct studies directly showing relativistic electrons are caused by whistler-mode waves.

1.3.2 Statistical Studies

Next, we want to highlight the wave and plasma parameters that affect resonant whistler-mode wave scattering of electrons as these are foundational inputs for modeling. First, Li et al. (2009, 2011a) presented a full global distribution of wave amplitudes and wave normal angles for lower and upper band whistler-mode waves using multiple years of THEMIS observations, showing which MLT sectors light up with the most intensity. These observations were improved upon with higher resolution insights in Li et al. (2016b). In general, large-amplitude chorus occur from premidnight to postdawn, with the most intense waves also fairly field-aligned (Meredith et al., 2012). This is corroborated with work from Zhang et al. (2018b), which further demonstrated that the occurrence rate of lower-band chorus waves interacting nonlinearly with electrons is predominantly field-aligned, and that suprathermal electrons control both coherence and wave normal angles. Statistics about wave occurrence, coherence, and more are further shown in Nunn et al. (2021); Zhang et al. (2020b, 2021). Especially important is that the efficacy of nonlinear wave interactions is also attenuated by wave phase decoherence (Tao et al., 2013), bridging the gaps between the timescales of quasi-linear theory and nonlinear theory (Zhang et al., 2020a). Used extensively in this dissertation is a whistler-mode wave empirical model built up using over a decade of Van Allen Probe and Cluster measurements (Agapitov et al., 2013, 2018). These models detail wave amplitude, wave normal angles, and wave frequencies for whistler-mode waves as a function of MLT, L-shell, and geomagnetic activity and are foundational for enabling us to realistically model whistler-mode waves for direct comparison with statistically averaged electron precipitation measured by ELFIN.

1.3.3 Theoretical Work

Now that we have statistically characterized waves and novel comprehensive measurements of precipitating particles from ELFIN, we want to see how well they agree. There are two theoretical frameworks for such modeling: (1) the diffusion model first proposed by Kennel and Petschek (1966), which describes electron interactions with low-amplitude broadband

waves quite well and (2) analytical particle tracing in prescribed wave fields by fast non-diffusive models, which is much more well suited for describing resonant interactions with intense coherent waves (Karpman et al., 1974; Nunn, 1971). Many aspects of these two models have been confirmed and verified with spacecraft observations of long-term (diffusive) electron flux evolution (Li et al., 2014b; Thorne et al., 2013) or rapid (non-diffusive) electron acceleration (Agapitov et al., 2015a; Foster et al., 2014; Gan et al., 2020b) and losses (Mourenas et al., 2016). The basic equations for the quasi-linear diffusion model have been initially derived for a homogeneous plasma (Andronov and Trakhtengerts, 1964; Kennel and Engelmann, 1966), and then generalized for inhomogeneous magnetic traps, such as Earth's dipolar field (Lyons and Williams, 1984; Trakhtengerts and Rycroft, 2008). An interesting and important aspect of such a generalization is the significant quantification of the broad wave spectrum requirement (Karpman, 1974; Le Queau and Roux, 1987). Indeed, for coherent waves the resonance width, a crucial parameter for the diffusive model can be determined by the magnetic field inhomogeneity (Albert, 1993; Karpman and Shklyar, 1977; Shklyar, 1981) and/or the wave frequency drift (Demekhov et al., 2006, 2009; Omura et al., 2007). Electron resonant interactions with coherent whistler-mode waves in Earth's magnetosphere can be described by a quasi-linear diffusion model (Albert, 2010) when wave intensity is sufficiently small. Therefore, both regimes of wave-particle interaction (quasi-linear diffusion and nonlinear resonances) can operate for the same coherent monochromatic wave, and only wave intensity determines the relevant regime. Thus, the question arises regarding the transition between these two regimes (see, e.g., discussion in Allanson et al. (2020); Mourenas et al. (2018); Tao et al. (2013)). As whistler-mode waves are often observed with amplitudes exceeding the threshold for nonlinear resonant interactions (Agapitov et al., 2014; Zhang et al., 2018b, 2019a), they may very quickly accelerate electrons (Agapitov et al., 2015a; Demekhov et al., 2006; Gan et al., 2020b; Katoh and Omura, 2007b; Omura et al., 2007) or scatter them into the loss cone (Breneman et al., 2017; Chen et al., 2019a, 2022; Miyoshi et al., 2021; Zhang et al., 2022c). Modeling of nonlinear wave-particle interactions is based either on short test particle runs (Allanson et al., 2020; An et al., 2022d; Artemyev et al., 2012; Bortnik et al., 2008; Katoh et al., 2008; Tsai et al., 2022; Zhang et al., 2020b) or on

sophisticated generalizations of the Fokker-Planck equation (Artemyev et al., 2018, 2021c; Furuya et al., 2008; Hsieh and Omura, 2017; Omura et al., 2015), often without direct verification using spacecraft observations prior to ELFIN. Now that we are equipped with ELFIN data sets, we will use both of these theoretical frameworks to validate modeling methods and probe the physics of the wave-particle interactions in order to determine the true contribution of energetic electron precipitation driven by intense whistler-mode waves.

1.4 Thesis Organization

The overall goal of this dissertation is to use modeling to determine the overall contribution of intense whistler-mode wave driven electron precipitation and, more specifically, what physical characteristics are necessary to drive the results quantified by ELFIN observations. To that end, this work is organized into the following 7 chapters:

Chapter 1 (this chapter) aims to set the scene for this investigation. It begins by contextualizing why studying resonant wave particle interactions between whistler-mode waves and energetic electrons is important in Earth's magnetosphere and introducing relevant scientific background. It also reviews previous research that enables the feasibility of my current work.

Importantly, this research would be impossible without ELFIN. I have spent the vast majority of the last decade working on the ELFIN CubeSat mission, the primary enabling technology for the work presented here (as well as work led by others, listed in the publications section of my CV). Chapter 2 details key work performed during the operational lifetime of ELFIN that enabled the scientific viability of the mission. In this chapter, we will also detail some other areas of research that ELFIN has been/can be used to study.

In Chapter 3, we return to theory by deriving the equations of motion that form the experimental test bed for these resonant wave-particle interactions. The remaining chapters are all dependent on various physics explored with these simulations, the methodologies of which are detailed throughout this chapter.

Chapter 4 pits the first iteration of our test particle simulation against reality. We present

two case studies in which modeled fluxes match multi-point spacecraft observed fluxes quite well, demonstrating the potential of using this test particle simulation to explore radiation belt dynamics using only ELFIN's electron precipitation measurements.

Chapter 5 extends the case studies to the realm of statistics. It compares 3 years of statistical ELFIN data of precipitating-to-trapped flux ratios with expectation based on empirical statistical models of wave amplitude binned by MLT, L-shells, and geomagnetic activity. This methodology sufficiently recovers the precipitation rates seen by ELFIN on the dusk, dawn, and daysides, but significantly underestimates the contribution of whistler-mode waves towards relativistic electron precipitation on the nightside.

Chapter 6 explores this nightside discrepancy by modeling secondary wave characteristics such as wave frequency, wave obliquity, and local plasma density, which we originally expected to have trivial effects. Aided by a 3-D quasi-linear diffusion code in addition to test particle simulations, we showed that each modifications individually made negligible changes at various energy ranges. Surprisingly, we concluded that all the effects, when combined, significantly amplified the wave-particle interactions with relativistic electrons compared to 100 keV electrons, and yielded potential solutions that aligned well with all statistically-averaged empirical data.

We end with Chapter 7 by presenting the best-fit whistler-mode wave properties for recovering accurate populations of whistler-driven energetic electron precipitation and discussing what the future of this work may hold.

CHAPTER 2

The ELFIN Mission and its Operations

2.1 Introduction

The Electron Loss and Fields INvestigation with a Spatio-Temporal Ambiguity-Resolving (officially ELFIN-STAR, but also ELFIN* or just ELFIN) mission comprises of two 3U+ CubeSats developed, built, and operated by several generations of undergraduate students at UCLA. Both ELFIN CubeSats launched together on Sept 15th, 2018 into a ∼450 km circular polar orbit with a 93° inclination. After 4 fulfilling years on orbit, ELFIN-A re-entered on Sept 17th, 2022 and ELFIN-B re-entered on Sept 30th, 2022, thereby concluding the operational phase of the mission. ELFIN was designed to capture, for the first time, capture the energy distributions of energetic electrons and ions with pitch-angle resolution high enough to resolve the bounce loss cone. The primary objective of ELFIN was to determine storm-time precipitation rates and elucidate the variety of different mechanisms that can lead to such particle losses. ELFIN accomplished this using an Energetic Particle Detector for Electrons and Ions (EPDE, EPDI) – capable of measuring the energy and pitch-angle distributions of energetic electrons and ions with $\Delta E/E = 40\%$ across 16 energy channels between 50 keV and 5 MeV – along with a Fluxgate Magnetometer (FGM) deployed at a distance of ∼75 cm to avoid noise from the spacecraft bus. By spinning at just over 21 revolutions per minute (spin period ≈ 2.8 sec) with its spin plane aligned with the orbital plane, ELFIN's 16 sectors per spin yielded a spin phase resolution of $\Delta\alpha = 22.5°$ and allowed for full pitch-angle coverage with sub-loss cone resolution. From its low-altitude vantage point, ELFIN turned ON its instruments to collect data as it traversed the L-shell ranges $3 < L < 18$, providing a radial snapshot of equatorial processes at a given MLT in

what we called a "Radiation Belt Crossing" or "Science Zone" (SZ).

This was unique because no previous mission had been able to achieve such measurements of precipitating particle distributions within the outer radiation belt. The loss cone during these science zones collections is around $\sim 65^\circ - 70^\circ$ – whereas it usually is $< 3^\circ$ at the equator – so equatorial missions, like the Time History of Events and Macroscale Interactions during Substorms (THEMIS) (Angelopoulos, 2008), Magnetospheric Multiscale (MMS) (Burch et al., 2016), and Van Allen Probes (VAP) (Mauk et al., 2013) cannot easily resolve any spectral details inside it. Although equatorial, the ERG mission has the ability to measure precipitating electrons from the equator with its high pitch-angle resolution. However, these electron precipitation measurements are limited in energy to < 100 keV due to its extremely narrow field of view (FOV) (Kasahara et al., 2018a). Unfortunately, this does not allow for the study of how particles can be accelerated to such relativistic energies and how off-equatorial processes may affect precipitation rates. There have been a number of low-altitude missions in orbits similar to ELFIN's – such as SAMPEX (Baker et al., 1993), POES (Evans and Greer, 2004), and Firebird II (Crew et al., 2016) – none of which provide either adequate pitch-angle resolution or the appropriate energy range in order to study electron precipitation driven by intense whistler-mode waves. ELFIN's ability to measure precipitating, trapped, and reflected populations of particles in a single spin provided the necessary capability to determine signatures of various types of wave-particle interactions. ELFIN's entire mission was optimized for this purpose, which therefore led to the implementation of a CubeSat with a highly customized, but efficient design.

The challenges associated with a lack of experience within the student-led team were compounded with the complexity of ELFIN's bespoke design, so the development philosophy was to preferentially perform verification by test, rather than analytically. We attribute the nearly flawless performance of the hardware for all four years on orbit to the rigorous testing that various ELFIN prototypes underwent in addition to support from the UCLA staff engineers and technical support from the Aerospace Corporation. A flow chart detailing the Engineering and Flight Model (EM and FM) tests leading up to Pre-Ship Review (PSR) is

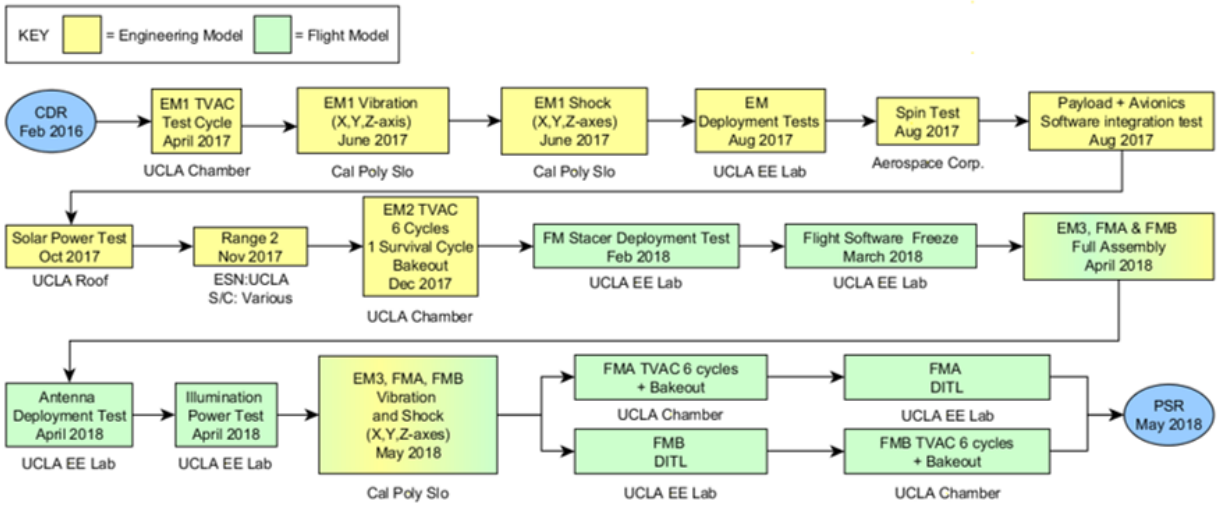


Figure 2.1: This shows ELFIN's major tests performed on the Engineering and Flight Model (EM and FM) ELFIN units between Critical Design Review (CDR) and Pre-Ship Review (PSR) and does not include the multitude of testing performed on Development Models (DM) 1-4, RF (Radio Frequency) models, thermal models, and mass models.

illustrated in Fig. 2.1, and some of the most important risk reduction tests are listed below.

1. Frequent TVAC tests at component, subsystem, and system levels weeded out electrical and thermal problems early in the design process.

2. Four vibration test campaigns using mostly mass models were performed prior to EM1 in order to identify problem areas that which could be fixed before actual hardware was put at risk.

3. Deployment tests for antennas and stacers were performed multiple times at expected thermal extremes, in vacuum, and after long stowage periods.

4. Range tests, where the UCLA ground station was used to communicate with an RF mockup far away enough to emulate the path loss associated with transmission to space, were performed to ensure that we could close the link. There were three Range test campaigns: Range 1 was a pathfinder and resolved exposed technical and logistical challenges; Range 2 successfully showed that we could close the downlink link budget; Range 3 (performed after PSR) showed that we could not close the link on uplink.

Operational Period	Time Range	Total RB Crossings	SZs/Month
Commissioning	Sept 2018 - March 2019	0	0
Calibration + Ops 1.0	April 2019 - June 2020	675	∼40
Refactor 2.0	June 2020 - Feb 2021	3255	∼360
Inner Belt Observations	Mar 2021 - Nov 2021	5436	∼600
Wokring Attitude Control	Dec 2021 - May 2022	2558	∼380
Calibrated Ions	June 2022 - Sept 2022	481	∼120
		Total: ∼12,500	

Table 2.1: This table shows the various phases within ELFIN's on-orbit operations. The mission reached a turning point in June 2020 with the release of Refactor 2.0, which greatly enhanced ELFIN's scientific feasibility. Outer Radiation Belt crossings are from $L \in [3, 18]$, while Inner Radiation Belt data collections span $L \in [1.1, 18]$. Only observations where data completeness $> 60\%$ over the whole L-shell range is counted and significantly more data exists for smaller fractions of SZs.

As a result, the team rapidly constructed a new VHF antenna tower prior to launch, without which ELFIN would not have received ground commands post-launch.

5. Spin tests performed at Aerospace Corporation facilities, where an air-bearing spin platform inside a Helmholtz coil was used to validate spin control functionality.

6. EPD calibration tests with radiation sources (performed after PSR) were performed in vacuum to calibrate the energy bins on both the EPDE and the EPDI in the final flight configuration. These tests showed that all detectors were fully functional and allowed us to precisely determine the preamplifier gain as a function of energy.

As challenging as it was to deliver the flight-ready ELFIN CubeSats on time, we were surprised to find how much more challenging it was to continuously operate a satellite for years while maintaining high data throughput. ELFIN data has enabled a wide range of study primarily due to its novel data products, multi-year statistics, full MLT coverage, and thousands of radiation belt crossings. None of this would be possible without smooth daily operations, even with a fully functioning satellite on orbit.

A good metric for assessing the data throughput of the mission is the number of science zones (SZs) ELFIN has successfully downlinked, as itemized throughout various phases of ELFIN's on-orbit life in Table 2.1. This table paints a clear picture of how challenging the

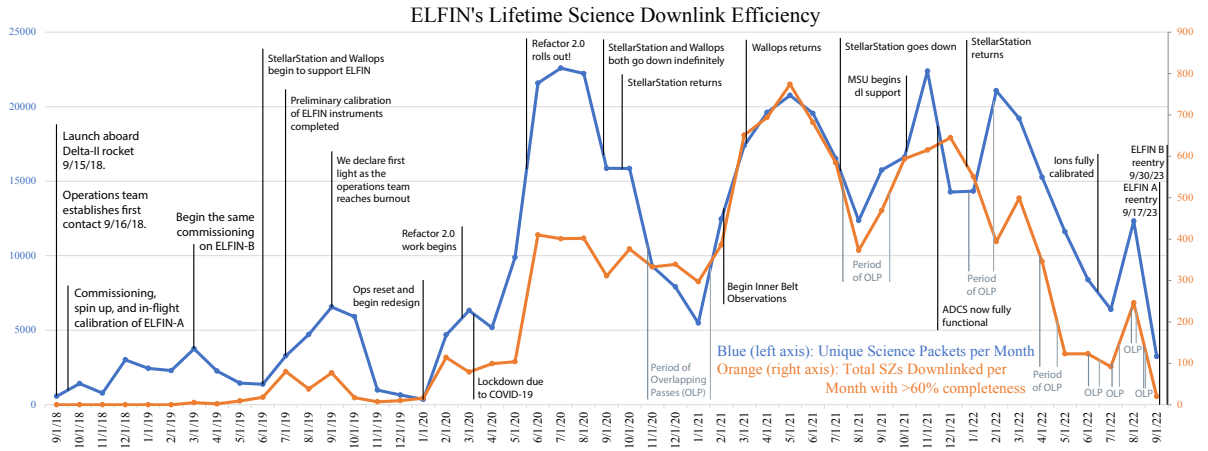


Figure 2.2: We show ELFIN's science packet downlink efficiency (blue, left axis), measured in science packets downlinked per month, as well as science zone downlink efficiency (orange, right axis), measured in number of radiation belt crossings with greater than 60% completeness ratio (ratio of downlinked to collected data packets) per month. We annotate various phases of the mission here, showing the large impact of Refactor 2.0 and how it turned ELFIN into a viable science mission. Various effects cause the efficiency to vary throughout the mission, such as variable external downlink support and increased downlink volume required to support more science/operational objectives.

first two years were, even after commissioning. The $> 12,500$ radiation belt crossings downlinked by ELFIN – from which > 68000 spins were used in statistics for Chapters 5 and 6 – would not have been possible without a complete rethinking of the operational paradigm, called Refactor 2.0, which was implemented in June 2020. This is seen in Fig. 2.2, where ELFIN science zone downlink rates improved considerably after the refactor and remained sustainable until the end of the mission. Science zone downlink efficiency after Refactor 2.0 fluctuated as a function of partner downlink station availability (partners included NASA's Near-Earth Network (NEN) dish-antenna on Wallops Island, StellarStation's antennas in Tokyo, and Montana State University's UHF downlink station), downlink complications from ELFIN overlapping passes (or OLPs, when both ELFINs are overhead during the same passes, effectively halving the available pass time), and desired data volume (SZs/month decreased when downlinking additional inner belt data, attitude data, and/or ion data corresponding with each of ELFIN's more advanced operational phases). It took several months to optimize our operations paradigm around the new software, and our first major update

was released shortly before the first set of overlapping passes (which included significantly more optimized science packets) occurred at the end of 2020. This significantly reduced the error rate at which we downlinked data, as exemplified by the sizable drop in the blue curve (the total number of science packets downlinked), while the orange curve (the total number of SZs downlinked with completeness $> 60\%$) remained relatively stable. When ADCS became fully operational in November 2021 – demonstrating attitude determination and control of both ELFINs to $< 1^\circ$ of precision – it significantly increased the quality of ELFIN science data at the cost of reduced overall science data due to the increased attitude data downlink requirements and even more constrained spacecraft resources. Combined with ion data becoming fully online in June 2022, where each science zone now required 50% more data to downlink, and the rapidly increasing OLPs, resulted in the decrease of SZs per month, although these science improvements drastically increased the value of the science data collected.

This chapter will cover the novel elements of ELFIN's technical execution that enabled such improved data return rates from Refactor 2.0. In Section 2.2, we will cover avionics and flight software. Instrumentation and other mission-level details are already covered in Angelopoulos et al. (2020) and will not be repeated in this chapter. Afterwards, we will focus on the unexpectedly challenging mission operations phase in Section 2.3 and present lessons learned before concluding with a review of the highlights of the scientific contributions that these improvements have enabled in Section 2.4.

2.2 Technical Overview

An expanded schematic view of ELFIN can be seen in Fig. 2.3. The ELFIN payload consists of three primary instruments: (1) an energetic particle detector for electrons (EPD-E) and an energetic particle detector for ions (EPD-I) and (2) the fluxgate magnetometer (FGM). The avionics unit is comprised of 8 PCBs and 4 Li-Ion batteries stacked inside of a PEEK (Polyether Ether Ketone, a type of thermoplastic) frame with a thin aluminum and MLI (Multi-Layer Insulation) blanket shielding for electrical and thermal purposes. The flight

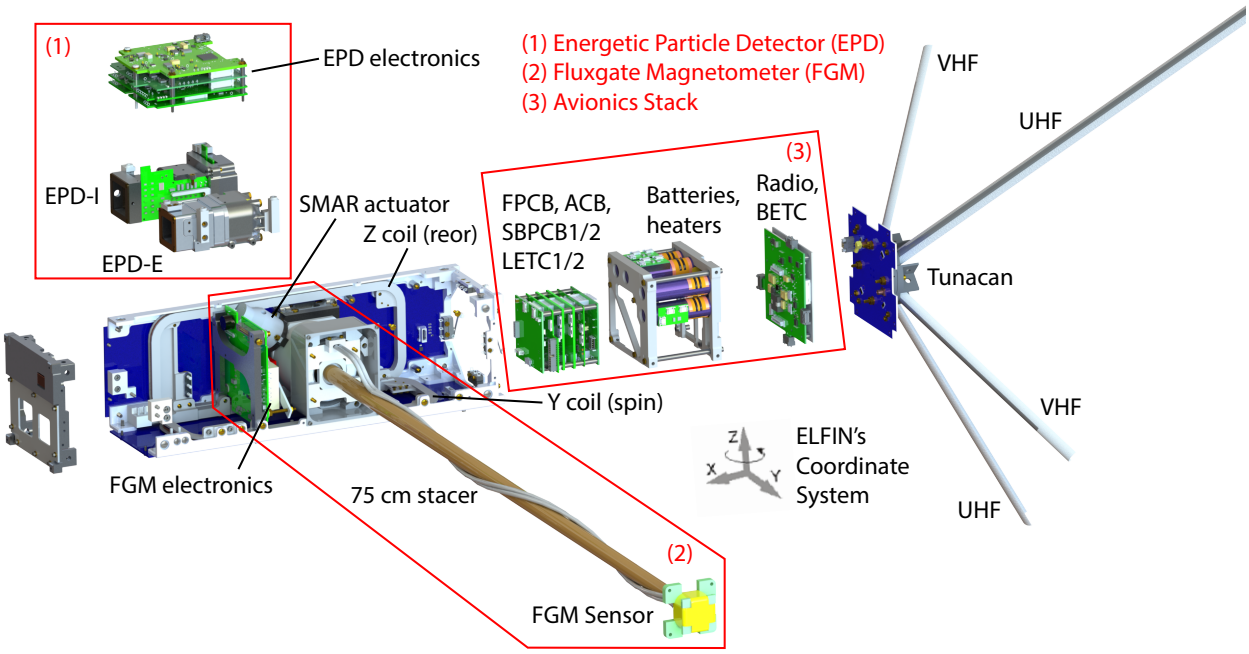


Figure 2.3: Interior components of ELFIN are shown in this expanded view. From left to right: (1) the energetic particle detector instrument (EPD) which includes the electronics (SIPS, IDPU, 2 EPD digital boards, preamplifier, and the front end bias supply) along with the electron and ion sensor heads; (2) the fluxgate magnetometer (FGM) sensor mounted at the end of a 75 cm deployable stacer; and (3) the avionics stack which consists of the flight computer, solar battery power boards, attitude control board, radio, and relevant interface boards. The two pairs of deployable bent-dipole antennas are shown on the right, with the two air coils attached to the chassis.

computer (FPCB), attitude control board (ACB), and two solar-battery boards (SBPCB) were built by the Aerospace Corporation. Each board contains one or two PIC microprocessors with custom software and firmware implemented by UCLA students. Interface and auxiliary boards were also designed and built at UCLA, including two Little Et Cetera boards (LETC1 and LETC2), a big Et Cetera board (BETC), and various small PCBs for battery heaters and harness interconnects. The radio is a custom form factor Helium-82 radio from AstroDev – which is a slightly smaller version of the Helium-100 – capable of VHF uplink and UHF downlink. Power was generated via 20 body-mounted Spectrolab UTJ cells on custom solar panels and stored in 4 Molicel ICR18650J Li-Ion batteries.

There are two deployables on ELFIN: the antennas and the stacer boom. The antennas are stowed in the bonus volume of the 3U+ form factor, and consist of custom rolled up

BeCu/fiberglass elements (built by Loadpath) held down by spectraline as shown in Fig. 2.4e. Deployment occurs when a series of redundant burn resistors are energized, which heat and melt the thin spectraline and allow the antennas to unfurl. The stacer boom is a miniaturized version of the axial booms that flew on THEMIS (designed and manufactured by Kaleva Design) and is pictured at the center of Fig. 2.4a. The chassis and mechanical structure were custom designed and machined in-house. Most components were manufactured at UCLA with 6061 aluminum or PEEK (although brass, copper, tantalum, delrin, and Windform were machined for some applications). The magnetotorquers were custom PEEK frame air coils wound with Elektrisola high-tensile-strength copper-clad aluminum (HTCCA) magnet wire, seen in Fig. 2.4b.

High-fidelity thermal simulations were performed in Thermal Desktop and validated by tests in our Thermal Vacuum (TVAC) chamber. These simulations informed the placement of various thermal treatments and blankets employed throughout the spacecraft. Custom MLI blankets, silver telfon, black kapton, and innovative use of PEEK brackets can be readily seen throughout Fig. 2.4.

Besides the standard challenges of miniaturizing three instruments, electronics, and deployables into a CubeSat form factor, ELFIN's unique science goals imposed unique challenges. By spinning at $\sim$21 RPM with the spin plane aligned with the orbital plane to within 20°, a custom ADCS solution, communication design, and power strategy needed to be implemented. Due to the sensitive fluxgate magnetometer onboard, the spacecraft had to be designed to be magnetically clean, limiting choices on materials, fabrication methods, and test practices. Finally, the spacecraft was designed, built, and operated almost entirely by a body of over 350 undergraduate students across the entire 9 year ELFIN mission (5 year development period, 4 years on-orbit operations), where retaining in-house knowledge and enforcing high technical standards was a significant management-level challenge. There could not be an expectation of full time commitment, and the development, testing, and satellite operations necessarily revolved around the academic calendar. Some of these challenges are touched on in Angelopoulos et al. (2020), but this chapter will focus on the most

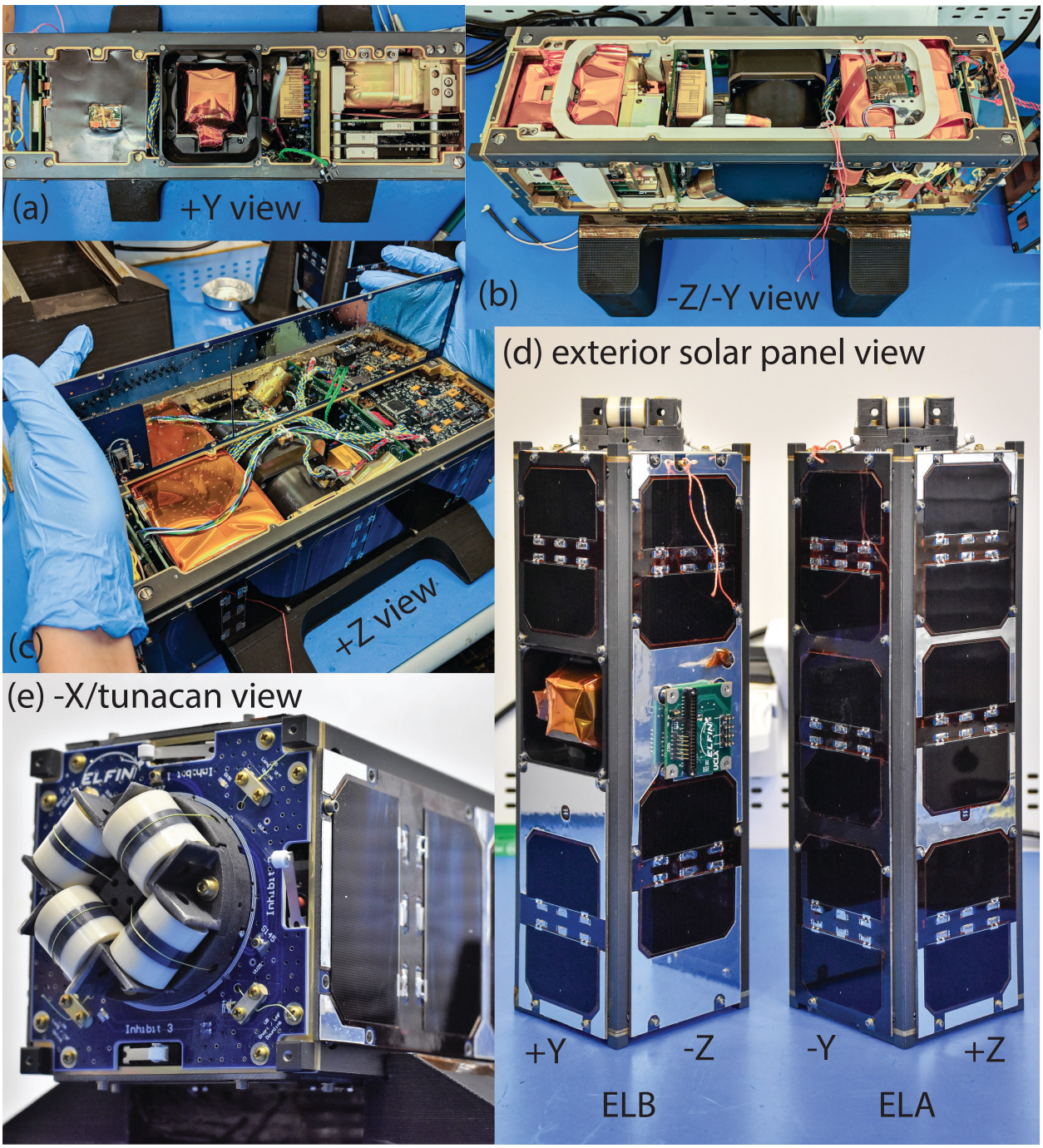


Figure 2.4: ELFIN's flight model from various perspectives using axes defined in Fig. 2.3.

consequential phase of ELFIN: satellite operations. To understand this, we will first describe the onboard avionics system before detailing Refactor 2.0.

2.2.1 Avionics

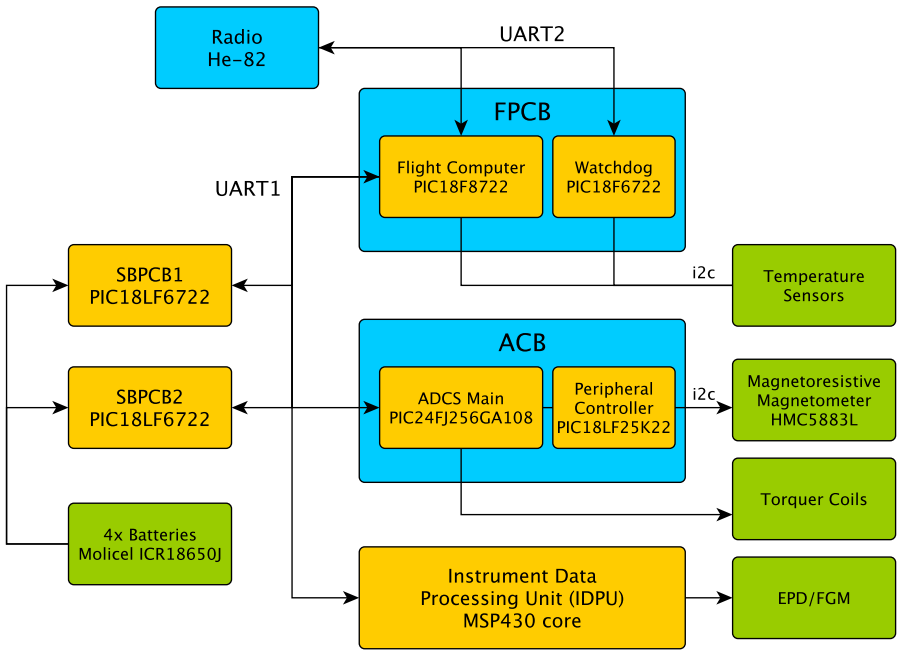


Figure 2.5: Digital block diagram showing ELFIN's two primary UART (Universal Asynchronous Receiver-Transmitter) lines. There are six PIC microcontrollers that work in tandem to maintain spacecraft power, telemetry, telecommanding, and attitude control.

FC+WD Paradigm ELFIN's high-level avionics system block diagram is shown in Fig. 2.5. There are two main UART (Universal Asynchronous Receiver-Transmitter) lines on the avionics stack: UART1 handled all intra-spacecraft communications, while UART2 handled all external communications via the radio. There are two PIC microprocessors on the FPCB: the main Flight Computer (FC), a PIC18F8722, and an external Watchdog (WD), a PIC18F6722. The FC is the central hub for the whole spacecraft and its main responsibilities were as follows:

1. Parse, authenticate, and execute commands received via UART2 from the radio

2. Send commands to the radio and send beacons at specified regular time intervals
3. Command and interface with other boards on the spacecraft (2x SBPCBs, an ACB, and an IDPU)
4. Host script and scheduler functionality and keep track of spacecraft time
5. Aggregate and store spacecraft housekeeping data
6. Maintain logic for safe mode entry and error logging
7. Control core functionality throughout the spacecraft, such as deployables, heaters, and instruments
8. Regularly check aliveness of the WD

The WD – not to be confused with the PIC's internal watchdog – serves as a more robust, programmable, and external watchdog. It sends/receives heartbeat pulses to the FC and resets the whole spacecraft bus if it detects the FC is unresponsive (conversely, if the WD is unresponsive, the FC will reset only the WD, as they are each on separate power rails). The WD resets the FC and main bus on an aggressive time-scale – once every 2 hours – to avoid latchups or undesired effects from extended runtimes on our main program loops. Having both FC and WD on the same UART2 line connected to the radio meant that even if the FC became unresponsive, the WD could parse commands and thus could attempt FC recovery procedures.

Command/Data Protocol The avionics stack runs on our own custom software and firmware across six PIC microcontrollers. Of these, the FC is the brains of the system, managing TT&C, as well as the scripts and scheduler. All of this is based on a simple command and data protocol which, minus authentication, contains a 1-byte start code, a 1-byte op code, a variable-length command payload, a 1-byte CRC (cyclic redundancy check), and a 1-byte stop code (Fig. 2.6). The start and stop codes signify the beginning and end of a command, while the op code is a single byte that maps to a particular activity that

can be executed by its corresponding PIC. The command payload would be the parameters (if any) for the op code; for example, a payload of `0x0E00F0` following a `0x05` (the `READ` op code) would make the FC read and return 240 (`0xF0`) bytes read from address `0x0E00`.

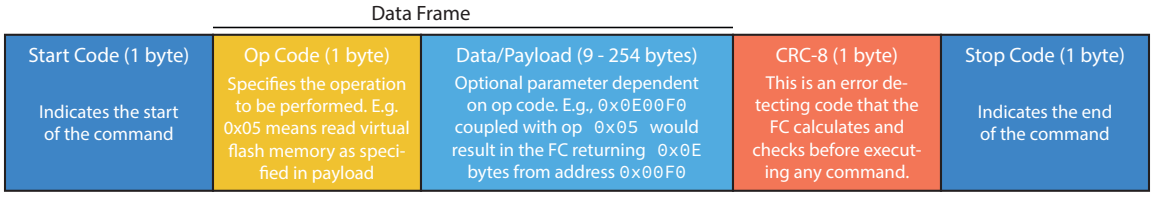


Figure 2.6: ELFIN's command protocol

Packet sizes are limited to the payload limit of the AX.25 packet, which is 256 bytes. If special codes (start, stop, or escape codes) appear in the payload, they would be escaped using the escape code. This could grow the size of packets by a few bytes, so in general, we would limit our command payload size to 246 bytes.

Although this limitation would govern uplink efficiency, most individual commands are much smaller than this maximum size. We take advantage of this by stuffing multiple ELFIN commands into a single AX.25 radio packet. When ELFIN receives a radio packet with multiple ELFIN commands, the FC's command handler processes each of them sequentially. Because radio packets are processed atomically by the FC, commands that are bundled together are guaranteed to also be executed together. This is how we acknowledge (ack) receipt of commands on ELFIN, for example: a `WRITE` command is accompanied with a `READ` command, which reads back what was just written such that it can be validated on the ground. In the original operations paradigm, this was validated by eye in real time during passes, but after Refactor 2.0, this was automatically compared to the desired intent of the command, and programmatically verified.

Despite our ack implementation necessarily meaning the successful uplink of the associated command, the inherent communications design between the Mission Operations Center (MOC) and ELFIN's FC still remains an unreliable service; that is, it does not notify the user if delivery fails. For example, sending a `WRITE` command to the spacecraft could be successful, but on the ground, it is possible to not receive the ack (e.g. due to a weak RF

link or an issue in the downlink pipeline). Because of that, we can no longer be sure of what is onboard the spacecraft, and without the right software, operators can easily lose track of spacecraft state. This uncertainty would pose major challenges to achieving error-free operations, and, therefore, more stringent precautions were taken to ensure consistent knowledge of spacecraft state in Refactor 2.0.

Authentication At the time of ELFIN's design, NASA CubeSat missions did not require uplink authentication or encryption. However, we wanted to ensure that our spacecraft was resilient to replay and DoS (Denial-of-Service)/spam attacks, so we began by implementing a SHA-1 (secure hash algorithm 1) hash, calculated using an incrementing salt, in every uplinked command. However, the FC's PIC18FLF8722 was not powerful enough, taking multiple seconds to calculate the hash onboard, forcing us to look for alternative solutions. In the end, we implemented a version of the lightweight SipHash function (Aumasson and Bernstein, 2012), modified to operate on 32-bit values.

$$\mathrm{MAC}\left(P, S, K\right) = \mathrm{Hash}\left(K, \left(\mathrm{Hash}\left(K, \left(P \parallel S\right)\right) \parallel S\right)\right) \tag{2.1}$$

For every uplinked command, a 64-bit hashed message authentication code (MAC) is appended to each packet, as formulated in Eq. 2.1, right before the CRC and stop code. This code is calculated by taking the byte payload and appending a 4-byte salt, which is hashed with a key. The 8-byte hash result is again hashed by a second key, to produce an 8-byte tag that can be used to authenticate our commands and is resistant to length-extension attacks.

The original idea was to have the 4-byte salt pseudo-randomly change as a function of RTCC, command counters, and various other hskp statistics. However, due to a push for simplicity and a fear that we would lose the ability to command the satellite in the event we lose sync with the clock (or lose the clock altogether), we chose to manually set the 4-byte salt and private key and regularly change them. The salt is publicly broadcasted in our beacon, and in the event ELFIN receives a command containing a bad hash, it will respond

with an 8-byte sync MAC concatenated with 2 bytes of the salt, shown in Eq. 2.2.

$$\text{Sync Mac}(S, K) = (\text{MAC}(\text{Sync Message}, S, K) \parallel S_1 S_2) \tag{2.2}$$

Due to the simplicity of the SipHash algorithm, we can quickly brute force the resynchronization in < 10 s using this bad hash response (this feature is toggleable since leaving it on makes ELFIN vulnerable to DoS/spam attacks).

The other layer of authentication simply relied on the standard AX.25 callsign, which is a part of the AX.25 packet structure and therefore comes for free without costing packet payload size. This feature is included in many modern amateur radios, but not on our Astrodev Radio. As a result, we had to add callsign filtering functionality as an over-the-air (OTA) update, as discussed over the next few paragraphs. These two simple authentication strategies incur little computational cost. Thanks to their simplicity, effectiveness, and successful implementation on ELFIN, NASA adopted authentication requirements into the Space System Protection standard (NASA-STD-1006) for CubeSats and SmallSats without propulsion.

Reprogrammability In-flight reprogrammability was a major risk reduction feature that was very rudimentarily implemented late in our development cycle. However, it proved to be incredibly useful both before and after launch. Over-the-air (OTA) reprogramming involved directly writing assembly instructions into program flash via UART commanding. This would be done by first setting several flags at disparate addresses which then allow the FC to directly write to its own program flash one page at a time. Our reprogrammability implementation on ELFIN had no fail-safes, and as such, was only used when no other options were viable. To make things easier, various configuration settings, default values, and other program constants were deliberately stored at fixed locations in program flash. Reprogramming something more complicated would often involve writing the new instruction set into a region of unused program memory, then strategically inserting jump instructions without altering other code. This strategy relied on the fact that the MPLAB PIC compiler

was not perfectly efficient, so to make room for a jump instruction, we would need to optimize and rewrite the assembly instruction set of a particular page to make enough space for the assembly injection.

During development, we had tested in-place single page reprogramming, multi-page writes (up to 64 pages, one page at a time), and jump insertions. Importantly, we relied on detailed procedures and pre-tested scripts to ensure spacecraft safety during reprogramming events. Our first opportunity to verify this was after ELFIN was already fully built for flight and shortly before delivery. We had realized that there were transients in the PIC GPIOs that could potentially lead to inadvertent early deployments and opted to surgically inject new code to rule out that potential fault path. In addition, we discovered how the Helium radio parsed and transmitted callsigns (it was not in their documentation), so we added a jump to a new callsign filtering function within the execution handler. This made ELFIN more resilient by allowing it to respond only to commands with the appropriate TX/RX callsigns. These were both performed on ELFIN A and ELFIN B after they had already been configured for flight, demonstrating how powerful this capability is while also practicing this capability should the need arise in flight.

Fortunately, an in-flight OTA reprogram occurred only once in flight. A few months after launch, the operations team needed to change the battery heater setpoints on the temperature sensors (TMPs) as the orbits were drifting into longer and colder eclipses. Our WD was originally responsible for initializing and controlling this thermostat behavior, but unfortunately, the communication between the WD and TMPs was found to be unreliable shortly after launch on both satellites. The root cause of this was never determined, but the primary FC-reset functions of the WD were unimpeded. However, we needed reliable TMP sensors and, because of the redundant control of the TMPs built into the hardware, the FC could actually be reprogrammed to initialize and write commands to the TMP sensors. As a result, we wrote new functions and op codes for FC-TMP initialization and setting configurations. This entire workflow was successfully implemented on both ELFIN satellites 3 months after launch, and led to full confidence in ELFIN's batteries remaining within

thermal limits.

Scripts and Scheduling Similar to chaining multiple commands in a radio packet, series of commands can be stored in flash and called upon to be executed altogether. This is called a script, where commands are sequentially stored in flash and are no longer limited by the byte-size limit of radio packets. The primary difference here is that the command sequences are bookended by script start and script stop commands. Scripts are identified by their stored address, and the FC can be commanded to execute any valid script (defined by containing valid commands (which must have valid op codes, payloads, CRCs bookended by start/stop codes) bookended by start and stop script commands). There is a unique script, the boot script, which is a script that is run on first boot. This is useful because scripts are flexible and can be easily modified in operations; throughout the mission, the boot script has been updated to change how successful boot has been signaled, configure battery usage, set particular battery heater setpoints (after the successful OTA reprogram mentioned earlier), or modify housekeeping configurations. It would have been helpful to implement these "checkpoint" scripts in more locations (i.e. every time instruments turn on, or whenever safe mode is entered) as these would allow for easy and safe modifications of onboard behavior via just scripting. To prevent infinite loops, scripts are unable to execute other scripts, but scripts are, instead, allowed to modify the scheduler and, in turn, the scheduler is designed to execute scripts at designated times.

The schedule is a region of flash space that consists of 256 8-byte entries. Each entry is made up of a 6-byte timestamp in Binary-Coded Decimal (BCD) format followed by a 2-byte address which points to a script. Bit flags within the 8-byte schedule entries in the most significant bits for the hour and minute bytes are used to flag the status of the schedule entry, ranging from live (unmodified), executed (MSB on hours), or stale (MSB on minutes). When the FC comes across a timestamp from a live entry that is greater than the current time, the FC will mark the entry as executed and then execute the script at the address of the associated schedule entry. If the FC finds an entry that is scheduled for a time later than one minute after the current time, the FC will mark the entry as stale and will not execute

its associated script. This prevents scripts from inadvertently going off at unintended times should a schedule entry fail for any reason (such as browning out from low battery or being busy with other tasks). The FC reads through the scheduler on each wake-up cycle, around two seconds, and thus, the precision of the scheduler is <2 seconds.

Scripts can schedule or reschedule new entries, and there are a 3 ways this can be done: reschedule to a new specified time, reschedule relative to the current time, and reschedule relative to the existing scheduler time. Rescheduling scripts allows for recursive events to occur (and were intentionally used on various occasions), but is not a flight risk because (1) we can disable the scheduler by entering safe mode and (2) the FC checks for commands after running a script.

Advanced functionality relied entirely on this interplay of using scripts to reschedule other scripts. It would not be until halfway through operations – when Refactor 2.0 was implemented – that we began to maximize the potential of this paradigm. An early example of the effectiveness of this simple design was our payload power ON sequence. This sequence is actually a series of a ∼300 precisely timed commands stored across 8 different scripts totaling a few kilobytes and is summarized below:

1. The first script initialized several other scripts using reschedule commands and is the only script address that will show up in the scheduler (i.e. one science collection takes only one schedule entry). This script had multiple responsibilities: (1) it set the science collection length by rescheduling the stop collection/payload off script; (2) it selected the script that booted the desired instrument program; and (3) it rescheduled the payload power initialization script for two seconds later (i.e. to be executed on the next wakeup cycle).

2. The power initialization script would immediately run on the next FC wakeup cycle, turning on the payload power rails one by one, in a safe and controlled manner. If stable, the last command in this script would reschedule the next script, a specific EPD configuration script, to be executed. Our reschedule command functionality had the capability of rescheduling without changing the associated script address, which

meant we had fixed schedule entries that served essentially as a particular configuration saved in flash. This means that choosing the desired EPD configuration is as simple as writing the two bytes associated with the address of the desired EPD configuration script into a fixed schedule entry.

3. The EPD configuration script – which configures energy bins, histogram settings, and coincidence logic – ends by rescheduling the sector configuration script, which is another fixed schedule entry.

4. The sector configuration script would have specific configurations for how sectoring would work (e.g. zero crossing determination algorithm, phase offsets, and other sectoring settings). The last command here would finally schedule the actual science recording to begin.

5. The stop collection, scheduled by the first script at another fixed schedule entry location, would finally be executed, ending the collection and shutting power down safely.

In this example, several scripts – which handled simultaneous payload housekeeping and attitude data collection – were left out to keep the example straightforward. This fairly simple software setup resulted in an easily adjustable way to schedule fairly complex science operations using just a single schedule entry. However, this hidden complexity was really a downside in disguise and hindered our operations as time progressed due to software that became progressively more challenging and unintuitive to use as the number of activities increased. It was difficult for operators to reliably keep track of both ground and spacecraft state, resulting in a large number of human errors and very poor operational efficiency. This problem was rectified with the complete operational overhaul, Refactor 2.0, described in the following section.

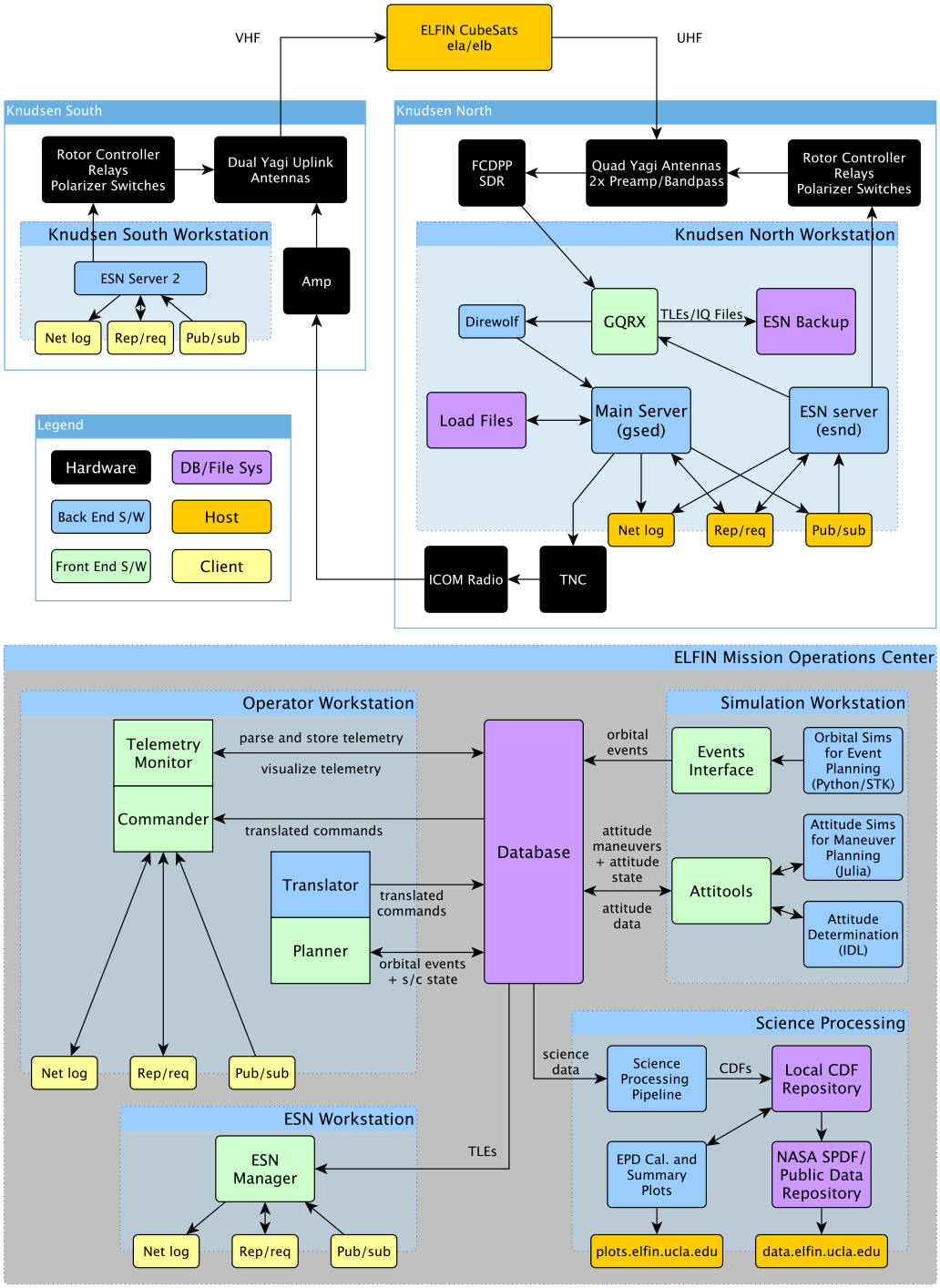


Figure 2.7: Block diagram showing all the various ground components necessary for daily ELFIN operations. The student operations team interfaces primarily with software in the MOC workstations, particularly via the planner and commander. The student developers are responsible for software that handles pass management, satellite tracking, and real time commanding, as well as orbit/attitude simulations, operational planning, science processing, and data distribution.

2.3 Refactor 2.0

In January 2020, we began working to identify flaws with our original operational paradigm while designing a new paradigm that would streamline satellite operations. In March 2020, a tiger team of undergraduates was assembled, and after a technical peer review, began intently working on what would ultimately be called Refactor 2.0. This team included Akhil Palla, Jason Mao, Sharvani Jha, Austin Norris, Chanel Young, James King, and myself. The release of Refactor 2.0 on June 12, 2020 immediately resulted in operators spending 6x less time doing operations (from 3 hrs every day to 1 hr every other day) while successfully downlinking nearly 10x more science zones per month (from ∼40 SZs/month to ∼360 SZs/month). This was achieved by rewriting all ground software and performing minor modifications to onboard FC behavior in order to conform to a newly abstracted structure. In a departure from previous paradigms, the new workflow sought to leave behind ground flexibility in pursuit of ground truth wherever possible. The graphical user interface (GUI) would also be completely redesigned to provide useful state information in a transparent and contextual manner. The following subsections will introduce and define the requisite operational abstractions before explaining the rules and core philosophy.

2.3.1 Key Concepts

The original operational design for planning and scheduling of spacecraft activities was accomplished in the **Planner** software module (running on Operator Workstations in Fig. 2.7). The original Planner had a timeline view which allowed the user to easily view all pertinent orbital events and add spacecraft activities anywhere and anytime. However, matching all these activities with resources used on the spacecraft was too complex to automate and was therefore done manually. As a result, this flexibility led to a confusing experience, where operators were oftentimes juggling several tens of different activities daily, manually keeping track of how the state of each activity evolved over time, and figuring out how the activities eventually mapped to memory to determine where future activities could be stored. As a

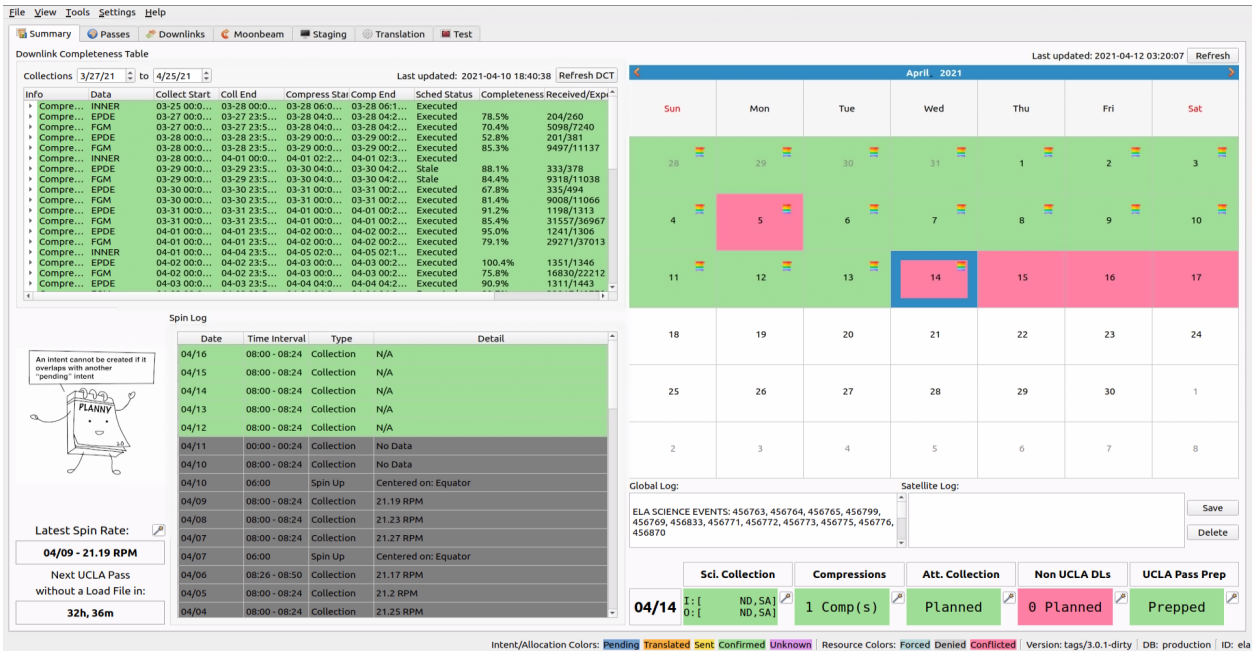


Figure 2.8: A screenshot of Planner version 3.0.1 in April 2021 (while Refactor 2.0 released on version 2.0, Planner 3.0 included new Inner Belt Collection Science collection intents). In the calendar view, green denotes when all necessary Intents are confirmed aboard the spacecraft for that day. This allows operators to quickly tell which days and what activities have yet to be planned. Intent/Allocation states are color coded on the bottom bar. Clicking on the wands will bring up Intent creation wizards for each type of Intent. Clicking on each day shows a summary of the Intents planned at the bottom right. The 14th is red because Downlinks Intents over non-UCLA stations have yet to be created. The Downlink Completeness Table (DCT) on the top left side provides up-to-date downlink completeness percentages and Intent states for each Science Compression Intent. Expanding each of those would show the associated downlink completeness and Allocation state for each of the associated science collections. The spin log on the lower left corner shows the latest spin rates.

result, the operations team had to maintain several supplemental spreadsheets just to assist with the daily operations of ELFIN.

The refactored Planner (Fig. 2.8) did away with the timeline view, instead opting to build the new workflow around "wizards" (similar to generic software installation wizards) where the user interface would guide operators through a sequence of small steps, allowing them to plan each spacecraft activity while following rigid rules. Each spacecraft activity would be associated with an **Intent** – which refers to a high level spacecraft activity, such as collecting science, collecting attitude data, performing attitude maneuvers, compressing science data, etc. – thus, each Intent would have its own dedicated wizard workflow. Each Intent contains a **Scope**, which is the property that allows Intents to be compared to each other, thus

allowing the software to ensure that Intents do not overlap or conflict. For example, science zones were scheduled on a daily basis, so the scope of a Science Collection Intent would be just the date itself. A single Science Collection Intent contains the instructions for all science zone collections for that particular day and the Planner would be responsible for ensuring only one Science Collection Intent for any given date can exist onboard the spacecraft.

To accomplish the activity associated with an Intent, there must be some utilization of physical resources (i.e., memory), either for schedule entries or script space. We therefore discretize the physical memory into **Resources** and define an abstraction called **Allocations**, which refers to the mapping of Intents to their respective Resources. For example, a Science Collection Intent which scheduled 12 science zones in a day would require 12 schedule entries. The Resource for a Science Collection Intent is defined as a chunk of 4 schedule entries (a predefined 32 bytes address space, since each schedule entry is 8 bytes), so there would need to be three Resources allocated for this particular Intent. The Allocation therefore refers to the association of these three Resources with this particular Intent and are thus the most important abstraction to track. Before the refactor, a significant fraction of operational errors involved inadvertent overwrites in memory. To prevent that, the Planner and Commander would enforce rules that disallowed partial modification of any component of Intents. Intents, Allocations, and its associated uplink commands must all be atomic in order to preserve the integrity of our assumptions made when tracking state. In the earlier example, we would still need three resources even if we were collecting 9 science zones in a particular Intent, preferring to often have unused schedule entries in favor of accountable resources.

Even with constraints and rules in place, operations often change, and the software must be flexible enough to change an Intent even after the Allocation has made it onto the spacecraft. This can be accomplished using **Wipes**, which are essentially blanked Allocations of equivalent size for a particular Intent. Atomicity is therefore preserved during Intent modifications. This prevented the existence of partial Allocations onboard the spacecraft, an unfortunately common occurrence before Refactor 2.0 which often led to non-deterministic

behavior from the perspective of ground operations.

Once Allocations are created within the Planner, they are translated into commands via the **Translator** – a software module within the Planner – and exported to the database. Operators can then use the **Commander** to convert the translated output into a **load file**. The Commander is a separate software module that manages both real-time commanding and Load Files: files that store series of commands and associate them with a specific pass. These Load Files are saved on the Main Server and can be executed autonomously even in the event of communication loss to the MOC. See Fig. 2.7 for further details.

With these abstractions in place, we now define the data and knowledge models that then allow for the specification of rules which govern Intents and Allocations. We first begin with the **Ground Truth Model**: an idealized representation of state assuming a perfect computer network with no risk of data loss. It splits the classification of Allocations into three categorizations:

- **Pending** refers to Allocations that do not yet exist aboard the spacecraft (i.e. they exist only in the Planner).
- **Live** refers to Allocations that have been written to the spacecraft and are therefore going to be executed.
- **Stale** refers to Allocations that that have been overwritten or are otherwise invalidated due to, for example, an elapsed timestamp.

However, our communications link is not perfectly reliable (it is possible to drop uplink or downlink packets due to RF nulls (from spinning) in our communications) and our infrastructure within a primarily educational institution – rather than a primarily space mission operations center – does not guarantee 100% uptime for both network access and power, meaning that our knowledge models must be resilient against failures in both uplink and downlink: we cannot always assume commands will successfully make it onto the spacecraft. To handle this, the Planner's state tracking relies on the **Planner Model**, which slightly expands upon the Ground Truth Model:

- **Pending** now refers to Allocations that have not yet been translated into a command (i.e. they are still within the Planner).
- **Translated** refers to Allocations that have been translated but not yet transmitted (i.e. they have left the Planner and are potentially in a Load File waiting to be uplinked during an upcoming pass).
- **Sent** refers to Allocations that have been sent to the spacecraft and may exist onboard, although they have not been verified yet.
- **Confirmed** refers to Allocations that have been verified to be written aboard the spacecraft.
- **Stale** refers to Allocations that have been overwritten by another "confirmed" Allocation or are otherwise invalidated by an elapsed timestamp.

Verifying commands is done by the Commander in real time upon sending/receiving each command. Each command contains both a `WRITE` and `READ` bundled into the same command (see Section 2.2.1) and is linked to an Intent ID and associated Allocation ID. If the readback of the onboard Resources onboard match expectations, the Allocations are marked Confirmed in real time. This is important because in special cases (e.g. wipes), it is desirable to only uplink commands if previous commands have been confirmed to be successful. An Intent state will reflect the weakest state of its Allocations, so that an Intent will only be confirmed if all Allocations within it are also confirmed. These states are color-coded in the Planner GUI (see Fig. 2.8) at both the Intent level (for the overall summary view) and Allocation level (when using the wizard).

The **constraint checker** is the underlying software running within the Planner, that handles logic and adherence to Refactor 2.0 rules throughout all the wizards and planner actions. The states from the Planner Model are further grouped into ground truth states which is used for constraint checking:

- **Possibly live:** "sent" and confirmed".

- **Possibly stale:** "stale" and all but the most recent from "possibly live".
- **Future live:** "translated", "sent", and "confirmed".
- **Future stale:** "stale" and all but the most recent from "future live".

The logical flowchart shown in Fig. 2.9 shows how the constraint checker enforces these rules and acts as a backend module within the Planner which other modules can interface with.

2.3.2 Rules, Assumptions and Overall Philosophy

Leveraging the framework described above, the constraint checker can now enforce the two directives that govern safe operating:

1. Prevent any scheduling conflicts between activities.
2. Handle uncertainty in the safest and strictest way possible.

Prevent scheduling conflicts: Intents with overlapping scopes cannot coexist onboard the spacecraft. If a new Intent overlaps with any existing Intents, the new Intent must include all the resources for which the overlapping Intents have non-stale Allocations that are not wipes. This allows us to make the Intent Scope Assumption: if two Intents of the same type overlap, their scopes are identical. Additionally, new Intents may not interfere with any other already-scheduled activity, and using scope, time-allocation rules must prevent overlap with all other non-stale Intents.

Handle uncertainty: Disallow overwriting active schedule entries and discourage situations in which a new Intent allocates a non-stale resource. If a new Intent allocates a non-stale resource, it must allocate all other non-stale resources which share the same Intent. We also enforce the ordering of Allocations such that any Allocation can only be replaced by a newer Allocation. Stale Allocations are no longer actionable, and an Allocation can only be translated or transmitted if it is not future stale. Because pending Intents

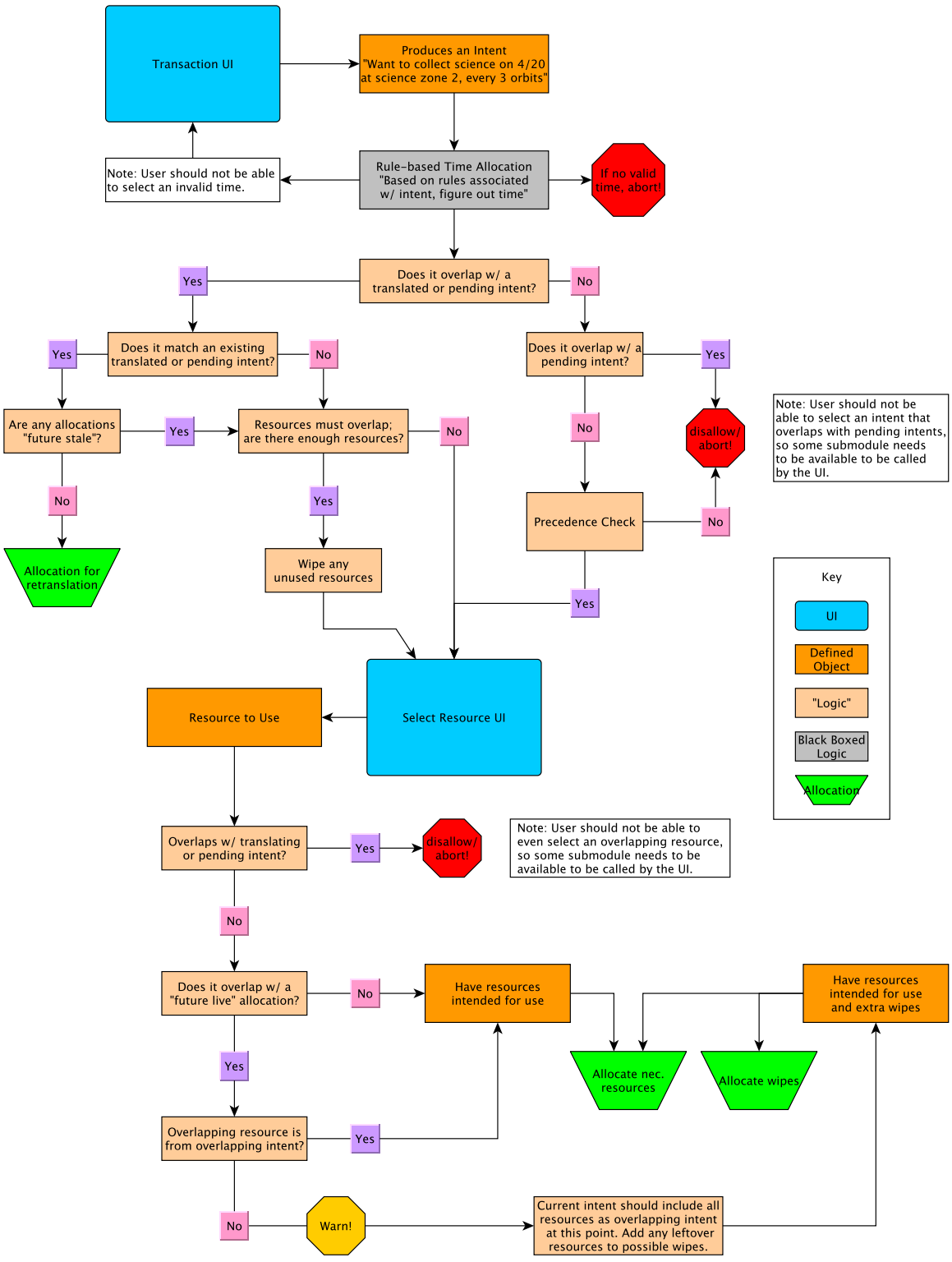


Figure 2.9: Logical flowchart demonstrating the type of decisions the constraint checker would make in order for operators to safely make Allocations.

have no explicit ordering when they exist within the planner, we enforce stricter rules for pending Allocations. Thus, a resource may not be re-allocated while there exists another pending Allocation, and an Intent may not be created if it overlaps with another pending Intent.

These lead to a few key assumptions. The In Order Assumption: Intents exist onboard the spacecraft in the same order in which they were allocated on the ground (FIFO), barring any Intents which were never successfully written. Only the latest translation output can be included in a load file, and if load files contain multiple translated Allocations for the same resource (i.e. wipes or overwriting of resources), the older Allocation only appears in earlier load files than any Allocations which are newer than it. This required upgrading the Commander to be capable of real time command verification and additionally have conditional commanding, opting not to send commands until its prerequisite commands are verified to also be onboard.

We can also make the atomicity assumptions: Allocations are atomic, and Intents are pseudo-atomic. Intents cannot be fully atomic – due to the byte-size limitation of AX.25 packets – and some Intents are too large to fit in a single radio packet. This requires Allocations to only be transmitted along with the rest of their Intent. The discrepancy between the atomicity of Intents and Allocations means special care must be taken to ensure that a mix of two Intents can never simultaneously exist (no "Frankenstein Intents"). If an Intent has too many Allocations to fit in a single uplink frame, the first frame includes a wipe of the entire resource, and the second frame is only transmitted after the wipe succeeds, relying on the conditional commanding framework alluded to in the previous section.

These rules served to provide structure to the complete operational freedom of the original design that allowed too much uncertainty. Whenever an option presented itself, the Planner would delegate set choices to the operator in a safe manner, as dictated by the constraint checker, rather than giving the operator free reign. For example, the resource-picking step in each Intent creation wizard would present a list of all resources with color-coded statuses; the operator can then see all resources and deliberately pick resources rather than allowing

software to automatically pick any free resource. There was still operational freedom, since the operator could pick a live conflicted resource if they so desired, but the constraint checker would force the selection of all other associated resources to preserve the atomicity rule. When generating commands, the Commander would automatically insert wipes as needed to ensure safe uplink of these Allocations. With thoughtful design, these choices were easy for the operator to make because we chose to keep the software transparent while avoiding hidden complexity and nondeterministic behavior.

2.3.3 The Downlink Completeness Table (DCT)

Presenting the operator with contextually useful information was the final major aspect of Refactor 2.0. By taking advantage of the framework described above, we could finally achieve an intuitive and linear operating experience, always providing only the information necessary whenever the operator was presented with decisions. For example, the attitude maneuver wizard would present historical spin rates, historical attitude states, and available/past resources, so operators could make informed decisions when making attitude maneuver intents. However, the most consequential impact from Refactor 2.0 came from the **Downlink Completeness Table** (DCT), a preview of which can be seen in the upper left side of Fig. 2.8. It worked by integrating key aspects of the science data processing pipeline into the Planner and leveraged the new layered levels of insight afforded by the paradigm of Intents and Allocations in order to give operators direct access to information regarding collections of science data, onboard data processing/compression status, and downlink status/completion rates.

The DCT shows all science collections (based on Science Collection Intents), grouped into uncompressed and compressed (based on Science Compression Intents). This was already very helpful because tracking all the different timestamps associated with successfully downlinking science data was very confusing. There are five different types of times that the operator must keep track of when downlinking data that come from each science collection intent: (1) the science collection intent scope; (2) the n timeranges associated with

the n planned radiation belt crossings throughout that given day; (3) the science compression intent scope; (4) up to four science compression timeranges (one for each product: EPDE, EPDI, FGM, and inner belt data); (5) the downlink time (of which data is typically downlinked over 3+ passes to ensure high completeness percentages). This quickly becomes confusing, as there is a large and growing number of new timestamps required for keeping track of command state and future command generation that are produced daily. The proper timerange for downlinking usually does not match what is naturally spoken and can lead to mistakes and confusion. For example, if a scientist communicates to the operations team that the data from January 1st is incomplete and important, the operator would first need to figure out when the data from January 1st was compressed – in this example, we will say it was compressed on January 2nd between 00:00 and 00:30 – then examine the future passes associated with downlinking the compressed data to see if there are still downlinks planned to retrieve this data. If there were issues with the compression, which was common in the earlier operations paradigm, the operator would schedule new compressions of the same data, which would now add even more timestamps to keep track of. Before Intents and the DCT, this was tediously tracked using error-prone spreadsheets. The DCT's transparent metrics were contextually presented to the operator throughout the wizard for generating data downlink Intents, allowing the operator to make the best decisions in prioritizing which data to downlink without ever having to type in timestamps or commands. The user could click and drag exactly what data was desired, and the DCT/Planner software would automatically determine the correct timerange to request. This intuitive selection process eliminated the risk of making typos, which was common when dealing with so many timestamps.

2.3.4 Autohban

The DCT not only saved a lot of time on operations, but also provided a means to rapidly analyze the new influx of science data and radiation belt observations. This was achieved with the Autohban, short for Automated Tohban report, which is a tool for aggregating science data and generating reports to monitor instrument health, performance, and data

quality. Tohban is the Japanese word for "operator" or "duty officer," and in the context of NASA science missions, refers to a scientist whose job is to monitor the science quality of observations and quickly notify the operations team if anything is amiss (sometimes referred to as the Scientist in the Loop (SITL)).

The Autohban aims to automate repetitive work, while still allowing scientists to easily add their own notes. Because of the science collection intents and the DCT, the science processing pipeline can now list all intended science collections (even when the data have yet to be downlinked) and its completeness, putting it all together in context with geomagnetic indicies (AE, Dst, and Kp) to save time for the Tohban.

Dst and Kp indices are easy to pull from the Potsdam and Kyoto servers. However, the daily AE charts provided by Kyoto do not supply the raw data. Instead, our new science processing pipeline pulls the images and uses edge detection to scrape the charts and produce a data product called "Proxy AE". Post-ELFIN, this service has now been moved to the THEMIS mission, and proxy AE can be accessed there.

Weekly (offset by downlink latency), Autohban reports are generated, giving scientists a framework where they only need to mark science zones as one of 5 flags: extremely interesting, potentially interesting, too many gaps (indicating to operators that this science zone needs to be redownlinked), bad data (indicating something wrong with the instruments), and test data (indicating data are used for calibration purposes and are not science worthy). Scientists can also add their own notes (e.g., indicating good conjunctions with other missions, or potential precipitation drivers). These Autohban outputs are evaluated weekly, allowing for a streamlined interface between scientists and operators. Onboard operational issues are therefore quickly found and resolved when they arise, and, compared to before, the operations team can react far more quickly to missing data.

2.4 Reflection and Lessons Learned

Ultimately, ELFIN is a small student-driven development and satellite operations team. An oft repeated phrase in spacecraft engineering is to "push complexity to the ground." In this case, however, a simple but flexible flight software design made satellite operations untenable, incurring significant team attrition and resulting in software that was incompatible with the team it was supposed to help. Instead, design should focus on being as simple and understandable as possible, prioritizing these facets at the cost of performance, flexibility, and other factors. Refactor 2.0 was a significant undertaking that vastly simplified the operational paradigm; as the mission neared reentry, the ELFIN ground operations codebase was over 300000 lines of code and comprised of 15 different custom software modules working in tandem. This is a testament to the difficulty of spacecraft operations, which remains deceptively hard even for small spacecraft missions like ELFIN.

Previously, both the science and operations teams barely understood the limitations of the operational software, so communication between the two was ineffective and often counterproductive. Additionally, the only people who understood the software, the developer team, did not understand the needs of the science and operations team. We fixed this by having developers operate and present metrics to the science team even after the initial rollout of Refactor 2.0. This led to a positive feedback cycle that continually fixed operational problems by focusing on metrics, usability, and transparency. It formalized and standardized both operations and scientific oversight, leading to streamlined operations and a significantly larger volume of science data.

Throughout this process, the development team also learned that simplifying the development process should generally be one of the top priorities. A student-based development team has less experience and less motivation to work on software they do not fully understand. For example, layered code abstracts complexity: this is useful when troubleshooting problems because you can easily isolate it from other layers. Layering should occur logically with a clear distinction (e.g., packets $\rightarrow$ science packets $\rightarrow$ EPD packets). At the architectural level, we divided the Planner into three separate layers: the Intent manager

(handles all interaction to the database, e.g., obtaining and inserting Intents and Allocations), the constraint checker (determines state and enforces rules and logic on Intents and Allocations), and the wizard (the GUI for the creation of Intents and Allocations that utilizes the constraint checker). At a more technical level, we followed layering to ensure that database access, for example, never directly used SQL or ORM in the code, relying instead on a layer of helper functions (in a library or several libraries) to act as an interface to the database. This clear delineation made it easier not only for the developer team to review, troubleshoot, and work on the code, but also for the operators to more easily point out areas for improvement.

A final important lesson learned is to account for the evolving nature of scientists' needs (motivated by new findings and the exploratory nature of science missions), which are often in direct conflict with a paradigm focused on simplification. In order to avoid coding ourselves into a corner, we expanded upon the open-closed principle: software entities should be open for extension but closed for modification. This is embodied by our Intents and Allocations paradigm which were easily extended to perform Inner Belt Collections, Ion collections, special 32-sector collections, and perform new attitude maneuvers. For example, the data structure and schema that made up Science Collection Intents were extended multiple times to support each new feature, but always remained backward compatible via versioning within the Planner framework.

ELFIN's successful mission operations was afforded by a large amount of work and dedication from many UCLA students over 4 years with generous support from scientists and limited support from staff. Both flight and ground software for upcoming UCLA missions greatly benefit from the knowledge acquired throughout this refactor endeavor. In order to advance towards the more affordable spacecraft missions of the future, it is crucial to acknowledge that mission operations hold the same level of importance as well-designed instruments and reliable spacecraft engineering. This recognition is essential to achieve meaningful scientific results as the number of small, low-cost science missions are increasing.

2.5 Electron Precipitation Studies Enabled by ELFIN

ELFIN has, for the first time, enabled studies of the efficiency (precipitating-to-trapped flux ratio) of different drivers of energetic electron precipitation, from the inner belt all the way to the plasma sheet. Without a doubt, these studies would be impossible without the rigorous testing prior to delivery and heroic team efforts that led to the implementation of Refactor 2.0. Throughout its mission lifetime, ELFIN has accumulated more than 12,500 high-quality radiation belt crossings that are usable for science. This unprecedented coverage of electron precipitation measurements has resulted in studies in essentially every facet of magnetospheric physics that result in electron precipitation. The large volume of data achieved by the revised operations paradigm described herein was critical for many aspects of ELFIN research. For multi-case studies and conjunction studies with equatorial missions, it enabled collections over a wide range of activities, local times and geometrical (spatial) configurations. This variety in observations increases confidence in the results often presented with prototypical examples of the impression gained from examining all available cases. Clearly, statistical studies have also been well served by the availability of a large dataset, enabling ensemble studies as a function of space and activity with statistically significant results. Below, we summarize some of the research enabled by ELFIN in just the last 2.5 years.

As discussed in Section 1.2.1, energetic electron precipitation is important to study because it contributes a significant amount of energy input to the atmosphere (especially relativistic electrons penetrating well below 100 km altitude), causing atmospheric changes and is oftentimes correlated with auroral physics (typically driven by the lower-energy range of the precipitating spectrum). Understanding how electrons interact with electromagnetic waves also contributes to the fundamental field of plasma physics. My dissertation covers relativistic energetic precipitation by intense field-aligned waves using magnetic conjunctions with ELFIN and equatorial spacecraft (Chapter 4 and Tsai et al. (2022)); it also uses statistical averages of ELFIN-measured precipitation to study the mechanisms by which whistler-mode waves can achieve such energetic precipitation (Chapters 5, 6, and Tsai et al. (2023); Tsai et al. (2023)). There are several complementary studies of electron scattering

by whistler-mode waves. Using more magnetic conjunctions between ELFIN and a variety of spacecraft and ground stations, Artemyev et al. (2021a) confirmed that ducted whistler-mode waves are likely a significant contributor to relativistic electron losses. An alternative scenario of relativistic precipitation driven by very oblique whistler-mode waves has been considered in Gan et al. (2022a), where a few events of ELFIN-THEMIS conjunction events in support of this hypothesis were analyzed. These very oblique waves were shown to cause similar (but less intense) relativistic electron precipitation by accounting for higher order resonances. Multiple conjunctions of ELFIN with near-equatorial measurements of very oblique whistler-mode waves also revealed new mechanisms of bursty precipitation of sub-relativistic electrons: nonlinear Landau trapping (Artemyev et al., 2022c) and the loss cone overfilling (Zhang et al., 2022c).

Storms are the primary dynamic and energetic phenomena in the inner magnetosphere. Operationally, the team would increase the number of collections/day if active times were predicted, and so there are many instances where ELFIN has multiple successive orbits that allow for outer radiation belt scans of the storm evolution at a relatively rapid 90 minute timestep. These consecutive ELFIN observations allow for the estimation of electron life-times and its comparison with state-of-the-art models. Mourenas et al. (2021) showed that statistical theoretical lifetime models agree reasonably well with electron pitch-angle diffusion rates inferred from the precipitated-to-trapped 100 keV electron flux ratio measured by ELFIN, as well as with timescales of trapped electron flux decay independently measured over several days by ELFIN. This result demonstrates, for the first time, a broad consistency between timescales of trapped electron flux decay, the pitch-angle distribution of precipitated electrons, and quasi-linear models of wave-driven electron loss, which validates the reliability of such statistical electron lifetime models. Using a similar approach, Mourenas et al. (2022b) later showed that measured precipitating electron fluxes were well recovered by quasi-linear diffusion models when the wave field consists of short chorus wave packets of moderate amplitudes (160-250 pT), i.e., wave field modulation to sub-packets essentially leads to more diffusive-like transport electrons toward the loss cone than long packets.

Another large source of relativistic precipitation is the interaction of electrons with electromagnetic ion cyclotron (EMIC) waves, which are very efficient in resonating with > 1 MeV electrons and predominately occur at dusk MLT sectors. Angelopoulos et al. (2023) comprehensively studied this resonant mechanism using ELFIN to characterize the spatial and temporal distribution of EMIC-driven precipitation and validated theoretical predictions of EMIC wave excitation, dispersion, and damping in multi-ion plasmas. Grach et al. (2022b) utilized modeling coupled with ELFIN data to highlight the role of nonlinear resonance with EMIC waves, while An et al. (2022b) demonstrated ELFIN observations of sub-MeV relativistic electron precipitation that could only be explained by non-resonant interactions with EMIC waves. Bashir et al. (2023) explored the combination of whistler-mode waves and EMIC waves working in concert in the post-midnight sector, demonstrating the ability of electrons to be first accelerated by whistlers before being scattered at multi-MEV energies. Finally, Capannolo et al. (2023b) performed a statistical investigation of ELFIN-observed EMIC-driven precipitation in conjunction with POES observations of EMIC-driven proton precipitations.

Recently, there has been a surge in interest in microbursts: short-lived and intense bursts of electron precipitation that can reach MeV energies but last for typically 100 ms. ELFIN was not originally designed to study microbursts, but we have shown that ELFIN can resolve them (Zhang et al., 2022b) when ELFIN observes intense precipitation at the sub-spin time resolution (in fact, within a single sector). For a long time, it was unclear whether microbursts were caused by EMIC and whistler-mode waves or whistler-mode waves alone. However, Chen et al. (2022) used modeling and a conjunction with the Van Allen probes to clearly show that the most probable mechanism for ELFIN-observed microburst generation is electron resonance with ducted whistler-mode waves. The geographic occurrence of microbursts, along with their spatial and temporal scales, was further constrained by Zhang et al. (2023), and exhibited many similarities with the origins of whistler-mode waves.

Despite being less dynamic, field line curvature (FLC) scattering is also a major loss mechanism (and therefore atmospheric energy source) and occurs when the field curvature

radius becomes comparable to the particle gyroradius, resulting in a violation of the first adiabatic invariant and subsequent pitch-angle scattering. When the magnetic fields are no longer able to constrain particles, the entire energy range above a specific minimum energy becomes isotropic at a particular latitude. The dependence of such minimum resonant energy on latitude (i.e. on both equatorial magnetic field intensity and magnetic field line curvature radius) yields an energy dispersion seen in FLC scattering patterns. That energy-latitude dependence marks the "isotropy boundary" (IB), of which their precipitation contribution had never been measured with decent energy resolution prior to ELFIN. Wilkins et al. (2023) used the entire ELFIN data set of electron loss measurements to remotely characterize the properties and locations of IBs and found that they were responsible for 10%-20% (10 MW) of the total average electron precipitation power. In fact, IB energy deposition during active times could reach nearly 100% (1 GW) of the total electron energy deposition across the entire subauroral and auroral zone.

Any mechanism that can cause electron precipitation can be remotely studied using ELFIN. Shen et al. (2022b, 2023b) investigated electron losses driven by kinetic Alfven waves during substorms and plasma injections, while Shi et al. (2022) demonstrated how ULF modulates whistler-mode waves, causing quasi-periodic electron precipitation. Because of the Refactor, ELFIN was able to expand its data acquisition from occasional to routine measurements of the inner belt as well, enabling studies of particle lifetimes and phenomena at lower L-shells. Although the inner belt is more stable, Shen et al. (2022a) found many instances of characteristic WISP precipitation caused by interactions with VLF transmitters. Because these short radiation belt crossings have equatorial footprints that span from the plasmasphere all the way to the plasmasheet, ELFIN's observations provide a radial snapshot of the entire magnetosphere, which is a uniquely rich data set that is applicable to almost every mangetospheric process, mapping anywhere from the inner radiation belt to the polar cap.

2.6 Summary

Despite ELFIN's four successful years on orbit, there were many points throughout the last decade when ELFIN's success seemed entirely out of reach. After successful post-launch operations (acquisition, spin up, and commissioning), a difficult battle of attrition shortly followed where students rotated and burned out too frequently, and motivation was hard to come by as mission operations became tedious, error-prone, and unrewarding. Refactor 2.0 marked a radical rethinking of satellite operations and significantly boosted downlinked science volume while reducing operational workload. This, in turn, provided the necessary statistics to confidently scale our science processing data pipeline. Improved coordination between software developers, spacecraft operators, and the science team enabled an expandable architecture that led to the sustainable relationship between mission operators and scientists. It still took another full year of software development, data analysis, and on-orbit instrument calibration, before ELFIN data was deemed science worthy, with several studies that show the validity and quality of ELFIN data sets using many equatorial comparisons (Angelopoulos et al., 2023; Artemyev et al., 2022a; Tsai et al., 2022, 2023). As of this writing, there have been over 40 ELFIN-enabled publications in scientific peer-reviewed journals, making ELFIN one of the most scientifically productive CubeSat missions across both NASA and NSF's entire CubeSat fleet to date. ELFIN is the strongest example yet of low-cost, high-impact science, made possible by a passionate and dedicated team of students, and enabled by the mentorship of UCLA EPSS staff and partnerships with industry.

In the following chapter, we will detail the test particle simulation used to replicate electron precipitation for comparison with ELFIN measurements. By combining ELFIN data and modeling, we can then analyze the various aspects of whistler-mode wave-particle interactions and quantify their contribution to relativistic electron precipitation.

CHAPTER 3

Test Particle Simulations

3.1 Introduction

Test particle simulations are often used to simplify the motion of particles in prescribed force fields (which are themselves unaffected by these particles). This modeling technique is commonly used to test transport and diffusion theories and is applicable to modeling radiation belt electrons where there are too few electrons to significantly contribute to the self-consistency of the background electric and magnetic fields. In addition, such simulations are able to faithfully represent many of the nonlinear interactions we intend to study, which are often not adequately captured in quasi-linear diffusion codes. This means that there is a fine balance between oversimplifying the dynamics of the system and retaining valid simulation results. And, despite the advent of more powerful computers, test particle simulations still have issues with scale, since each particle is tracked individually. The feasibility of simulating thousands of particles, if not millions, depends significantly on the complexity of the governing equations of motion and the speed of the dynamics.

The goal of this thesis is to understand the resonant interactions between test particles and whistler-mode waves. There are two theoretical approaches to describing this interaction: (1) a direct integration of the Lorentz force equation (e.g. Li et al., 2015a), and (2) a Hamiltonian formulation (e.g. Albert, 1993)), the latter of which we will proceed with here. This chapter will detail the implementation of the large ensemble test particle simulation used throughout the remaining chapters.

3.2 Derivation of Equations of Motion

3.2.1 Basic Simulation Setup

We will begin with a curvature free dipole magnetic field background (Bell, 1984) defined by:

$$\vec{A}_{bg} = -xB_0(z)\,\hat{y} \tag{3.1}$$

$$\vec{B}_{bg} = B_0(z)\,\hat{z} - x\frac{\partial B_0}{\partial z}\,\hat{x} \tag{3.2}$$

The Hamiltonian of a relativistic electron in a magnetic field has the form (Albert et al., 2013):

$$\mathcal{H} = \sqrt{m^2c^4 + c^2\left(\vec{p} + \frac{e}{c}\vec{A}\right)^2} \tag{3.3}$$

where m is electron mass and e is electron charge. Note that (x, y, z) are Cartesian coordinates, implying that dipole field curvature is not accounted for; however, $B_0(z)$ should adequately simulate the effects of a dipole field along a magnetic field line. In our scenario here, the particle will experience both the background magnetic field, $\vec{A}_{bg}$, and the circularly polarized magnetic field from the wave, $\vec{A}_w$. We can presume that the wave magnetic vector potential takes the form

$$\vec{A}_w = A_w \sin\phi\,\hat{x} + A_w \cos\phi\,\hat{y} \tag{3.4}$$

where ϕ is the wave phase and A_w will be defined later as a wave amplitude parameter when we convert to dimensionless variables in Section 3.2.4. Plugging in the whole vector potential:

$$A_{total} = A_w \sin\phi\,\hat{x} + [A_w \cos\phi - xB_0]\,\hat{y} \tag{3.5}$$

gives:

$$\mathcal{H} = \Bigg[m^2c^4 + c^2 \left(p_x - \frac{e}{c} A_w \sin\phi \right)^2 + c^2 \left(p_y - \frac{e}{c} \left(-xB_0 + A_w \cos\phi \right) \right)^2 + c^2 p_z^2 \Bigg]^{1/2} \tag{3.6}$$

3.2.2 Adiabatic Invariant I_x

Before we begin involving any wave interactions, we first obtain adiabatic invariant I_x of the particle with $A_w = 0$ (i.e., no wave contribution, only background field) in order to be able to express (x, p_x) state variables as (θ, I_x) instead, where θ is the gyrophase and the magnetic moment I_x is the conjugated θ momentum. This step allows us to obtain the phase dependence of both the electrons and waves in one equation. Note that the Hamiltonian does not depend on y (i.e., $\frac{\partial \mathcal{H}}{\partial y} = 0$) thus the conjugated momentum p_y is constant. As a result, we can shift the origin of the coordinate system in such a way that $p_y = 0$. Thus the Hamiltonian becomes:

$$\begin{aligned} \mathcal{H} &= mc^2 \sqrt{1 + \left(\frac{p_x}{mc} \right)^2 + \frac{1}{m^2c^2} \left(p_y + \frac{exB_0}{c} \right)^2 + \left(\frac{p_z}{mc} \right)^2} \\ \mathcal{H} &= mc^2 \underbrace{\sqrt{1 + \left(\frac{p_x}{mc} \right)^2 + \left(\frac{p_z}{mc} \right)^2 + \frac{e^2x^2B_0^2}{m^2c^4}}}_{\gamma} = mc^2\gamma \end{aligned} \tag{3.7}$$

With the basic Hamiltonian form (Eq. 3.7), the canonical momenta change becomes:

$$\dot{p}_z = -\frac{\partial \mathcal{H}}{\partial z} = -\frac{mc^2}{\gamma} \frac{x^2e^2B_0^2}{m^2c^4} \frac{\partial B_0}{\partial z} \tag{3.8a}$$

$$\dot{p}_x = -\frac{\partial \mathcal{H}}{\partial x} = -\frac{mc^2}{\gamma} \frac{2xe^2B_0^2}{m^2c^4} \tag{3.8b}$$

These equations demonstrate that the (x, p_x) variables change significantly faster than the (z, p_z) variables, since $\dot{p}_x/\dot{p}_z \sim xB_0/\frac{\partial B_0}{\partial z} \sim R/x \gg 1$ (assuming that our model field varies as the dipole field, so B_0 scales along magnetic field lines as $\partial B_0/\partial z \sim B_0/R$ with the

curvature radius $R \sim LR_E$. Note that the amplitude of x variation is on the order of the electron gyroradius, which is $\ll R$). This makes sense, as the gyro-rotation is prescribed by the phase variables (x, p_x) which should be faster than the bounce oscillations that are described by the (z, p_z) variables. We can now integrate p_x to solve for the adiabatic invariant (the full integral derivation is shown in Section B.1):

$$I_x \equiv \frac{\oint p_x dx}{2\pi} = \frac{mc^2\left[\left(\frac{\mathcal{H}}{mc}\right)^2 - \left(\frac{p_z}{mc}\right)^2 - 1\right]}{2\Omega_{ce}} \tag{3.9}$$

where $\Omega_{ce} = eB_0/mc$. The phase portraits of electron gyromotion can be described as left-handed circular motion, which is expressed by:

$$x = a_x \sin\theta \quad \text{and} \quad p_x = a_p \cos\theta \tag{3.10}$$

where a_x and a_p are newly defined constants that we can solve for using our new fast Hamiltonian and magnetic moment I_x. We do this by collecting all quasi-constants on one side, defining it as h, and leaving (x, p_x) on the other, which yields:

$$\overbrace{\left(\frac{\mathcal{H}}{mc}\right)^2 - \left(\frac{p_z}{mc}\right)^2 - 1}^{h} = \left(\frac{p_x}{mc}\right)^2 + \left(\frac{x\Omega_{ce}}{c}\right)^2$$
$$h = \left(\frac{a_x\Omega_{ce}}{c}\right)^2 \sin^2\theta + \left(\frac{a_p}{mc}\right)^2 \cos^2\theta$$

By virtue of circular motion, both coefficients must be equal to h. From our adiabatic invariant (Eq. 3.9), we can rearrange to get:

$$I_x = \frac{mc^2 h}{2\Omega_{ce}} \rightarrow h = \frac{2\Omega_{ce} I_x}{mc^2}$$

which results in:

$$a_x = \frac{c\sqrt{h}}{\Omega_{ce}} = \frac{c}{\Omega_{ce}}\sqrt{\frac{2\Omega_{ce}I_x}{mc^2}} = \sqrt{\frac{2I_x}{m\Omega_{ce}}} \tag{3.11a}$$

$$a_p = mc\sqrt{h} = mc\sqrt{\frac{2\Omega_{ce}I_x}{mc^2}} = \sqrt{2m\Omega_{ce}I_x} \tag{3.11b}$$

allowing us to convert $\mathcal{H}(x, p_x, z, p_z) \rightarrow \mathcal{H}(\theta, I_x, z, p_z)$:

$$x = \sqrt{\frac{2I_x}{m\Omega_{ce}}}\sin\theta \tag{3.12a}$$

$$p_x = \sqrt{2m\Omega_{ce}I_x}\cos\theta \tag{3.12b}$$

3.2.3 Full Hamiltonian

Combining the original Hamiltonian (Eq. 3.6) and new phase variables allows us to write the complete Hamiltonian equation (refer to Section B.2 for the full derivation):

$$\mathcal{H} = mc^2\left[1+\left(\frac{p_z}{mc}\right)^2 + \frac{2I_x\Omega_{ce}}{mc^2}+\left[\frac{eA_w}{mc^2}\right]^2 - \frac{2\sqrt{2mI_x\Omega_{ce}}}{m^2c^2}\frac{e}{c}A_w\sin(\phi+\theta)\right]^{1/2} \tag{3.13}$$

We now need to incorporate wave interactions, which can be done using perturbation theory. Since $\nabla \times A = B \rightarrow k \times A = B$, then $A_w = B_w/k$. The fourth term in the square root then becomes:

$$\left[\frac{eA_w}{mc^2}\right]^2 = \left[\frac{eB_w}{mc}\frac{1}{kc}\right]^2 = \left[\overbrace{\frac{B_w}{B_0}}^{\ll 1}\overbrace{\frac{\Omega_{ce}}{kc}}^{\approx 1}\right]^2$$

We can clearly see that $A_w \ll 1$, allowing us to Taylor expand around that to first order thereby ridding ourselves of second and higher order terms. That allows us to obtain our

main Hamiltonian with a first order perturbation effect $\mathcal{H}_1$ added on top:

$$\mathcal{H}_0 = mc^2\sqrt{1+\left(\frac{p_z}{mc}\right)^2+\frac{2I_x\Omega_{ce}}{mc^2}} = mc^2\gamma \tag{3.14a}$$

$$\mathcal{H}_1 = \frac{eA_w}{mc\gamma}\sqrt{2mI_x\Omega_{ce}}\sin(\phi+\theta) \tag{3.14b}$$

3.2.4 Dimensionless Variables

We can convert our variables to dimensionless ones with the following substitutions/normalizations:

$$\begin{aligned} z &\to \frac{z}{R} & k &\to kR \\ p_z &\to \frac{p_z}{mc} & \mathcal{H} &\to \frac{\mathcal{H}}{mc^2} \\ t &\to t\frac{c}{R} & I_x &\to \frac{I_x}{mcR} \\ \omega &\to \omega\frac{R}{c} & b &= \frac{\Omega_{ce,eq}}{\Omega_{ce}} \\ \eta &= \frac{R}{c}\Omega_{ce,eq} & \epsilon &= \frac{B_w}{B_0} \end{aligned} \tag{3.15a}$$

$$A_w = \frac{B_w}{k} = \frac{\epsilon B_0(0)}{k} \tag{3.15b}$$

where the new parameters are ϵ, the normalized wave amplitude to equatorial field, η, the normalized spatial scale of the background magnetic field inhomogeneity.

The R-mode whistler wave dispersion relation is given by the R-mode Stix coefficient (Stix, 1962):

$$R = \frac{c^2k^2}{\omega^2} = 1 - \frac{\Omega_{pe}^2/\omega^2}{1-\Omega_{ce}/\omega}$$

which leads to

$$\omega = \frac{\Omega_{ce}}{1 + \left(\frac{\Omega_{pe}}{kc}\right)^2}$$

for parallel propagating waves. We can rearrange this to isolate k, allowing us to define and solve for a dimensionless wave number $K = kc/\Omega_{ce,eq}$:

$$1 + \left(\frac{\Omega_{pe}}{kc}\right)^2 = \frac{\Omega_{ce}}{\omega} = \frac{\Omega_{ce}}{\omega_m \Omega_{ce,eq}} = \frac{b}{\omega_m}$$

where $\omega_m \equiv \omega/\Omega_{ce,eq}$. The plasma density n changes along magnetic field lines, so we use an empirical model $n = n_{eq}\cos^{-5}\lambda$ from (Denton et al., 2006). As a result, $\Omega_{pe}(\lambda) = \Omega_{ce}\Omega_{pe}\cos^{-5/2}\lambda$, where $\Omega_{pe} \equiv \omega_p/\Omega_{ce,eq}$ is the normalized equatorial plasma frequency, thus

$$\begin{aligned}
\left(\frac{\Omega_{pe}}{kc}\right)^2 &= \frac{b}{\omega_m} - 1 \\
kc &= \frac{\Omega_{pe}}{\sqrt{\frac{b}{\omega_m} - 1}} = \frac{\Omega_{pe}\Omega_{ce,eq}\cos^{-5/2}(\lambda)}{\sqrt{\frac{b}{\omega_m} - 1}} \\
K = \frac{kc}{\Omega_{ce,eq}} &= \frac{\Omega_{pe}\cos^{-5/2}(\lambda)}{\sqrt{\frac{b}{\omega_m} - 1}}
\end{aligned} \tag{3.16}$$

We can now convert (Eqs. 3.14) into dimensionless Hamiltonian equations:

$$\mathcal{H}_0 = \sqrt{1 + p_z^2 + 2I_x\eta b} = \gamma \tag{3.17a}$$

$$\mathcal{H}_1 = \frac{\epsilon\eta}{\gamma K}\sqrt{2I_x\eta b}\sin(\phi + \theta) \tag{3.17b}$$

3.2.5 Equations of Motion

The Hamiltonian equations of motion are now:

$$\dot{z} = \frac{\partial \mathcal{H}}{\partial p_z} = \frac{p_z}{\gamma} \tag{3.18a}$$

$$\dot{p}_z = -\frac{\partial \mathcal{H}}{\partial z} = -\frac{I_x \eta b'}{\gamma} - \frac{\epsilon\eta\sqrt{2I_x\eta b}}{\gamma}\cos(\phi+\theta) \tag{3.18b}$$

$$\dot{\theta} = \frac{\partial \mathcal{H}}{\partial I_x} = \frac{b\eta}{\gamma} + \frac{1}{2I_x}\frac{\epsilon\sqrt{2I_x\eta b}}{\gamma K}\sin(\phi+\theta) \tag{3.18c}$$

$$\dot{I}_x = -\frac{\partial \mathcal{H}}{\partial \theta} = -\frac{\epsilon\sqrt{2I_x\eta b}}{\gamma K}\cos(\phi+\theta) \tag{3.18d}$$

$$\dot{\phi} = \eta(Kp_z/\gamma - \omega_m) \tag{3.18e}$$

Note that normalized magnetic field b is dependent on latitude λ (and thus z), so we can derive $b' = \frac{\partial b}{\partial z}$ then as follows:

$$\begin{aligned} b &= \frac{\sqrt{1+3\sin^2\lambda}}{\cos^6\lambda} \rightarrow \frac{\partial b}{\partial \lambda} = \frac{3(27\sin\lambda - 5\sin 3\lambda)}{4\cos^7\lambda\sqrt{1+3\sin^2\lambda}} \\ \frac{\partial \lambda}{\partial z} &= \frac{1}{\cos\lambda\sqrt{1+3\sin^2\lambda}} \\ \frac{\partial b}{\partial z} &= \frac{\partial b}{\partial \lambda}\frac{\partial \lambda}{\partial z} = \frac{3(27\sin\lambda - 5\sin 3\lambda)}{\cos^8\lambda(4+12\sin^2\lambda)} \end{aligned} \tag{3.19}$$

We can do a final variable substitution of $\zeta = \phi + \theta$ and $\mu = I_x\eta$, where ζ is the relative phase difference between the electron gyrophase and the whistler wave phase, and μ is the normalized magnetic moment. Since $\dot{\zeta} = \dot{\phi} + \dot{\theta}$ and we already have $\dot{\theta}$ from Eq. (3.18c), $\dot{\phi}$ comes from $\dot{\phi} = (\partial\phi/\partial z)\dot{z} + \partial\phi/\partial t$ with $\partial\phi/\partial z = k$ and $\partial\phi/\partial t = -\omega$. Rearranging with dimensionless terms, we then get:

$$\begin{aligned} \phi = kz - \omega t \rightarrow \phi &= \frac{K\Omega_{ce,eq}R}{c}z - \omega\frac{R}{c} \\ \dot{\phi} &= \frac{\Omega_{ce,eq}R}{c}K\dot{z} - \frac{\Omega_{ce,eq}R}{c}\omega_m \\ \dot{\phi} &= \eta(K\dot{z} - \omega_m) \end{aligned} \tag{3.20}$$

The final equations of motion are then:

$$\dot{z} = \frac{p_z}{\gamma} \tag{3.21a}$$

$$\dot{p}_z = -\frac{\mu b'}{\gamma} - \frac{\epsilon\eta\sqrt{2\mu b}}{\gamma}\cos\zeta \tag{3.21b}$$

$$\dot{\zeta} = \eta\left(K\dot{z} - \omega_m + \frac{b}{\gamma}\right) + \frac{\epsilon\eta}{2\mu}\frac{\sqrt{2\mu b}}{\gamma K}\sin\zeta \tag{3.21c}$$

$$\dot{\mu} = -\frac{\epsilon\eta\sqrt{2\mu b}}{\gamma K}\cos\zeta \tag{3.21d}$$

3.3 Simulation Implementation

3.3.1 System Parameters

To establish a sense of scale, we first discuss the system parameters representative of the radiation belts. The ratio $\eta = R\Omega_{ce,eq}/c$ depends only on L-shell (for a dipole magnetic field) and is plotted in Fig. 3.1 in black, where the $1/L^2$ dropoff can be seen. By choosing $L = 5$, where chorus waves typically have their largest amplitudes, we see $\eta(5) \approx 4.5 \times 10^3$ (left horizontal line). This is important because from Eq. 3.21, we see that ζ is the variable that changes the fastest since $\dot{\zeta} \sim \eta$. Therefore, for accurate numerical integration of the entire system, the time step dt should be an order of magnitude less than $1/\eta$ (to have $\Delta\zeta \sim \Delta t\eta \ll 1$ for one time step). For reproducible results, we actually find that an integration time step at least 15 times smaller than $1/\eta$ is necessary. This is the main reason the model takes so long to run and efforts to mitigate that are discussed in the next section.

The second key system parameter, ϵ, is defined as $B_w/B_0 \sim L^3$. Nonlinear wave-particle interaction generally occurs when $\epsilon\eta > 1$ (gray curve) (because this results in wave field terms $\epsilon\eta\cos\zeta$ becoming comparable with the background magnetic field terms $\sim \mu b'/\gamma$ in Eq. 3.21. The curve shows that larger amplitude waves are necessary to enter the nonlinear wave particle interaction regime, and that at $L = 5$, we can expect to begin seeing nonlinear effects

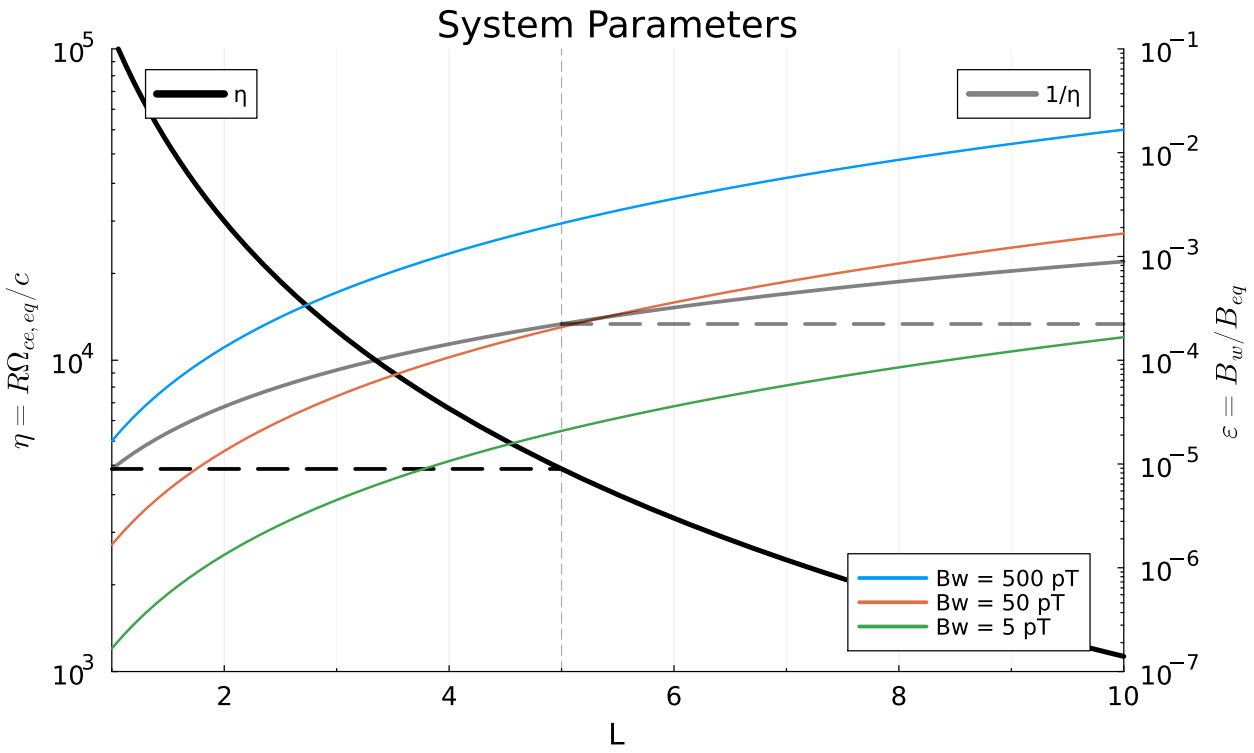


Figure 3.1: System parameters η (left axis, black) and ϵ (right axis, color) are plotted as a function of L-shell. The different colors of ϵ represent three different wave amplitudes. The left horizontal dashed, black line denotes $\eta(L = 5) \approx 4.5 \times 10^3$ and the right horizontal dashed, gray line denotes $1/\eta(5) \approx 2.2 \times 10^{-3}$. Nonlinear effects begin roughly around 50 pT where $\eta\epsilon \geq 1$ (gray curve) for $L = 5$.

when $B_w \geq 50$ pT. Note that this is the typical range for whistler-mode wave amplitudes (Li et al., 2011a,b).

3.3.2 Julia

A single bounce period is typically on the order of ∼100 ms of real time, which corresponds to about ∼5 model normalized time units ($dt = \frac{tc}{R}$). This then requires about 750,000 integration steps to simulate a single bounce period, which becomes prohibitively expensive when scaling to thousands, if not millions of particles. To be able to observe long-term scattering and diffusion, we would normally run the simulation for tens of bounce periods ($\sim 100dt$) with minimum $\sim 10^5$ particles. Luckily, true test particles are the most optimal to parallelize because they do not interact with each other, so each trajectory can be integrated

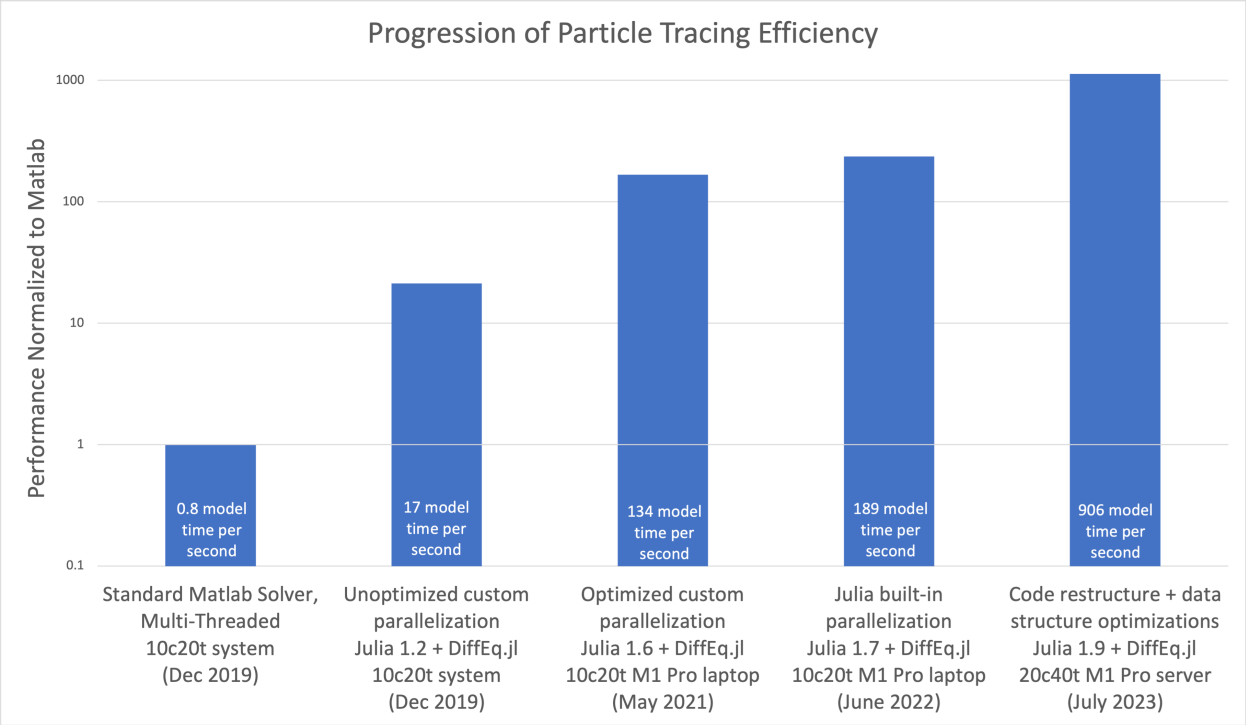


Figure 3.2: Performance improvement over time of my Julia-based test particle simulation code. For reference, performance is normalized to a multi-threaded MATLAB instance. The text in each bar indicates the actual performance in units of model time units integrated per second. Note the various types of software version and hardware.

on a different thread. However, MATLAB parallelized on 20 threads can only calculate 0.8 model time units per second, meaning that this would take $\sim$ 150 days to complete (see performance progression in Fig. 3.2). To optimize the simulation procedure, the integration code is written in Julia (Bezanson et al., 2017), a relatively new scientific computing language that is as performant as C and Fortran for most differential equation solvers (Rackauckas and Nie, 2017).

At the beginning of this research work, Julia was still in its early development days and parallelizing code was not straightforward at all. Fig. 3.2 shows the progression in performance of the simulation of the test particles as Julia versions, compute hardware, and software implementation evolved. In the beginning, great effort was put into writing safe, multi-threaded simulation work and my first attempt achieved only a 20x performance improvement over MATLAB on the same hardware. As Julia documentation improved,

I gained a much deeper understanding of the inner workings of Julia and its differential equations package. With the help of code profilers, I was able to improve my efficiency of the thread safety aspects of my simulation and actual integration itself, gaining nearly another order of magnitude of performance. It was at this time, powerful *and* efficient ARM processors were becoming available on the market, meaning that these heavy test particle simulations could be run on laptops instead of bulky workstations. By the time Julia 1.6 was released, both Julia and DifferentialEquations.jl package had matured significantly and provided built-in threading and significant performance boosts. By replacing all my custom threading code with a single argument, I was able to obtain a 40% speed improvement using the built-in Julia threading. Julia 1.9 brought huge performance improvements to Julia, but also broke a lot of compatibility with previous packages, including many of my data storage techniques. In addition, a continual addition of new effects and modifications, described in later sections, slowed down the solver and a change in the primary goals of the test particle simulation (from modeling many bounce periods to modeling only a single bounce period but orders of magnitude more particles) meant that there needed to be a focus on rapid configurability and the ability to integrate far more particles. A complete code restructure and more optimized data storage of simulation results yielded twice the efficiency as compared to before. Around this time, the ELFIN lab obtained a server with double the ARM cores, which yielded an additional 2x performance boost. By the end of this project, we have increased particle tracing efficiency by 2 orders of magnitude, achieving integration times of far more complex trajectories three orders of magnitude faster than MATLAB's far simpler particle tracing implementation. The earlier example of 150 days on MATLAB would only take 4 hours with my test particle simulation while including the ability to prove a wide range of wave particle interaction physics.

3.3.3 Phase Bunching/Trapping

The energy and pitch angle of electrons only change when the resonance condition is met, thus breaking the adiabatic invariance that corresponds to the crossing of the separatrix in

phase space (Bortnik et al., 2008). By adjusting the amplitude of whistler-mode waves, we can obtain either linear or nonlinear effects. Smaller amplitude waves result in quasi-linear diffusion (Albert, 2010), where

$$D_{\alpha\alpha} \approx \frac{\langle(\Delta\alpha)^2\rangle}{\Delta t_{bounce}}, \quad D_{EE} \approx \frac{\langle(\Delta E)^2\rangle}{\Delta t_{bounce}} \tag{3.22}$$

However, in the case of sufficiently large wave amplitudes, as as previously described in Section 3.3.1, the resonant change in adiabatic invariant is no longer diffusive and rather determined by nonlinear dynamics that manifest as asymmetric changes to the electrons' energy and pitch angle (Albert, 1993). These effects are phase bunching:

$$V_\alpha \approx \frac{\langle\Delta\alpha\rangle}{\Delta t_{bounce}}, \quad V_E \approx \frac{\langle\Delta E\rangle}{\Delta t_{bounce}} \tag{3.23}$$

with negative mean changes of energy and pitch angle (i.e., scattering), whereas phase trapping:

$$\begin{aligned} &\alpha \to \alpha', \quad |\alpha' - \alpha| \gg \alpha \\ &E \to E', \quad |E' - E| \gg E \end{aligned} \tag{3.24}$$

is defined as large jumps that further trap electrons for much longer periods of time (i.e., acceleration). We demonstrate these effects in Fig. 3.3, where we recreate Fig. 1.5 using our own test particle simulation with N=64 particles for $E = 100$ keV and $\alpha = 60°$ for either small or large wave amplitudes.

In the small wave amplitude case, where $\eta\epsilon \approx .1$, the left plots in Fig. (3.3) show that pitch angles diffuse out symmetrically, exhibiting random walk-like motion, as expected in the quasi-linear diffusion regime. The mean energy and mean pitch angle remain constant over time, and only spread 0.1 keV or 0.1°, respectively, within a bounce period. There is no mean change in pitch angle $\langle\Delta\alpha\rangle = 0$, and only a limited increase in variance $\langle(\Delta\alpha)^2\rangle \approx 0.01°$. Therefore, particles would exhibit random spread in their pitch angles in the diffusive regime

$\alpha \sim \sqrt{\langle(\Delta\alpha)^2\rangle t/\tau_{bounce}}$. If we consider particles to be lost at $\alpha_{LC} < 50°$, it would take $\tau_D \sin t_0(\alpha_0 - \alpha_{LC})^2/\langle(\Delta\alpha)^2\rangle \sim \tau_{bounce} \cdot 10^4$ to eventually become lost (where α_0 is the initial pitch angle. Since $\tau_D/\tau_{bounce} \gg 1$, this is an example of weak diffusion. This diffusion rate becomes even smaller at higher energies as the waves resonate far less effectively, which is why the quasi-diffusive treatment of whistler-mode waves has been generally considered incapable of scattering relativistic electrons.

In the large wave amplitude case, where set $\eta\epsilon \approx 15$, the right plots in Fig. (3.3) show nonlinear scattering or phase bunching. This occurs when there is a negative mean change to the energy and pitch-angle at each bounce. Occasionally, there will be a lucky resonance that can kick an electron into a significantly higher pitch angle. This is called trapping, when electrons spend quite a long time in resonance. In this figure, only 1 out of the 64 simulated particles became trapped; however, the probability of this depends on wave parameters and can be quite large for some cases (Omura et al., 2007). The bulk of the electrons will be scattered down in larger steps of 3.5° or 4 keV. This means that the electrons will reach the loss cone in a matter of seconds, orders of magnitude faster than if they were undergoing weak diffusion. Although this could potentially be a very fast way for large pitch-angle electrons to suddenly precipitate into the loss cone, as electrons approach the loss cone they also exhibit greater chance of trapping. This was demonstrated recently by Gan et al. (2020a); Kitahara and Katoh (2019), where both anomalous trapping (i.e., large jumps from within the loss cone or low pitch angles) and positive phase bunching occurred for electrons at low pitch angles. These effects make the overall nonlinear dynamics diffusive over many bounce periods, although on short time intervals with dynamic loss conditions (e.g., bursty precipitations), these nonlinear effects still are important.

3.4 Model Parameters

Test particle simulations are useful to investigate the detailed physics of the wave particle interactions, but, without proper assumptions, or model parameters, they accurately assess

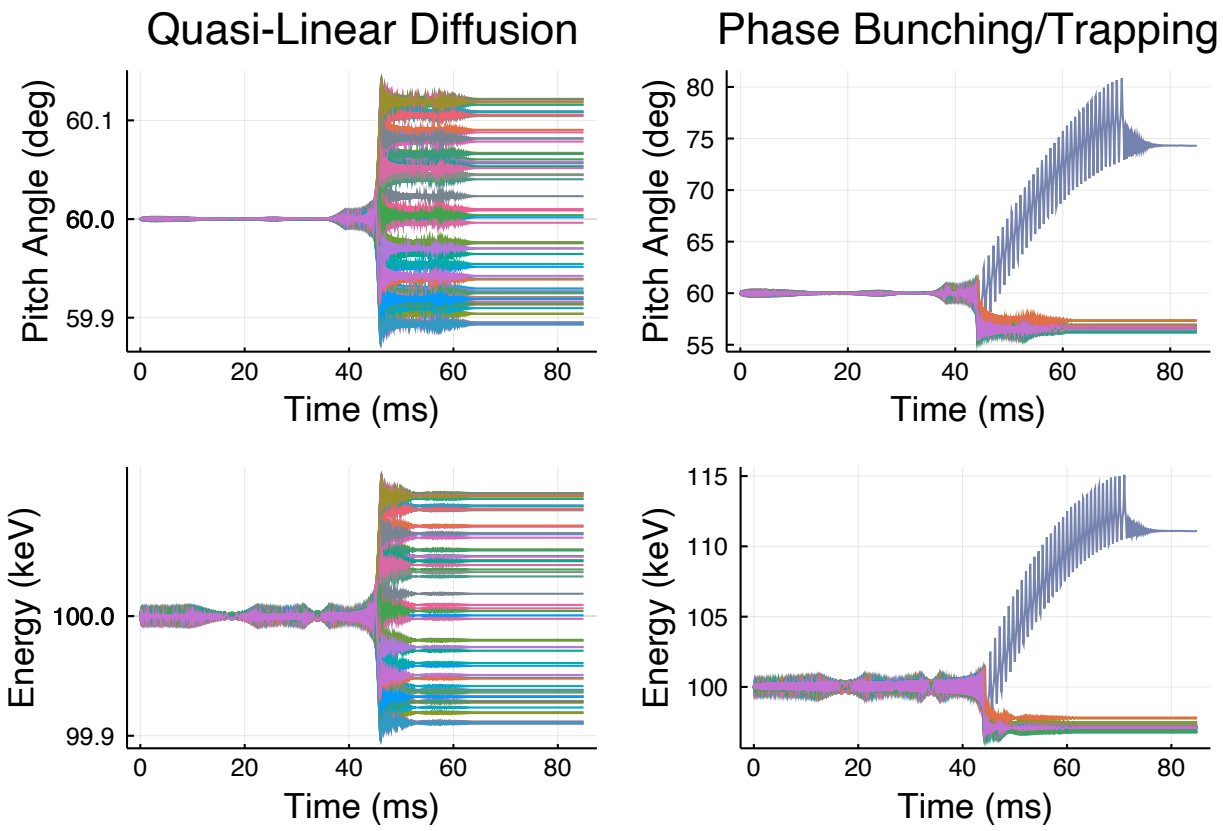


Figure 3.3: The top row shows pitch-angle trajectories over a single bounce period, while the bottom row shows energy trajectories. The panels on the left show the case of quasi-linear diffusion with small wave amplitude ($\eta\epsilon \approx 0.1$). On the right, the panels demonstrate what happens when using large amplitude waves ($\eta\epsilon \approx 15$), which produce either phase bunching (discrete scattering) or phase trapping (large jumps in energy). The only difference within each ensemble of particles is the initial phase difference ζ, which is distributed randomly between 0 and 2π.

the collective behavior of large ensembles of electrons, in the particular system under study. Each of the following subsections will describe such model parameters used in each of the following chapters to add more realism to the system.

3.4.1 Wave Amplitude and Modulation

In Chapter 4, we parameterize the variation of the wave field with latitude and incorporate wave modulation by expressing the vector potential as $A_w/mc^2 = \epsilon f(\lambda)g(\phi)/K(\lambda)$, where $f(\lambda)$ determines the distribution of wave amplitude along magnetic field lines and $g(\phi)$

describes the shape of wave-packets.

Wave amplitude is one of the most important wave properties that determine the outcome of electron trajectories. Whistler-mode chorus waves are typically generated around the equator and propagate toward higher latitudes (Helliwell, 1967). Such propagation is associated with an increase in wave obliquity (e.g., Breuillard et al., 2012; Watt et al., 2013) and the resulting damping due to Landau resonance with suprathermal electrons (Bortnik et al., 2007; Chen et al., 2013). The exception to this wave evolution is the situation where, due to ducting, whistler-mode waves propagate to high latitudes while remaining quasi-parallel, thus avoiding damping (e.g., Karpman and Kaufman, 1982; Pasmanik and Trakhtengerts, 2005; Streltsov and Bengtson, 2020). Statistical data sets collected by off-equatorial spacecraft provide relevant latitudinal wave intensity models (Agapitov et al., 2018; Haque et al., 2010; Wang et al., 2019) which we can incorporate using the function $f(\lambda)$:

$$f(\lambda) = \tanh(\lambda/\delta\lambda_1) \cdot \exp(-(\lambda/\delta\lambda_2)^2) \tag{3.25}$$

where $\delta\lambda_1$ describes the spatial scale of the wave source region ($\delta\lambda_1 \sim$ few degrees; see estimates in (Agapitov et al., 2018)) and $\delta\lambda_2$ describes the spatial scale of wave intensity decay due to damping/wave field divergence ($\delta\lambda_2 \sim$ tens of degrees). We can use this simple analytical model to incorporate the exponential damping of wave amplitude as a function of latitude.

Fig. 3.4 shows 60 trajectories simulated over one bounce period all pertaining to electrons of energy 100 keV and with 6 different initial pitch angles from $\alpha_0 = [5, 80]$. It shows a clear example of anomalous trapping, as lower pitch angles exhibit a significantly higher chance of phase trapping. The electrons that begin trapped, however, are strongly pushed towards the loss cone (phase bunching). The energy plot on the left shows how effective this can be towards electron acceleration as well.

Most whistler mode chorus waves propagate in the form of short packets with $10-30$ wave periods per packet (Zhang et al., 2018b). Additionally, strong modulation of wavepackets can

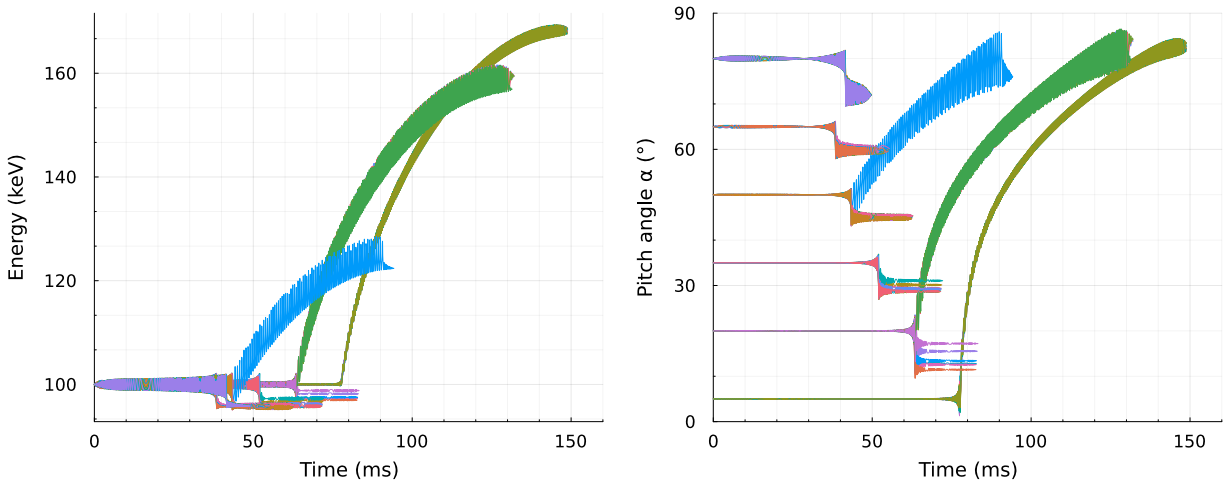


Figure 3.4: Energy and pitch-angle trajectories for electrons interacting with whistler-mode waves that are exponentially damped with latitude. The whole range of diffusive scattering, phase bunching, and phase trapping is on display here.

negate the effects of resonance with individual sub-packets over the long run (Allanson et al., 2020, 2021; Tao et al., 2013) and lead to inefficient nonlinear wave resonance with electrons (e.g., An et al., 2022a; Gan et al., 2020a; Hiraga and Omura, 2020; Mourenas et al., 2018; Zhang et al., 2020b). To account for the effects of finite-size wavepackets and the existence of sub-packet structure, we use the function $g(\phi)$ which specifies the wave-packet modulation in accordance with available observations:

$$g(\phi) = \exp(-a\cos^2(\phi/2\pi\delta\phi)) \tag{3.26}$$

where a controls the depth of the modulation (wave field drops to nearly zero between wave-packets if $a \gg 1$) and $\delta\phi$ controls the number of wavelengths within each wave-packet.

Fig. 3.5 shows the effects of packet modulation, which can disrupt the nonlinear wave particle interactions, restricting large jumps from occurring. Positive phase bunching and negative phase bunching occur at different pitch angles. This effect plays an important role in moderating electron dynamics to more realistic levels.

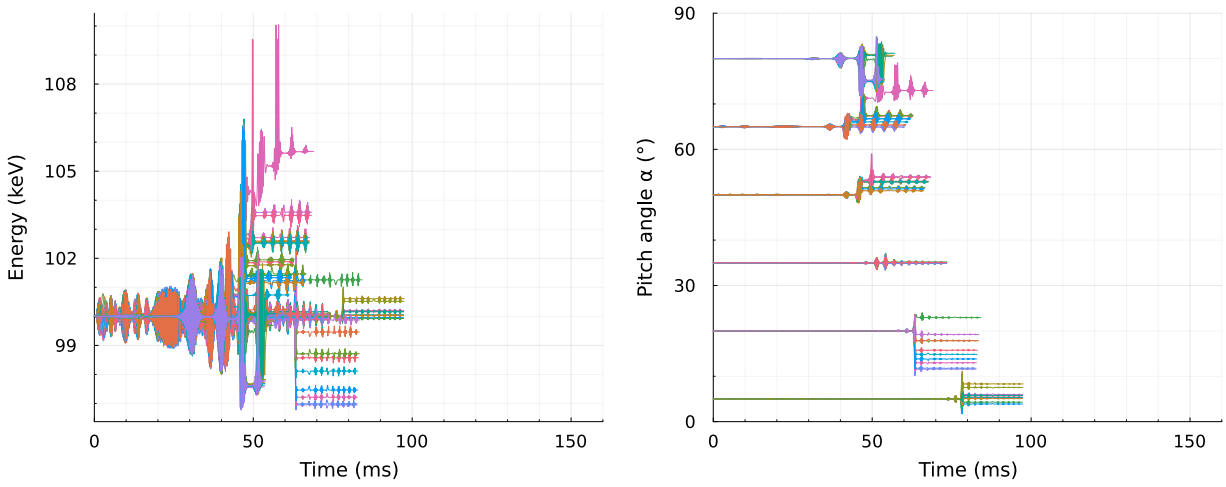


Figure 3.5: Energy and pitch-angle trajectories for electrons interacting with the same whistler-mode waves from Fig. 3.4 except now they propagate as short wave packets, with fairly deep modulation ($a = 5$) and 30 wave periods per packet.

3.4.2 Empirical Wave Amplitude

In Chapter 5, we will replace the exponential decay function $f(\lambda)$ with an empirical model that more realistically describes wave damping as a function of latitude. Now, $f(\lambda) \rightarrow B_w(\lambda, L, MLT, Kp)$ (see model and coefficients in Agapitov et al., 2018) which allows us to use the test-particle simulations to compute the expected precipitation rate consistent with statistically averaged wave intensity latitudinal profiles:

$$\log_{10}\left(B_w(\lambda, \mathrm{Kp}, \mathrm{L}, \mathrm{MLT})\ [\mathrm{nT}]\right) = b_0(\lambda - b_3) \cdot \exp(-\lambda b_2 - b_1) \tag{3.27}$$

$$f(\lambda) = C \cdot B_w \cdot \tanh(\lambda/1^\circ) \tag{3.28}$$

where coefficients b_i are provided by the empirical model as a function of L and MLT, and λ is the latitude in degrees. C normalizes the wave amplitude function to a maximum at unity, while the $\tanh(\lambda/1^\circ)$ term describes wave growth out of the source region (Demekhov, 2011; Katoh and Omura, 2007a; Tao et al., 2017). Fig. 3.6 shows the model used, and we will see that there are two minor differences between our implementation in this study compared to the model in Agapitov et al. (2018).

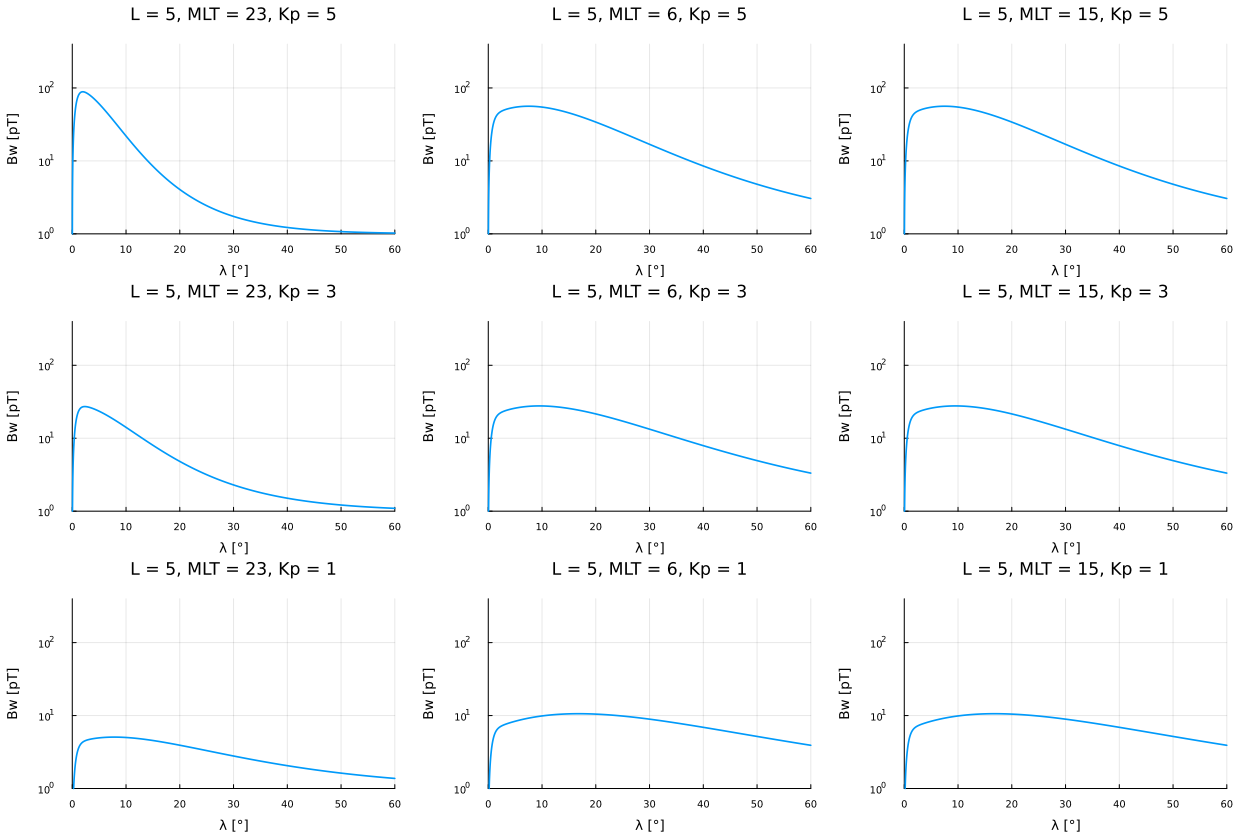


Figure 3.6: Recreation of the empirical wave model shown in Fig. 7 from Agapitov et al. (2018) at a variety of MLTs and Kp indices for L=5. This is slightly modified as described in the text for use in our studies.

First, we change the MLT classification since the coefficients for $12 < \text{MLT} < 23$ are skewed by the relative lack of whistlers in the dusk flank range of $15 < \text{MLT} < 23$. As a result, we use $18 < \text{MLT} < 4$ instead of $23 < \text{MLT} < 4$ for nightside scenarios and $4 < \text{MLT} < 15$ instead of $4 < \text{MLT} < 12$ for dayside scenarios. Thus, the dusk flank is restricted to outside of $15 < \text{MLT} < 18$ and, at least for the case studies, we simply avoid choosing ELFIN observations from this MLT range.

Second, we set the minimum Kp in this model to 3, even if in reality the ELFIN measurements occur when $\text{Kp} < 3$. This is because strong, short-lived precipitation does not correlate well with Kp-index; it is instead more appropriately associated with AE activity tracing electron injections (see dependence of wave intensity on AE in Meredith et al., 2012, and references therein). As such, the presence of intense and bursty precipitation indicates

locally active geomagnetic conditions that would be associated with Kp = 3 for test-particle simulation purposes, despite the reported value of Kp being < 3. For quiet conditions $Kp \leq 2$, the wave intensity provides insufficient levels of precipitating electron fluxes, which is generally corroborated by the extremely low levels (i.e., near background) of precipitating fluxes observed by ELFIN during quiet periods. During disturbed storm times ($Kp > 4$), the precipitating and locally trapped fluxes are occasionally too large and approach saturation of ELFIN's EPDE instrument (see details in Zhang et al., 2022b). Since these types of ELFIN observations (either background-level precipitation or nearly-saturated measurements) will be excluded from statistical analysis, we opt to use $Kp \geq 3$ from Agapitov et al. (2018) as well.

3.4.3 Wave Frequency and Wave Normal Angle

In Chapter 6, we will explore how different wave characteristics affect the efficiency of electron precipitation. In particular, we mostly consider wave frequency, wave obliquity, and their variation along magnetic field lines. To incorporate wave frequency as a function of latitude, we simply modify $\omega_m \to \omega_m(\lambda < 20)^\circ = 0.41 - 0.0125\lambda$ and $\omega_m(\lambda > 20^\circ) = 0.2$ to match the empirical model from Agapitov et al. (2018) (and further discussed in Section 6.1). In order to incorporate wave obliquity, we must first obtain a model of wave normal angle θ (from observations, see Agapitov et al., 2013), which will be further described in Section 6.3. For completeness, including higher-order resonances requires expansion of the wave field over cyclotron harmonics and computing an infinite sum of the contributions from these harmonics:

$$H = mc^2\gamma + \frac{mc^2}{\gamma}\sum_{n=-\infty}^{n=\infty} C_n \sin(\phi - n\psi) \tag{3.29}$$

where ψ is now the electron gyrophase to avoid confusion with wave normal angle θ, with:

$$\dot{\phi} = k(z)\cos\theta(z)\dot{z} - \omega, \quad k(z) = \frac{\Omega_{pe}(z)}{c}\left(\frac{\Omega_{ce}(z)}{\omega}\cos\theta(z)\right)^{-1/2}, \tag{3.30}$$

and C_n (Albert et al., 2013):

$$C_n = \frac{e}{mc\omega}\sqrt{\frac{2I_x\Omega_{ce}(z)}{mc^2}}\left[\frac{E_x - E_y}{2}J_{n-1}\left(k(z)\sin\theta(z)\sqrt{\frac{2I_x}{m\Omega_{ce}(z)}}\right) + \frac{E_x + E_y}{2}J_{n+1}\left(k(z)\sin\theta(z)\sqrt{\frac{2I_x}{m\Omega_{ce}(z)}}\right)\right] + \frac{eE_z}{mc\omega}\frac{p_\parallel}{mc}J_n\left(k(z)\sin\theta(z)\sqrt{\frac{2I_x}{m\Omega_{ce}(z)}}\right) \tag{3.31}$$

and (Tao and Bortnik, 2010):

$$\frac{E_x - E_y}{2} = \frac{B_y}{2}\frac{P - N^2\sin^2\theta}{NP\cos\theta}\left(1 - \frac{D}{N^2 - S}\right) \tag{3.32a}$$

$$\frac{E_x + E_y}{2} = \frac{B_y}{2}\frac{P - N^2\sin^2\theta}{NP\cos\theta}\left(1 + \frac{D}{N^2 - S}\right) \tag{3.32b}$$

$$E_z = -B_y\frac{N\sin\theta}{P} \tag{3.32c}$$

$$N^2 = \frac{k^2c^2}{\omega^2} \tag{3.32d}$$

where P, S, D are coefficients to the dielectric tensor for cold plasma waves as defined in Stix (1962). Every higher order of resonance added to the system increases computational cost by $\mathcal{O}(3n)$, meaning that including up to third-order resonances results in a slowdown of an order of magnitude. Nevertheless, the first-order resonance, $n = 1$, is simple to incorporate and has the biggest effect for moderately oblique or field-aligned waves, with significantly smaller contributions from the next few orders $n = 0, -1, 2, -2, \ldots$. Therefore, we can still incorporate most obliquity effects from a non-zero wave normal angle by setting $n = 1$ which simplifies Eq. 3.31 into:

$$C_n = \frac{e}{mc\omega}\sqrt{\frac{2I_x\Omega_{ce}(z)}{mc^2}}\frac{B_y}{N}\cancel{J_{n+1}(0)}^{\,1} \tag{3.33}$$

The only change then comes from the extra $\cos\theta(z)$ term from Eq. 3.30, which results in wave frequency:

$$\omega = \frac{\Omega_{ce}\cos\theta(z)}{1+\left(\frac{\Omega_{pe}}{kc}\right)^2} \tag{3.34}$$

turning Eq. 3.16 into:

$$K \to K(\lambda) = \frac{\Omega_{pe}\cos^{-5/2}(\lambda)}{\sqrt{\frac{bcos(\theta)}{\omega_m}-1}} \tag{3.35}$$

So, for particle tracing of wave-particle interactions with oblique waves, we can afford the computational cost of incorporating first order resonance, but to see the contributions from higher order resonances, we must use quasi-linear diffusion methods, explained in Section 6.3.1, along with further discussion about wave obliquity in Section 6.1.

3.5 Summary

This chapter details the implementation of test particle simulations used to model linear and nonlinear interactions between electron and whistler-mode waves. A complete derivation of the fundamental Hamiltonian equations of motion is presented, along with several additional modifications to make the system more realistic. Future chapters will refer to work progressively done to improve the realism and ultimately determine what the most important properties are that govern the acceleration and scattering of electrons. Chapter 4 uses finite wave packets and an exponential decay model for wave intensity as a function of magnetic latitude. Absolute fluxes are calculated and reshaped based on equatorially measured electron PSDs. Chapter 5 replaces the exponential decay model with an empirical wave model and statistically examines the global contribution of whistler-mode wave interactions. As such, we are no longer interested in long-term behavior over many bounce periods, but rather just the precipitating-to-trapped flux ratio changes after just one bounce period. Chapter 6 adds in more empirical wave parameters, such as wave obliquity and frequency

models, and additionally compares them with results from quasi-linear diffusion methods. As alluded to in Section 1.3, resonant wave-particle interactions in Earth's magnetosphere can be described either via a quasi-linear diffusion model (Albert, 2010) (typically if the wave intensity is low enough) or by test particle simulations. The regimes in which either methods are valid is still an open question (Allanson et al., 2020; Mourenas et al., 2018; Tao et al., 2013) and will be further evaluated for the case of energetic radiation belt electrons in Chapter 6.

We implemented this test particle simulation in Julia, which is a modern language that is easy to use. The code is publicly available on Github, and various versions are available on the releases page or via Zenodo (Tsai, 2023, 2024). Because the resulting simulation data is very large (a 1 million particle run save file can take $\sim$2 GB), much of the data is made available in a Box link also linked in the Github readme.

A great next step is to use Graphical Processing Units (GPUs) to take advantage of parallelism, which often have many thousands of less sophisticated compute cores. Although consumer-grade GPUs operate in lower floating point precision (often FP16), it should be quite possible to rewrite the test particle simulation for use on enterprise GPUs with full FP64 precision. In its current state, this tool is very useful for quickly checking the trajectories of a variety of physics and nonlinear wave-particle interactions, and can even play a role in being a remote sensing tool to obtain wave characteristics based on electron precipitation measurements from, perhaps, a future CubeSat mission (see Section 7.2). We find that the CPU implementation was generally good enough for simulating millions of particles for a few different cases, as we will present in this thesis, but will require a GPU implementation for forecasting that may rely on real-time input from satellite constellation measurements.

CHAPTER 4

Simulation Validation using In Situ Measurements

4.1 Introduction

Chapter 1 introduced the relevance of studying electron losses driven by whistler-mode waves. In particular, previous work has shown a very strong correlation between whistlers and aurora, reinforced by multi-spacecraft observations during magnetic conjunctions – when two or more separate satellites make simultaneous observations while in the vicinity of similar magnetic field lines – between equatorial and high-latitude locations, such as Van Allen Probes/POES (Li et al., 2013; Ni et al., 2014) or THEMIS/POES (Nishimura et al., 2010). Although these studies have shown a correlation between whistlers and electron precipitation with high certainty, they lack the energy and pitch-angle resolution to investigate precipitating electron distributions. A more recent JAXA mission, the mostly equatorial ERG (Miyoshi et al., 2017) mission, includes a very high pitch-angle resolution electron instrument, MEPe (Kasahara et al., 2018b), which is capable of resolving the loss cone even at low latitudes. Using a single spacecraft, ERG has reinforced previous work, demonstrating very high correlation between the presence of whistler-mode waves and the presence of electrons inside the bounce loss cone (Kasahara et al., 2018a). However, MEPe measurements are limited to < 60 keV. While this is the energy range that has generally been correlated with whistler-driven scattering (Ni et al., 2016; Nishimura et al., 2020; Thorne et al., 2010), such resonant interactions can accelerate plasma sheet electrons to relativistic (e.g., Meredith et al., 2002; Millan and Baker, 2012; Thorne et al., 2013) or even ultra-relativistic (Allison and Shprits, 2020) energies, and pitch-angle scatter energetic electrons into the loss cone causing their precipitation to the atmosphere (e.g., Millan and Thorne, 2007).

This is why the ELFIN mission, presented in Chapter 2, is necessary. These two CubeSats can deliver high pitch-angle and energy resolution measurements of electron fluxes at low altitudes ($\sim 400-450$ km) (Angelopoulos et al., 2020). ELFIN conjunctions with equatorial missions, like Time History of Events and Macroscale Interactions during Substorms (THEMIS) (Angelopoulos, 2008) and Magnetospheric Multiscale (MMS) (Burch et al., 2016) provide an unprecedented opportunity for analyzing whistler-driven electron precipitation and will be the focus of this chapter.

In order to properly compare observations from such disparate locations, we will employ the large ensemble test particle simulations discussed in Chapter 3. This simulation includes all necessary nonlinear physics, such as phase bunching and phase trapping (Albert et al., 2021; Bortnik et al., 2008; Demekhov et al., 2006; Katoh et al., 2008; Kitahara and Katoh, 2019; Omura et al., 2007). In terms of realistic additions to replicate the radiation belt, we will begin with only the simple modifications discussed in Section 3.4.1: exponential wave decay as a function of latitude and wave packet modulation.

We first describe the data sets and spacecraft instruments in Section 4.2.1 before presenting the two selected conjunction events in Sections 4.2.2 and 4.2.3. In the first conjunction, THEMIS-A and -E showed bursts of intense whistler-mode waves propagating in the lower band chorus wave frequency range ($0.1f_{ce}-0.5f_{ce}$), while ELFIN-B observed strong electron precipitation from tens of keV to beyond 300 keV. In the second event, MMS measured three spatially localized sources of intense whistler-mode waves distributed between the inner edge of the plasma sheet and the plasmasphere. Around the same time, ELFIN-A rapidly traversed three bursts of strong electron precipitation (10s to $\sim$ 300 keV) distributed across the outer radiation belt. To compare these data sets with modeled wave-particle resonant interactions, we used a test particle simulation previously introduced in Chapter 3. Detailed results are shown in Section 4.3 and discussed in Section 4.4, where we show that the latitudinal extent of whistler-mode waves is a key parameter controlling the observed scattering of energetic electrons.

4.2 Observations

4.2.1 Datasets

In this chapter, energetic electron fluxes, magnetic field, and/or wave data are used from three missions to analyze two events that reveal the effects of electron scattering due to nonlinear resonance with whistler-mode waves. We used measurements from the ELFIN mission (Angelopoulos et al., 2020): two identical CubeSats, ELA and ELB, each equipped with an Energetic Particle Detector for Electrons (EPDE) instrument measuring pitch-angle resolved fluxes from 50 keV to 5 MeV over 16 energy bins while spinning at roughly 21 RPM. The energy resolution ($\Delta E/E < 40\%$) and angular resolution (16 sectors per spin, or $\sim 22.5^\circ$ spin phase resolution), allow ELFIN to adequately resolve the bounce loss cone in their low-altitude polar orbit and therefore distinguish between precipitating and trapped electron populations. These precipitating electron fluxes are then used for verification of theoretical models predicting equatorial electron scattering by whistler-mode waves.

In the first conjunction event, we utilized two spacecraft (TH-A and TH-E) from the THEMIS mission (Angelopoulos, 2008) for equatorial measurements. The background magnetic field is provided by the fluxgate magnetometer (Auster et al., 2008) and the electron differential fluxes and pitch-angle distributions are provided by a pair of instruments: the electrostatic analyzer (McFadden et al., 2008) for <25 keV electrons and the solid state telescope (Angelopoulos et al., 2008) for $30 - 700$ keV electrons. We use magnetic field and electric field measurements of waves between 10 Hz and 4 kHz obtained by the search-coil magnetometer (SCM) (Le Contel et al., 2008) and the electric fields instrument (EFI) (Bonnell et al., 2008), respectively. During this event, Fast Survey spectra (the FFF data product) was available on THEMIS-A, whereas magnetic and electric field wave-burst waveforms (the SCW and EFW data products, 8192 samples per second) from the search coil magnetometer (SCM) and EFI were available from THEMIS-E.

For the second conjunction event, MMS (Burch et al., 2016) provides the equatorial measurements. The MMS mission consists of four spacecraft that are held in tight formation,

so data from any one spacecraft provide near-identical results for our purposes; thus, we use measurements from MMS-1 here. The Fly's Eye Energetic Particle Spectrometer (FEEPS) (Blake et al., 2016) provides differential flux measurements of electrons in the range of $25 - 600$ keV. Analog and digital fluxgate magnetometers (Russell et al., 2016) provide background magnetic field information, and the search coil magnetometer (Le Contel et al., 2016a) provides magnetic field wave measurements in the range between 2 Hz and 6 kHz. Data was only available in survey mode at this time, so with only 32 samples per second on the SCM, we must infer some equatorial wave properties.

4.2.2 Conjunction Event #1

Fig. 4.1 shows the orbital configuration of the conjunction between THEMIS-A, THEMIS-E, and ELFIN-B that occurred on April 29, 2021. THEMIS-A and -E begin at the plasmasphere around 03:00 UT in an outbound track through the outer radiation belt and into the plasma sheet. The energy spectra (Fig. 4.2a) shows a gradual decrease of relativistic electron fluxes from $L = 5.2$ to $L = 9$ (L in IGRF field is used throughout our analysis). For the entirety of this three-hour period, the FFF data set from THEMIS-A (Fig. 4.2b) shows a clear presence of whistler-mode waves in the lower band chorus wave frequency range (i.e., $0.1 - 0.5$ of the local electron gyrofrequency, f_{ce}). Wave bursts are observed for the entire L-shell range of the outer radiation belt; in particular, two intense wave bursts are seen at $L \in [5.2, 5.5]$ and $L \in [5.8, 6.0]$, close to the observed plasmapause at $L \sim 5.1$ (not shown).

During this conjunction, a six-minute-long equator-ward ELFIN-B crossing of the plasma sheet and outer radiation belts occurred around 03:15 UT. Fig. 4.3a shows the distribution of trapped electron fluxes as a function of L-shell. The plasma sheet (prior to 03:13 UT) is characterized by < 300 keV highly isotropic electrons (average fluxes of precipitating and trapped are about the same; see Fig. 4.3c). The energy of trapped electrons increases as ELFIN moves from the plasma sheet to the outer radiation belt until it crosses the plasmapause at around $L \sim 4$ (shortly after 03:16 UT), where we see a characteristic rapid decrease of energetic electron fluxes. Within the outer radiation belt (from 03:14 to 03:16 UT), ELFIN

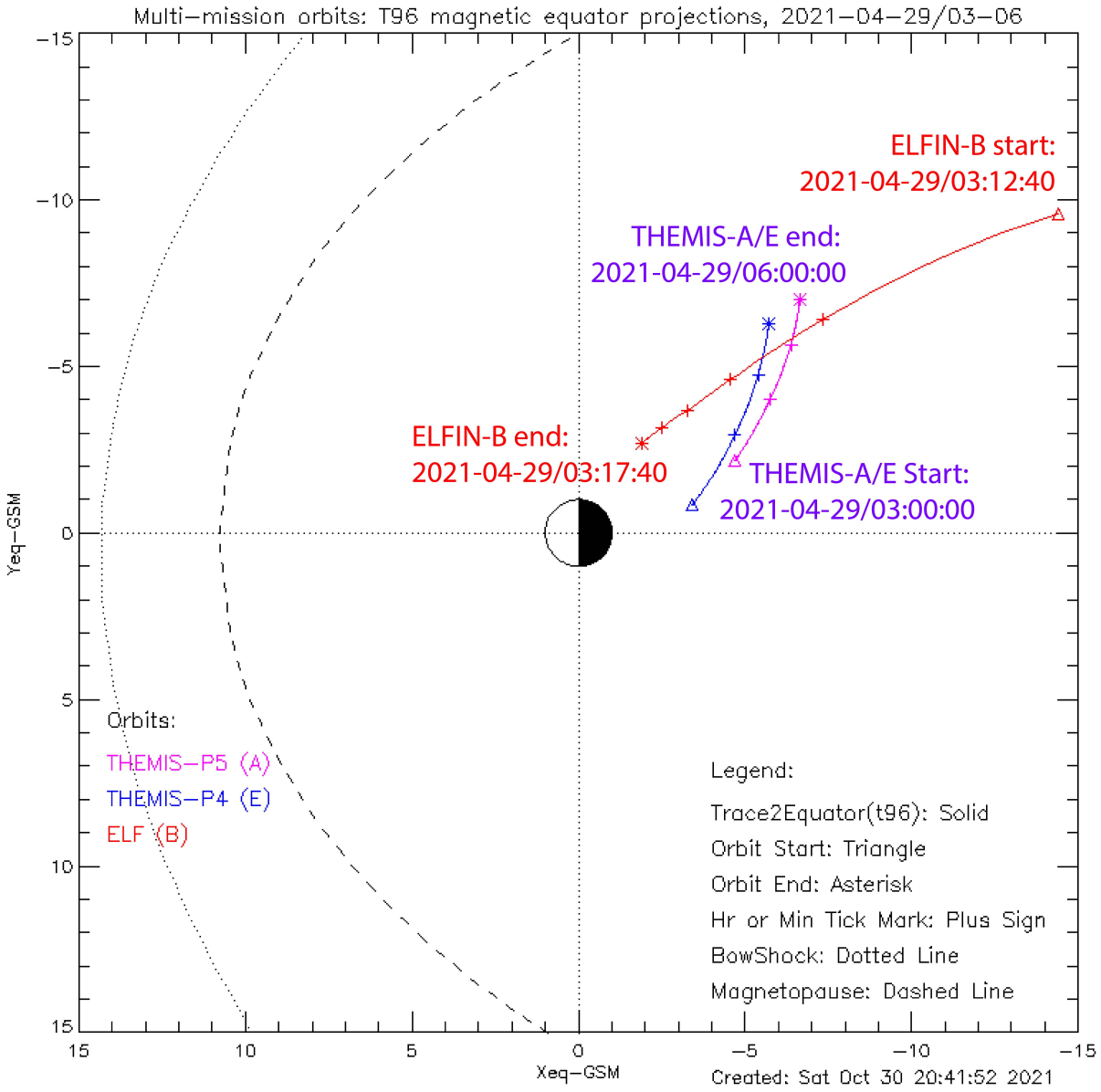


Figure 4.1: Magnetic footprints of the spacecraft orbits traced to the equator are shown using the T96 model (Tsyganenko, 1995) during a conjunction between THEMIS and ELFIN-B. Three-hour intervals are shown for THEMIS-A/E (pink and blue lines), whereas a single radiation belt crossing is shown for ELFIN-B (red line). The plus signs demarcate one-minute intervals for ELFIN-A and one-hour intervals for THEMIS.

observed several bursts of electron precipitation (see electron fluxes in Fig. 4.3b), with the most intense burst at $L \in [5.1, 5.3]$ (between 03:14:45-03:15:00 UT, as marked by the red rectangle). In this burst, ELFIN measures electrons precipitating with energies up to 800

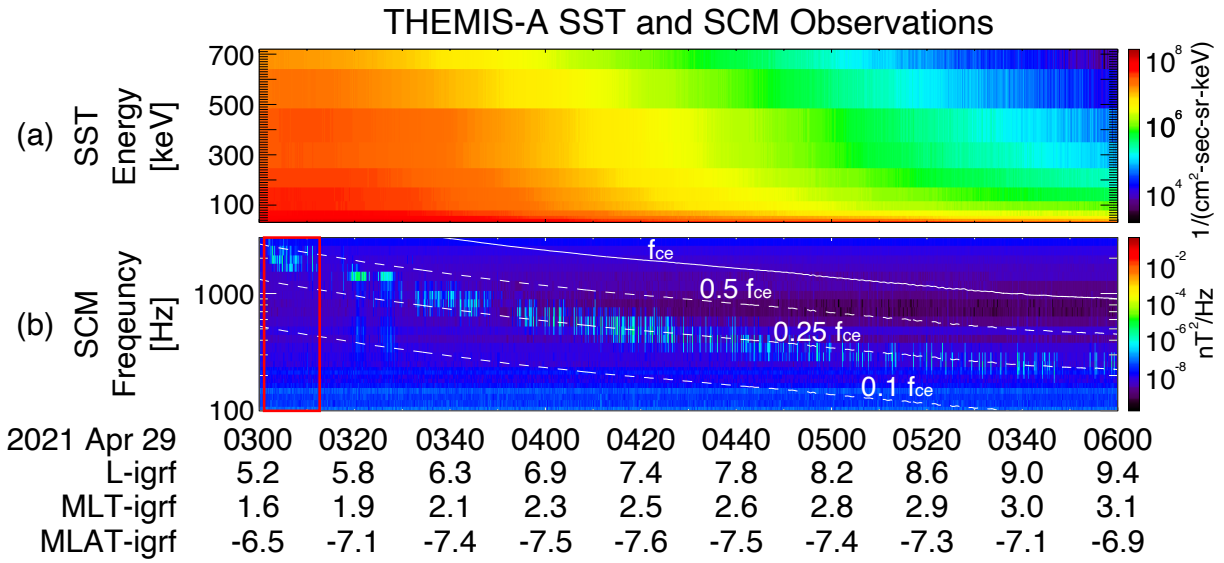


Figure 4.2: THEMIS energetic electron number fluxes and SCM measurements for the first conjunction event on April 29, 2021. The red lines centered at around 03:10 UT indicate the conjunction with ELFIN-B (at $L \in [5.2, 5.5]$), while the dashed white lines denote fractions of the equatorial electron gyrofrequency f_{ce} (solid white line). Whistler-mode waves in the lower band chorus frequency range are evident throughout the entirety of this observation.

keV (see Fig. 4.3b), with the most intense precipitating fluxes (where the precipitating-to-trapped flux ratios are near one) at 300 keV and below (see Fig. 4.3c). We will use THEMIS and ELFIN measurements at this particular precipitation burst to compare with results from our theoretical model of wave-particle resonant interactions.

4.2.3 Conjunction Event #2

The second event occurred on September 22, 2020 and was a conjunction between MMS and ELFIN-A. MMS was on an inbound trajectory (Fig. 4.4), leaving the plasma sheet at around 08:00 UT and entering the plasmasphere around 09:20 UT. During this crossing of the outer radiation belt (between 08:00 and 09:20 UT, as evidenced by the electron spectra measured by FEEPS in Fig. 4.5a), MMS detected three bursts of whistler-mode waves at 08:28 UT, 08:44 UT, and 09:15 UT (Fig. 4.5b). At around 09:16 UT, ELFIN-A observed three bursts of precipitation up to 300 keV (Figures 4.6b and 4.6c) while traversing the outer radiation belt in the southern hemisphere poleward.

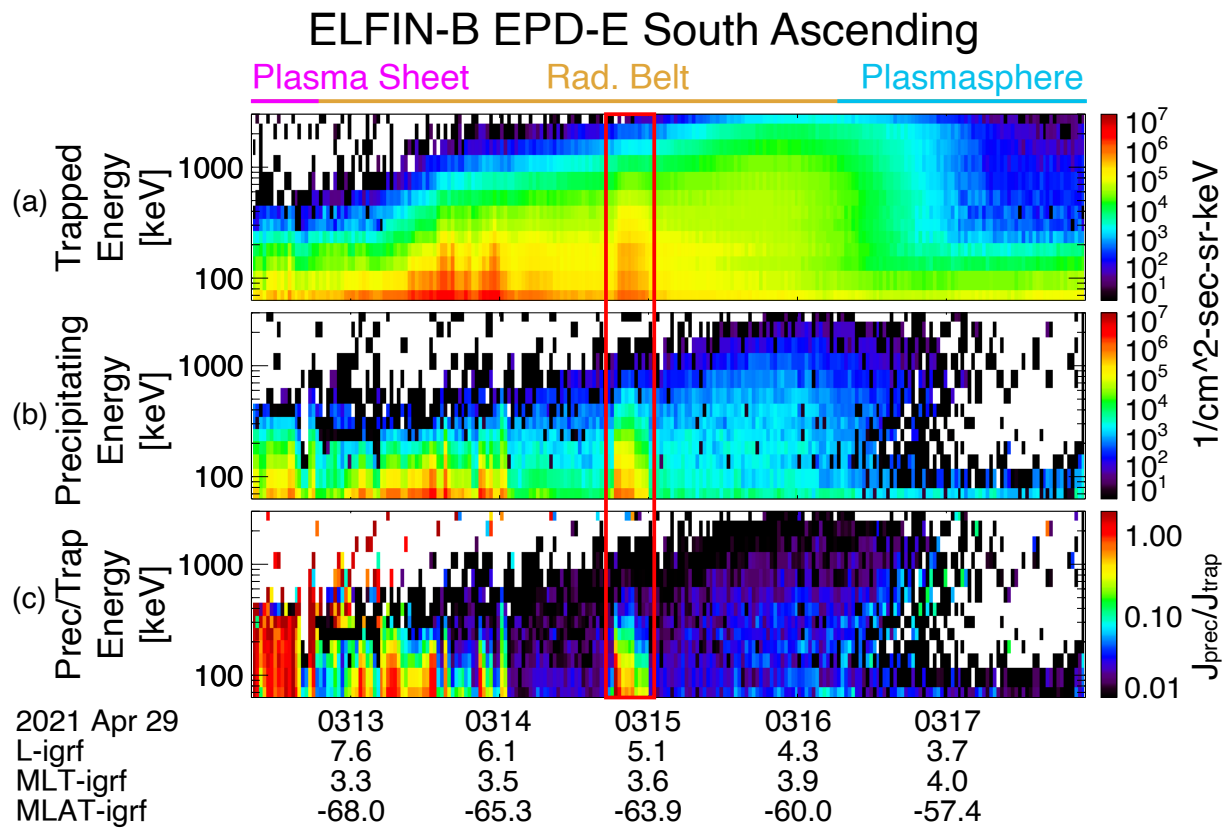


Figure 4.3: Trapped (a) and precipitating (b) electron fluxes are shown from a five minute crossing of the outer radiation belt as ELFIN-B heads away from the geographic South Pole. It begins in the plasma sheet, observes precipitation in the outer radiation belt, before exiting into the plasmasphere. Panel (c) denotes the ratio of precipitating to trapped electron fluxes, which conveys the strength of the precipitation. The red box denotes precipitation of up to 300 keV at $L \in [5.1, 5.3]$ which corresponds to the whistler waves shown in Fig. 4.2.

The energetic electron spectrum seen by MMS during this two-hour period (Fig. 4.5a) shows a clear signature of a plasma sheet injection starting around 08:20 UT, evidenced by a rapid increase in electron fluxes up to 500 keV (compare this with the typical injection signatures described in, e.g., Gabrielse et al., 2014; Turner et al., 2016). The first burst of intense whistler-mode waves was observed behind the injection, around 08:30 UT (Fig. 4.5(b), likely driven by thermal anisotropy of injected electrons (e.g., Le Contel et al., 2009; Zhang et al., 2018a). At lower L-shells, MMS observed two other whistler-mode bursts (numbered (2) and (3) atop Fig. 4.5b), with the last one occurring right before MMS crossed the plasmapause, around 09:20 UT. The plasmapause is seen as a sharp boundary separating discrete whistler-mode emissions in the low band chorus frequency range and broadband

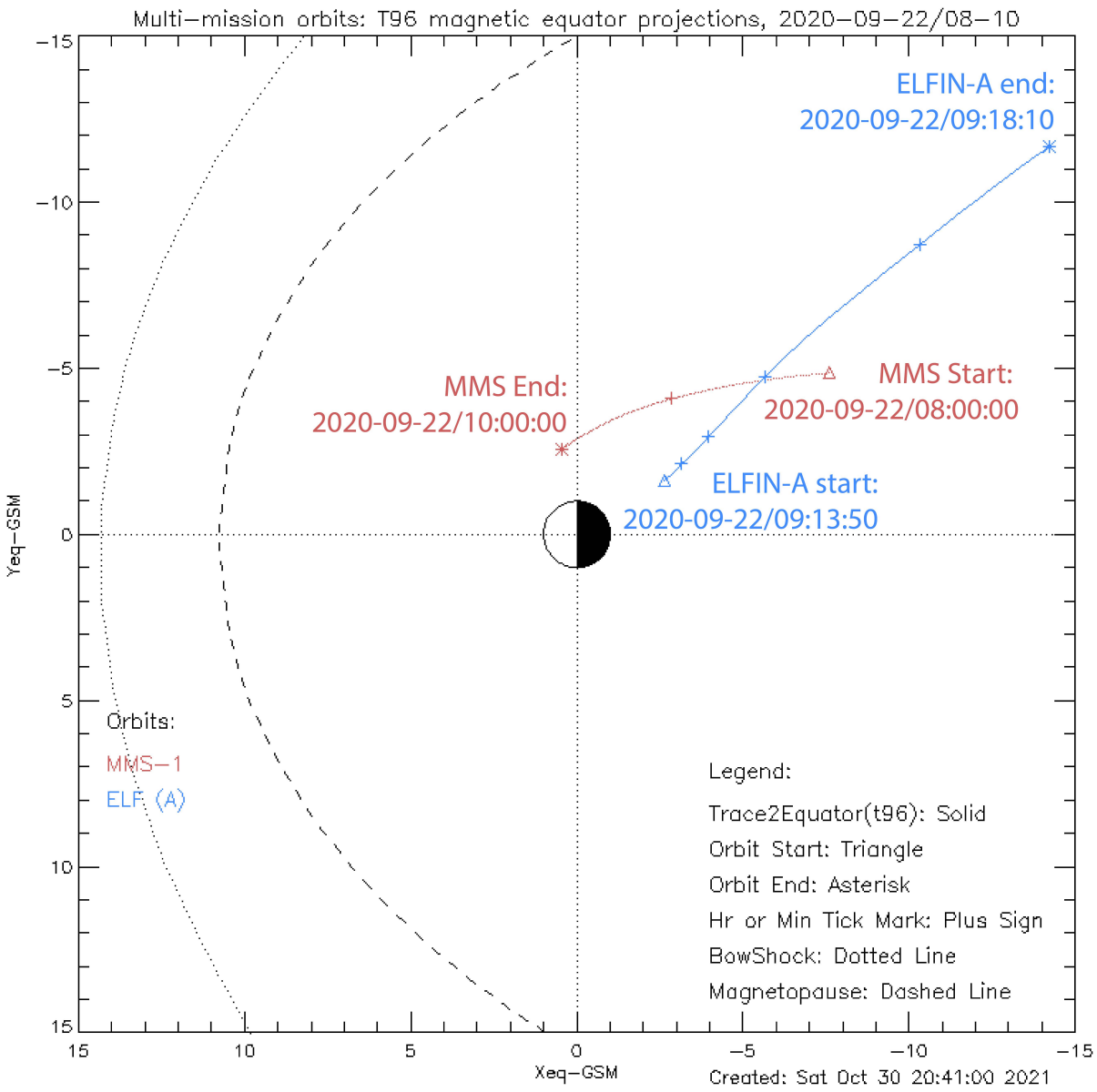


Figure 4.4: Magnetic footprints of the conjunction between MMS-1 (brown) and ELFIN-A (blue) traced to the equator using the T96 model (Tsyganenko, 1995). The plus signs demarcate one-minute intervals for ELFIN-A and one-hour intervals for MMS.

whistler-mode emissions in the hiss frequency range $f < 0.1 f_{ce}$ (see, e.g., Malaspina et al., 2017).

ELFIN-A crossed a wide L-shell range over a five-minute interval centered around 09:16 UT, seen in Fig. 4.6. The precipitating-to-trapped electron flux ratios in panel (c), ex-

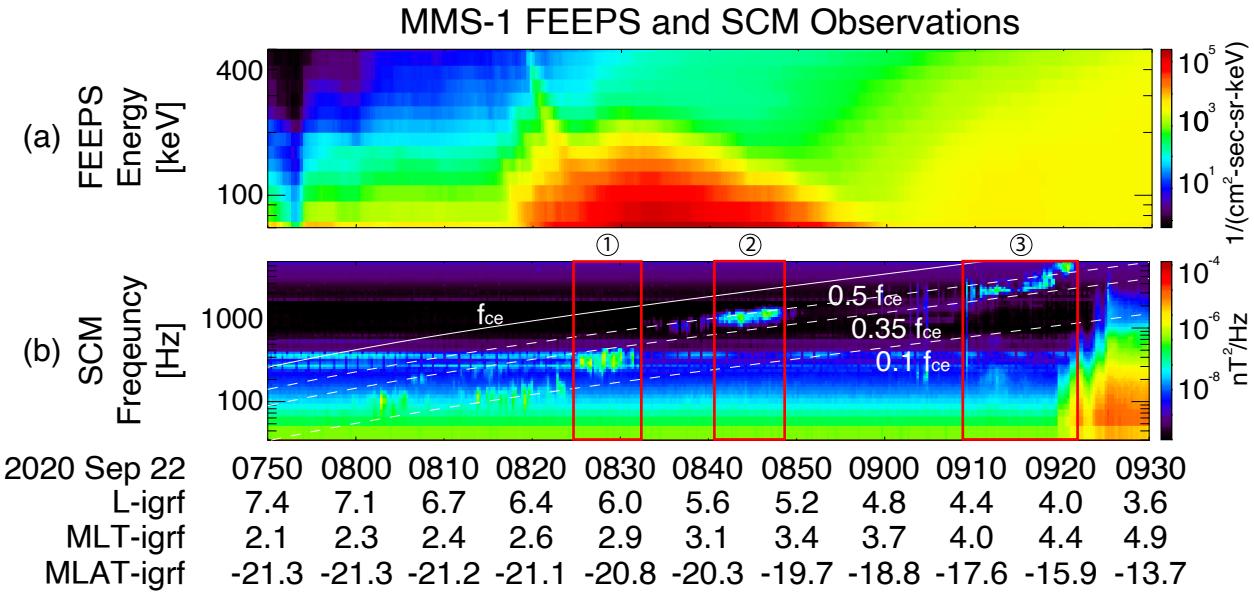


Figure 4.5: MMS-1 electron and SCM measurements are shown for this inbound observation of the radiation belt on Sept 22, 2020. MMS begins in the plasma sheet before encountering the outer radiation belt (significant increase in electron flux) and eventually enters the plasmasphere (hiss waves are apparent in SCM measurements). Dashed white lines denote fractions of equatorial electron gyrofrequency f_{ce} (solid white line). The three bursts of whistler waves in the lower band chorus frequency range are evident and numbered 1 through 3.

amined together with the trapped fluxes in panel (a), reveal three main regions: plasma sheet, corresponding to highly isotropized electrons below 300 keV; outer radiation belt, corresponding to energetic (50 keV - 1 MeV) electrons which do not exhibit continuous, but only occasional, isotropization; and the plasmasphere, corresponding to mostly relativistic ($>$ 500 keV) electrons. The plasmapause is likely crossed around 09:15:50 UT at $L \sim 5.6$. In the plasmasphere, whistler-mode hiss waves scatter energetic $<$ 500 keV electrons and form the clear low-energy boundary of electron fluxes with the observed inverse energy/L-shell dispersion (see model/data comparison in, e.g., Ma et al., 2016; Mourenas et al., 2017). Within the outer radiation belt (between 09:15:50 and 09:17:00 UT), ELFIN-A observes three bursts of electron precipitation (numbered 1-3 above Fig. 4.6a). The precipitating fluxes during those bursts are limited to $<$ 300 keV (Fig. 4.6b), but the precipitation is quite intense, with precipitating-to-trapped ratios of around 1 (Fig. 4.6c). We use the third burst of precipitation (numbered (1) in Fig. 4.6, at $L = 7$ between 09:16:38-09:16:45 UT) to

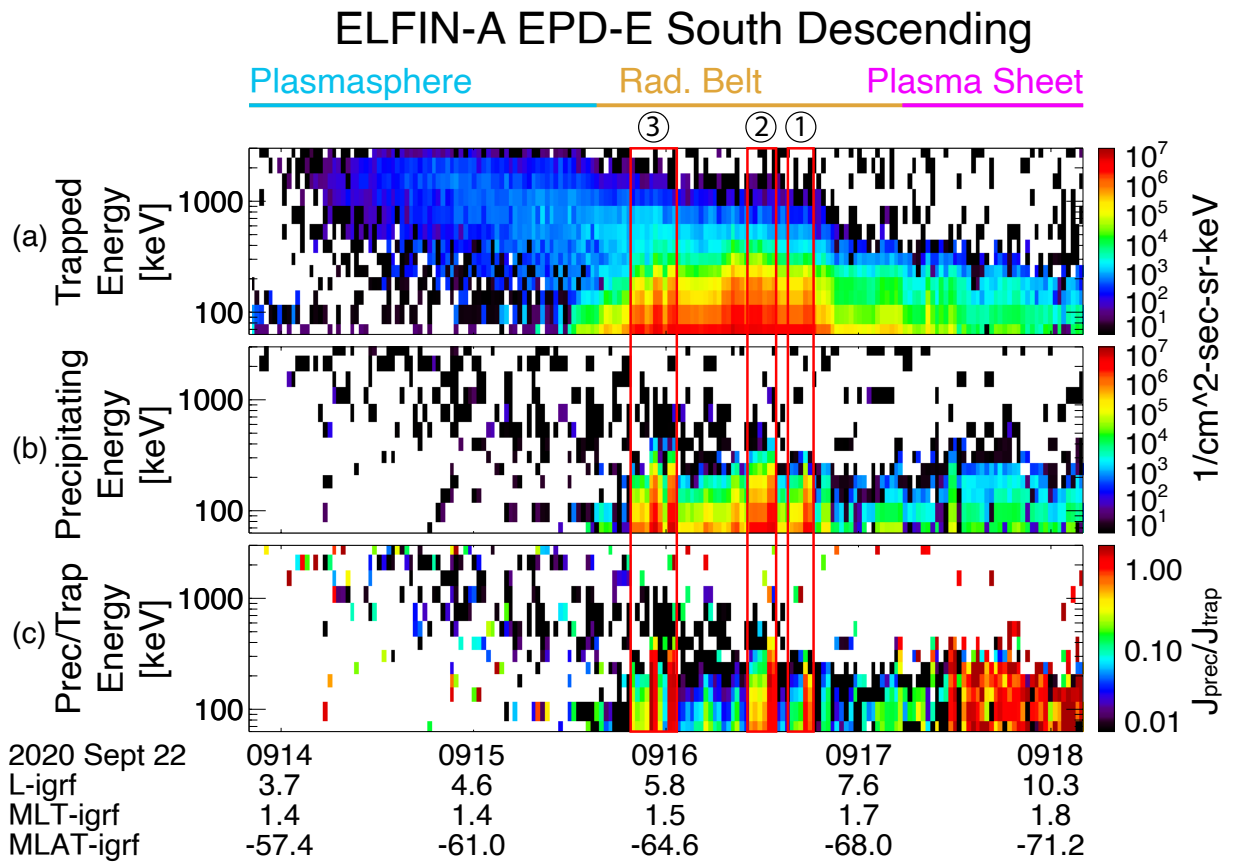


Figure 4.6: Trapped (a) and precipitating (b) electron fluxes are shown for ELFIN-A's five minute crossing, with panel (c) showing the precipitating to trapped ratios. The three bursts of electron precipitation up to 300 keV are highlighted in red and numbered, likely corresponding to the three bursts of whistler activity seen by MMS in Fig. 4.5. In the text, we will focus on conjunction data from (1) at $L = 7$.

compare with our model.

4.3 Simulation Results

For the following two conjunction case studies, we utilize the test particle simulation detailed in Chapter 3 with modifications specified in Section 3.4.1. The simulation is run with 96600 particles with initial energies distributed logarithmically between 50 keV and 1 MeV in 20 bins and initial pitch angles between 10° and 90° in 21 linearly spaced bins. This results in 230 particles per bin in each of the 420 bins. Each particle is given a randomized starting relative phase ζ. After tweaking system parameters to fit equatorially measured conditions, the

simulation generates 96600 trajectories. The precipitating fluxes can be extracted at every given time by looking at the particles that are just about to precipitate. These PSDs are then converted to physical units (number flux) and compared directly with ELFIN measurements.

4.3.1 Conjunction Event #1

In the first event, we use $B_{eq} = 188$ nT based on THEMIS FGM measurements (as also evident from f_{ce} line in Fig. 4.2b). During the pertinent portion of THEMIS-A observations (03:00-03:30 UT), the normalized wave frequency remained fairly constant around $\omega_m = \omega/\Omega_- \approx 0.35 f_{ce}$, as did the normalized plasma frequency $\Omega_p = \omega_p/\Omega_- \approx 8$, obtained using density measurements inferred from the spacecraft potential measurements of the EFI instrument. THEMIS' electron phase space density (PSD) as a function of pitch angle and energy and its fits are shown in Fig. 4.7, at around the time of the closest conjunction between THEMIS-A and ELFIN-B ($L = 5.2$). These fits determine the initial equatorial PSD for numerical simulations.

THEMIS-E SCM measurements for two out of the three magnetic field components were not fully calibrated at the time of this writing, so we used electric field measurements (and compared them with the one calibrated SCM Z component spectra) to estimate the wave-packet shape and magnetic field amplitude. Fig. 4.8 shows examples of wave-packets captured by THEMIS-E SCM and EFI in the Wave-Burst (WB) mode of operation. We find an average of $\delta\phi \approx 30$ waves/packet (see Eq. 3.26), in line with previous statistical models and wave generation simulations (see Zhang et al., 2021, and references therein). We used 3D EFI electric field measurements to determine the magnetic field from the cold plasma dispersion relation (see details in, e.g., Agapitov et al., 2014; Ni et al., 2011; Tao and Bortnik, 2010). Using Minimum Variance Analysis (MVA) (Sonnerup and Cahill, 1968), we can find E_N along the minimum variation of the electric field in the LMN principle axis coordinate system. The other two components E_L and E_M have similar amplitudes, implying that these waves are field-aligned and circularly polarized. We then estimate the wave magnetic field amplitude $B_{wave} = E_w \cdot n$, where $E_w = \sqrt{E_L^2 + E_M^2}$ (red in Fig. 4.8) and

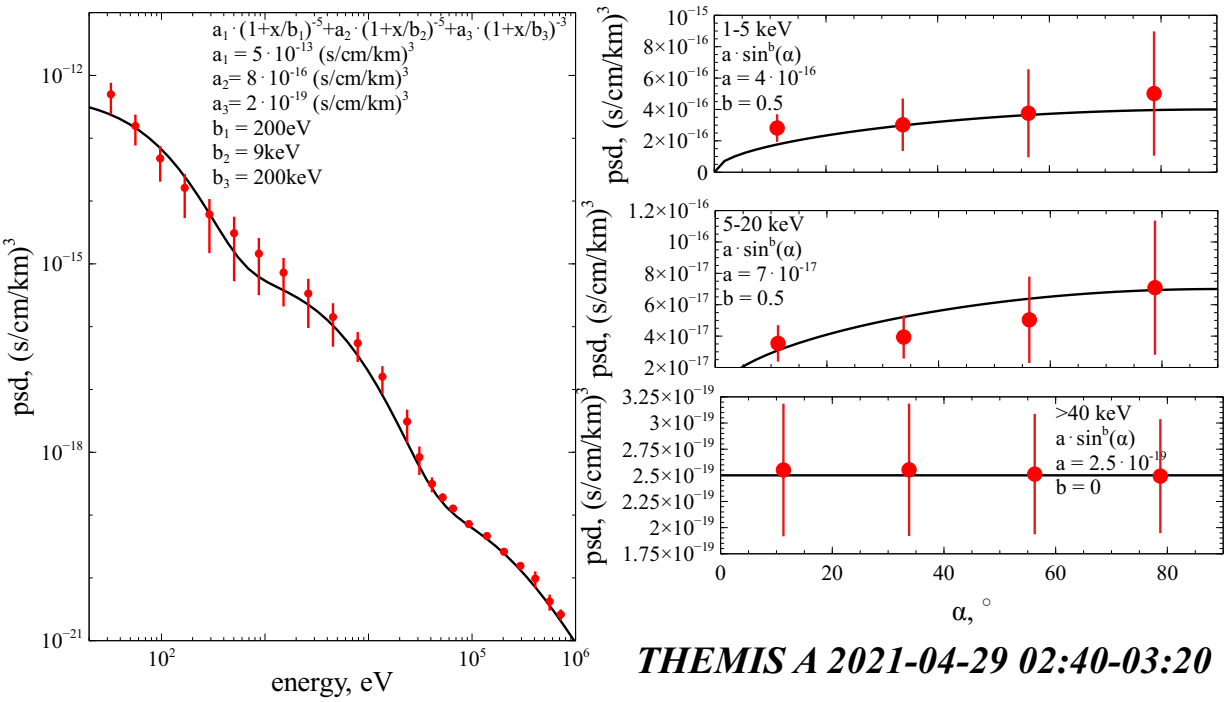


Figure 4.7: PSD fits for THEMIS-A based on ESA and SST measurements as a function of energy (left) and pitch angle (right three panels). Data are shown as red filled points, with error bars denoting the PSD variation during the 40-min average interval; fitted results are shown in black lines, with fitting function and parameters inserted within.

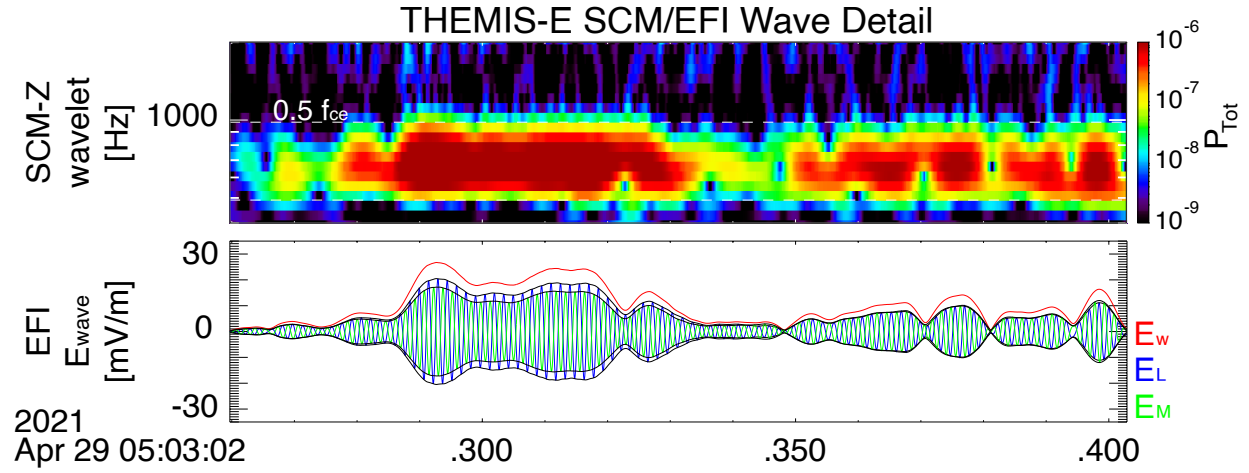


Figure 4.8: The first panel shows a wavelet transform of SCM data for just one whistler packet train from a five-second waveburst collection on THEMIS-E. Because two of the axes of the SCM were not fully calibrated, we used EFI burst data to obtain the amplitude of the wave. We transform to LMN coordinates (using Minimum Variance Analysis, see Sonnerup and Cahill, 1968) and use the main electric field components to find a proxy magnitude of the wave magnetic field amplitude (see text for details).

$n = (\Omega_p/\omega_m)/\sqrt{1/\omega_m - 1}$. Averaging over all waveburst measurements gives $\langle B_w \rangle \approx 162$ pT with peak values for individual wave-packets commonly reaching 0.9 nT. Thus, we use wave-packets with packet-averaged wave amplitude of $B_w/2 \approx 450$ pT ($\langle g \rangle_\phi \approx 1/2$; since we do not have waves roughly half the time) and normalize the wave occurrence rate to attain the average wave amplitude: $162/450 \approx 36\%$.

To obtain the input wave field distribution along magnetic field lines in our simulation, we use the empirical model of (Agapitov et al., 2013) showing that in the range of $4 < L < 5.5$ and for $Kp < 3$, the ratio of whistler wave occurrence rates between $\lambda < 20°$ and $\lambda \approx 30° - 40°$ is ~ 5. Therefore, we use three simulation runs with different $\delta\lambda_2$ (see Eq. 3.25) and whistler-mode wave occurrence rates: $\delta\lambda_2 = 20°$ and occurrence rate of 30%, $\delta\lambda_2 = 30°$ and occurrence rate of 4%, $\delta\lambda_2 = 40°$ and occurrence rate of 2% (so the total wave occurrence rate is 36%, while the net occurrence rate at $< 20°$ (30%) is 5 times that between $30° - 40°$ (6%)).

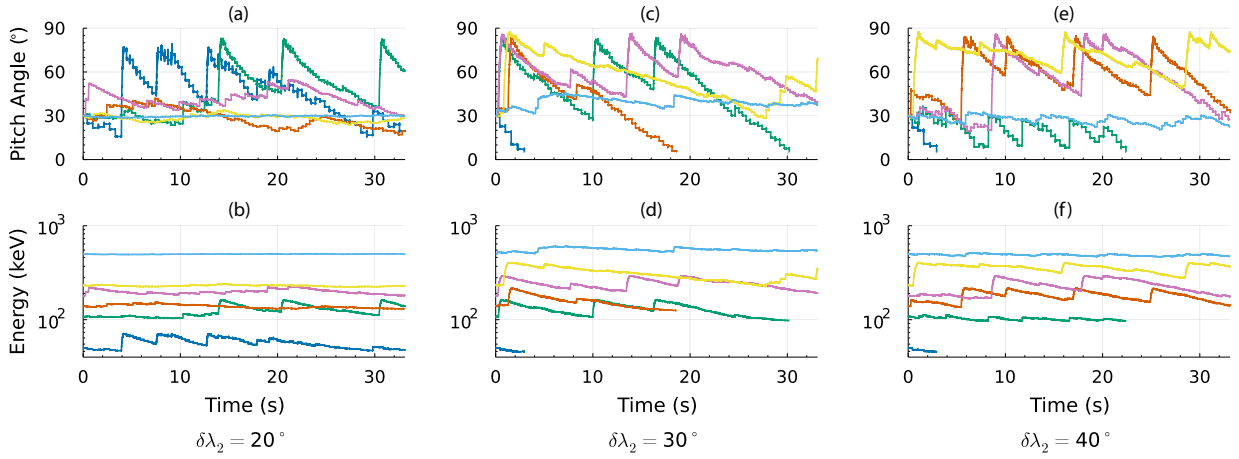


Figure 4.9: Several test particle trajectories for different initial energies of around [50, 100, 150, 200, 250, 500 keV] and initial pitch angle of $\alpha_{eq} = 30°$. Panels in the top row show pitch angle time series, while those in the bottom row show energy time series. Each column shows results for $\delta\lambda_2 = 20°$, $30°$, and $40°$, respectively.

Fig. 4.9 shows simulated trajectories of electrons in pitch angle and energy, as a function of time, for six example electrons. The initial pitch angles are fixed at 30°, but the initial energies and $\delta\lambda_2$ were varied (as indicated in the plots) in order to demonstrate the variation of resonant energy with higher latitude propagation. The ensemble simulation was run for

just over $\sim$ 100 bounce periods ($\sim$ 11s with a typical bounce period of $\sim$ 0.1s), which is sufficiently long enough to densely sample the particle energy spectrum given the two resonances per bounce period (wave-particle interactions occur on both sides of the equator); however, the individual trajectories in Fig. 4.9 were run for triple the length for illustration purposes ($\sim$ 33 s). In Figures 4.9a and 4.9b, chorus waves are limited to $\lambda < 20°$, and thus are not expected to resonate with high-energy electrons. While plenty of phase bunching and trapping are evident for the two example electrons at energies < 100 keV, the higher-energy electron energies and pitch angles remain fairly constant, implying that there are no abrupt changes from their interactions with the fixed-frequency input waves. The two resonant electron trajectories (< 100 keV) exhibit evidence of the less common phase trapping (large energy and pitch angle increases) mixed with regular phase bunching (small energy and pitch angle decreases). The combination of multiple phase trapping and phase bunching generally tends to uniformly distribute electrons in energy/pitch angle space (not shown, but see also Hsieh and Omura, 2017; Vainchtein et al., 2018). As $\delta\lambda_2$ is increased to 30° (Figures 4.9c and 4.9d), even higher energies (up to 500 keV) efficiently resonate with waves; after consistent bunching and some phase trapping, they appear within the model loss cone, i.e., wave-particle interaction results in electron precipitation. For $\delta\lambda_2 = 40°$, the same phase trappings and bunchings are seen but now also for relativistic electrons (Figures 4.9e and 4.9f). Fig. 4.9 thus confirms the importance of parameter $\delta\lambda_2$ and strongly suggests the nonlinear nature of wave-particle resonances for this event.

To model the observed precipitation spectrum, we use an ensemble of electrons with initial energies $\in [50, 1000]$ keV and pitch angles $\in [3, 90°]$. Each electron represents a fraction of its initial phase space density which, by combining all test electrons, contributes to (and matches) the distribution function derived by fitting the THEMIS flux measurements seen in Fig. 4.10 (top-most line). The simulation period is then divided into 10 segments; in each of these intervals, we evaluate the electron phase space density within the loss cone. Such phase space density is recalculated to electron precipitating fluxes, and we show both time-averaged precipitating flux and its standard deviation in Fig. 4.10 from the three sets of

simulations plus their sum (black line). The three runs, corresponding to different $\delta\lambda_2$, show the importance of wave propagation to high latitudes for scattering of relativistic electrons: only the two runs with $\delta\lambda_2 \geq 30°$ provide electron precipitation with energies $\geq$ 600 keV. It is evident from this figure that, albeit small, some fraction of whistler-mode waves must propagate to $\lambda \sim 40°$ (orange line) in order to produce the high energy precipitating tail seen in ELFIN's observations (see dark blue curve in Fig. 4.10). However, this wave population alone does not occur frequently enough to account for ELFIN's observations of $<$ 300 keV precipitation, and higher occurrence rates of waves which are more confined around the equatorial plane are required. We accomplish this by incorporating wave populations at 30° and 20° as well. Note that Fig. 4.10 also clearly shows that waves with $\delta\lambda_2 = 30°$ cannot scatter energies $>$ 600 keV, and waves with $\delta\lambda_2 = 20°$ cannot scatter energies $>$ 200 keV electrons.

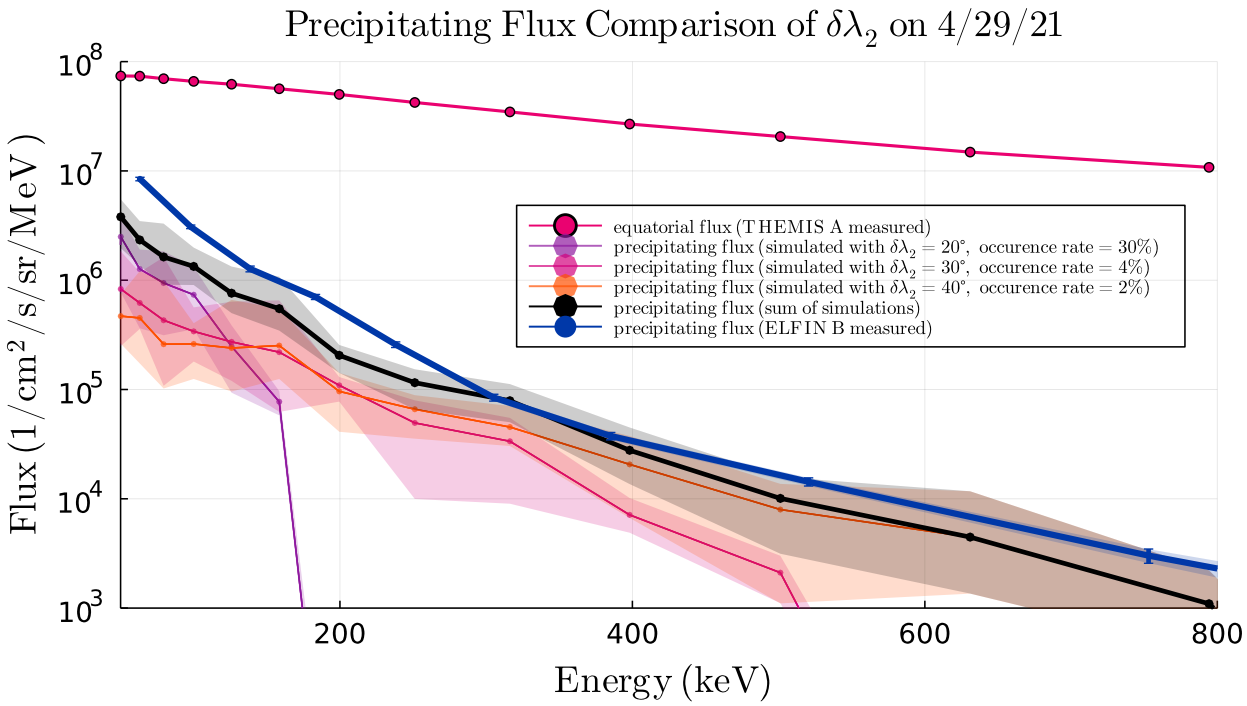


Figure 4.10: Near equatorial fluxes measured by THEMIS-A are shown at the top. The thin orange, pink, and purple lines at the bottom are simulation results for runs with $\delta\lambda_2 = [20°$, 30°, 40°] and wave occurrence rates derived from (Agapitov et al., 2013) (see text for details). The black line shows the summed simulation results (for a total occurrence rate of 36%). The blue line shows the precipitating fluxes as measured by ELFIN-B.

Precipitating fluxes at ELFIN-B, shown in Fig. 4.10 (blue line) were averaged over five spins from 03:14:45 - 03:15:00 UT (red lines in Fig. 4.3), and error bars denote statistical variance (which are small due to fairly uniform fluxes over the short duration of precipitation). The precipitating fluxes obtained from the test particle simulation, driven by the equatorial waves and electrons' measurements, agree well with ELFIN-B observations. The deviation in the lower energy range is most likely due to electron resonant interactions with lower-amplitude waves, which were not included since monochromatic waves were utilized in the simulation. The simulation/data comparison in Fig. 4.10 and electron trajectory examples in Fig. 4.9 emphasize the key role of nonlinear electron interactions with waves that can reach high latitudes. These are likely ducted waves (see discussion in Artemyev et al., 2021a, and references therein), since without ducting, whistler waves already become oblique at $\lambda \sim 20 - 30^\circ$ (e.g., Breuillard et al., 2012; Katoh, 2014) and become quickly damped by Landau resonance with suprathermal electrons (Bortnik et al., 2007; Chen et al., 2013).

4.3.2 Conjunction Event #2

In the second event, we do not have waveform data because the MMS dataset was only available in slow survey mode. Thus, we use $\delta\phi = 30$ (same as the first event and fairly typical for intense whistler-mode waves based on statistics, see (Zhang et al., 2018b)) and vary latitudinal extension $\delta\lambda_2$ and modulation depth a to match ELFIN observations. We use $B_{eq} = 65$ nT, $\Omega_p = \omega_p/\Omega_- = 6$, $\omega_m = \omega/\Omega_- = 0.3$, and $L = 6$ based on MMS observations and a plasma density model (Sheeley et al., 2001). From MMS FEEPS measurements, we obtain the PSD fits shown in Fig. 4.11 in a similar format to that of Fig. 4.7.

Precipitating flux measurements from ELFIN show electron fluxes only up to 300 keV within the loss cone (see dark blue curve in Fig. 4.12). When $\delta\lambda_2 = 30^\circ$, there is a high energy tail beyond 300 keV of precipitating electron fluxes, which does not match ELFIN observations, and when waves are too confined around the equator, with $\delta\lambda_2 = 15^\circ$, resonant wave scattering is incapable of providing the observed 300 keV electron fluxes. Thus, we can expect that equatorially confined whistler-mode waves with $\delta\lambda_2 \sim 20^\circ$ (typical for night-side

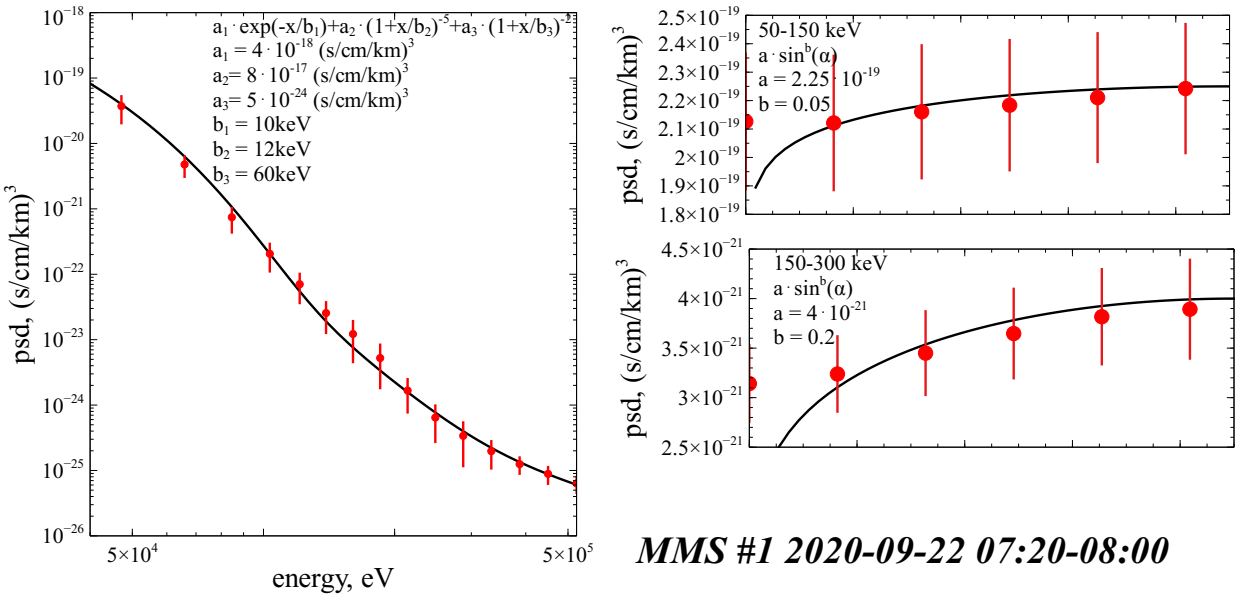


Figure 4.11: PSD fits for MMS-1 based on FEEPS measurements, as a function of energy (left) and pitch angle (right three panels). Data are shown in red filled points, with error bars denoting the PSD variation during the 40-min average interval; fitted results are shown in black lines, with fitting function and parameters inserted within.

injections, see Agapitov et al., 2018; Meredith et al., 2012) are likely responsible for the observed precipitation.

Next, we investigate parameter a in Eq. 3.26, which controls the depth of wave-packet modulation (e.g., $a = 0$ is an infinite sin wave). Deeper modulation (large a) can change phase trapping efficiency (An et al., 2022a; Tao et al., 2012b, 2013) by (1) increasing the probability of phase trapping due to sharper wave-packet edges, resulting in electron transport away from the loss cone (Hiraga and Omura, 2020), and (2) decreasing electron diffusive scattering to the loss cone due to the reduced intensity of low-amplitude waves away from wave-packet peaks. Indeed, for fixed $\delta\phi$, Fig. 4.13 matches our expectations of reduced scattering into the loss cone as a increases: for $a = 3$ (max / min wave field is 1/0.05), modeled fluxes match ELFIN observations well, whereas for $a = 7$ (max / min wave field is $1/10^{-3}$), a combination of strong trapping and insufficient scattering results in the inability to precipitate > 150 keV electrons. Fig. 4.13 demonstrates that for the second event, $a = 3$ provides a reasonable explanation for ELFIN-measured precipitation (Zhang et al., 2018b, which agrees well with statistical wave observations, see). Figures 4.12 and 4.13 thus demonstrate that

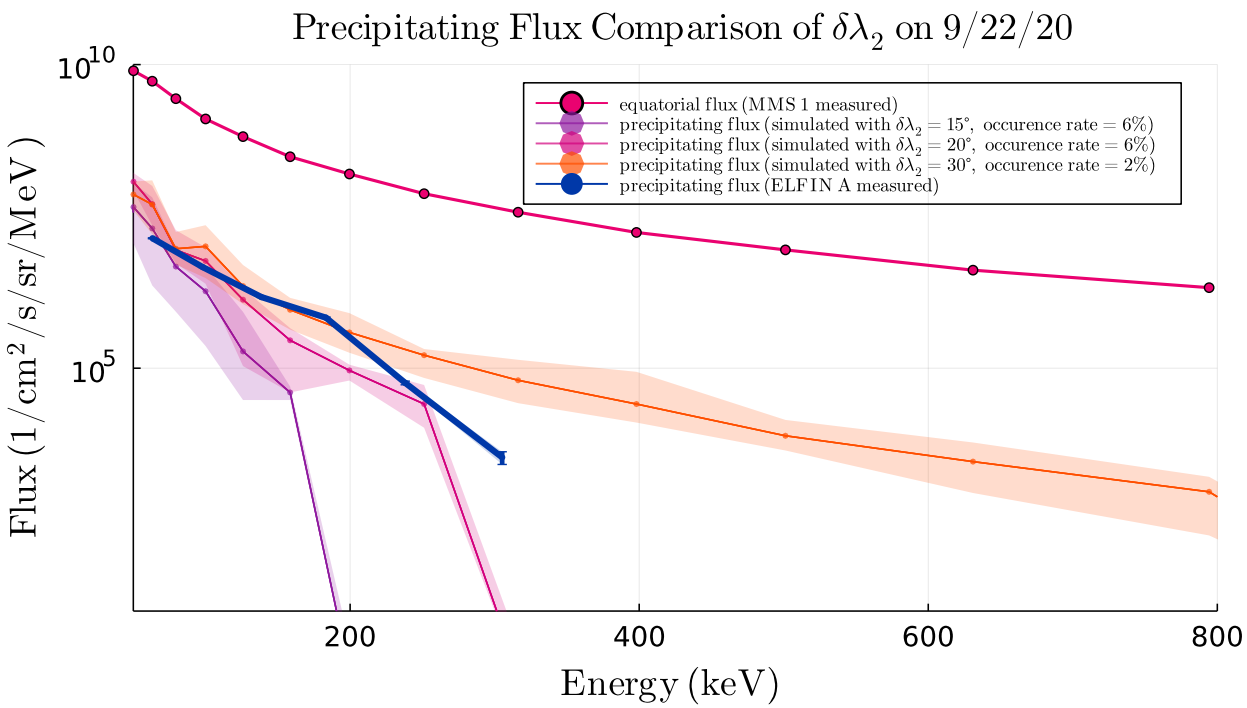


Figure 4.12: The line at the top shows the fitted equatorial fluxes as measured by MMS-1. The dark blue line shows that the precipitating fluxes as observed by ELFIN-A only reach 300 keV. The three lines behind (purple, pink, orange) show simulated precipitating fluxes based off of the initial equatorial PSD with varying latitudinal distributions of whistler waves. The run with $\delta\lambda_2 = 20°$ matches simulations the closest. (Ratio of whistler wave occurrence rates between $\lambda < 20°$ and $\lambda \approx 30° - 40°$ is ~ 3 for 5.5<L<10 based off of empirical models (Agapitov et al., 2013))

ELFIN observations of rapidly precipitating fluxes can be used to provide a good estimate of both the latitudinal distribution and wave modulation characteristics of electron scattering by whistler-mode waves.

4.4 Discussion

In this chapter, we investigated energetic electron scattering by large-amplitude whistler-mode waves and the associated electron precipitation. Test particle simulations showed that nonlinear wave-particle interaction with whistler-mode waves can explain energetic electron precipitation seen by the low-altitude ELFIN CubeSats using conjugate observations of strong whistler waves near the equator. While a relatively simplified model for whistler-mode

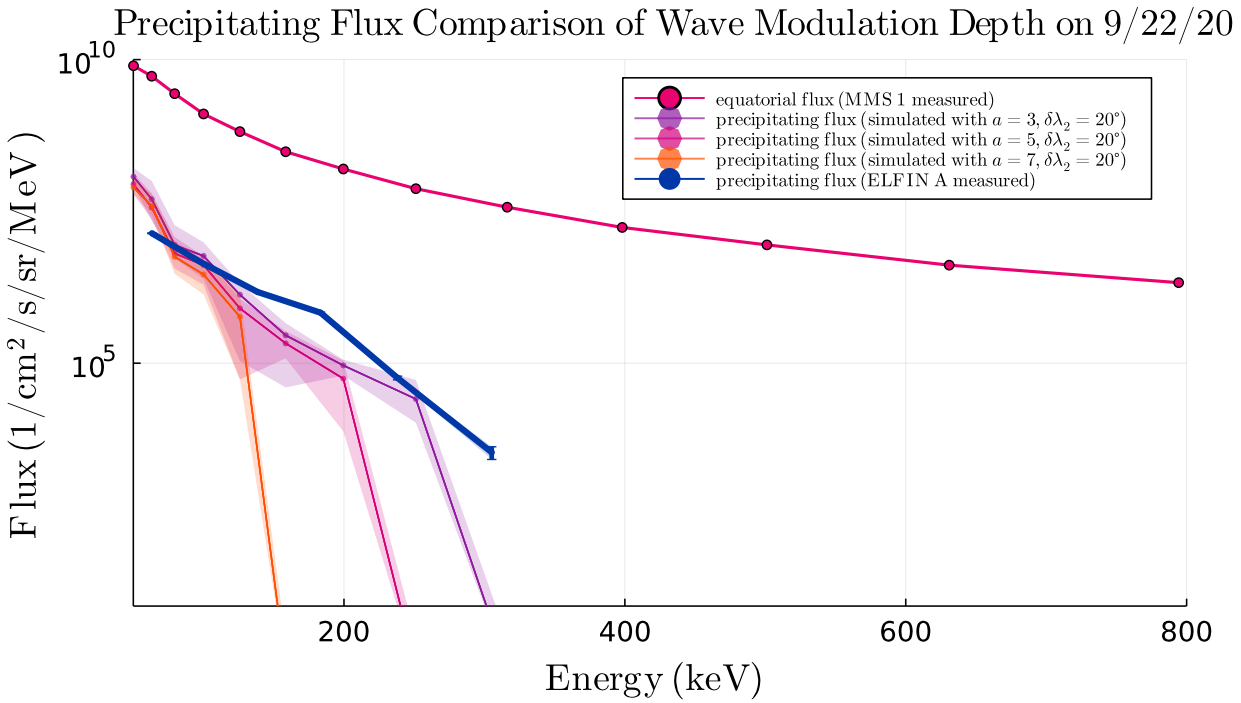


Figure 4.13: Similar to Fig. 4.12, except this plot compares the depth of wave modulation by varying a. Packet lengths are kept to a constant $\delta\phi = 30$ wavelengths per packet.

waves was used in this chapter, we still included several important wave characteristics which play a potentially significant role in wave-particle interaction. Specifically, in our model:

- We incorporated the finite size of wave-packets, which mimics wave-packet modulation (Zhang et al., 2021) and restricts the efficiency of phase trapping (Hiraga and Omura, 2020; Kubota and Omura, 2018; Tao et al., 2013; Zhang et al., 2020a). Based on near-simultaneous conjugate THEMIS observations (consistent with previous statistical studies (Zhang et al., 2018b)), our simulated wave-packets contained 30 wavelengths. Such wave-packet modulation also reduces the efficiency of anomalous trapping (see Appendix in Mourenas et al., 2021), which may block precipitation of < 100 keV electrons when waves are especially intense (Albert et al., 2021; Artemyev et al., 2021b; Gan et al., 2020a; Kitahara and Katoh, 2019).

- We did not include wave frequency variation within wave-packets (i.e., an approximation of $\omega = const$), which may reduce efficiency of electron acceleration by trapping (see

discussion of the importance of $\partial\omega/\partial t \neq 0$ for trapping acceleration in, e.g., Demekhov et al., 2006; Katoh and Omura, 2007b). This simplification should not affect the results of short-term electron precipitation modeling; however, the effects of $\partial\omega/\partial t \neq 0$ should be considered for long-term electron acceleration due to nonlinear resonances (e.g., Hsieh and Omura, 2017; Omura et al., 2015).

- We incorporated a realistic wave intensity decay as a function of distance from the equatorial plane $B_w \sim \exp\left(-(\lambda/\delta\lambda_2)^2\right)$, which mimics the effects of wave propagation in an inhomogeneous magnetic field (Breuillard et al., 2012; Katoh, 2014; Watt et al., 2013) and Landau damping at mid-latitudes (Bortnik et al., 2007; Chen et al., 2013), both of which are often seen in whistler-mode wave empirical models (e.g., Agapitov et al., 2018; Wang et al., 2019). In order to reproduce ELFIN observations of relativistic electron precipitation, we showed that a small fraction of waves should be assumed to propagate without strong damping or divergence from the field lines up to $\lambda \sim 40°$. This likely corresponds to ducted wave propagation (Chen et al., 2021b; Demekhov et al., 2017; Martinez-Calderon et al., 2020) that can be supported by small plasma density variations (Hanzelka and Santolík, 2019; Hosseini et al., 2021; Ke et al., 2021; Shen et al., 2021) and is important for precipitation of relativistic electrons (Artemyev et al., 2021a; Chen et al., 2020, 2021a).

- We did not incorporate realistic phase decoherence for wave-packets: i.e., there are no perturbations of the wave phase ϕ within each packet. While observed whistler-mode waves are typically highly coherent (Tsurutani et al., 2011, 2020), frequency/phase jumps are often detected around packet edges (Santolík et al., 2014a; Zhang et al., 2020b). Such wave decoherence affects the efficiency of trapping acceleration (Artemyev et al., 2015; Brinca, 1978; Tao et al., 2013) and probably requires additional investigation in the long-term modeling of electron flux dynamics. The effect of wave decoherence on electron scattering due to the phase bunching around the loss cone, however, is expected to be minimal.

To summarize, we show here that ELFIN CubeSat measurements, when combined with

equatorial missions like THEMIS and MMS, enable direct quantification of the contributions of nonlinear wave-particle interaction to energetic electron scattering and losses. We have additionally demonstrated the validity of using the test particle approach, and clearly showed how important it is to consider the latitudinal extent of the whistler-mode wave field. In a conjunction between ELFIN and THEMIS, we showed that the precipitation seen by ELFIN can only be explained if we take into account a small population of waves (present only about 2% of the time) that propagate up to 40° in latitude. Such waves can scatter up to nearly 1 MeV electrons, as ELFIN shows. Comparing two events (with and without relativistic electron precipitation) shows that ELFIN observations and test particle simulations are a viable way to characterize the mechanisms behind electron scattering.

In fact, ELFIN has measured many thousands of events with relativistic electron precipitation characteristic of interactions with whistler-mode waves. In this chapter, we showed that even small populations of ducted waves (propagating to mid-latitudes in the field-aligned regime) may play a crucial role in shaping the energy spectra of precipitating electrons. It logically follows, then, that we next focus on the global relevance of relativistic electron precipitation driven by whistler-mode waves by investigating the properties of waves as a function of magnetic latitude. In the next chapter, we will adapt our new computational tool to compare empirical wave models with ELFIN observations primarily to reveal the importance of field-aligned waves at high latitudes (i.e., ducting).

CHAPTER 5

Investigating Whistler-Mode Wave Intensity Along Field Lines

5.1 Introduction

Energetic electron fluxes in the Earth's radiation belts vary significantly in response to resonant electron interactions with whistler-mode waves (and references therein Shprits et al., 2008b). Such interactions can accelerate plasma sheet electrons to relativistic (e.g., Meredith et al., 2002; Millan and Baker, 2012; Thorne et al., 2013) or even ultra-relativistic (Allison and Shprits, 2020) energies, and pitch-angle scatter energetic electrons into the loss cone causing their precipitation to the atmosphere (e.g., Millan and Thorne, 2007). This multi-faceted role of whistler-mode waves makes them a key element of radiation belt dynamics (see discussion in Bortnik and Thorne, 2007; Thorne, 2010) and motivates the investigation of whistler-mode wave characteristics and their relationship to electron precipitation (see Agapitov et al., 2013; Li et al., 2011a; Meredith et al., 2001, 2012; Santolík et al., 2003; Wang et al., 2019). In addition to the importance of the wave frequency (which is typically fixed for very intense chorus mode waves, see Li et al., 2011a; Tsurutani and Smith, 1974), there are two other defining wave characteristics: wave intensity (which determines electron scattering amplitudes, see reviews by Lyons and Williams, 1984; Schulz and Lanzerotti, 1974) and wave normal angle (which determines the resonance energy range, see Albert, 2017; Artemyev et al., 2016; Lorentzen et al., 2001; Shprits and Ni, 2009), both of which vary with magnetic latitude (i.e., along magnetic field lines, or henceforth referred to simply as just latitude) (Agapitov et al., 2013, 2018; Santolík et al., 2014b). Therefore, the latitudinal profiles of these

wave characteristics along field lines define the relative efficiency of electron acceleration and scattering as a function of energy (e.g., Agapitov et al., 2018; Mourenas et al., 2012a, 2014a; Summers and Ni, 2008; Wang and Shprits, 2019). In particular, intense field-aligned whistler-mode waves can effectively resonate with relativistic electrons at mid-to-high latitudes since higher latitudes result in a monotonic increase of electron cyclotron-to-plasma frequency ratio, thereby increasing the minimum resonance energy (see, e.g., Summers et al., 2007a; Thorne et al., 2005). Because intense relativistic electron precipitation is a fairly common observation (e.g., Artemyev et al., 2021a; Chen et al., 2022; Grach et al., 2022b; Mourenas et al., 2022a; Tsai et al., 2022), it is important to quantify the latitudinal extent of whistler-mode wave power that might enable such precipitation. This insight would help determine under what ambient wave propagation conditions and equatorial source properties mid-to-high latitude wave propagation might take place.

Most intense whistler-mode waves are near-equatorial ($\lesssim 20^\circ$ in latitude) and are typically found at the nightside injection region (Meredith et al., 2012). Their near-equatorial localization has been attributed to the increasing wave obliquity expected with propagation away from their equatorial source (Agapitov et al., 2013; Breuillard et al., 2012; Chen et al., 2013) and their severe damping by Landau resonance with suprathermal electrons (e.g., Bell et al., 2002; Bortnik et al., 2007). This effect is moderated at the dayside, where low intensity waves are observed at much higher latitudes than at the nightside (Meredith et al., 2012). This moderation is attributed to wave propagation in the presence of more gradual gradients in the ambient dayside magnetic field (due to magnetospheric compression) and the lower density of suprathermal electrons (Li et al., 2010a; Walsh et al., 2020) – both of which reduce wave damping. The reduced damping then allows whistler-mode waves on the dayside to propagate up to $30 - 40^\circ$ (Agapitov et al., 2018). This day-night asymmetry in the propagation latitude of whistler-mode waves has been used to explain the preponderance of relativistic microburst precipitation (i.e., very intense short-lived precipitation events, see Blum et al., 2015b; Breneman et al., 2017; Douma et al., 2019; O'Brien et al., 2004; Zhang et al., 2022b) in the dawn-noon sector (see discussion in Thorne et al., 2005). However, an

observational determination of the mid-latitude wave intensity needed to explain the precipitating fluxes of relativistic electrons has not yet been undertaken. In the past, this has been in great part due to the lack of availability of keV to MeV energy electron flux data with sufficient energy resolution and precipitating-to-trapped flux ratio fidelity. Several recent case studies of relativistic electron microbursts have examined precipitating electron fluxes and energy ranges (e.g., Chen et al., 2022; Miyoshi et al., 2020, 2021) using ducted wave propagation (when wave rays are trapped by local density perturbations that form a duct along field lines, see general theory in, e.g., Helliwell, 1965; Karpman and Kaufman, 1982; Pasmanik and Trakhtengerts, 2005; Streltsov and Bengtson, 2020), i.e., excluding any damping and wave intensity decay away from the equatorial source region. Both ray tracing simulations and spacecraft observations have confirmed that even weak density perturbations can result in ducting (Chen et al., 2021b; Hanzelka and Santolík, 2022, 2019; Hosseini et al., 2021; Shen et al., 2021; Yearby et al., 2011), while more effective ducting would allow waves to propagate so far that even ground-based VLF receivers can pick them up (e.g., Demekhov et al., 2017; Martinez-Calderon et al., 2016, 2020; Titova et al., 2017). However, statistical studies using ground-based observations (Douma et al., 2018; Martinez-Calderon et al., 2015; Simms et al., 2019) and mid-to-high latitude spacecraft measurements have yet to yield an estimate of the occurrence rate of ducted waves due to their low occurrence rates and sparse coverage. As a result, the contribution of ducted waves to statistical wave-power averages is likely smoothed out in current empirical models of whistler-mode waves (Agapitov et al., 2013; Meredith et al., 2012). Yet, Chapter 2 previously showed that even the infrequent presence of large amplitude, bursty, and likely-ducted waves at mid latitudes could have an appreciable effect on radiation belt dynamics (Tsai et al., 2022). In this chapter, we will use recently acquired, high energy- and pitch-angle resolution electron data from the ELFIN mission, to provide further insight into the contribution of high-latitude whistler-waves to radiation belt electron losses.

We will compare directly measured precipitating electron spectra, as measured by the ELFIN CubeSats (Angelopoulos et al., 2020), to precipitation simulated in realistic plasma

and magnetic field conditions, with typical whistler-mode waveforms and statistical models of wave-power latitudinal and L-shell distributions. This investigation is a natural continuation of several previous case-studies demonstrating the potential importance of whistler-mode wave ducting utilizing ELFIN observations (Artemyev et al., 2021a; Chen et al., 2022; Tsai et al., 2022). To begin, we judiciously select a number of precipitation events that span different MLT sectors and L-shell ranges to study with our test particle simulations. We find that sub-relativistic electron precipitation is in good agreement with expectation from our simulation when utilizing prior models of statistically averaged wave-power latitudinal distributions. However, relativistic electron precipitation spectra, especially on the nightside, cannot be explained by whistler-mode wave-scattering of electrons from the same statistically averaged wave-power latitudinal distributions. This mismatch therefore either suggests that a transient population of mid-to-high latitude whistler-mode waves must be present to enable bursty and energetic precipitation, but remain ephemeral enough so as to not increase the wave-power averages in statistical models, or, there is missing physics in the modeling. We present the results of our case study in Section 5.4. Section 5.5 covers statistical results using our test-particle model and ELFIN observations with wide MLT coverage. In Section 5.6, we conclude with a summary of our results and possible approaches for how to rectify the inclusion of whistler-mode wave populations that accurately reflect electron losses into future radiation belt models.

5.2 Data Sets

To begin, we select only twelve events as representative examples of whistler-mode wave-driven electron precipitation (although later, we will use several years of ELFIN mission data for the full statistical portion of this chapter). Each case study features at least one bursty precipitation event, classified as 1-7 contiguous spins ($\sim 3\text{s} < t < 21\text{s}$) with a strong ($j_{prec}/j_{trap} > 0.5$) precipitating-to-trapped flux ratio (hereafter, trapped refers to fluxes near-perpendicular to the magnetic field, i.e., locally trapped, but may be within the drift loss cone) while spanning all MLTs except for the dusk sector. Note that this relatively long

Figure	CubeSat	Prec. Timerange (UTC)	MLT	L-shell	MLT	Kp	Match
2a	ELA	21-02-03 20:46:37-20:46:50	Dawn/Day	6.2	5.8	3	✅
2b	ELA	21-02-03 20:47:13-20:47:33	Dawn/Day	7.5	5.7	3	✅
1a,2c	ELB	21-01-06 11:53:50-11:54:01	Dawn/Day	7.1	8.4	2	✅
2d	ELA	21-10-01 08:10:02-08:10:13	Dawn/Day	6.6	8.8	3	❌
2e	ELA	21-10-01 04:59:57-05:01:18	Dawn/Day	6.4	10.2	4	✅
2f	ELA	21-11-01 04:23:34-04:23:44	Dawn/Day	6.1	13.1	3	❓
3a	ELA	21-01-11 17:50:50-17:50:58	Night	4.8	19.0	3	❓
3b	ELA	21-02-03 13:42:25-13:42:32	Night	6.6	19.3	3	❓
3c	ELA	21-02-03 09:01:43-09:01:56	Night	5.1	20.2	2	✅
3d	ELA	21-11-02 22:18:21-22:18:35	Night	4.5	20.8	2	❌
3e	ELB	20-09-26 01:01:12-01:01:20	Night	4.8	2.6	4	❌
1b,3f	ELA	20-09-04 01:12:24-01:12:33	Night	6.5	3.8	3	❌

Table 5.1: Locations of and geomagnetic activity conditions for the 12 events chosen for study in Section 5.4 on the basis of signatures of nonlinear wave particle interaction. Half were chosen in the dawn/day sector, while the other half were chosen in the night sector. Events were selected to have fairly uniform coverage in each sector. The "Match" column reflects how well the model agrees with ELFIN data which will be discussed further in Section 5.4 using Figures 5.2 and 5.3.

precipitation observation that is on the order of seconds are typically attributed to either ELFIN's crossing of multiple whistler-mode equatorial source regions (see details regarding temporal/spatial variation of ELFIN-observed precipitation patterns in Zhang et al., 2023) or to the natural spread of whistler-mode waves propagating along curved magnetic field lines (see Kang et al., 2022, for further discussion regarding the spatial spread of precipitation produced by a very localized equatorial whistler-mode source).

Table 5.1 itemizes these events and their properties. We took special care to exclude ambiguous events that had signatures of EMIC-wave driven precipitation (see examples of EMIC-driven precipitation events observed by ELFIN in An et al., 2022a; Angelopoulos et al., 2023; Capannolo et al., 2023a; Grach et al., 2022a) or field line scattering signatures (see, e.g., Artemyev et al., 2022a) not only in these 12 case studies, but also for the ∼6000 orbits (∼8500 science zones) used for the statistical portion of this chapter. In addition, we only included events where energy spectra was monotonically decreasing to reduce rare phenomena such as microbursts (see Zhang et al., 2022b, for more details regarding ELFIN observations of microbursts) that may skew results. All data were processed to exclude low

counts/statistically insignificant data points (i.e., electronic noise).

Here, we used three data products derived from ELFIN's EPDE dataset: the energy spectrograms of trapped electron fluxes $j_{trap}(E)$ (outside the local bounce loss cone), the energy spectra of precipitating electron fluxes $j_{prec}(E)$ (moving toward the ionosphere within the local bounce loss cone), and the precipitating-to-trapped flux ratio j_{prec}/j_{trap}. Fig. 5.1 shows two example events from our data set: the first two panels of 5.1a and 5.1b show the spectrograms of precipitating and trapped fluxes for each event, respectively, whereas the third panels show the spectrograms of the ratio of precipitating to trapped fluxes. The precipitation bursts marked by red and purple boxes are observed well inside the outer radiation belt, the region characterized by high intensity relativistic electron trapped fluxes (horizontal orange bar above panels). Sporadic peaks of the j_{prec}/j_{trap} ratio due to localized electron scattering by whistler-mode waves are seen at those times. The plasmasphere is also denoted (horizontal cyan line) and is defined as occurring immediately below the latitude where 300 keV trapped electron fluxes first fall below the sensitivity level (presumably due to whistler-mode hiss waves; see further discussions regarding identifying different

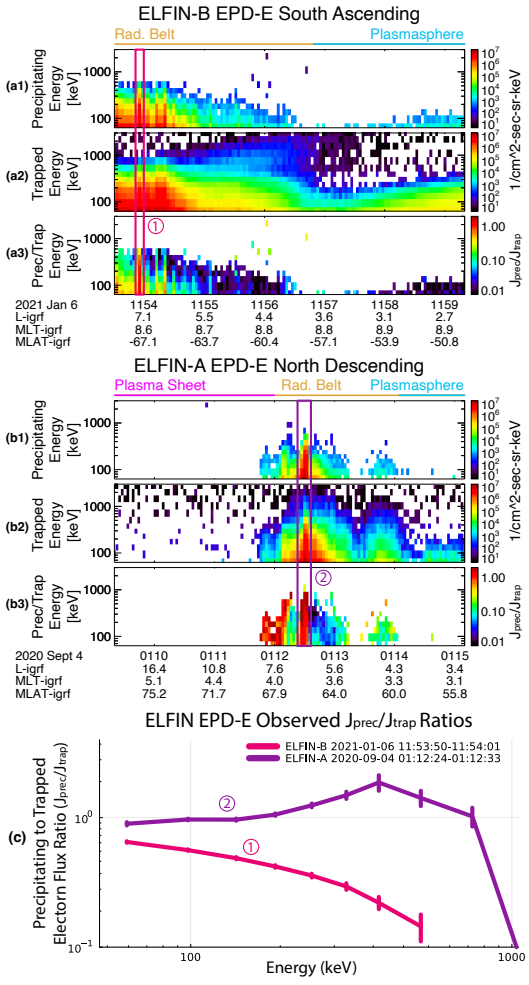


Figure 5.1: Panels (a) and (b) show ELFIN observations of two science zone crossings. The three sub-panels show, from top to bottom, energy spectra of precipitating fluxes, trapped fluxes, and precipitating-to-trapped flux ratios, respectively. Panel (c) shows the energy spectra of the precipitating to trapped electron flux ratios for their respective boxed time-ranges (1) and (2) during which short-lived but intense precipitation is observed.

magnetospheric regions in ELFIN observations in Angelopoulos et al., 2023; Mourenas et al., 2021). Fig. 5.1c shows the primary derived data product used for this (and the next) chapter: the energy spectrum of the flux ratio j_{prec}/j_{trap} averaged over the duration of the precipitation burst.

5.3 Simulation of Wave-Particle Interactions

We next compare ELFIN's *in situ* flux ratios j_{prec}/j_{trap} with those from test-particle simulations in the presence of waves with amplitudes determined by an empirical chorus wave-power distribution model. This is detailed in Section 3.4.2, where the wave-amplitude model, which is based on a combination of 4 years of Van Allen Probe observations and 10 years of Cluster observations (Agapitov et al., 2018), provides the latitudinal distribution of simulated whistler-mode wave intensity.

For each event of our case study, we perform a forward-modeling (as opposed to an inverse-modeling) procedure, where we obtain the latitudinal wave amplitude distribution based on the ELFIN's L, MLT, and Kp during the precipitation burst and then check whether the precipitation spectrum from our test-particle simulations is in agreement with the observations. In Fig. 5.1a event, for example, ELFIN-B observed a precipitation burst on 6 January 2021 between 11:53:50-11:54:01 UTC. We use T89 (Tsyganenko, 1989) to map ELFIN-B's location at L = 7.1 and MLT = 8.4. For this event, Kp= 2 was obtained from the WDC and GFZ databases (WDC for Geomagnetism, Kyoto (`http://wdc.kugi.kyoto-u.ac.jp/wdc/Sec3.html`) and GFZ Helmholtz Centre, Potsdam (`https://kp.gfz-potsdam.de/en/`)), but for modeling, we use minimum Kp= 3. Then, all three variables are used to determine the coefficients used in Eq. 3.27 (Agapitov et al., 2018). A test-particle simulation is then run using the following parameters:

1. an empirical model B_w for whistler-mode wave intensity, modified as described in Equation 3.28

2. a plasma density model for equatorial plasma density (Sheeley et al., 2001)

3. an empirical model to account for plasma density variation along the field line as: $\omega_p/\omega_p(0) = \cos^{-5/2}\lambda$ (Denton et al., 2006)

4. a large ensemble consisting of $N = 2.5 \times 10^5$ particles spanning initial pitch angles $3^\circ \leq \alpha_0 \leq 15^\circ$ (we only care about electrons near the loss cone, which is set to 3°, further explained below)

5. 32 energy bins from 50 keV to 1 MeV with 50× more particles in the highest energy bin compared to lowest to increase high energy precipitation statistics

Particles are then simulated for just one bounce period, i.e., particle tracing is terminated upon return to the equatorial plane, $z = 0$. This allows us to understand the scattering efficiency of a single interaction between the electron and the whistler-mode wave packet. Since wave occurrence, max amplitude, and equatorial electron phase space density are not known, we cannot use our simulation to predict absolute fluxes like we did previously in Chapter 4. Rather, we are instead interested in determining and comparing the relative fluxes of precipitating electrons, especially at higher energies where we expect the differences between our simulations and observations to be greatest.

In order to obtain the simulated precipitating-to-trapped electron flux ratio, we first set the equatorial loss cone to $\alpha_{LC} = 3^\circ$. At ELFIN's altitude, the locally mirroring electrons map to around twice α_{LC}, so we consider simulated electrons with $\alpha_{final} < 3^\circ$ as precipitating (j_{prec}) and those $3^\circ < \alpha_{final} < 6^\circ$ as trapped (j_{trap}). In a single interaction, the electrons cannot lose more than a couple of degrees in pitch angle, so we limit the upper bound of our simulation to 15° to save simulation time. Finally, j_{prec}/j_{trap} can easily be computed for each of the 32 energy bins and directly compared to ELFIN's 16 energy bins.

5.4 Precipitation Events

Figures 5.2 and 5.3 show comparisons between j_{prec}/j_{trap} derived from test particle simulations and ELFIN-observed j_{prec}/j_{trap} during the precipitation bursts of all 12 case studies.

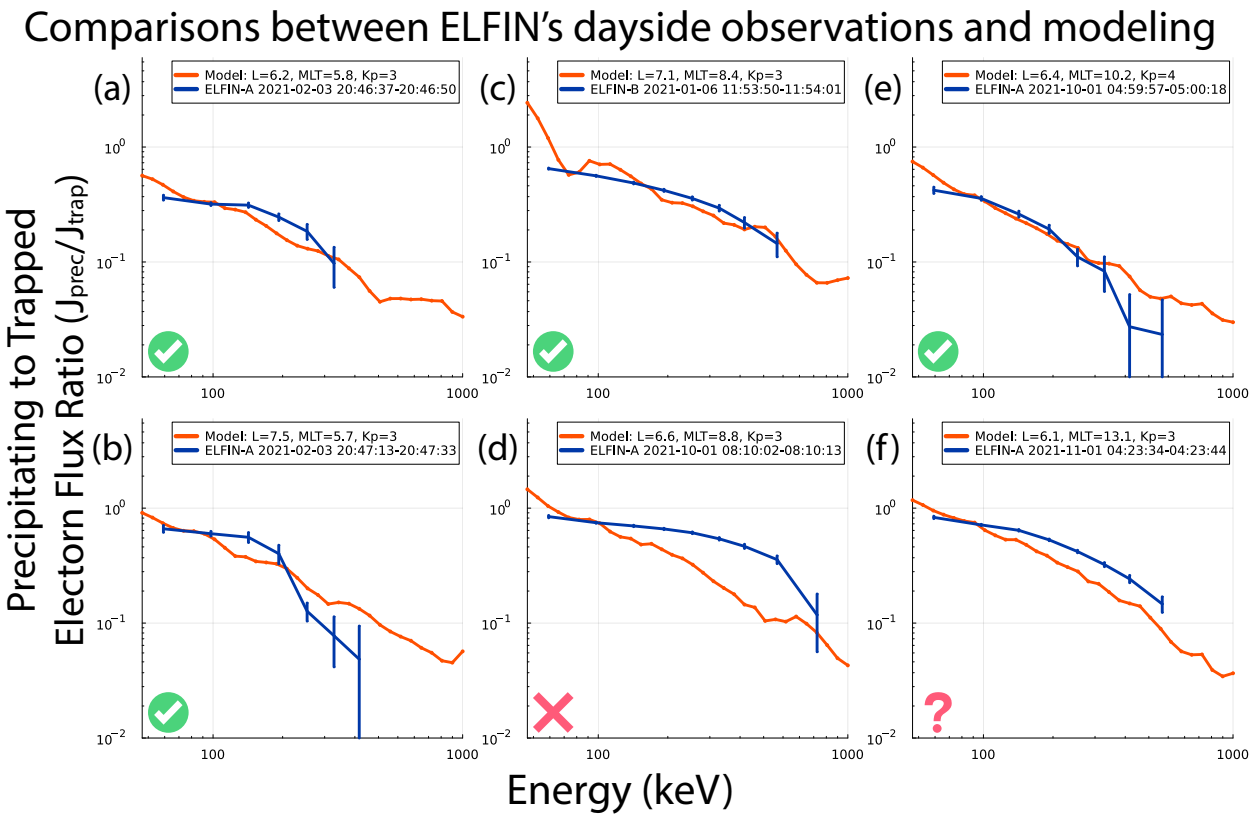


Figure 5.2: Comparisons between ELFIN observations (dark blue) and modeling using empirical wave model (orange) on the dayside ($4 < \text{MLT} < 15$). The error bars on ELFIN data denote statistical variance. Checkmarks, question marks, and crosses denote good, questionable, and bad matches, respectively.

Both figures are meant to demonstrate the viability of the comparisons; as such, the conclusions drawn in this section serve only to qualitatively foreshadow the statistical results in Section 5.5. Additionally, note that simulated j_{prec}/j_{trap} is normalized to the mean of ELFIN's first two energy bins ($j_{prec}/j_{trap}(\sim 80$ keV)): this is functionally equivalent to setting the equatorial wave amplitude consistent with ELFIN observations of electron precipitation (the $\sim 30-100$ keV precipitating-to-trapped electron flux ratio has been known to correlate well with the equatorial wave amplitude, see Li et al., 2013; Ni et al., 2014). As mentioned above, the main quantity to compare between our simulation output and data is the relative energy profile (not the absolute value) of j_{prec}/j_{trap}. We use three important properties of radiation belt electron scattering to justify this comparison: 1) electrons can be diffusively scattered even by monochromatic waves due to the strong background (dipole) magnetic

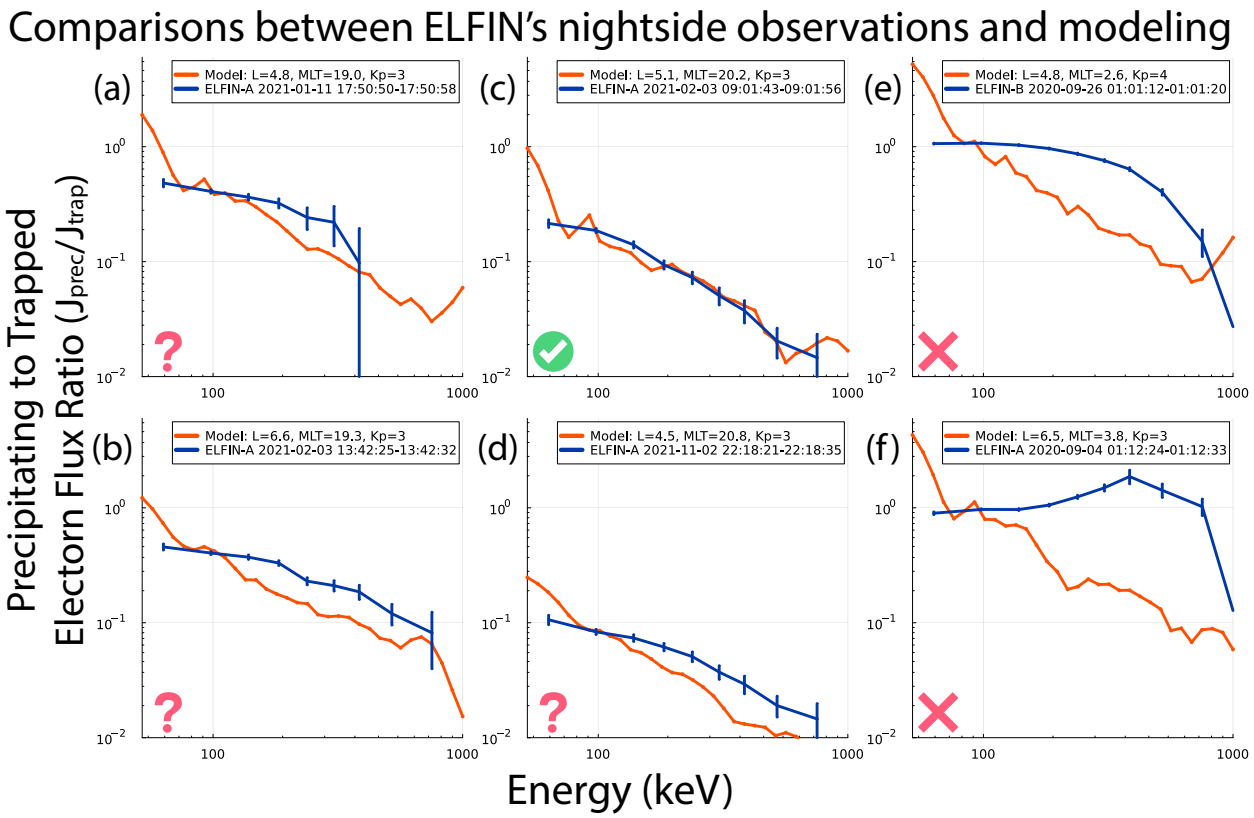


Figure 5.3: Comparisons between ELFIN observations (dark blue) and modeling using empirical wave model (orange) on the nightside ($18 < \text{MLT} < 4$). The error bars on ELFIN data denote statistical variance. Checkmarks, question marks, and crosses denote good, questionable, and bad matches, respectively.

field gradient (Albert, 2001, 2010; Shklyar, 2021), 2) for monochromatic waves, each latitude corresponds to a specific resonance energy for fixed equatorial pitch angle (equal to the loss cone pitch angle), and 3) the diffusion coefficient at the loss cone determines the j_{prec}/j_{trap} ratio (Kennel and Petschek, 1966; Li et al., 2013). Thus, the energy spectrum of j_{prec}/j_{trap} is primarily determined by the wave intensity profile along the magnetic field lines.

On the dayside, the simulated energy spectra of j_{prec}/j_{trap} agree reasonably well with observations: Fig. 5.2 shows that in four out of six events, the simulated precipitation ratio energy profile is quite similar to the observations. In those cases, the empirical whistler-mode wave distribution agrees well with the instantaneous latitudinal profile of wave power, including at mid-to-high latitudes (Agapitov et al., 2018). The upper energy limit of precipitating electrons is dictated by the maximum energy of trapped electrons that has sufficient

flux to result in precipitation above the sensitivity level of the instrument. In other words, test-particle simulations with a trapped spectrum of up to 1 MeV always have a longer energy tail of the j_{prec}/j_{trap} ratio than the observed j_{prec}/j_{trap} ratio. The examples shown in Fig. 5.2 suggest that the wave-power distribution model qualitatively agrees with observations.

The same figure shows that the observed j_{prec}/j_{trap} profiles extend up to $500 - 700$ keV. Scattering such energies requires that waves propagate to at least $\sim 30°$ in latitude (see, e.g., Fig. 1.4). As the dayside latitudinal distribution of whistler-mode waves exhibits significant wave intensity at mid-latitudes (Agapitov et al., 2018), it makes sense to observe relativistic electron scattering in this MLT sector (Thorne et al., 2005).

Fig. 5.2f shows a questionable case, where the spectral slope of the precipitating flux ratio consistently underestimates ELFIN observations beyond uncertainty. Such discrepancy could be due to differences in the assumptions made regarding equatorial plasma conditions, or it could possibly be resolved by a minor corrective wave power increase at higher latitudes. On the other hand, Fig. 5.2d shows a stark difference between simulation and observation with very strong j_{prec}/j_{trap} ratio (~ 0.5) at relativistic energies (~ 500 keV). Such strong precipitation cannot be described by a statistically averaged wave intensity model, and requires nearly constant wave amplitude up to mid-latitudes, i.e., possibly ducted waves. In both cases, the discrepancy is quite evident at energies > 200 keV.

Fig. 5.3 shows six examples of ELFIN observations of nightside relativistic electron precipitation. The nightside magnetosphere has a large population of suprathermal electrons (Li et al., 2010a; Walsh et al., 2020) which quickly damp the waves when they propagate off their equatorial source location if they become oblique there. As a result, the observed wave-power distribution exhibits a rapid decay with distance from the equator (or equivalently, with latitude along field lines) in this MLT sector (Meredith et al., 2012). Therefore, only ELFIN events with a rapid falloff of their precipitation ratio with energy can be consistent with the results of our simulations that rely on the statistical models of the above wave-power distributions (as is the case for only one of the six nightside events, shown in Fig. 5.3c). Three other nightside events (Figures 5.3a, 5.3b, and 5.3d) show excessive precipitation at

$>$ 200 keV; the j_{prec}/j_{trap} ratio for these events clearly deviates from expectation based on the simulation results for the aforementioned reason.

The remaining two events (Figures 5.3e, 5.3f) show excessive precipitation with $j_{prec}/j_{trap} \sim 1$ up to 400 keV and 800 keV, respectively. These events certainly cannot be described by the statistically averaged wave-power distribution that we assumed. The event in 5.3f is the same as that in Fig. 5.1b, where the ratio exceeding 1 can be seen in the context of the rest of the radiation belt crossing. When $j_{prec}/j_{trap} > 1$ at $>$ 300 keV, this is usually indicative of sub-spin electron flux variations, where the time difference of $\sim$ 0.7s between precipitating and trapped flux measurements is longer than the timescale of the flux variation. Indeed, looking at sub-spin data confirms that multiple microbursts are included in this particular observation, which is not included in statistical results in Section 5.5 below due to the precipitating-to-trapped flux ratio increasing with energy (see Figure 1 in Zhang et al., 2022b, for another example of multiple microbursts in a single ELFIN science zone crossing).

Figures 5.2 and 5.3 demonstrate that statistical averages of wave-power distribution (Agapitov et al., 2018) can reasonably describe most dayside relativistic electron precipitation and nightside sub-relativistic ($<$ 200 keV) electron precipitation. The primary differences between simulations and observations occur for extreme events; i.e., those with relativistic energies, either having $j_{prec}/j_{trap} > 0.5$ at dayside or $j_{prec}/j_{trap} > 0.1$ on night side. These events could be explained by wave propagation with anomalously high wave intensity at mid-latitudes, which is possible either through ducting or through equatorial generation with moderately oblique wave normal angles at the equator and subsequent refraction towards field-aligned propagation at higher latitudes (e.g., Chen et al., 2022; Miyoshi et al., 2020).

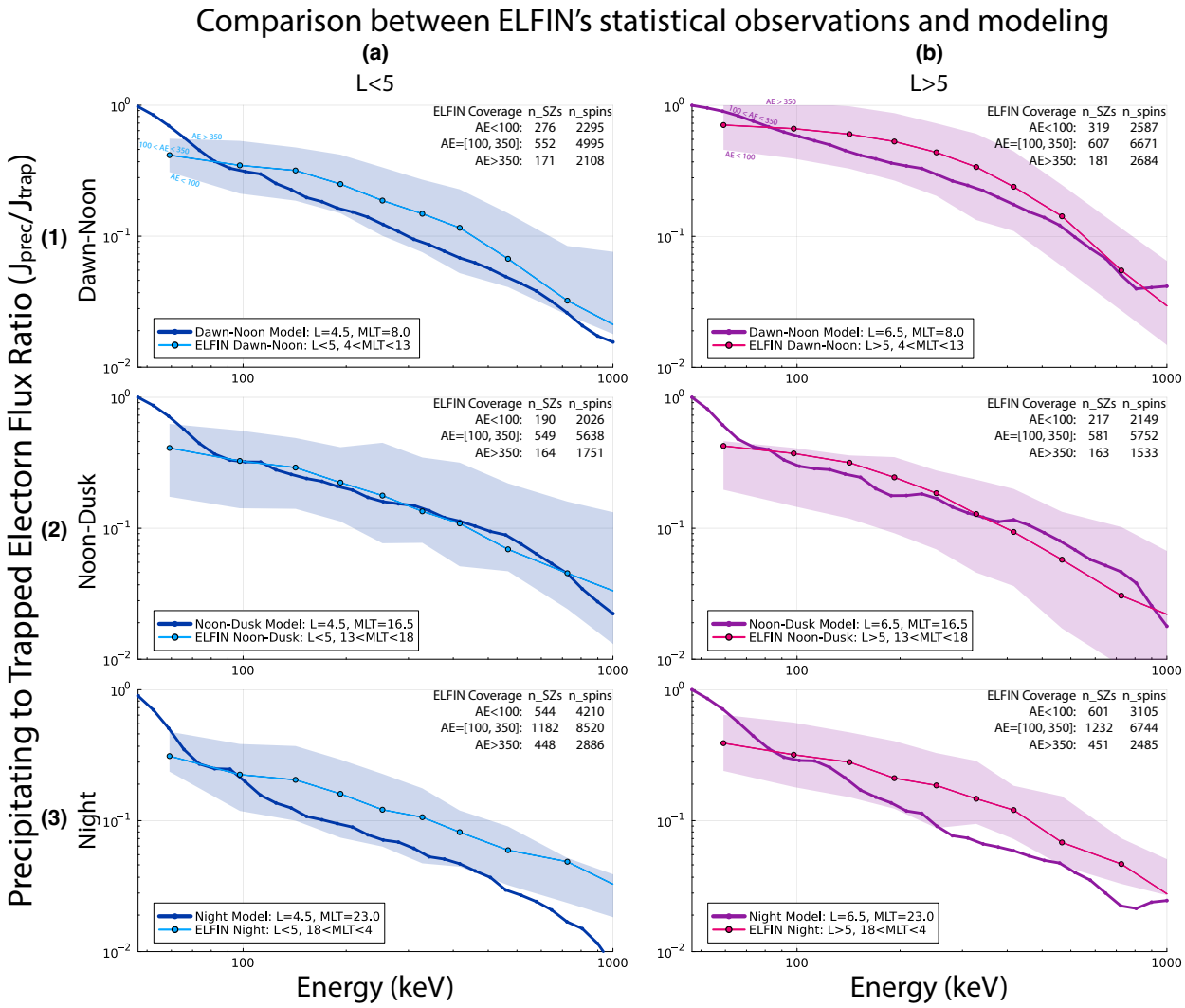


Figure 5.4: Rows (1), (2), and (3) show model/observation comparisons of normalized precipitating energy spectra at three different MLT sectors, whereas columns (a) and (b) show model/observation comparisons at either low or high L shells. Each plot uses light blue (ELFIN observations) and dark blue (model) at low L-shells plus magenta (ELFIN observations) and purple (model) at high L-shells. Shaded regions represent boundaries of low (AE < 100 nT) and high (AE > 350 nT) geomagnetic activity. The statistical coverage used for the ELFIN data is shown in Fig. 5.5. Modeled precipitation is consistent with observations for the dusk MLT sector ($13 <$ MLT < 18) and high L-shells on the dawn/dayside ($4 <$ MLT < 13). However, there is a slight underestimation at lower L-shells on the dawn/day side above 200 keV, while the deviation becomes much more significant at all L-shells on the nightside.

5.5 Statistical Results

To confirm the generality of the conclusions drawn from Figures 5.2 and 5.3, we compare test-particle simulations for three MLT sectors and two L-shell ranges ($L \in [4, 5]$ and $L \in [5, 7]$) with statistically-averaged ELFIN precipitating-to-trapped flux ratio observations. Since the empirical wave model has discrete bins, we pick a single MLT/L shell for modeling which represents that particular function of $B_w(\lambda)$ from the associated MLT/L bin. Fig. 5.4 shows j_{prec}/j_{trap} profiles for the three MLT sectors: dawn-noon (MLT$\in [4, 13]$), noon-dusk (MLT$\in [13, 18]$), and night (MLT$\in [18, 24]$ or $\in [0, 4]$). ELFIN measurements are also separated by geomagnetic activity: low (AE $<$ 100 nT), medium (100 nT $<$ AE $<$ 350 nT), and high (AE $>$ 350 nT). This is indicated by the light shading enveloping the solid lines marked with outlined circles: the center lines denote the moderate activity level, whereas the low and high activity levels are denoted by the lower and upper bounds of the shaded region – they can be considered as an uncertainty range for the ELFIN-observed precipitation rates. The breakdown of the statistical coverage of ELFIN data used for the statistical portion of this chapter is summarized in Fig. 5.5. Like before, we use the same normalization of j_{prec}/j_{trap} at 80 keV to the medium geomagnetic activity ELFIN curve; however, to increase consistency of statistics in the simulation, we increase the number of particles in each simulation ensemble to $N = 10^6$.

Simulation results describe the statistically-averaged precipitation rate for dawn-noon at high L-shells (Fig. 5.4.1b) and noon-dusk (Fig. 5.4.2) quite well, remaining within the uncertainty range up to 1 MeV. For low L-shells on the dawn-noon sector (Fig. 5.4.1a), the empirical wave-power distribution as a function of latitude decreases too quickly, and thus the simulated precipitation rates slightly underestimate the observed scattering rates. Similar to the dayside case studies in Fig. 5.2, this minor underestimation is most apparent $\sim$ 200 keV. However, in the nightside MLT sector (Fig. 5.4.3), the discrepancy between simulations and observations is most apparent: test-particle simulations suggest a steep decrease in precipitation rate with energy, while ELFIN observations show statistically important losses of relativistic electrons. This discrepancy cannot be attributed to curvature scattering (which

can also increase relativistic electron precipitation on the nightside during active times, see, e.g., ELFIN observation analysis in Artemyev et al., 2022a), because we took provisions to specifically exclude all j_{prec}/j_{trap} profiles showing curvature scattering features from the dataset (i.e., those with increasing j_{prec}/j_{trap} with energy at lower L-shells, see discussion of such features in Dubyagin et al., 2002; Sergeev et al., 1993). Therefore, there are two potential main sources for the aforementioned simulation-observation discrepancy: 1) relativistic electron scattering by intense, bursty, field-aligned, mid-to-high latitude nightside whistler-mode waves which are currently unaccounted for in statistical wave models or 2) uncertainties of ELFIN orbit projections onto the equatorial plane (the uncertainties of such projections are expected to be largest on the nightside due to how stretched magnetic field lines are during substorm activity). To address the latter issue, we checked that Fig. 5.4 did not significantly change between the usage of the default non-storm magnetic field model used (Tsyganenko, 1989) and a more accurate model (Tsyganenko, 1995). Note that we did not use the storm-time model (Tsyganenko and Sitnov, 2005) because most of our observations events are not associated with storm activity. The primary uncertainty in night-side projections should be attributed to substorm dynamics with the formation of the thin current sheet along with very strong magnetic field-line stretching (see examples and discussion in Artemyev et al., 2022a). Such dynamics may be better handled by more advanced magnetic field models (such as, e.g., Sitnov et al., 2019; Stephens et al., 2019), and thus, it may be a good idea to revisit ELFIN projections during substorm dynamics when such models become publicly available.

Another possibility, to be discussed in Section 5.6, is the presence of very oblique, near-equatorial chorus that results in relativistic electron precipitation due to high-order resonances (recently discussed using the ELFIN data set in Gan et al., 2023), though the resulting flux-ratio energy-spectra in their case study appear different from the measured ones presented herein. Regardless, Fig. 5.4 statistically validates our multi-case-study results from Figures 5.2 and 5.3: the simulated energetic (sub-relativistic and relativistic) precipitation ratio as a function of energy inferred from statistical averages of the whistler-

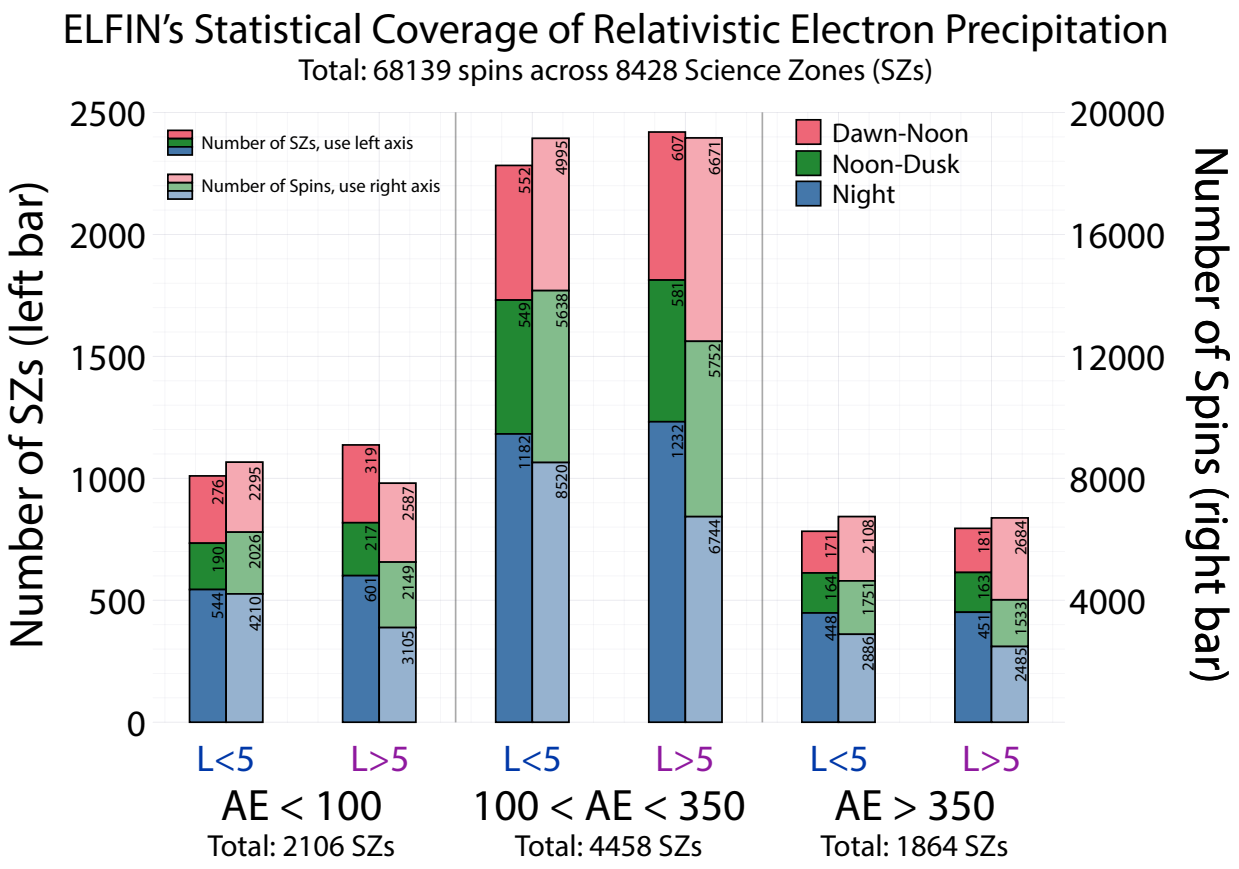


Figure 5.5: ELFIN's data coverage of energetic bursty electron precipitation over a ∼1 year period utilized in Fig. 5.4's statistical averages, broken down into instantaneous AE disturbance levels and low/high L shells (shown by each individual bar graph) as well as MLT sector (shown by stacked bars). Left bars/primary axis show the number of science zones (SZs) (i.e., radiation belt crossings) while right bars/secondary axis show the number of spins that actually constituted the empirical average. Note that field-line curvature scattering and EMIC-driven precipitation were excluded from this data set.

mode wave-power distribution agrees reasonably well with observations of precipitation at the dawn-noon-dusk MLT sector (except during strong relativistic precipitation events), as well as at the nightside for sub-relativistic energies, but seems to consistently underestimate relativistic precipitation on the nightside.

5.6 Discussion

This chapter shows that low-altitude observations of precipitating electron energy spectra can often contain more energetic losses than would be expected from electron scattering by typical (i.e., statistically averaged) whistler-mode wave amplitudes. In both our case and statistical studies, we selected only events with unambiguous signatures of whistler-driven precipitation. Specifically, we excluded events exhibiting electron precipitation due to field line curvature scattering (based on their dispersive energy signature) or electromagnetic ion cyclotron (EMIC) waves (based on their increasing precipitating-to-trapped ratio with energy, peaking at relativistic energies). Modern radiation belt simulation and modeling tools mostly rely on EMIC-driven electron precipitation to explain relativistic electron losses (see, e.g., Drozdov et al., 2017; Ma et al., 2015, and references therein), partly because whistler-mode wave models cannot provide sufficiently large rates of relativistic electron scattering. Our results indicate, however, that inclusion of higher wave-power at mid-to-high latitudes (e.g., due to ducted whistler-mode waves or moderately oblique source whistlers that become field-aligned away from the equator due to refraction; see, e.g., (Breuillard et al., 2012; Chen et al., 2013; Watt et al., 2013)) could appreciably enhance the contribution of whistler-mode waves to relativistic electron scattering. Thus, EMIC waves may not be unique in their ability to scatter relativistic electrons (especially those $\lesssim$ 1 MeV, which are at the limit of the expected minimum EMIC wave resonance energy in typical inner magnetosphere density and magnetic field conditions; see discussions regarding the importance of EMIC-driven scattering of $\lesssim$ 1 MeV in (Bashir et al., 2022; Capannolo et al., 2019; Chen et al., 2016; Hendry et al., 2017)).

The question then arises: if mid-to-high latitude whistler-mode waves are important, how can we quantify this population of waves in the radiation belt? Simultaneous equatorial and mid-latitude observations of whistler-mode waves require multi-spacecraft wave measurements and are quite rare (e.g., Colpitts et al., 2020). Realistic ray-tracing simulations (Bortnik et al., 2007; Chen et al., 2013; Katoh, 2014; Watt et al., 2013) require detailed information about suprathermal electron populations and their anisotropy (see discussion

in Bortnik et al., 2006; Li et al., 2010a; Ma et al., 2017). Ground-based VLF wave observations (which are often associated with ducted whistler-mode wave propagation to the ionosphere, see Demekhov et al., 2020; Douma et al., 2018; Martinez-Calderon et al., 2015; Simms et al., 2019; Titova et al., 2015) capture only some of the fully ducted waves that reach the ground and clearly cannot cover those that only reach mid-latitudes. Work presented in this chapter suggests a new approach for performing such investigations, which may involve a statistical investigation of electron precipitating spectra, where $<$ 100 keV fluxes can be attributed to equatorial whistler-mode waves (Li et al., 2013, 2014a; Ni et al., 2014), while $>$ 200 keV fluxes can be associated with the latitudinal profiles of the whistler-mode wave intensity (see discussion in Artemyev et al., 2021a; Zhang et al., 2022b). However, recent theoretical and observational work suggests that very oblique (nearly electrostatic) whistler-mode waves can also effectively scatter electrons up to several hundreds of keV (see Li et al., 2014a; Lorentzen et al., 2001; Mourenas et al., 2014a). This explanation is less likely for two reasons: 1) oblique waves are significantly less efficient at scattering electrons beyond 200 keV in comparison with 50 keV electrons (e.g., Artemyev et al., 2022c; Gan et al., 2023) and 2) electron scattering via oblique waves are statistically less efficient on the nightside as compared to the dayside (e.g., Aryan et al., 2020, and references therein), the latter of which contradicts this chapter's findings. Regardless, the potential of bursty oblique waves that are smoothed out in statistically averaged models cannot be discarded, so the aforementioned approach alone cannot separate the contributions to relativistic electron precipitation by intense, field-aligned, mid-latitude whistler-mode waves from those by intense, highly oblique, near-equatorial whistler-mode waves. A preliminary look at published observational and modeled flux-ratio energy spectra suggests that the spectral slope of j_{prec}/j_{trap} due to oblique whistler-electron high-order resonance interactions may be steeper than the case studies presented in this chapter (i.e., scattering by near-equatorial oblique waves is less efficient at higher energies). In a similar vein, lower wave frequency (Li et al., 2010b; Mourenas et al., 2012b) and reduced plasma density (Agapitov et al., 2019; Allison and Shprits, 2020; Thorne et al., 2013) have previously been implicated in causing higher energy resonance, but these mechanisms are still unlikely as they affect the entire spectra, vertically

shifting the j_{prec}/j_{trap} flux ratio without significantly changing its slope. The solution to this discrepancy must drastically increase the precipitating rate of relativistic electrons 50-100% higher than the the ratio for $\sim$ 100 keV electrons. Careful examination of these processes, including their effects on pitch-angle spectra, may allow us to disambiguate their relative contributions to the global relativistic precipitation from that of ducted waves. Furthermore, accurate quantitative estimation of the relative contribution of ducted whistler-mode waves to mid-to-high latitude wave power (and thus to relativistic electron scattering and losses) requires careful, detailed studies of low-altitude energy and pitch-angle electron flux spectra combined with either conjugate equatorial wave measurements (see cases studies in Capannolo et al., 2018; Shi et al., 2022; Zhang et al., 2022c) or local (i.e., low-altitude, see examples in Benck et al., 2008; Hayosh et al., 2013; Shen et al., 2021) wave measurements.

In this chapter, we compared ELFIN energy spectra of energetic electron precipitation-to-trapped flux ratios due to pitch angle scattering by nonlinear interactions with whistler-mode waves with expected precipitation spectra using test-particle simulations of such scattering by empirical models of wave-power distributions of whistler-mode waves. The results suggest that these empirical models are inconsistent with the observed relativistic electron precipitation by such waves on the nightside, and occasionally also inconsistent with observed precipitation on the dayside. The discrepancy between the observed average wave-power distribution and observed precipitation spectra was further reinforced by simulation comparisons with statistical averages of ELFIN observations using over two years of data at three local time sectors. Further investigation is needed to clarify the mechanisms behind higher-than-expected relativistic electron precipitation rates on the nightside: are they really caused by ducted waves that are underrepresented in empirical models, or do we really need to incorporate wave properties beyond just wave intensity as a function of latitude? This is the question we aim to answer in the next chapter, with the ultimate goal of explaining the inconsistencies in nightside energetic electron losses.

CHAPTER 6

Explaining Nightside Relativistic Electron Precipitation

6.1 Introduction

In the previous chapter, we used modeled electron precipitation spectra derived from statistically-averaged wave intensity distributions from Agapitov et al. (2018) to directly compare with statistical observations of electron precipitating fluxes from ELFIN (Angelopoulos et al., 2020). The analysis revealed a day-night difference in energetic electrons scattered by whistler-mode waves, with more intense electron precipitation on the dayside than on the nightside. This is attributed to two system-level properties – (1) nightside regions generally have a lower plasma density, and (2) nightside wave activity is generally more confined to the equatorial plane (Agapitov et al., 2013; Meredith et al., 2001, 2003) – both of which cause strong resonant wave particle interactions to preferentially occur on the dayside, resulting in more extreme energetic electron losses (e.g., Aryan et al., 2020; Mourenas et al., 2014a; Thorne et al., 2005; Wang and Shprits, 2019). The model-data comparisons in Fig. 5.4 thus showed good agreement between electron precipitation and wave power in the dusk and daysides, but ELFIN-measured nightside relativistic ($\gtrsim$ 500 keV) precipitating flux rates were still substantially larger than anticipated (i.e., modeled) and nearly comparable to those on the dayside. Understanding the mechanisms that can cause such intense energetic precipitation is a prerequisite for accurately modeling electron loss in the radiation belts, and therefore motivates the need to explore what key factors actually determine nightside electron losses.

There are a few prime candidates that determine the efficiency of wave-particle resonant interactions (and, particularly, the energy dependence of whistler-mode wave driven electron scattering):

1. Wave intensity distribution along magnetic field lines (see discussion in Thorne et al., 2005; Wang and Shprits, 2019).

2. Obliquity of wave propagation relative to the background magnetic field (see discussion in Artemyev et al., 2016; Lorentzen et al., 2001; Mourenas et al., 2014a).

3. Wave frequency spectrum and its variation along magnetic field lines (see discussion in Agapitov et al., 2018)

4. Equatorial plasma density magnitude (see discussion in Agapitov et al., 2019; Allison and Shprits, 2020; Thorne et al., 2013) and its variation along magnetic field lines (see discussion in Artemyev et al., 2013; Summers and Ni, 2008).

Having examined the importance of incorporating empirical wave amplitude in Chapter 5, we now study the remaining three mechanisms, which could potentially modulate nightside electron precipitating spectra. First, intense nightside whistler-mode waves are typically associated with strong plasma sheet injections (Fu et al., 2014; Tao et al., 2011; Zhang et al., 2018a), which are often accompanied by an enhanced convection electric field that transports cold plasma Earthward, thereby decreasing equatorial plasma density (Agapitov et al., 2019; Vasko et al., 2017b). A lower plasma density results in a lower plasma frequency; a lower plasma frequency to gyrofrequency ratio, f_{pe}/f_{ce} yields a higher cyclotron resonance energy $E_R \propto (f_{ce}/f_{pe})^2$ to f_{ce}/f_{pe} (from low to high energy) of electrons for given wave frequencies, wave normal angles, and electron pitch angles (Allison et al., 2021; Li et al., 2010b; Stix, 1962; Summers et al., 2007b). This nightside localized density reduction can thus potentially increase the scattering rate of relativistic electrons.

Second, statistical observations have shown a clear trend of the average wave frequency decreasing with latitude along field lines (i.e., increasing distance from the equatorial plane)

(Agapitov et al., 2018). This is likely caused by preferential Landau damping of higher-frequency waves resonating with suprathermal electrons (Chen et al., 2013; Maxworth and Golkowski, 2017; Watt et al., 2013). A lower normalized wave frequency f/f_{ce} means a higher cyclotron resonance energy $E_R \propto (f_{ce}/f)(1-f/f_{ce})^3$ to $(f_{ce}/f)^{1/2}(1-f/f_{ce})^{3/2}$ from low to high energy (Li et al., 2010b; Mourenas et al., 2012b). Thus, this reduction in the mean wave frequency in the nightside off-equatorial region may also increase the scattering rate of relativistic electrons.

Third, plasma injections are often associated with enhanced electrostatic turbulence (Agapitov et al., 2015b; Malaspina et al., 2018; Mozer et al., 2015; Vasko et al., 2017a) that forms a plateau in the field-aligned velocity distribution and significantly reduces Landau damping of oblique whistler-mode waves (see discussion in Artemyev and Mourenas, 2020; Ma et al., 2017; Mourenas et al., 2015). In this regime, oblique (with wave normal angles below the Gendrin angle $\theta_G \approx \mathrm{acos}(2f/f_{ce})$) and very oblique (with wave normal angle up to the resonant cone angle $\theta_r \approx \mathrm{acos}(f/f_{ce})$) waves may survive Landau damping (see Chen et al., 2019b; Ke et al., 2022; Min et al., 2014; Sauer et al., 2020). These waves then become oblique off the equatorial plane (Bortnik et al., 2007; Chen et al., 2013), or, in more unusual cases, are generated within the equatorial source region (Agapitov et al., 2016; Artemyev et al., 2016; Li et al., 2016a). Wave obliquity not only increases the resonant interaction energy with electrons as $E_R \propto 1/k_\parallel^2 \propto 1/\cos^2\theta$ (e.g., Mourenas et al., 2015; Verkhoglyadova et al., 2010), but also allows for interactions with electrons at higher-order cyclotron resonances ($n \gg 1$, e.g., Albert, 2017; Artemyev et al., 2013; Mourenas et al., 2012b; Shklyar and Matsumoto, 2009) which can drastically increase the resonance energy $E_R \propto n^2$ (e.g., Gan et al., 2023; Lorentzen et al., 2001). Thus, nightside whistler-mode wave obliquity could also potentially increase the scattering rate of relativistic electrons.

Here, we examine each of these three mechanisms to see whether they can explain the enhanced precipitation of relativistic electrons in the nightside MLT sector using a combination of statistics from ELFIN observations (Angelopoulos et al., 2020), test particle simulations (Tsai et al., 2022, 2023), and quasi-linear diffusion code (Ma et al., 2012, 2015). This chap-

ter is organized as follows: Section 6.2 details ELFIN observations/statistics and presents observational evidence of intense nightside precipitation of relativistic electrons; Section 6.3 describes the basics of the test particle simulation and quasi-linear diffusion codes; Section 6.4 compares ELFIN data to results from a variety of runs exploring the three main modifications – reduced plasma density, wave obliquity, wave frequency variation along magnetic field lines; finally, Section 6.5 summarizes and discusses the obtained results.

6.2 Data Sets

Fig. 6.1 exemplifies two nightside ELFIN science zones, with $j_{trap}(E)$ (a,d) and j_{prec}/j_{trap} (b,e) distributions, demonstrating representative examples of various types of precipitation that were either removed (field-line curvature scattering, EMIC-driven precipitation, hiss-driven precipitation, and microbursts) or included (intense whistler-mode wave driven precipitation) for analysis. Our data selection process detailed in Section 5.5 removes curvature scattering at the isotropic boundary (Büchner and Zelenyi, 1989; Imhof et al., 1977; Sergeev et al., 1983; Wilkins et al., 2023), isotropic precipitation from the plasma sheet ($j_{prec}/j_{trap} \sim 1$ of < 300 keV electrons poleward from the isotropy boundary (Artemyev et al., 2022a)), EMIC-driven precipitation (seen at 10:08:05 in Fig. 6.1e and, more ambiguously at 1:56:50 in Fig. 6.1b) (Angelopoulos et al., 2023; Blum et al., 2015a,b; Capannolo et al., 2019; Yahnin et al., 2016, 2017), hiss-driven precipitation (see discussion of ELFIN observations of such precipitation in Angelopoulos et al., 2023; Mourenas et al., 2021; Shen et al., 2023a), and microburst-like precipitation (often characterized by precipitating-to-trapped flux ratio exceeding one for relativistic electron energies, as shown in, e.g., Zhang et al., 2022b). This results in only one type of precipitating energy distribution: a precipitating-to-trapped ratio monotonically decreasing with energy, observed primarily within L-shells $\in [4, 8]$, corresponding to the outer radiation belt outside the plasmasphere (e.g., Mourenas et al., 2021). This type of precipitation can only be caused by whistler-mode waves (see more details and examples in Tsai et al., 2022; Zhang et al., 2022b, 2023), and is shown to reach relativistic energies in Fig. 6.1(b,e).

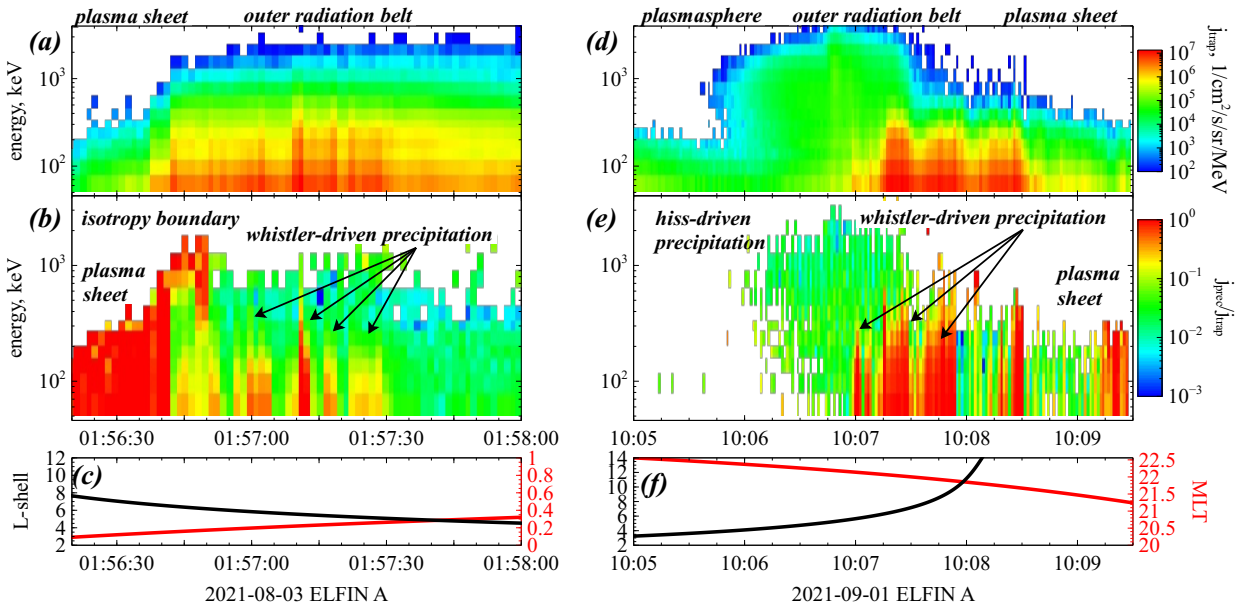


Figure 6.1: Two examples of ELFIN observations with strong precipitation of energetic electrons in the nightside MLT sector showing locally trapped electron fluxes (a,d), precipitating-to-trapped flux ratio (b,e), and ELFIN's MLT, L-shell coordinates from (Tsyganenko, 1989) model (c,f).

In particular, we combine these observations from only the nightside MLT sector (27950 spins across 4458 radiation belt crossings) and plot the averaged precipitating-to-trapped flux spectra for three geomagnetic activity levels and two L-shell domains ($4.5-5.5$ and $5.5-7.5$) for $AE \in [100, 300]$ nT in Fig. 6.2d. Fig. 6.2(a-c) show that the precipitating-to-trapped electron flux ratio j_{prec}/j_{trap} above 100 keV increases significantly as AE increases. The precipitating-to-trapped flux ratio reaches $j_{prec}/j_{trap} \sim 0.1$ up to $200-400$ keV when $AE > 300$ nT. This result is consistent with previous observations of stronger energetic electron injections from the plasma sheet during periods of higher AE (Gabrielse et al., 2014; Runov et al., 2015; Tao et al., 2011), leading to even more intense whistler-mode waves (Meredith et al., 2001; Zhang et al., 2018b) which can efficiently precipitate $50-500$ keV electrons (Agapitov et al., 2018; Aryan et al., 2020; Summers et al., 2004; Thorne et al., 2005). The ratio j_{prec}/j_{trap} is also higher at $L = 5.5-7.5$ than at $L = 4.5-5.5$ in Fig. 6.2, in agreement with the higher chorus wave power at higher $L > 5.0-5.5$ in the night sector in spacecraft statistics (Agapitov et al., 2018; Meredith et al., 2020). The smooth decrease of

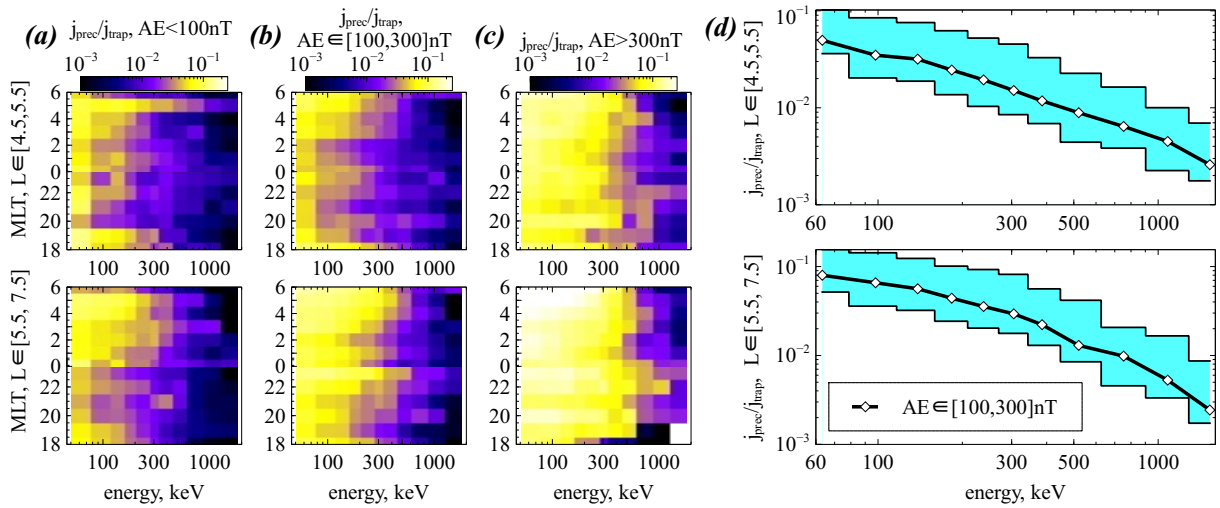


Figure 6.2: Plots (a-c) show the statistical distributions of precipitating-to-trapped electron spectra in (MLT, energy) space for several levels of geomagnetic activity. Plots (d) show energy profiles of precipitating-to-trapped fluxes for three geomagnetic activity levels in the nightside MLT $\in [18, 4]$. The shaded blue range regions represent the upper ($AE > 300$ nT) and lower ($AE < 100$ nT) bounds of geomagnetic activity levels while the central black curve depicts AE $\in [100, 300]$ nT.

j_{prec}/j_{trap} as electron energy increases in Fig. 6.2d is consistent with the expectation that at higher latitudes, wave power decreases while minimum cyclotron resonance energy increases, therefore precipitating higher energy electrons at lower absolute flux levels (Agapitov et al., 2018; Meredith et al., 2020).

6.3 Simulation

Calculating precipitating-to-trapped flux ratios, as described in Section 5.3, is useful because it eliminates the trapped flux variability (which can vary by orders of magnitude). The slope of the ratio's energy spectra now represents only the relative effects of resonant interactions with whistler-mode waves. To then compare with ELFIN statistics, we obtain modeled precipitating-to-trapped flux ratios using two different types of simulations: (1) a test particle simulation for electron resonant interactions, as used in previous chapters, and (2) a quasi-linear diffusion code which has been used in previous radiation belt simulations (Ma et al., 2012, 2015). These two theoretical frameworks differ in that test particle simu-

lations include potential nonlinear resonant effects and consider only purely monochromatic waves, whereas the quasi-linear diffusion code models electron scattering by an ensemble of oblique waves with higher order resonant interactions across a distribution of frequencies. Thus, by comparing the results obtained by these two approaches, we can fully capture the importance of different resonant effects for electron scattering and losses. The only difference in the test particle simulations for this chapter is detailed in Section 3.4.3, where we have now augmented the equations of motion to add latitudinal dependence of wave frequency and obliquity so that wave frequency $\omega(\lambda, \theta)$ is a function of both latitude and wave normal angle.

6.3.1 Quasi-linear Diffusion Code

To instill further confidence in the test particle simulation results, we calculate the quasi-linear diffusion coefficients using the Full Diffusion Code (Ma et al., 2018; Ni et al., 2008, 2011; Shprits and Ni, 2009) and model the precipitating electron flux using the Fokker-Planck diffusion code (Ma et al., 2012, 2015). This quasi-linear diffusion code physically differs from the test particle simulations primarily in the fact that it prescribes Gaussian distributions for the wave frequency (Glauert and Horne, 2005):

$$\hat{B}^2(\omega) \sim \exp\left[-\frac{(\omega - \omega_m(\lambda))^2}{\delta\omega^2}\right]$$

and the wave normal angle:

$$g(\theta) \sim \exp\left[-\frac{(\tan\theta - \tan\theta_m(\lambda))^2}{(\tan\delta\theta)^2}\right]$$

where mean values ω_m and θ_m with bandwidths $\delta\omega$ and $\delta\theta$ represent wave frequency and normal angle, respectively. These distributions are provided relative to mean values, $\omega_m(\lambda)$ and $\theta_m(\lambda)$, which are given as functions of magnetic latitude λ and discussed in the next section (see details in Agapitov et al., 2018; Artemyev et al., 2013; Aryan et al., 2020).

We use the bounce-averaged Fokker-Planck equation to model the electron precipitation rate (Glauert and Horne, 2005; Lyons et al., 1972):

$$\frac{\partial f}{\partial t} = \frac{1}{\tau_b\left(\alpha_{eq}\right)\sin 2\alpha_{eq}}\frac{\partial}{\partial \alpha_{eq}}\left(\tau_b\left(\alpha_{eq}\right)\sin 2\alpha_{eq}\left(\left\langle D_{\alpha\alpha}\right\rangle \frac{\partial f}{\partial \alpha_{eq}}\right)\right) - \frac{f}{\tau_{loss}} \tag{6.1}$$

where α_{eq} is the equatorial pitch angle, $\tau_b \approx 1.38 - 0.32\left(\sin\alpha_{eq} + \sin^2\alpha_{eq}\right)$ (see Orlova and Shprits, 2011), $\left\langle D_{\alpha\alpha}\right\rangle$ is the bounce-averaged diffusion rate, and $\tau_{loss}(t)$ is the bounce loss time (and is set to be a quarter of the bounce period inside the local loss cone and infinity outside the loss cone). We use the quasi-linear diffusion code to numerically solve Eq. 6.1, with diffusion rates derived from distributions $\hat{B}^2\left(\omega\right)$ and $g\left(\theta\right)$ (see Ma et al., 2015, 2018; Ni et al., 2008, 2011). Zero-gradient boundary conditions in the pitch angle are set to simulate the loss cone filling of electrons due to wave scattering (Ma et al., 2022).

6.3.2 Wave Frequency and Obliquity Models

In both simulations, we use the following two models to compare the effects of the frequency of the whistler-mode wave (normalized to the equatorial gyrofreqency) $\omega_m = \omega/\Omega_{ce,eq}$:

Model 1: normalized wave frequency held constant at $\omega_m = 0.35$, the typical frequency of whistler mode chorus waves near the equator (Agapitov et al., 2018).

Model 2: function $\omega(\lambda)$ linearly decreasing from $0.41\Omega_{ce,eq}$ at the equator until reaching a constant $0.16\Omega_{ce,eq}$ for $\lambda \geq 20°$. This model is based on statistics of off-equatorial parallel and oblique lower-band chorus waves from the Van Allen Probes (Agapitov et al., 2018).

We use the following four models to describe the mean wave normal angle (WNA) θ_m. A scaling factor $\Theta(\lambda) = \lambda/(15° + \lambda)$ is adopted which increases the WNA modifier from 0 at the equator to $\Theta(45°) = 0.75$ at 45° latitude in WNA1 and WNA2.

FAW: a field-aligned wave model (with $\theta = 0°$ in test particle simulations and $\theta_m = 0°$, $\delta\theta = 30°$ or $\delta\theta = 5°$ in the quasi-linear diffusion code) that describes the most intense

population of waves (Agapitov et al., 2013; Li et al., 2016b) as they remain field-aligned off equator due to wave ducting by small-scale density structures (Hanzelka and Santolík, 2019; Hosseini et al., 2021; Ke et al., 2021; Shen et al., 2021).

WNA1: a moderately oblique WNA model with $\theta_1(\lambda) = \theta_G(\lambda) \cdot \Theta(\lambda)$, where $\theta_G = \arccos(2\omega/\Omega_{ce})$ is the Gendrin angle (Gendrin, 1961). This model describes field-aligned waves that are generated at the equator, but become mildly oblique as they propagate through the inhomogeneous plasma (e.g. Breuillard et al., 2012; Chen et al., 2013; Ke et al., 2017).

WNA2: a very oblique WNA model with $\theta_2(\lambda) = \theta_r(\lambda) \cdot \Theta(\lambda)$, where $\theta_r = \arccos(\omega/\Omega_{ce})$ is the resonance cone angle. This describes field-aligned waves that are generated at the equator, but become very oblique as they propagate through the inhomogeneous plasma in the case of suppressed Landau damping (see discussion in Artemyev and Mourenas, 2020).

WNA3: an extremely oblique WNA model with $\theta_3(\lambda) = \theta_r(\lambda) - 2°$. This model describes very oblique waves that are generated in the equatorial source region in the presence of field-aligned electron streams suppressing Landau damping (Chen et al., 2019b; Kong et al., 2021; Li et al., 2016a; Mourenas et al., 2015).

The quasi-linear simulations also require a bandwidth parameter which sets the width of the wave frequency and normal angle Gaussian distributions, defined in Section 6.3.1. Frequency bandwidth $\delta\omega$ is set to 0.125, and the lower and upper cutoff frequencies are set to be $\omega_m - 2\delta\omega$ and 0.5, respectively. Wave normal angle bandwidth is set to either $\delta\theta = 5°$ or $\delta\theta = 30°$ for FAW, and $\delta\theta = 10°$ for the other models; if $\theta_r(\lambda) - \theta_m(\lambda) < 20°$, we set $\delta\theta = (\theta_r(\lambda) - \theta_m(\lambda))/2$. The lower ($\theta_{LC}$) and upper ($\theta_{UC}$) cutoff wave normal angles are set as $\tan\theta_{LC} = \max(0, \tan\theta_m - 2\tan\delta\theta)$ and $\tan\theta_{UC} = \min(\tan 89.9°, \tan\theta_m + 2\tan\delta\theta)$, respectively.

Finally, the magnetic wave power distribution $B_w^2(\lambda)$ is taken from an empirical statistical model (Agapitov et al., 2018) at 23 MLT and $L = 6$ for $Kp = 3$, just like we did for test

particle simulations in Chapter 5 (recall that we use $Kp = 3$ as a reasonable estimate of average geomagnetic activity level for ELFIN observations of electron precipitation driven by resonance with whistler-mode waves, see Section 3.4.2).

6.4 Data-model Comparison

In this section, the precipitating-to-trapped electron flux ratios j_{prec}/j_{trap}, calculated through test particle simulations (TPS) or Quasi-Linear Diffusion Code (QLDC), are compared with j_{prec}/j_{trap} as measured by ELFIN. This allows us to assess the different roles that plasma density, wave obliquity, and wave frequency potentially play based on j_{prec}/j_{trap} flux ratio variation with energy.

For proper comparison, the simulated j_{prec}/j_{trap} flux ratio is normalized to the observed j_{prec}/j_{trap} flux ratio, thus removing wave amplitude variability such that the spectral slope can be compared across various scenarios. This time, however, we normalize at ELFIN's second energy bin ($\sim$ 97 keV) rather than $\sim$ 80 keV, as we did in the previous chapter (Section 5.4). This is to avoid spurious variations in j_{prec}/j_{trap} modeled using our test particle simulations, which tend to become larger below 97 keV despite the large number of particle runs per energy bin. These oscillations are absent from results of the quasi-linear diffusion code, which correlate well with test particle simulation results above 97 keV only after normalization.

6.4.1 Role of Plasma Density

Fig. 6.3 shows a comparison between the precipitating-to-trapped electron flux ratio j_{prec}/j_{trap} measured by ELFIN at $L > 5$ and 18-4 MLT (black) with j_{prec}/j_{trap} obtained from TPS (solid red) and QLDC (dashed red) with parallel (FAW model) lower-band chorus waves (adopting $\theta = 0°$ in test particle simulations, $\delta\theta = 30°$ in the quasi-linear diffusion code), using wave frequency Model 1 of constant frequency ($\omega_m = 0.35$) chorus waves and a typical plasma frequency to gyrofrequency ratio $\Omega_{pe} = 6.5$ at $L = 6.5$ and 23 MLT (Sheeley et al., 2001).

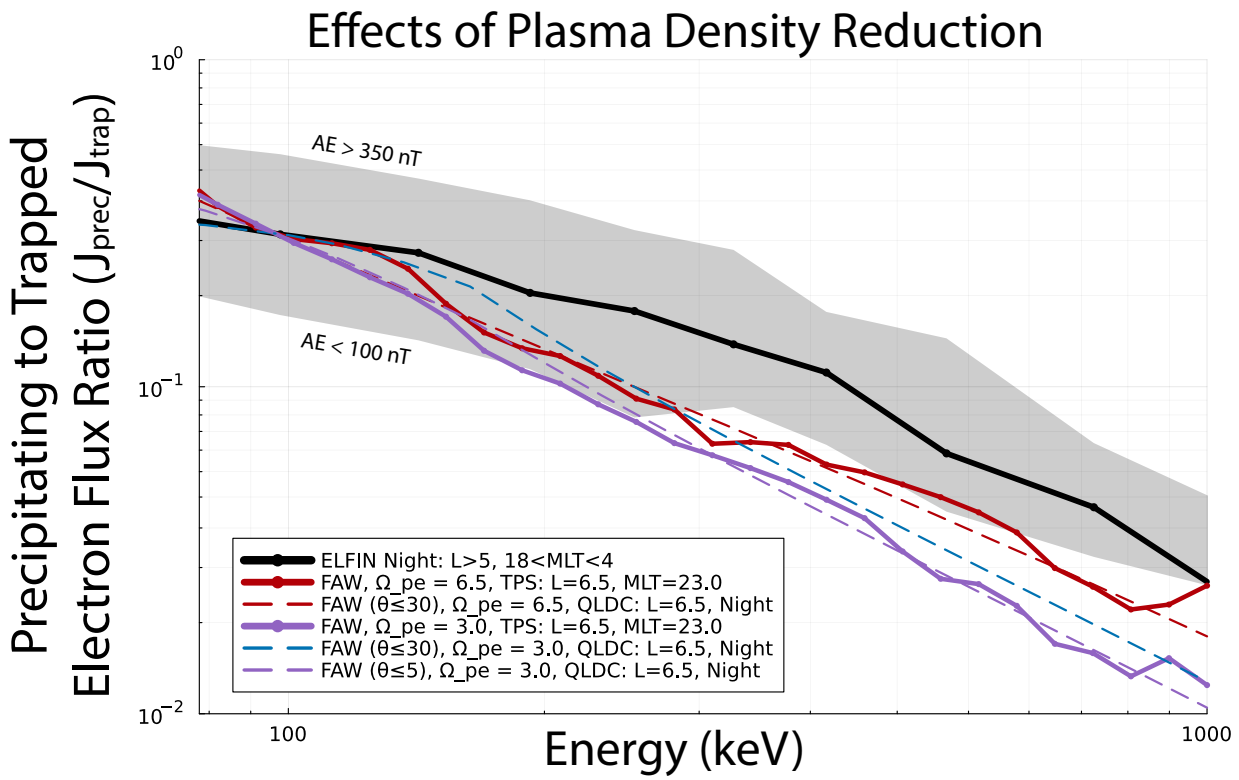


Figure 6.3: ELFIN-measured precipitating-to-trapped electron flux ratio at $L > 5$ on the nightside ($18 - 4$ MLT) as a function of energy (black curve). The corresponding j_{prec}/j_{trap} flux ratio obtained from test particle simulations is shown for parallel (FAW model, $\theta = 0°$) lower-band chorus waves, using frequency Model 1 ($\omega_m = constant$) and a typical $\Omega_{pe} = 6.5$ at $L = 6.5$ and 23 MLT (solid red). Results from the quasi-linear diffusion code using the same parameters is shown in dashed red. Similarly, the cases of reduced density $\Omega_{pe} = 3$ modeled with test particle simulation (solid purple), quasi-linear diffusion code using narrow-band field aligned waves ($\delta\theta = 5°$, dashed purple), and more quasi-linear field aligned waves ($\delta\theta = 30°$, dashed blue), are shown. All simulation results are normalized to observations at 97 keV.

In this plot (and remaining Figures 6.3-6.7), the gray shaded regions of ELFIN data denote the boundaries of quiet (AE $<$ 100 nT) and active (AE $>$ 350 nT) times. The normalized ratios j_{prec}/j_{trap} obtained from TPS and QLDC are quite similar (compare solid with dashed lines of the same color), validating the reliability of the quasi-linear approach (Albert, 2005; Glauert and Horne, 2005; Kennel and Engelmann, 1966; Lyons et al., 1972; Mourenas et al., 2012b, 2014a), especially in the case of field aligned waves, as demonstrated in previous studies (An et al., 2022c; Gan et al., 2022b; Mourenas et al., 2022a; Tao et al., 2012a). However, despite their normalization to the measured j_{prec}/j_{trap} at 97 keV, these similar ratios

of j_{prec}/j_{trap} (red curves) obtained from test particle simulations and from the quasi-linear diffusion code become $\sim 1.5-2$ times smaller than the measured j_{prec}/j_{trap} at $200-1000$ keV (black), corresponding to a deficiency of pitch-angle diffusion occurring at higher energies. For reference, this baseline case (red) represents the same discrepancy on the nightside as first described in Tsai et al. (2023).

A reduced plasma density should lower the latitude of first-order cyclotron resonance with chorus waves for electrons near the loss cone (Mourenas et al., 2012b). Since chorus wave power B_w^2 is higher at lower latitudes (Agapitov et al., 2018), a reduced density is therefore expected to yield higher electron pitch-angle diffusion rate $D_{\alpha\alpha} \propto B_w^2$ near the loss cone leading to higher precipitation rates and fluxes at all energies. However, adopting a reduced plasma density ($\Omega_{pe} = 3$) in test particle simulations (purple line in Fig. 6.3) and normalizing the flux ratio at 97 keV leads to an even larger discrepancy across the $300-1000$ keV range with a $\sim 2-3$ times smaller j_{prec}/j_{trap} ratio than ELFIN statistics show. We therefore interpret this density effect as more important at lower energies (~ 100 keV) compared to higher energies (> 300 keV) due to $B_w^2(\lambda)$ increasing, in our model and in observations, more steeply towards lower latitudes at $\lambda \lesssim 25°$ (where resonance with ~ 100 keV electrons occurs) than at $\lambda > 25°$ (where resonance with ~ 1 MeV electrons occurs) during disturbed periods at 21-3 MLT (Agapitov et al., 2018). Therefore, the wave power $B_w^2(\lambda)$ seen by electrons near the loss cone increases only marginally at higher energies for both $\theta = 0°$ in test-particle simulations and $\theta < 5°$ or $\theta < 30°$ in QLDC simulations (solid/dashed purple and dashed blue lines). This then reduces the normalized pitch-angle diffusion rate $D_{\alpha\alpha}$ near the loss cone and the normalized j_{prec}/j_{trap} flux ratio, which varies roughly like $\approx \sqrt{D_{\alpha\alpha}}$ (Kennel and Petschek, 1966; Li et al., 2013; Mourenas et al., 2022b, 2023).

Adopting a more realistic spread of WNAs for quasi-field aligned waves ($\delta\theta = 30°$, blue dashed line) in the quasi-linear diffusion code leads to the effects of additional, higher-order cyclotron resonances to become more significant (Artemyev et al., 2016), which is clearly shown as the difference between the blue and purple dashed lines in Fig. 6.3. Due to moderate obliqueness, this effect is most prominent in the lower energies – resonating with

waves around the equator – extending now to about 180 keV. However, it is not enough to reproduce ELFIN observations up to 1 MeV, because the relative scattering efficiency decreases with the purple curve at higher energies, causing the blue curve to underestimate ELFIN statistics beyond $>$ 250 keV. Despite the fact that, in observations, the plasma frequency to gyrofrequency ratio Ω_{pe} does decrease at 18-4 MLT during disturbed periods (O'Brien and Moldwin, 2003), often down to $\Omega_{pe} \approx 3-4$ at $L \sim 6$ when $AE > 150$ nT (Agapitov et al., 2019), results in Fig. 6.3 show that plasma density reduction alone cannot account for a relative increase of electron scattering at higher energies.

6.4.2 Role of Wave Frequency

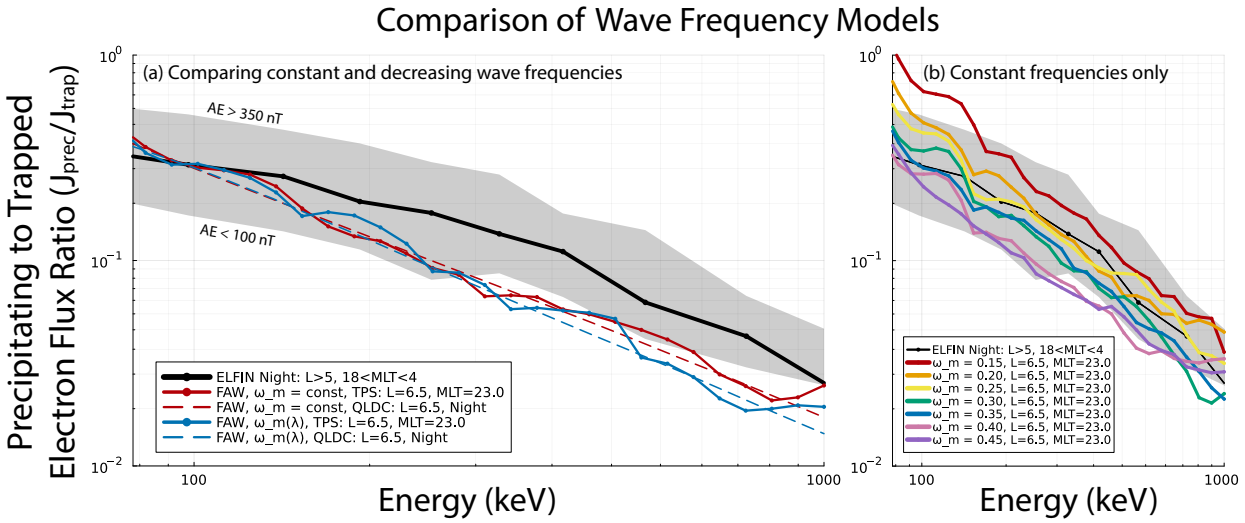


Figure 6.4: To compare the effects of two frequency models, precipitating-to-trapped electron flux ratio j_{prec}/j_{trap} plotted for ELFIN statistics on the nightside (black) is shown in comparison with j_{prec}/j_{trap} ratios obtained from test particle simulations (TPS, solid lines) and quasi-linear diffusion code (QLDC, dashed lines). In (a), Frequency Model 2 (frequency decreasing toward higher latitudes, blue) produces slightly higher precipitation rates at 100 keV relative to 1 MeV as compared to a constant $\omega_m = 0.35$ (red). Plot (b) shows results from a variety of normalized wave frequency values that do not vary as a function of magnetic latitude, demonstrating that absolute frequency has little effect on the slope of the precipitation energy spectra.

As noted earlier, statistical observations of lower-band chorus waves show that their normalized frequency is not constant as a function of latitude (as assumed in frequency Model

1), but rather, decreases due to preferential Landau damping affecting higher frequencies at higher latitudes (Agapitov et al., 2018; Bunch et al., 2013; Chen et al., 2013), as reflected by frequency Model 2. Fig. 6.4a shows that the j_{prec}/j_{trap} ratios obtained for wave normal angle model FAW from test particle simulations (solid curves) and from the quasi-linear diffusion code (dashed curves) are both slightly decreased at $E = 200 - 1000$ keV when using wave frequency Model 2 (blue curves), rather than when using Model 1. This is because a reduction of wave frequency alone, when adopting a fixed plasma density $\Omega_{pe} = 6.5$ at $L = 6.5$, has essentially the same effect as decreasing plasma density in Section 6.4.1 – albeit weaker in magnitude – by allowing first-order cyclotron resonance for electrons near the loss cone to occur at lower latitudes (Mourenas et al., 2012b). In turn, this preferentially increases precipitation rates at low energies $E \lesssim 100$ keV, the typical resonance energies at low-latitude plasma conditions.

Fig. 6.4b shows that decreasing the wave frequency by a fixed amount significantly increases electron precipitation rates by lowering the latitude of resonance with chorus waves. But at the same time, it leads to only a slight increase of the slope of the energy spectrum once normalized to ELFIN statistics, because the amplitude of resonant waves is slightly more increased for 100 keV electrons than for 1 MeV electrons. For a large plasma density, $\Omega_{pe} = 6.5$, this effect on the normalized j_{prec}/j_{trap} remains weak, and both wave frequency Models 1 and 2 end up giving very similar results. Therefore, the effects of frequency variation with latitude alone cannot account for the spectral shape of the precipitation ratio in ELFIN's nightside observations.

6.4.3 Role of Wave Obliquity

Fig. 6.5a compares ELFIN-observed precipitating-to-trapped flux ratio on the nightside (black) with that of simulations in order to explore the effects of a variety of wave-normal angle distributions paired with constant wave frequency (Model 1) and baseline plasma density (Sheeley et al., 2001). Results from test particle simulations (solid curves) and from the quasi-linear diffusion code (dashed curves) are displayed for four different models

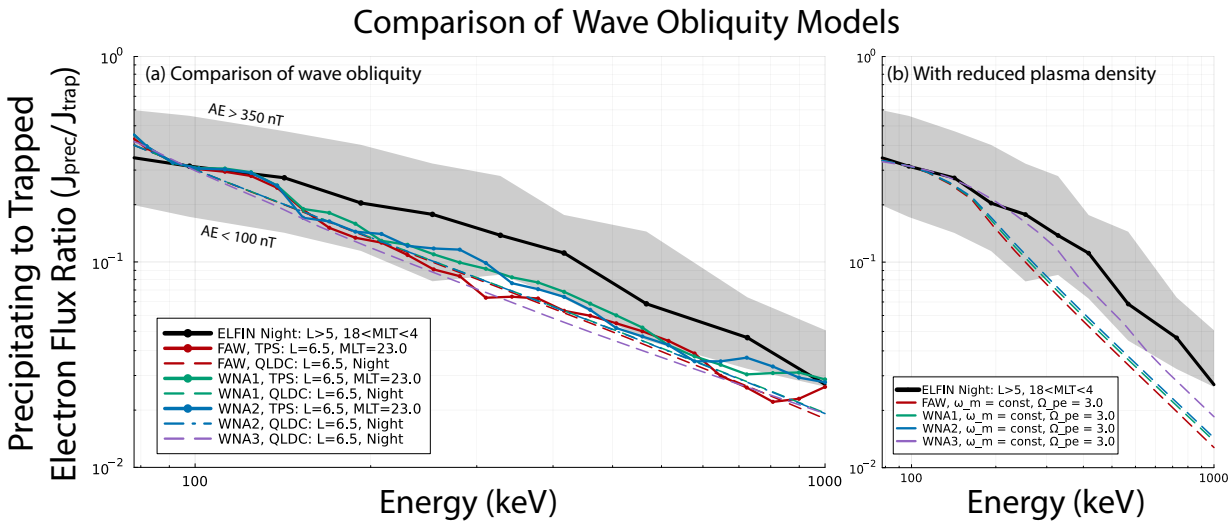


Figure 6.5: ELFIN-observed j_{prec}/j_{trap} flux ratio at $L > 5$ on the nightside ($18-4$ MLT) as a function of electron energy (black). The corresponding ratios j_{prec}/j_{trap} obtained from test particle simulations (TPS, solid curves) and from the quasi-linear diffusion code (QLDC, dashed curves) are displayed for lower-band chorus waves in (a), using frequency Model 1 of constant frequency, and parameterized by four wave normal angle models: FAW (red), WNA1 (green), WNA2 (blue), and WNA3 (purple), with a normalization to observations at 97 keV, adopting a typical $\Omega_{pe} = 6.5$ at $L = 6.5$ and 23 MLT. (b) shows QLDC results for the same four wave normal angle models but for a reduced plasma density of $\Omega_{pe} = 3.0$.

of wave normal angle: FAW (red), WNA1 (green), WNA2 (blue), and WNA3 (purple), corresponding to a progressively larger amount of wave power in oblique waves closer to the resonance cone angle (see Section 6.3.2). Despite the large number of particles ($N = 5\times10^6$), unnatural oscillations in the test particle simulations make it difficult to quantify the exact contribution differences between the FAW, WNA1, and WNA2 models. Especially because the test particle simulation only includes first-order oblique wave interactions, it is reasonable to conclude that including wave obliquity in the TPS does not significantly alter precipitation efficiency. However, results from the quasi-linear diffusion code generally agree with test particle simulation results, indicating the reliability of the quasi-linear approach (described, e.g., by Albert, 2005; Glauert and Horne, 2005; Kennel and Engelmann, 1966; Lyons et al., 1972; Mourenas et al., 2012b, 2014a). Our quasi-linear simulations show that wave obliquity is ineffective at increasing high-energy electron precipitation compared to low-energy electron precipitation (in the case of $\Omega_{pe} = 6.5$). Note that the WNA1 and WNA2 models correspond

to wave-normal angle distributions that extend up to three-quarters of the Gendrin angle and resonance cone angle, respectively, at $\lambda > 45°$, while the WNA3 model corresponds to highly oblique waves, at about 2° from the resonance cone angle. Yet, the results are nearly identical (dashed blue, dashed green, and dashed purple curves).

Oblique chorus waves can resonate with electrons via high-order cyclotron resonances ($n \geq 1$ or $n \leq -2$, e.g., Albert, 2017; Artemyev et al., 2013, 2016; Mourenas et al., 2012b; Shklyar and Matsumoto, 2009), which can significantly increase diffusion rates at high energy (Gan et al., 2023; Lorentzen et al., 2001). However, diffusion rates near the loss cone due to higher-order cyclotron resonances decrease rapidly in magnitude as $|n|$ increases, especially from $|n| = 1$ to $|n| = 2$ (Shprits and Ni, 2009), although this reduction is weaker for highly oblique waves (Artemyev et al., 2016). To increase the ratio of 1 MeV to 100 keV pitch-angle diffusion rates near the loss cone, therefore, the waves must be sufficiently oblique and/or plasma density and wave frequency should be sufficiently low to enable only first-order resonance at $\sim$ 100 keV, but higher-order resonances at 1 MeV (Artemyev et al., 2016; Gan et al., 2023; Mourenas and Ripoll, 2012; Shprits and Ni, 2009). Fig. 6.5b indeed shows that when plasma density is reduced to $\Omega_{pe} = 3$ (or equivalently, when wave frequency decreases with latitude, see Section 6.4.4), electron precipitation increases greatly at 1 MeV relative to 100 keV as wave obliquity increases, especially in the case of highly oblique waves (WNA3). These results therefore suggest that wave obliquity, alone, has a nearly negligible effect on the high-energy to low-energy electron loss ratio; however, when combined with a density reduction, it can significantly enhance energetic electron losses.

6.4.4 Combined Results

Fig. 6.6a shows comparisons between the precipitating-to-trapped electron flux ratio j_{prec}/j_{trap} measured by ELFIN at $L > 5$ on the nightside (black), overlaid with j_{prec}/j_{trap} obtained from the quasi-linear diffusion code for the three modifications in question – reduced plasma density $\Omega_{pe} = 3$, Frequency Model 2, and WNA3 – alone or in combination. As surmised in previous sections, each individual modification fails to agree with the observed spectrum.

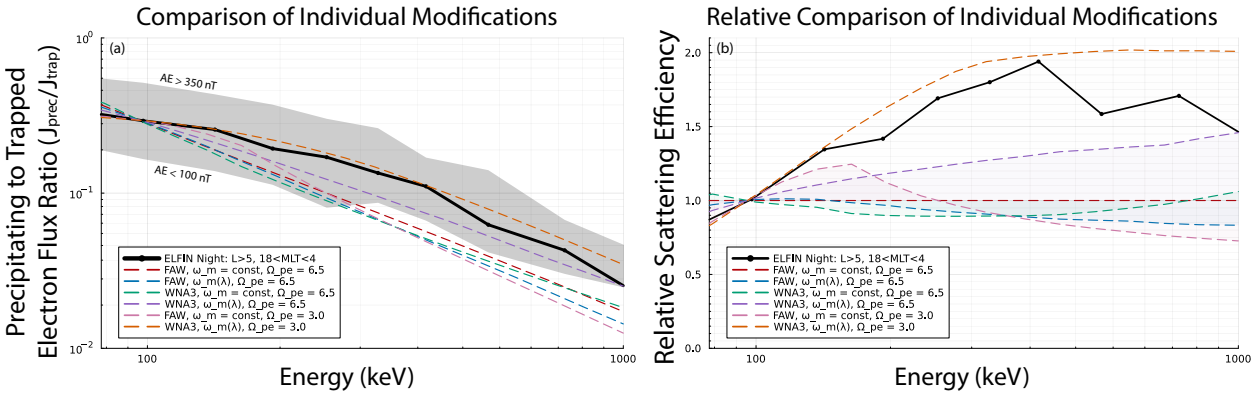


Figure 6.6: ELFIN-observed nightside ($18-4$ MLT) j_{prec}/j_{trap} electron flux ratio shown as a function of energy (black). (a) shows j_{prec}/j_{trap} flux ratios obtained from quasi-linear diffusion code (QLDC) for parallel (FAW) lower-band chorus waves (red), very oblique waves using wave normal angle model WNA3 (green), waves with a realistic wave frequency distribution (blue), WNA3 with a realistic wave frequency distribution (purple), FAW with reduced density (pink), and everything combined (orange). (b) shows the same flux ratios all normalized to the base case with no modifications (red) demonstrating which energy range each modification is most effective at on a linear scale. This shows that each effect examined alone cannot reproduce results from ELFIN individually.

With wave frequency Model 2 (blue) and WNA3 (green) underestimating across entire energy range (i.e., increasing precipitation at 100 keV) and reduced density (pink) providing a relative efficiency bump of j_{prec}/j_{trap} only at $E < 200$ keV. Interestingly, however, ELFIN's statistical observations are only slightly underestimated when combining WNA3 and Frequency Model 2 (purple), and best matched when all three modifications are combined (orange). Fig. 6.6b shows the relative difference produced by each modification compared to the baseline red curve. We see that these effects synergistically enhance j_{prec}/j_{trap} flux ratios at higher energies. For example, Model 2 (blue) becomes relatively less effective at higher energy, while WNA3 (green) immediately loses effectiveness, but catches back up closer to 1 MeV. However, when combined (purple), the relative precipitation is drastically enhanced throughout the $200-1000$ keV range, which leads to a much better agreement with observations. Further combining WNA3 and Frequency Model 2 with a reduced plasma density (orange) significantly enhances precipitation past levels observed by ELFIN (black). This is likely due to two phenomena: first, the combined effects of a reduced plasma density and a decreasing wave frequency decrease the latitude at which cyclotron resonance with

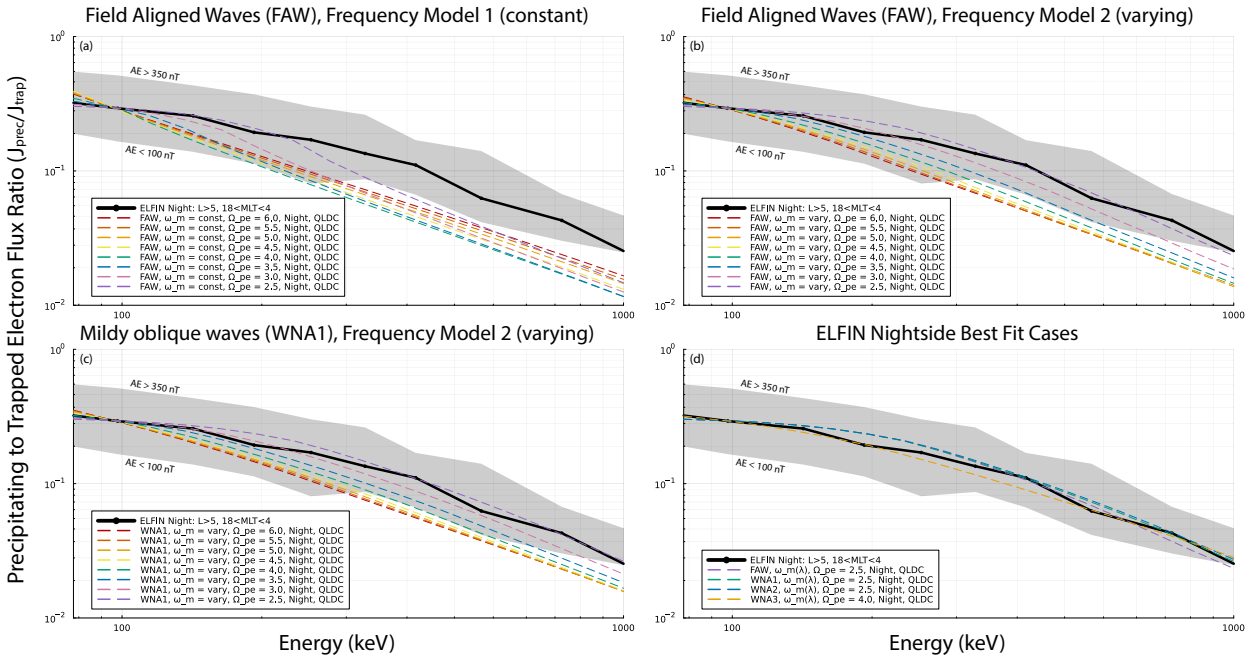


Figure 6.7: The comparison between observed electron precipitation ratios and simulation results using different wave frequency models, Ω_{pe} ratios, and wave normal angle models. In each plot, the black line denotes statistical averages of j_{prec}/j_{trap} flux ratios for nightside ELFIN observations with $L > 5$. Plots (a-c) show QLDC results with various modifications parameterized by Ω_{pe}: (a) shows field aligned waves with Frequency Model 1; (b) shows field aligned waves with Frequency Model 2; and (c) shows WNA1 combined with Frequency Model 2. (d) shows that all three effects – $\omega_{pe} \in [2.5, 4]$, combined with Frequency Model 2 and some level of wave obliquity – are necessary for recreating ELFIN nightside statistics.

quasi-parallel waves occurs far more significantly than each effect alone (Mourenas et al., 2012b), leading to a larger increase of resonant wave power for higher energy electrons that best match ELFIN's observed precipitation spectra; second, the supplementary higher-order cyclotron resonances contributing at $\sim$ 1 MeV, but not at $\sim$ 150 keV, are of lower order ($|n| = 2$) than for higher density or frequency, allowing for a more dramatic increase of the 1 MeV to 150 keV pitch-angle diffusion rate ratio (Artemyev et al., 2016; Gan et al., 2023; Mourenas and Ripoll, 2012; Shprits and Ni, 2009).

Fig. 6.7 summarizes the findings from each wave parameter combination throughout a range of reduced equatorial plasma densities to better understand the interplay between the three effects considered. Fig. 6.7a shows that only below a certain threshold of $\Omega_{pe} \lesssim 4$ does the interaction of higher-order resonances begin to increase precipitation at higher energies.

Using the total electron density with $\Omega_{pe} = 2.5$, this effect becomes very pronounced above 100 keV and up to 300 keV, whereas above that energy this effect alone is still incapable of matching observations, as discussed in Section 6.4.1. The effect of plasma density combined with wave frequency becomes significantly more pronounced throughout the whole energy range when $\Omega_{pe} \lesssim 4$, as shown in Fig. 6.7b, and matches very well with ELFIN's nightside observations when a more extreme $\Omega_{pe} = 2.5$ is used. Adding mild wave obliquity (Fig. 6.7c) results in the best match with ELFIN statistics, demonstrating that all three effects combined are necessary.

Fig. 6.7d shows the best fit scenarios for forward-modeling of ELFIN-observed precipitating-to-trapped flux ratios, which all require the varying frequency model in addition to reduced plasma density to various degrees. Here, we show that it is possible to obtain decent agreement without the need for wave obliquity by significantly reducing Ω_{pe} to 2.5 (purple). By adding moderately oblique waves (green and blue), more $\sim$ 1 MeV electrons are precipitated, which marginally improves matching with observations. Using extremely oblique waves (WNA3) – which describes a population of very oblique waves generated around the equator when the Landau damping is largely reduced by field-aligned electron streams (Li et al., 2016a; Mourenas et al., 2015) – requires increasing plasma density $\Omega_{pe} = 4$ in order to avoid significant overestimation. Therefore, ELFIN observations of nightside electron precipitation spectra (from $50 - 1000$ keV) can be described either under the assumption of a significant plasma density reduction or a more moderate plasma density reduction coupled with a strongly oblique wave population. This required plasma density ($\omega_{pe} \in [2.5, 4]$) is fully consistent with the average measured ω_{pe} levels at 18-4 MLT and $L = 5 - 6.5$ in Van Allen Probes statistics during disturbed periods with $AE \in [150, 600]$ nT (Agapitov et al., 2019). These conditions indicate the importance of plasma injections and/or enhanced convection periods and how they cause enhanced nightside electron losses. Such Earthward plasma transport (convection and injections), especially during increased geomagnetic activity, justifies our choice of the reduction of the cold plasma density (Agapitov et al., 2019). These injections are also associated with electron field-aligned streams caused by electrostatic tur-

bulence around injection regions or by secondary electron ionosphere outflow in response to enhanced precipitation of plasma sheet electron fluxes (see Artemyev and Mourenas, 2020; Artemyev et al., 2020; Khazanov et al., 2014, 2018, and references therein).

6.5 Conclusion

Analysis presented in this chapter shows that the inclusion of realistic whistler-mode wave properties can significantly increase relativistic electron scattering rates, thereby explaining the nightside underestimation of electron losses presented in Chapter 5. We found that, in addition to the prerequisite, empirically-provided $B_w(\lambda)$, inclusion of all three modifications – realistic Ω_{pe}, $\omega_m(\lambda)$, and $\theta(\lambda)$ – was sufficient to recover the more intense nightside energetic precipitation observed by ELFIN. This is significant because each individual effect made a trivial impact which was then reflected in our original hypothesis that these effects were therefore unlikely to resolve this discrepancy. Despite that, we were able to show that a reduced plasma density, indicative of geomagnetically active times, results in a relative enhancement of precipitation in the sub-relativistic regime (< 300 keV), while wave obliquity significantly increases relativistic electron scattering > 500 keV. Additionally, it appears that a decrease in wave frequency as a function of latitude helps balance the two out, leading to a smooth recovery of the $200 - 600$ keV range, without severely overestimating either end of the precipitation flux ratio spectrum. These results highlight the importance of combining whistler-mode wave characteristics and background plasma for accurately modeling relativistic electron losses from the outer radiation belt. To summarize, we note that:

- The latitudinal distribution of wave amplitude alone cannot account for the intense nightside precipitation of $\sim 0.1 - 1$ MeV electrons scattered at mid-to-high latitudes relative to precipitation of ~ 100 keV electrons scattered near the equator.
- Very oblique waves are important for scattering more energetic electrons, becoming more effective in the ~ 1 MeV range, but only in the presence of reduced plasma density or decreasing wave frequency.

- The wave frequency decrease with latitude, caused by high-frequency wave damping, is not very important on its own. However, together with a reduced plasma density (with or without oblique waves), it can lead to more precipitation of high-energy electrons relative to ~ 100 keV electrons.

- Equatorial plasma density decrease during geomagnetically active conditions (characterized by enhanced whistler-mode wave intensity) improves the relative efficiency of resonant electron scattering toward the loss cone at 100 keV compared to 1 MeV, but alone, it is in poor agreement with ELFIN statistics. However, when combined with increasing WNA and decreasing wave frequency as a function of latitude, this plasma density reduction becomes a catalyst, significantly boosting electron precipitation rates across the energy range up to 1 MeV.

Therefore, in order to best explain the increased precipitation observed by ELFIN on the nightside, modeled whistler-mode waves must have a realistic latitudinally-dependent wave frequency model (Model 2) coupled with a reduced plasma density ($\Omega_{pe} \in [2.5, 4]$) and an associated range of wave obliquity from quasi-field aligned ($\theta < 30^\circ$) to extremely oblique (WNA3) waves. While these computational tools are available for comprehensive modeling of electron precipitation, any further investigation of these effects likely requires either detailed simulations using modern ray-tracing techniques (e.g., Chen et al., 2021a, 2022; Hanzelka and Santolík, 2022; Hosseini et al., 2021; Kang and Bortnik, 2022; Kang et al., 2022) or a new generation of satellite missions equipped to make simultaneous measurements of whistler-mode waves and precipitating/trapped electron populations.

CHAPTER 7

Summary and Future Work

7.1 Research Summary

This dissertation focuses on the physics of energetic (> 100 keV) and relativistic (> 500 keV) electron precipitation. Although prior theoretical and observational works over the past six decades have described how whistler-mode waves can produce such energetic and relativistic electron losses in the radiation belt, they have yet to quantify or verify the proposed mechanisms with direct spacecraft observations. Due to the perceived near-equatorial confinement of nightside whistler-mode waves (Meredith et al., 2012), the waves were previously expected to resonate with sub-relativistic electrons. Hence, today's radiation belt simulations primarily rely on EMIC-driven electron precipitation to explain relativistic electron losses at the nightside (see, e.g., Drozdov et al., 2017; Ma et al., 2015, and references therein), in addition to dropouts related to magnetopause shadowing loss (e.g., see Boynton et al., 2016, 2017; Olifer et al., 2018; Shprits et al., 2006a; Turner et al., 2014; Xiang et al., 2018). Although dayside whistler-mode wave contribution to relativistic electron losses is discussed (Thorne et al., 2005), this mechanism was also believed to be less important in comparison with EMIC-driven precipitations and magnetopause shadowing. With the advent of thousands of radiation belt observations from the ELFIN mission, we have, for the first time, quantified outer radiation belt electron losses due to interactions with intense whistler-mode waves, and developed new computational tools to explain the important wave characteristics responsible for this mechanism.

We first anchored our study in Chapter 4 by explaining conjugate observations of intense, bursty electron precipitation by ELFIN with equatorially observed whistler-mode waves. In

the first case study, we fully established the equatorial wave parameters using THEMIS SCM waveforms (including wave amplitude, occurrence rate, and packet size). Combined with measured plasma and magnetic field properties, we used a test particle simulation to demonstrate that ELFIN would observe significantly more relativistic electron precipitating fluxes than expected unless we included a small fraction of waves (2% occurrence rate) that were allowed to propagate up to $\lambda \sim 40°$. Although we used a relatively simplified model for whistler-mode waves, we still included wave characteristics that generally produce realistic results (such as finite wave packets and realistic wave intensity decay as a function of latitude). A second case study, this time using MMS, did not record high-resolution equatorial waveforms during the magnetic conjunctions. However, we were able to demonstrate that we could instead use ELFIN to remotely sense equatorial wave characteristics using electron precipitation (at least for up to $\sim$ 300 keV in this particular example). This is an improvement over Li et al. (2013); Ni et al. (2014), where they previously showed a good correlation between 30-100 keV electrons and equatorial wave power.

Because ELFIN sees many instances of short-lived intense precipitation far more often than there are magnetic conjunctions with equatorial spacecraft, we proceeded to explore more case studies, this time incorporating a global empirical wave-power model into the test particle simulation for comparison. In the absence of absolute equatorial measurements of particle fluxes and plasma waves, we resort to comparing precipitating-to-trapped flux ratios and normalize modeling to observations, effectively normalizing away the fluctuations associated with wave amplitude variability, and allowing comparisons between the slopes of the energy spectra. Armed with a test particle simulation that can now directly compare whistler-mode waves and electron precipitating-to-flux ratio spectra, we show generally good agreement between ELFIN-measured electron precipitation and the latitudinal distribution of whistler-mode waves on the dayside with more uncertainty and variance on the nightside. In order to study this comprehensively, we had to incorporate all ELFIN-observed electron precipitation while specifically excluding all data exhibiting signatures of field-line curvature scattering, EMIC waves, and any signatures of noise or poor statistics. The re-

sulting ELFIN statistics are 3 years of unambiguous whistler-mode wave-driven energetic electron precipitating-to-trapped flux ratios across a range of MLT, L-shells, and geomagnetic activity. By simulating millions of test particles interacting with a statistically averaged wave model across these same geographic and geomagnetic activity bins, we expect to find good agreement. Chapter 5 showed that using only field-aligned, monochromatic whistler-mode waves with realistic wave amplitudes as a function of magnetic latitude was generally sufficient to approximate relativistic electron losses in the dawn, noon, and dusk sectors. However, the modeled precipitating-to-trapped flux ratio significantly underestimated the ELFIN-obtained statistics of precipitating energy spectra in the nightside MLT sector. We sought to explain this in Chapter 6.

At first, we used test particle simulations to examine various wave and plasma characteristics that may potentially cause this discrepancy. However, test particle simulations showed that, while some effects led to better agreement, the discrepancy was still large. However, by additionally utilizing a state-of-the-art quasi-linear diffusion code, we were able to quantify each key wave parameter – alone and in combination – relative to ELFIN observations, thereby determining the importance of including empirically-obtained equatorial plasma frequency, wave-normal angle distributions, and wave frequency distributions. Analysis presented here shows that the inclusion of realistic whistler-mode wave properties can meaningfully enhance relativistic electron scattering rates relative to 100 keV rates. This results in better agreement with observations and reduces the relative importance of EMIC waves scattering on the nightside, at least for electrons below 1 MeV. While whistler-mode waves have been known for a long time to accelerate electrons to relativistic energies (Allison and Shprits, 2020; Hsieh and Omura, 2017; Li et al., 2014b; Mourenas et al., 2014b; Omura et al., 2015; Thorne et al., 2013), the contribution of this wave mode to relativistic electron losses may be underestimated in modern-day simulations due to the lack of observations that can reliably quantify these losses. We present here both statistically averaged precipitating-to-trapped flux ratio, as well as the necessary wave physics to include on the nightside, which will lead to better inclusion of relativistic electron precipitation in models like the UCLA

Full Diffusion code.

7.2 Future Work

7.2.1 Determining Key Wave Characteristics on the Dayside

On the nightside, the equatorial confinement of whistler-mode waves is attributed to the increase of wave obliquity – or more precisely, the increase of statistical averages of wave normal angles – as expected from wave propagation away from their equatorial source (Agapitov et al., 2013; Breuillard et al., 2012; Chen et al., 2013) due to the severe damping by Landau resonance with suprathermal electrons (e.g., Bell et al., 2002; Bortnik et al., 2007). This effect is substantially less important on the dayside as compared to the nightside, as evidenced by the significantly larger amplitudes of waves at higher latitudes on the dayside (Meredith et al., 2012). Reduced Landau damping is caused by an increase in the density of cold plasma on the dayside and a lower density of suprathermal electrons (Li et al., 2010a; Walsh et al., 2020). As a result, waves on the dayside propagate in higher densities, are less oblique, and have a less pronounced decrease in wave frequencies, in direct opposition to what is observed on the nightside. This explains why an empirical model of $B_w(\lambda)$ and field aligned waves can sufficiently recover dayside energetic electron precipitation and generally results in better agreement, as demonstrated by Fig. 5.4. Regardless, there still is a slight underestimation of the precipitating rate at sub-relativistic energies (100-500 keV) by up to a factor of $\sim$1.4x. We expect combining realistically mild obliquity and decreasing wave frequency would be the logical next step in reproducing these fluxes. Doing so would result in a refining of our understanding of the wave properties necessary to achieve accurate precipitating flux contributions from radiation belt models.

7.2.2 Remote Sensing of Chorus Waves Properties

The test particle simulation developed for this study, along with the quasi-linear diffusion code, has allowed us to relate equatorial wave properties and electron precipitation mea-

surements. In the absence of simultaneous equatorial wave and low-altitude precipitation measurements, these tools can be incredibly useful for probing wave and plasma characteristics – such as Landau damping, wave characteristics, and plasma density along field lines. The work of Li et al. (2013) and Ni et al. (2014) has enabled remote sensing of the amplitude of the equatorial whistler-mode waves using 30-100 keV electron precipitation, which we relied upon for our studies. However, by looking at precipitating-to-trapped flux ratio spectra in the range of 100 keV to 1 MeV, we can now remotely determine the latitudinal profiles of the wave intensity in context of its location and geomagnetic activity. This is helpful because low-altitude electron precipitation measurements can be made at much faster cadences (with $\sim$ 90-minute orbital periods) and can be used even in the absence of mid-latitude wave measurements. Beyond using the precipitating-to-trapped flux ratios, absolute precipitating fluxes can be used in tandem with modern equatorial flux models (in lieu of the equatorial spacecraft measurements exemplified in Chapter 4). In combination with test particle simulations (or quasi-linear diffusion codes), one may derive actual wave amplitudes from precipitating flux spectra. This is less useful when using ELFIN data sets, since measurements are packetized on a per spin basis (i.e., precipitating and trapped fluxes are always captured together), but could be useful for missions that only capture precipitating fluxes. While there have yet to be any missions with reliable electron precipitation measurement capabilities, we may not have to wait long, as the Relativistic Electron Atmospheric Loss (REAL) CubeSat mission (Millan et al., 2018) should have this capability and is slated for a March 2024 launch. In fact, we can take this parametric study even further by identifying a range of solutions given to each precipitating-to-trapped spectra. This can be accomplished statistically for various activity levels with significantly smaller MLT and L-shell bins (based on historical ELFIN data or upcoming REAL data), or with new data from constellations (now-casting). One can conceivably use a limited dataset of precipitating-to-trapped flux ratios to build a model for use with future LEO constellations, such as the Cross-scale INvestigation of Earth's Magnetotail and Aurora (CINEMA) mission, which can then remotely constrain wave amplitude and characteristics along entire MLT sectors in near-real time.

7.2.3 Future In Situ Electron Precipitation Measurements

Even with low-altitude precipitation measurements, it remains difficult to capture the nonlinear physics that occurs at much faster timescales. Not only do we need faster time resolution, but also simultaneous wave measurements as well. This research has laid the groundwork for future ELFIN follow-on missions, such as the DUCHESS CubeSat mission, which will measure electron precipitation < 300 keV in four simultaneous look directions with time resolution faster than 80 ms while providing direct measurements of whistler-mode waves at high latitudes using a custom UCLA-built Search Coil Magnetometer (SCM). With such direct measurements of the wave spectrum, we will be able to determine the exact ducted wave contribution and further characterize the key properties of ducted wave propagation contribution, such as ω_{pe}/Ω_{ce} ratio and latitude along the field line of the dominant resonant interactions.

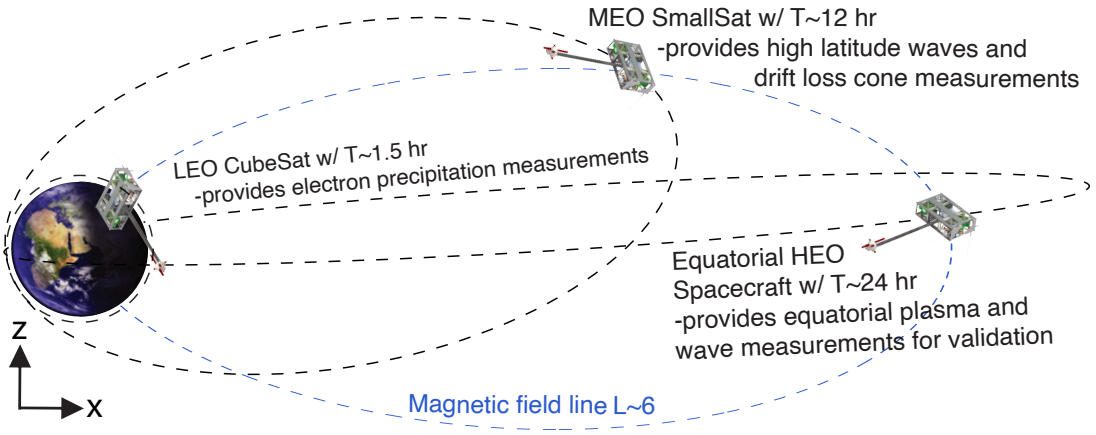


Figure 7.1: A three CubeSat constellation with a CubeSat in LEO, MEO, and HEO, made possible by miniaturized propulsion systems.

However, not all ducted waves make it to high latitudes, so this mission concept could be further augmented with a Mid-Earth Orbit (MEO, 1.1x6.6Re) spacecraft in, e.g., a 12-hr polar orbit. This could be a smallsat or CubeSat with propulsion, capable of residing at mid-high latitudes for much longer periods of time (similar to a Molniya orbit with a large argument of periapsis), with full wave measurements and density measurements capable of

discerning density ducts and plasma waves. Electron precipitation measurements made at these latitudes could also resolve the drift loss cone, providing new insights into another significant electron loss mechanism. The LEO satellite would have a 1.5 hr orbit, traveling underneath with electron precipitation measurements every 90 minutes. By launching each satellite into deliberate inclinations, we can lock their orbital drifts together, walking 45°/year relative to the Sun-Earth line. The MEO satellite could even host an optical auroral imager, much like the Reimei (Japenese for "dawn") satellite (Saito et al., 2011), so as the MEO satellite approaches lower altitudes, we can use the LEO satellite to observe *in situ* particle precipitation as the MEO satellite captures the total auroral dynamics and energy input into the atmosphere. An optional equatorial HEO satellite with a 1-day period would remove any uncertainty from mapping to the equator and also provide direct measurements of the equatorial waves and particle spectrum subject to whistler-mode wave scattering at $<$ 100 keV energies. This 2-3 satellite concept could be additionally scaled to multiple MLT planes for mesoscale or global coverage.

There is a potentially exciting future, where constellations of small satellites with strategically designed orbits are used to study the wider context of magnetospheric and ionospheric physics. In my thesis, we used ELFIN to show that electron precipitation measurements are a valuable proxy for the magnetosphere. With the next generation of ELFIN-derived satellites, we can make great strides in the field of heliophysics, both observationally and theoretically.

APPENDIX A

Acronyms

Acronyms are defined below in order of appearance:

A.1 Chapter 1

- **ULF:** Ultra Low Frequency waves (below 3 Hz, in magnetospheric sciences)
- **ELF:** Extra Low Frequency waves (3 Hz - 3 kHz, in magnetospheric sciences)
- **VLF:** Very Low Frequency waves (3 kHz - 30 kHz, in magnetospheric sciences)
- **GNSS:** Global Navigation Satellite System
- **ELFIN:** Electron Losses and Fields INvestigation mission
- **LEO:** Low Earth Orbit
- **JAXA:** Japan Aerospace Exploration Agency
- **ERG/Arase:** Exploration of energization and Radiation in Geospace (or Arase) mission
- **THEMIS:** Time History of Events and Macroscale Interactions during Substorms mission
- **MMS:** Magnetospheric Multiscale mission
- **NOAA:** National Oceanic and Atmospheric Administration

- **POES:** Polar-orbiting Operational Environmental Satellite mission
- **ADCS:** Attitude, Determination, and Control Subsystem
- **MLT:** Magnetic Local Time
- **VAP/RBSP:** Van Allen Probes / Radiation Belt Storm Probes mission
- **PWING:** study of dynamical variation of Particles and Waves in the INner magnetosphere using Ground-based network observations
- **EISCAT:** European Incoherent Scatter Scientific Association

A.2 Chapter 2

- **ELFIN-STAR:** Electron Losses and Fields INvestgiation with Spatio-Temporal Ambiguity Resolution mission
- **EPD:** Energetic Particle Detector
- **EPDE:** Energetic Particle Detector for Electrons
- **EPDI:** Energetic Particle Detector for Ions
- **FGM:** Fluxgate Magnetometer
- **SZ:** Science Zone (Radiation Belt Crossing)
- **FOV:** Field of View
- **SAMPEX:** Solar Anomalous and Magnetospheric Particle Explorer
- **DM:** Development Model
- **EM:** Engineering Model
- **FM:** Flight Model

- **CDR:** Critical Design Review
- **PSR:** Pre-Ship Review
- **NEN:** Near Earth Network
- **OLP:** Overlapping Passes
- **UHF:** Ultra High Frequency (ITU band, 300 MHz - 1 GHz)
- **VHF:** Very High Frequency (ITU band, 30-300 MHz)
- **PCB:** Printed Circuit Board
- **PEEK:** Polyether ether ketone, a type of thermoplastic
- **MLI:** Multi-Layer Insulation
- **FPCB:** Flight computer PCB
- **ACB:** Attitude Control Board
- **SBPCB:** Solar Battery PCB
- **PIC:** Peripheral Interface Controller, or Programmable Intelligent Computer
- **LETC:** Little Et Cetera Board
- **BETC:** Big Et Cetera Board
- **UTJ:** Ultra Triple Junction, a type of solar cell
- **HTCCA:** High Tensile Copper Clad Aluminum
- **TVAC:** Thermal Vacuum Chamber
- **FC:** Flight Computer (main PIC)
- **WD:** Watch Dog (external PIC)

- **UART:** Universal Asynchronous Receiver-Transmitter (a type of digital serial bus)
- **CRC:** Cyclic Redundancy Check
- **MOC:** Mission Operations Center
- **DoS:** Denial of Service
- **SHA1:** Secure Hash Algorithm-1, a type of hash function
- **RTCC:** Real Time Clock-Calendar
- **OTA:** Over the Air
- **TX:** Transmit
- **RX:** Receive
- **BCD:** Binary-Coded Decimal
- **MSB:** Most Significant Bit
- **GUI:** Graphical User Interface
- **FIFO:** First In, First Out
- **DCT:** Downlink Completeness Table
- **SITL:** Scientist in the Loop
- **SQL:** Structured Query Language
- **ORM:** Object-Relational Mapping
- **EMIC:** Electromagnetic Ion Cyclotron waves (a type of plasma wave)

APPENDIX B

Derivations

B.1 Derivation of I_x

Rearranging our Hamiltonian (Eq. 3.7) for p_x yields

$$\begin{aligned}
\mathcal{H} &= mc^2\sqrt{1+\left(\frac{p_x}{mc}\right)^2+\left(\frac{p_z}{mc}\right)^2+\frac{e^2x^2B_0^2}{m^2c^4}} \\
\left(\frac{p_x}{mc}\right)^2 &= \left(\frac{\mathcal{H}}{mc^2}\right)^2-1-\left(\frac{p_z}{mc}\right)^2-\frac{e^2x^2B_0^2}{m^2c^4} \\
p_x &= mc\sqrt{\left(\frac{\mathcal{H}}{mc}\right)^2-1-\left(\frac{p_z}{mc}\right)^2-\left(\frac{exB_0}{mc^2}\right)^2} \\
p_x &= \sqrt{\mathcal{H}^2-(mc)^2-p_z^2-\left(\frac{eB_0}{mc}mx\right)^2} \\
p_x &= \sqrt{\mathcal{H}^2-(mc)^2-p_z^2-(\Omega_{ce}mx)^2} \qquad \text{(B.1)}
\end{aligned}$$

Integrating Eq. 3.9 then goes as follows:

$$\begin{aligned}
I_x &= \frac{1}{2\pi}\int \overbrace{\mathcal{H}^2-(mc)^2-p_z^2}^{A}-\overbrace{(\Omega_{ce}m)^2}^{b}x^2\,dx \\
I_x &= \frac{1}{2\pi}\int \sqrt{A-bx^2}\,dx
\end{aligned}$$

Substitute in $x = \sqrt{\frac{A}{b}} \sin u$, and $dx = \sqrt{\frac{A}{b}} \cos u \, du$:

$$\begin{aligned}
I_x &= \frac{1}{2\pi} \int \sqrt{A - A\sin^2(u)} \sqrt{\frac{A}{b}} \cos u \, du \\
&= \frac{A}{2\pi\sqrt{b}} \int (1 - \sin^2 u) \, du \\
&= \frac{A}{2\pi\sqrt{b}} \int cos^2 u \, du \\
&= \frac{A}{4\pi\sqrt{b}} \int \cos(2u) + 1 \, du \\
&= \frac{A}{4\pi\sqrt{b}} \left[\frac{1}{2} \sin(2u) + u \right] \\
&= \frac{A}{4\pi\sqrt{b}} \left[\sin u \cos u + u \right] \\
&= \frac{A}{4\pi\sqrt{b}} \left[\sin u \sqrt{1 - \sin^2 u} + u \right]
\end{aligned}$$

$u = \sin^{-1} \sqrt{\frac{b}{A}} x$ and $p_x = \sqrt{A - bx^2}$, which yields:

$$\begin{aligned}
&= \frac{A}{4\pi\sqrt{b}} \left[\sqrt{\frac{b}{A}} x \sqrt{1 - \frac{b}{A} x^2} + \sin^{-1} \sqrt{\frac{b}{A}} x \right] \\
&= \frac{1}{4\pi} \left[x\sqrt{A - bx^2} + \frac{A}{\sqrt{b}} \tan^{-1} \left(\frac{\sqrt{b} x}{\sqrt{A - bx^2}} \right) \right] \\
&= \frac{1}{4\pi} \left[x p_x + \frac{A}{\sqrt{b}} \tan^{-1} \left(\frac{\sqrt{b} x}{p_x} \right) \right]
\end{aligned}$$

This is integrated over one full gyro period, which is double the path integral one side to the other side of its rotation where $p_x = 0$ at either points.

$$\begin{aligned}
&= \frac{2A}{4\pi\sqrt{b}} \overbrace{\left[\tan^{-1}(\infty) - \tan^{-1}(-\infty) \right]}^{[\pi/2] - [-\pi/2] = \pi} \\
&= \frac{2A}{4\sqrt{b}} = \frac{\mathcal{H}^2 - (mc)^2 - p_z^2}{2m\Omega_{ce}} \\
I_x &= \frac{2A}{4\sqrt{b}} = \frac{mc^2 \left[\left(\frac{\mathcal{H}}{mc} \right)^2 - \left(\frac{p_z}{mc} \right)^2 - 1 \right]}{2\Omega_{ce}}
\end{aligned} \tag{B.2}$$

B.2 Derivation of Full Hamiltonian

Pulling out the mc^2 from Eq. (3.6), we can then substitute in new values for (x, p_x), given by Eqs. (3.12), and simplify:

$$\mathcal{H} = mc^2\left[1+\left(\frac{p_z}{mc}\right)^2 + \frac{1}{m^2c^2}\left[p_x - \frac{e}{c}A_w\sin\phi\right]^2 + \frac{e^2}{m^2c^4}\left[xB_0 + A_w\cos\phi\right]^2\right]^{1/2}$$

$$\mathcal{H} = mc^2\left[1+\left(\frac{p_z}{mc}\right)^2 + \frac{1}{m^2c^2}\left[\sqrt{2m\Omega_{ce}I_x}\cos\theta - \frac{e}{c}A_w\sin\phi\right]^2 + \frac{e^2}{m^2c^4}\left[B_0\sqrt{\frac{2I_x}{m\Omega_{ce}}}\sin\theta + A_w\cos\phi\right]^2\right]^{1/2}$$

$$\mathcal{H} = mc^2\left[1+\left(\frac{p_z}{mc}\right)^2 + \frac{1}{m^2c^2}\left[\sqrt{2m\Omega_{ce}I_x}\cos\theta - \frac{e}{c}A_w\sin\phi\right]^2 + \frac{1}{m^2c^2}\left[\sqrt{2mI_x\Omega_{ce}}\sin\theta + A_w\cos\phi\right]^2\right]^{1/2}$$

$$\mathcal{H} = mc^2\left[1+\left(\frac{p_z}{mc}\right)^2 + \frac{1}{m^2c^2}\left[2mI_x\Omega_{ce}\cos^2\theta + \left(\frac{e}{c}A_w\sin\phi\right)^2 - 2\sqrt{2mI_x\Omega_{ce}}\frac{e}{c}A_w\cos\theta\sin\phi + 2mI_x\Omega_{ce}\sin^2\theta + \left(\frac{e}{c}A_w\cos\phi\right)^2 - 2\sqrt{2mI_x\Omega_{ce}}\frac{e}{c}A_w\sin\theta\cos\phi\right]\right]^{1/2}$$

$$\mathcal{H} = mc^2\left[1+\left(\frac{p_z}{mc}\right)^2 + \frac{2I_x\Omega_{ce}}{mc^2} + \left[\frac{eA_w}{mc^2}\right]^2 - \frac{2\sqrt{2mI_x\Omega_{ce}}}{m^2c^2}\frac{e}{c}A_w\left[\cos\theta\sin\phi + \sin\theta\cos\phi\right]\right]^{1/2}$$

$$\mathcal{H} = mc^2\left[1+\left(\frac{p_z}{mc}\right)^2 + \frac{2I_x\Omega_{ce}}{mc^2}+\left[\frac{eA_w}{mc^2}\right]^2 - \frac{2\sqrt{2mI_x\Omega_{ce}}}{m^2c^2}\frac{e}{c}A_w\sin(\phi+\theta)\right]^{1/2} \tag{B.3}$$

Bibliography

O. V. Agapitov, A. Artemyev, V. Krasnoselskikh, Y. V. Khotyaintsev, D. Mourenas, H. Breuillard, M. Balikhin, and G. Rolland. Statistics of whistler mode waves in the outer radiation belt: Cluster STAFF-SA measurements. *J. Geophys. Res.*, 118:3407–3420, June 2013. doi: 10.1002/jgra.50312.

O. V. Agapitov, A. Artemyev, D. Mourenas, V. Krasnoselskikh, J. Bonnell, O. Le Contel, C. M. Cully, and V. Angelopoulos. The quasi-electrostatic mode of chorus waves and electron nonlinear acceleration. *J. Geophys. Res.*, 119:1606–1626, 2014. doi: 10.1002/2013JA019223.

O. V. Agapitov, A. V. Artemyev, D. Mourenas, F. S. Mozer, and V. Krasnoselskikh. Nonlinear local parallel acceleration of electrons through Landau trapping by oblique whistler mode waves in the outer radiation belt. *Geophys. Res. Lett.*, 42:10, December 2015a. doi: 10.1002/2015GL066887.

O. V. Agapitov, V. Krasnoselskikh, F. S. Mozer, A. V. Artemyev, and A. S. Volokitin. Generation of nonlinear electric field bursts in the outer radiation belt through the parametric decay of whistler waves. *Geophys. Res. Lett.*, 42:3715–3722, May 2015b. doi: 10.1002/2015GL064145.

O. V. Agapitov, D. Mourenas, A. V. Artemyev, and F. S. Mozer. Exclusion principle for very oblique and parallel lower band chorus waves. *Geophys. Res. Lett.*, 43(21):11,112–11,120, 2016. ISSN 1944-8007. doi: 10.1002/2016GL071250. URL http://dx.doi.org/10.1002/2016GL071250.

O. V. Agapitov, D. Mourenas, A. V. Artemyev, F. S. Mozer, G. Hospodarsky, J. Bonnell, and V. Krasnoselskikh. Synthetic Empirical Chorus Wave Model From Combined Van Allen Probes and Cluster Statistics. *Journal of Geophysical Research (Space Physics)*, 123 (1):297–314, January 2018. doi: 10.1002/2017JA024843.

O. V. Agapitov, D. Mourenas, A. Artemyev, G. Hospodarsky, and J. W. Bonnell. Time Scales for Electron Quasi-linear Diffusion by Lower-Band Chorus Waves: The Effects of ω_{pe}/Ω_{ce} Dependence on Geomagnetic Activity. *Geophys. Res. Lett.*, 46(12):6178–6187, June 2019. doi: 10.1029/2019GL083446.

J. M. Albert. Cyclotron resonance in an inhomogeneous magnetic field. *Physics of Fluids B*, 5:2744–2750, August 1993. doi: 10.1063/1.860715.

J. M. Albert. Comparison of pitch angle diffusion by turbulent and monochromatic whistler waves. *J. Geophys. Res.*, 106:8477–8482, May 2001. doi: 10.1029/2000JA000304.

J. M. Albert. Evaluation of quasi-linear diffusion coefficients for whistler mode waves in a plasma with arbitrary density ratio. *J. Geophys. Res.*, 110:A03218, March 2005. doi: 10.1029/2004JA010844.

J. M. Albert. Diffusion by one wave and by many waves. *J. Geophys. Res.*, 115:A00F05, March 2010. doi: 10.1029/2009JA014732.

J. M. Albert. Quasi-linear diffusion coefficients for highly oblique whistler mode waves. *J. Geophys. Res.*, 122:5339–5354, May 2017. doi: 10.1002/2017JA024124.

J. M. Albert, X. Tao, and J. Bortnik. Aspects of Nonlinear Wave-Particle Interactions. In D. Summers, I. U. Mann, D. N. Baker, and M. Schulz, editors, *Dynamics of the Earth's Radiation Belts and Inner Magnetosphere*, American Geophysical Union, 2013. doi: 10.1029/2012GM001324.

J. M. Albert, A. V. Artemyev, W. Li, L. Gan, and Q. Ma. Models of resonant wave-particle interactions. *Journal of Geophysical Research: Space Physics*, 126(6):e2021JA029216, 2021. doi: 10.1029/2021JA029216.

O. Allanson, C. E. J. Watt, H. Ratcliffe, H. J. Allison, N. P. Meredith, S. N. Bentley, J. P. J. Ross, and S. A. Glauert. Particle-in-Cell Experiments Examine Electron Diffusion by Whistler-Mode Waves: 2. Quasi-Linear and Nonlinear Dynamics. *Journal of Geophysical Research (Space Physics)*, 125(7):e27949, July 2020. doi: 10.1029/2020JA027949.

O. Allanson, C. E. J. Watt, H. J. Allison, and H. Ratcliffe. Electron Diffusion and Advection During Nonlinear Interactions With Whistler Mode Waves. *Journal of Geophysical Research (Space Physics)*, 126(5):e28793, May 2021. doi: 10.1029/2020JA028793.

Hayley J. Allison and Yuri Y. Shprits. Local heating of radiation belt electrons to ultra-relativistic energies. *Nature Communications*, 11:4533, September 2020. doi: 10.1038/s41467-020-18053-z.

Hayley J. Allison, Yuri Y. Shprits, Irina S. Zhelavskaya, Dedong Wang, and Artem G. Smirnov. Gyroresonant wave-particle interactions with chorus waves during extreme depletions of plasma density in the Van Allen radiation belts. *Science Advances*, 7(5): eabc0380, January 2021. doi: 10.1126/sciadv.abc0380.

T. Amano, T. Katou, N. Kitamura, M. Oka, Y. Matsumoto, M. Hoshino, Y. Saito, S. Yokota, B. L. Giles, W. R. Paterson, C. T. Russell, O. Le Contel, R. E. Ergun, P. A. Lindqvist, D. L. Turner, J. F. Fennell, and J. B. Blake. Observational Evidence for Stochastic Shock Drift Acceleration of Electrons at the Earth's Bow Shock. *Phys. Rev. Lett.*, 124(6):065101, February 2020. doi: 10.1103/PhysRevLett.124.065101.

X. An, A. Artemyev, V. Angelopoulos, X. Zhang, D. Mourenas, and J. Bortnik. Nonresonant scattering of relativistic electrons by electromagnetic ion cyclotron waves in Earth's radiation belts. *Phys. Rev. Lett.*, 129:135101, 2022a. doi: 10.1103/PhysRevLett.129.135101.

Xin An, Anton Artemyev, Vassilis Angelopoulos, Xiaojia Zhang, Didier Mourenas, and Jacob Bortnik. Nonresonant Scattering of Relativistic Electrons by Electromagnetic Ion Cyclotron Waves in Earth's Radiation Belts. *Phys. Rev. Lett.*, 129(13):135101, September 2022b. doi: 10.1103/PhysRevLett.129.135101.

Z. An, Y. Wu, and X. Tao. Electron dynamics in a chorus wave field generated from particle-in-cell simulations. *Geophys. Res. Lett.*, 49(3):e2022GL097778, 2022c. doi: 10.1029/2022GL097778.

Zeyu An, Yifan Wu, and Xin Tao. Electron Dynamics in a Chorus Wave Field Generated From Particle-In-Cell Simulations. *Geophys. Res. Lett.*, 49(3):e97778, February 2022d. doi: 10.1029/2022GL097778.

A. A. Andronov and V. Yu. Trakhtengerts. Kinetic instability of the Earth's outer radiation belt. *Geomagnetism and Aeronomy*, 4:233–242, 1964.

V. Angelopoulos. The THEMIS Mission. *Space Sci. Rev.*, 141:5–34, December 2008. doi: 10.1007/s11214-008-9336-1.

V. Angelopoulos, D. Sibeck, C. W. Carlson, J. P. McFadden, D. Larson, R. P. Lin, J. W. Bonnell, F. S. Mozer, R. Ergun, C. Cully, K. H. Glassmeier, U. Auster, A. Roux, O. Lecontel, S. Frey, T. Phan, S. Mende, H. Frey, E. Donovan, C. T. Russell, R. Strangeway, J. Liu, I. Mann, J. Rae, J. Raeder, X. Li, W. Liu, H. J. Singer, V. A. Sergeev, S. Apatenkov, G. Parks, M. Fillingim, and J. Sigwarth. First Results from the THEMIS Mission. *Space Sci. Rev.*, 141:453–476, December 2008. doi: 10.1007/s11214-008-9378-4.

V. Angelopoulos, E. Tsai, L. Bingley, C. Shaffer, D. L. Turner, A. Runov, W. Li, J. Liu, A. V. Artemyev, X. J. Zhang, R. J. Strangeway, R. E. Wirz, Y. Y. Shprits, V. A. Sergeev, R. P. Caron, M. Chung, P. Cruce, W. Greer, E. Grimes, K. Hector, M. J. Lawson, D. Leneman, E. V. Masongsong, C. L. Russell, C. Wilkins, D. Hinkley, J. B. Blake, N. Adair, M. Allen, M. Anderson, M. Arreola-Zamora, J. Artinger, J. Asher, D. Branchevsky, M. R. Capitelli, R. Castro, G. Chao, N. Chung, M. Cliffe, K. Colton, C. Costello, D. Depe, B. W. Domae, S. Eldin, L. Fitzgibbon, A. Flemming, I. Fox, D. M. Frederick, A. Gilbert, A. Gildemeister, A. Gonzalez, B. Hesford, S. Jha, N. Kang, J. King, R. Krieger, K. Lian, J. Mao, E. McKinney, J. P. Miller, A. Norris, M. Nuesca, A. Palla, E. S. Y. Park, C. E. Pedersen, Z. Qu, R. Rozario, E. Rye, R. Seaton, A. Subramanian, S. R. Sundin, A. Tan, W. Turner, A. J. Villegas, M. Wasden, G. Wing, C. Wong, E. Xie, S. Yamamoto, R. Yap, A. Zarifian, and G. Y. Zhang. The ELFIN Mission. *Space Sci. Rev.*, 216(5):103, July 2020. doi: 10.1007/s11214-020-00721-7.

V. Angelopoulos, X.-J. Zhang, A. V. Artemyev, D. Mourenas, E. Tsai, C. Wilkins, A. Runov,

J. Liu, D. L. Turner, W. Li, K. Khurana, R. E. Wirz, V. A. Sergeev, X. Meng, J. Wu, M. D. Hartinger, T. Raita, Y. Shen, X. An, X. Shi, M. F. Bashir, X. Shen, L. Gan, M. Qin, L. Capannolo, Q. Ma, C. L. Russell, E. V. Masongsong, R. Caron, I. He, L. Iglesias, S. Jha, J. King, S. Kumar, K. Le, J. Mao, A. McDermott, K. Nguyen, A. Norris, A. Palla, Roosnovo, J. Tam, E. Xie, R. C. Yap, S. Ye, C. Young, L. A. Adair, C. Shaffer, M. Chung, P. Cruce, M. Lawson, D. Leneman, M. Allen, M. Anderson, M. Arreola-Zamora, J. Artinger, J. Asher, D. Branchevsky, M. Cliffe, K. Colton, C. Costello, D. Depe, B. W. Domae, S. Eldin, L. Fitzgibbon, A. Flemming, D. M. Frederick, A. Gilbert, B. Hesford, R. Krieger, K. Lian, E. McKinney, J. P. Miller, C. Pedersen, Z. Qu, R. Rozario, M. Rubly, R. Seaton, A. Subramanian, S. R. Sundin, A. Tan, D. Thomlinson, W. Turner, G. Wing, C. Wong, and A. Zarifian. Energetic electron precipitation driven by electromagnetic ion cyclotron waves from ELFIN's low altitude perspective. *Space Science Reviews*, 219(37), 2023. doi: 10.1007/s11214-023-00984-w.

A. V. Artemyev and D. Mourenas. On Whistler Mode Wave Relation to Electron Field-Aligned Plateau Populations. *Journal of Geophysical Research (Space Physics)*, 125(3): e27735, March 2020. doi: 10.1029/2019JA027735.

A. V. Artemyev, V. Krasnoselskikh, O. Agapitov, D. Mourenas, and G. Rolland. Non-diffusive resonant acceleration of electrons in the radiation belts. *Physics of Plasmas*, 19: 122901, 2012. doi: 10.1063/1.4769726.

A. V. Artemyev, D. Mourenas, O. V. Agapitov, and V. V. Krasnoselskikh. Parametric validations of analytical lifetime estimates for radiation belt electron diffusion by whistler waves. *Annales Geophysicae*, 31:599–624, April 2013. doi: 10.5194/angeo-31-599-2013.

A. V. Artemyev, D. Mourenas, O. V. Agapitov, D. L. Vainchtein, F. S. Mozer, and V. V. Krasnoselskikh. Stability of relativistic electron trapping by strong whistler or electromagnetic ion cyclotron waves. *Physics of Plasmas*, 22:082901, 2015. doi: 10.1063/1.4927774.

A. V. Artemyev, O. Agapitov, D. Mourenas, V. Krasnoselskikh, V. Shastun, and F. Mozer. Oblique Whistler-Mode Waves in the Earth's Inner Magnetosphere: Energy Distribution,

Origins, and Role in Radiation Belt Dynamics. *Space Sci. Rev.*, 200(1-4):261–355, April 2016. doi: 10.1007/s11214-016-0252-5.

A. V. Artemyev, A. I Neishtadt, A. A. Vasiliev, and D. Mourenas. Long-term evolution of electron distribution function due to nonlinear resonant interaction with whistler mode waves. *Journal of Plasma Physics*, 84:905840206, 2018. doi: 10.1017/S0022377818000260.

A. V. Artemyev, X. J. Zhang, V. Angelopoulos, D. Mourenas, D. Vainchtein, Y. Shen, I. Vasko, and A. Runov. Ionosphere Feedback to Electron Scattering by Equatorial Whistler Mode Waves. *Journal of Geophysical Research (Space Physics)*, 125(9):e28373, September 2020. doi: 10.1029/2020JA028373.

A. V. Artemyev, A. G. Demekhov, X. J. Zhang, V. Angelopoulos, D. Mourenas, Yu V. Fedorenko, J. Maninnen, E. Tsai, C. Wilkins, S. Kasahara, Y. Miyoshi, A. Matsuoka, Y. Kasahara, T. Mitani, S. Yokota, K. Keika, T. Hori, S. Matsuda, S. Nakamura, M. Kitahara, T. Takashima, and I. Shinohara. Role of Ducting in Relativistic Electron Loss by Whistler-Mode Wave Scattering. *Journal of Geophysical Research (Space Physics)*, 126 (11):e29851, November 2021a. doi: 10.1029/2021JA029851.

A. V. Artemyev, A. I. Neishtadt, J. M. Albert, L. Gan, W. Li, and Q. Ma. Theoretical model of the nonlinear resonant interaction of whistler-mode waves and field-aligned electrons. *Physics of Plasmas*, 28(5):052902, May 2021b. doi: 10.1063/5.0046635.

A. V. Artemyev, V. Angelopoulos, X. J. Zhang, A. Runov, A. Petrukovich, R. Nakamura, E. Tsai, and C. Wilkins. Thinning of the Magnetotail Current Sheet Inferred From Low-Altitude Observations of Energetic Electrons. *Journal of Geophysical Research (Space Physics)*, 127(10):e2022JA030705, October 2022a. doi: 10.1029/2022JA030705.

A. V. Artemyev, D. Mourenas, X. J. Zhang, and D. Vainchtein. On the Incorporation of Nonlinear Resonant Wave-Particle Interactions Into Radiation Belt Models. *Journal of Geophysical Research (Space Physics)*, 127(9):e30853, September 2022b. doi: 10.1029/2022JA030853.

A. V. Artemyev, X. J. Zhang, Y. Zou, D. Mourenas, V. Angelopoulos, D. Vainchtein, E. Tsai, and C. Wilkins. On the Nature of Intense Sub-Relativistic Electron Precipitation. *Journal of Geophysical Research (Space Physics)*, 127(6):e30571, June 2022c. doi: 10.1029/2022JA030571.

Anton V. Artemyev, Anatoly I. Neishtadt, Alexei. A. Vasiliev, Xiao-Jia Zhang, Didier Mourenas, and Dmitri Vainchtein. Long-term dynamics driven by resonant wave-particle interactions: from Hamiltonian resonance theory to phase space mapping. *Journal of Plasma Physics*, 87(2):835870201, March 2021c. doi: 10.1017/S0022377821000246.

Homayon Aryan, Oleksiy V. Agapitov, Anton Artemyev, Didier Mourenas, Michael A. Balikhin, Richard Boynton, and Jacob Bortnik. Outer Radiation Belt Electron Lifetime Model Based on Combined Van Allen Probes and Cluster VLF Measurements. *Journal of Geophysical Research (Space Physics)*, 125(8):e28018, August 2020. doi: 10.1029/2020JA028018.

Jean-Philippe Aumasson and Daniel J. Bernstein. Siphash: A fast short-input prf. pages 489–508, 2012.

H. U. Auster, K. H. Glassmeier, W. Magnes, O. Aydogar, W. Baumjohann, D. Constantinescu, D. Fischer, K. H. Fornacon, E. Georgescu, P. Harvey, O. Hillenmaier, R. Kroth, M. Ludlam, Y. Narita, R. Nakamura, K. Okrafka, F. Plaschke, I. Richter, H. Schwarzl, B. Stoll, A. Valavanoglou, and M. Wiedemann. The THEMIS Fluxgate Magnetometer. *Space Sci. Rev.*, 141:235–264, December 2008. doi: 10.1007/s11214-008-9365-9.

D. N. Baker. What is space weather? *Advances in Space Research*, 22(1):7–16, Jan 1998. doi: 10.1016/S0273-1177(97)01095-8.

D.N. Baker, G.M. Mason, O. Figueroa, G. Colon, J.G. Watzin, and R.M. Aleman. An overview of the solar anomalous, and magnetospheric particle explorer (sampex) mission. *IEEE Transactions on Geoscience and Remote Sensing*, 31(3):531–541, 1993. doi: 10.1109/36.225519.

L. P. Barbieri and R. E. Mahmot. October-November 2003's space weather and operations lessons learned. *Space Weather*, 2(9):S09002, September 2004. doi: 10.1029/2004SW000064.

M. Fraz Bashir, Anton Artemyev, Xiao-Jia Zhang, and Vassilis Angelopoulos. Hot Plasma Effects on Electron Resonant Scattering by Electromagnetic Ion Cyclotron Waves. *Geophys. Res. Lett.*, 49(11):e99229, June 2022. doi: 10.1029/2022GL099229.

Muhammad Fraz Bashir, Anton V Artemyev, Xiao-Jia Zhang, Vassilis Angelopoulos, Ethan Tsai, and Colin Wilkins. Observations of relativistic electron precipitation due to combined scattering of whistler-mode and emic waves. *Authorea Preprints*, 2023.

T. F. Bell. The nonlinear gyroresonance interaction between energetic electrons and coherent VLF waves propagating at an arbitrary angle with respect to the earth's magnetic field. *J. Geophys. Res.*, 89:905–918, February 1984. doi: 10.1029/JA089iA02p00905.

T. F. Bell, U. S. Inan, J. Bortnik, and J. D. Scudder. The Landau damping of magnetospherically reflected whistlers within the plasmasphere. *Geophys. Res. Lett.*, 29:1733, August 2002. doi: 10.1029/2002GL014752.

S. Benck, M. Cyamukungu, and J. Cabrera. Study of correlations between waves and particle fluxes measured on board the DEMETER satellite. *Advances in Space Research*, 42(9): 1538–1549, November 2008. doi: 10.1016/j.asr.2008.03.024.

Jeff Bezanson, Alan Edelman, Stefan Karpinski, and Viral B Shah. Julia: A fresh approach to numerical computing. *SIAM review*, 59(1):65–98, 2017. URL https://doi.org/10.1137/141000671.

J. B. Blake and T. P. O'Brien. Observations of small-scale latitudinal structure in energetic electron precipitation. *Journal of Geophysical Research (Space Physics)*, 121(4):3031–3035, April 2016. doi: 10.1002/2015JA021815.

J. B. Blake, B. H. Mauk, D. N. Baker, P. Carranza, J. H. Clemmons, J. Craft, W. R. Crain, A. Crew, Y. Dotan, J. F. Fennell, R. H. Friedel, L. M. Friesen, F. Fuentes, R. Galvan,

C. Ibscher, A. Jaynes, N. Katz, M. Lalic, A. Y. Lin, D. M. Mabry, T. Nguyen, C. Pancratz, M. Redding, G. D. Reeves, S. Smith, H. E. Spence, and J. Westlake. The Fly's Eye Energetic Particle Spectrometer (FEEPS) Sensors for the Magnetospheric Multiscale (MMS) Mission. *Space Sci. Rev.*, 199:309–329, March 2016. doi: 10.1007/s11214-015-0163-x.

L. W. Blum, A. Halford, R. Millan, J. W. Bonnell, J. Goldstein, M. Usanova, M. Engebretson, M. Ohnsted, G. Reeves, H. Singer, M. Clilverd, and X. Li. Observations of coincident EMIC wave activity and duskside energetic electron precipitation on 18-19 January 2013. *Geophys. Res. Lett.*, 42:5727–5735, July 2015a. doi: 10.1002/2015GL065245.

L. W. Blum, X. Li, and M. Denton. Rapid MeV electron precipitation as observed by SAMPEX/HILT during high-speed stream-driven storms. *J. Geophys. Res.*, 120:3783–3794, May 2015b. doi: 10.1002/2014JA020633.

J. W. Bonnell, F. S. Mozer, G. T. Delory, A. J. Hull, R. E. Ergun, C. M. Cully, V. Angelopoulos, and P. R. Harvey. The Electric Field Instrument (EFI) for THEMIS. *Space Sci. Rev.*, 141:303–341, December 2008. doi: 10.1007/s11214-008-9469-2.

J. Bortnik and R. M. Thorne. The dual role of ELF/VLF chorus waves in the acceleration and precipitation of radiation belt electrons. *Journal of Atmospheric and Solar-Terrestrial Physics*, 69:378–386, March 2007. doi: 10.1016/j.jastp.2006.05.030.

J. Bortnik, U. S. Inan, and T. F. Bell. Landau damping and resultant unidirectional propagation of chorus waves. *Geophys. Res. Lett.*, 33:L03102, February 2006. doi: 10.1029/2005GL024553.

J. Bortnik, R. M. Thorne, N. P. Meredith, and O. Santolík. Ray tracing of penetrating chorus and its implications for the radiation belts. *Geophys. Res. Lett.*, 34:L15109, August 2007. doi: 10.1029/2007GL030040.

J. Bortnik, R. M. Thorne, and U. S. Inan. Nonlinear interaction of energetic electrons with large amplitude chorus. *Geophys. Res. Lett.*, 35:L21102, November 2008. doi: 10.1029/2008GL035500.

J. Bortnik, L. Chen, W. Li, R. M. Thorne, N. P. Meredith, and R. B. Horne. Modeling the wave power distribution and characteristics of plasmaspheric hiss. *Journal of Geophysical Research (Space Physics)*, 116(A12):A12209, December 2011. doi: 10.1029/2011JA016862.

R. J. Boynton, D. Mourenas, and M. A. Balikhin. Electron flux dropouts at Geostationary Earth Orbit: Occurrences, magnitudes, and main driving factors. *Journal of Geophysical Research (Space Physics)*, 121:8448–8461, September 2016. doi: 10.1002/2016JA022916.

R. J. Boynton, D. Mourenas, and M. A. Balikhin. Electron Flux Dropouts at $L \sim 4.2$ From Global Positioning System Satellites: Occurrences, Magnitudes, and Main Driving Factors. *Journal of Geophysical Research (Space Physics)*, 122:11, November 2017. doi: 10.1002/2017JA024523.

A. W. Breneman, A. Crew, J. Sample, D. Klumpar, A. Johnson, O. Agapitov, M. Shumko, D. L. Turner, O. Santolík, J. R. Wygant, C. A. Cattell, S. Thaller, B. Blake, H. Spence, and C. A. Kletzing. Observations Directly Linking Relativistic Electron Microbursts to Whistler Mode Chorus: Van Allen Probes and FIREBIRD II. *Geophys. Res. Lett.*, 44 (22):11,265–11,272, November 2017. doi: 10.1002/2017GL075001.

H. Breuillard, Y. Zaliznyak, V. Krasnoselskikh, O. Agapitov, A. Artemyev, and G. Rolland. Chorus wave-normal statistics in the Earth's radiation belts from ray tracing technique. *Ann. Geophys.*, 30:1223–1233, 2012. doi: 10.5194/angeo-30-1223-2012.

A. L. Brinca. Turbulence effects in the cyclotron resonance of monochromatic whistlers. *Geophys. Res. Lett.*, 5:839–842, October 1978. doi: 10.1029/GL005i010p00839.

J. Büchner and L. M. Zelenyi. Regular and chaotic charged particle motion in magnetotaillike field reversals. I - Basic theory of trapped motion. *J. Geophys. Res.*, 94:11821–11842, September 1989. doi: 10.1029/JA094iA09p11821.

N. L. Bunch, M. Spasojevic, Y. Y. Shprits, X. Gu, and F. Foust. The spectral extent of chorus in the off-equatorial magnetosphere. *J. Geophys. Res.*, 118:1700–1705, April 2013. doi: 10.1029/2012JA018182.

J. L. Burch, T. E. Moore, R. B. Torbert, and B. L. Giles. Magnetospheric Multiscale Overview and Science Objectives. *Space Sci. Rev.*, 199:5–21, March 2016. doi: 10.1007/s11214-015-0164-9.

W. J. Burtis and R. A. Helliwell. Banded chorusA new type of VLF radiation observed in the magnetosphere by OGO 1 and OGO 3. *J. Geophys. Res.*, 74:3002, 1969. doi: 10.1029/JA074i011p03002.

Paul Cannon, Matthew Angling, Leslie Barclay, Charles Curry, Clive Dyer, Robert Edwards, Graham Greene, Mike Hapgood, Richard B Horne, David Jackson, et al. *Extreme space weather: impacts on engineered systems and infrastructure*. Royal Academy of Engineering, 2013.

L. Capannolo, W. Li, Q. Ma, X.-J. Zhang, R. J. Redmon, J. V. Rodriguez, C. A. Kletzing, W. S. Kurth, G. B. Hospodarsky, M. J. Engebretson, H. E. Spence, and G. D. Reeves. Understanding the Driver of Energetic Electron Precipitation Using Coordinated Multisatellite Measurements. *Geophys. Res. Lett.*, 45:6755–6765, July 2018. doi: 10.1029/2018GL078604.

L. Capannolo, W. Li, Q. Ma, L. Chen, X. C. Shen, H. E. Spence, J. Sample, A. Johnson, M. Shumko, D. M. Klumpar, and R. J. Redmon. Direct Observation of Subrelativistic Electron Precipitation Potentially Driven by EMIC Waves. *Geophys. Res. Lett.*, 46(22): 12,711–12,721, November 2019. doi: 10.1029/2019GL084202.

L. Capannolo, W. Li, Q. Ma, M. Qin, X. C. Shen, V. Angelopoulos, A. Artemyev, X.-J. Zhang, and M. Hanzelka. Electron precipitation observed by elfin using proton precipitation as a proxy for electromagnetic ion cyclotron (emic) waves. *Geophysical Research Letters*, 2023a. doi: https://doi.org/10.1029/2023GL103519.

L. Capannolo, W. Li, Q. Ma, M. Qin, X. C. Shen, V. Angelopoulos, A. Artemyev, X. J. Zhang, and M. Hanzelka. Electron Precipitation Observed by ELFIN Using Proton Pre-

cipitation as a Proxy for Electromagnetic Ion Cyclotron (EMIC) Waves. *Geophys. Res. Lett.*, 50(21):e2023GL103519, November 2023b. doi: 10.1029/2023GL103519.

C. Cattell, J. R. Wygant, K. Goetz, K. Kersten, P. J. Kellogg, T. von Rosenvinge, S. D. Bale, I. Roth, M. Temerin, M. K. Hudson, R. A. Mewaldt, M. Wiedenbeck, M. Maksimovic, R. Ergun, M. Acuna, and C. T. Russell. Discovery of very large amplitude whistler-mode waves in Earth's radiation belts. *Geophys. Res. Lett.*, 35:L01105, January 2008. doi: 10.1029/2007GL032009.

C. A. Cattell, B. Short, A. W. Breneman, and P. Grul. Narrowband Large Amplitude Whistler-mode Waves in the Solar Wind and Their Association with Electrons: STEREO Waveform Capture Observations. *Astrophys. J.*, 897(2):126, July 2020. doi: 10.3847/1538-4357/ab961f.

Cynthia Cattell and Tien Vo. Modeling Interactions of Narrowband Large Amplitude Whistler-mode Waves with Electrons in the Solar Wind inside 0.3 au and at 1 au Using a Particle Tracing Code. *Astrophys. J. Lett.*, 914(2):L33, June 2021. doi: 10.3847/2041-8213/ac08a1.

L. Chen, R. M. Thorne, W. Li, and J. Bortnik. Modeling the wave normal distribution of chorus waves. *J. Geophys. Res.*, 118:1074–1088, March 2013. doi: 10.1029/2012JA018343.

Lunjin Chen, Richard M. Thorne, Jacob Bortnik, and Xiao-Jia Zhang. Nonresonant interactions of electromagnetic ion cyclotron waves with relativistic electrons. *J. Geophys. Res.*, 121(10):9913–9925, 2016. ISSN 2169-9402. doi: 10.1002/2016JA022813. URL http://dx.doi.org/10.1002/2016JA022813.

Lunjin Chen, Hui Zhu, and Xiaojia Zhang. Wavenumber Analysis of EMIC Waves. *Geophys. Res. Lett.*, 46(11):5689–5697, Jun 2019a. doi: 10.1029/2019GL082686.

Lunjin Chen, Aaron W. Breneman, Zhiyang Xia, and Xiao-jia Zhang. Modeling of Bouncing Electron Microbursts Induced by Ducted Chorus Waves. *Geophys. Res. Lett.*, 47(17): e89400, September 2020. doi: 10.1029/2020GL089400.

Lunjin Chen, Xiao-Jia Zhang, Anton Artemyev, Liheng Zheng, Zhiyang Xia, Aaron W. Breneman, and Richard B. Horne. Electron microbursts induced by nonducted chorus waves. *Frontiers in Astronomy and Space Sciences*, 8:163, October 2021a. doi: 10.3389/fspas.2021.745927.

Lunjin Chen, Xiao-Jia Zhang, Anton Artemyev, Vassilis Angelopoulos, Ethan Tsai, Colin Wilkins, and Richard B. Horne. Ducted Chorus Waves Cause Sub-Relativistic and Relativistic Electron Microbursts. *Geophys. Res. Lett.*, 49(5):e97559, March 2022. doi: 10.1029/2021GL097559.

Rui Chen, Xinliang Gao, Quanming Lu, and Shui Wang. Unraveling the Correlation Between Chorus Wave and Electron Beam-Like Distribution in the Earth's Magnetosphere. *Geophys. Res. Lett.*, 46(21):11,671–11,678, November 2019b. doi: 10.1029/2019GL085108.

Rui Chen, Xinliang Gao, Quanming Lu, Lunjin Chen, Bruce T. Tsurutani, Wen Li, Binbin Ni, and Shui Wang. In Situ Observations of Whistler Mode Chorus Waves Guided by Density Ducts. *Journal of Geophysical Research (Space Physics)*, 126(4):e28814, April 2021b. doi: 10.1029/2020JA028814.

Mariana C.A. Clare, Omar Jamil, and Cyril J. Morcrette. Combining distribution-based neural networks to predict weather forecast probabilities. *Quarterly Journal of the Royal Meteorological Society*, 147(741):4337–4357, 2021. ISSN 1477-870X. doi: 10.1002/qj.4180. URL https://onlinelibrary.wiley.com/doi/abs/10.1002/qj.4180. _eprint: https://onlinelibrary.wiley.com/doi/pdf/10.1002/qj.4180.

Chris Colpitts, Yoshizumi Miyoshi, Yoshiya Kasahara, Gian Luca Delzanno, John R. Wygant, Cynthia A. Cattell, Aaron Breneman, Craig Kletzing, Greg Cunningham, Mitsuru Hikishima, Shoya Matsuda, Yuto Katoh, Jean-Francois Ripoll, Iku Shinohara, and Ayako Matsuoka. First Direct Observations of Propagation of Discrete Chorus Elements From the Equatorial Source to Higher Latitudes, Using the Van Allen Probes and Arase Satellites. *Journal of Geophysical Research (Space Physics)*, 125(10):e28315, October 2020. doi: 10.1029/2020JA028315.

Alexander B. Crew, Harlan E. Spence, J. Bernard Blake, David M. Klumpar, Brian A. Larsen, T. Paul O'Brien, Shane Driscoll, Matthew Handley, Jason Legere, Stephen Longworth, Keith Mashburn, Ehson Mosleh, Nicholas Ryhajlo, Sonya Smith, Larry Springer, and Mark Widholm. First multipoint in situ observations of electron microbursts: Initial results from the NSF FIREBIRD II mission. *Journal of Geophysical Research (Space Physics)*, 121(6):5272–5283, Jun 2016. doi: 10.1002/2016JA022485.

C. M. Cully, J. W. Bonnell, and R. E. Ergun. THEMIS observations of long-lived regions of large-amplitude whistler waves in the inner magnetosphere. *Geophys. Res. Lett.*, 35: L17S16, June 2008. doi: 10.1029/2008GL033643.

L. A. Davis, C. A. Cattell, III Wilson, L. B., Z. A. Cohen, A. W. Breneman, and E. L. M. Hanson. ARTEMIS Observations of Plasma Waves in Laminar and Perturbed Interplanetary Shocks. *Astrophys. J.*, 913(2):144, June 2021. doi: 10.3847/1538-4357/abf56a.

A. G. Demekhov. Generation of VLF emissions with the increasing and decreasing frequency in the magnetosperic cyclotron maser in the backward wave oscillator regime. *Radiophysics and Quantum Electronics*, 53:609–622, April 2011. doi: 10.1007/s11141-011-9256-x.

A. G. Demekhov, V. Y. Trakhtengerts, M. J. Rycroft, and D. Nunn. Electron acceleration in the magnetosphere by whistler-mode waves of varying frequency. *Geomagnetism and Aeronomy*, 46:711–716, December 2006. doi: 10.1134/S0016793206060053.

A. G. Demekhov, V. Y. Trakhtengerts, M. Rycroft, and D. Nunn. Efficiency of electron acceleration in the Earth's magnetosphere by whistler mode waves. *Geomagnetism and Aeronomy*, 49:24–29, February 2009. doi: 10.1134/S0016793209010034.

A. G. Demekhov, J. Manninen, O. Santolík, and E. E. Titova. Conjugate Ground-Spacecraft Observations of VLF Chorus Elements. *Geophys. Res. Lett.*, 44(23):11,735–11,744, December 2017. doi: 10.1002/2017GL076139.

A. G. Demekhov, E. E. Titova, J. Maninnen, D. L. Pasmanik, A. A. Lubchich, O. Santolík, A. V. Larchenko, A. S. Nikitenko, and T. Turunen. Localization of the Source of

Quasiperiodic VLF Emissions in the Magnetosphere by Using Simultaneous Ground and Space Observations: A Case Study. *Journal of Geophysical Research (Space Physics)*, 125 (5):e27776, May 2020. doi: 10.1029/2020JA027776.

M. H. Denton, M. F. Thomsen, H. Korth, S. Lynch, J. C. Zhang, and M. W. Liemohn. Bulk plasma properties at geosynchronous orbit. *J. Geophys. Res.*, 110:A07223, July 2005. doi: 10.1029/2004JA010861.

R. E. Denton, K. Takahashi, I. A. Galkin, P. A. Nsumei, X. Huang, B. W. Reinisch, R. R. Anderson, M. K. Sleeper, and W. J. Hughes. Distribution of density along magnetospheric field lines. *J. Geophys. Res.*, 111:A04213, April 2006. doi: 10.1029/2005JA011414.

E. Douma, C. J. Rodger, L. W. Blum, T. P. O'Brien, M. A. Clilverd, and J. B. Blake. Characteristics of Relativistic Microburst Intensity From SAMPEX Observations. *Journal of Geophysical Research (Space Physics)*, 124(7):5627–5640, July 2019. doi: 10.1029/2019JA026757.

Emma Douma, Craig J. Rodger, Mark A. Clilverd, Aaron T. Hendry, Mark J. Engebretson, and Marc R. Lessard. Comparison of Relativistic Microburst Activity Seen by SAMPEX With Ground-Based Wave Measurements at Halley, Antarctica. *Journal of Geophysical Research (Space Physics)*, 123(2):1279–1294, February 2018. doi: 10.1002/2017JA024754.

A. Y. Drozdov, Y. Y. Shprits, M. E. Usanova, N. A. Aseev, A. C. Kellerman, and H. Zhu. EMIC wave parameterization in the long-term VERB code simulation. *J. Geophys. Res.*, 122:8488–8501, August 2017. doi: 10.1002/2017JA024389.

W. E. Drummond and D. Pines. Nonlinear stability of plasma oscillations. *Nuclear Fusion Suppl.*, 3:1049–1058, 1962.

S. Dubyagin, V. A. Sergeev, and M. V. Kubyshkina. On the remote sensing of plasma sheet from low-altitude spacecraft. *Journal of Atmospheric and Solar-Terrestrial Physics*, 64 (5-6):567–572, March 2002. doi: 10.1016/S1364-6826(02)00014-7.

D. S. Evans and M. S. Greer. Polar orbiting environmental satellite space environment monitor-2: instrument description and archive data documentation, 2004.

L. V. Filatov and V. F. Melnikov. Influence of Whistler Turbulence on Fast Electron Distribution and Their Microwave Emissions in a Flare Loop. *Geomagnetism and Aeronomy*, 57(8):1001–1008, December 2017. doi: 10.1134/S0016793217080084.

J. C. Foster, P. J. Erickson, D. N. Baker, S. G. Claudepierre, C. A. Kletzing, W. Kurth, G. D. Reeves, S. A. Thaller, H. E. Spence, Y. Y. Shprits, and J. R. Wygant. Prompt energization of relativistic and highly relativistic electrons during a substorm interval: Van Allen Probes observations. *Geophys. Res. Lett.*, 41:20–25, January 2014. doi: 10.1002/2013GL058438.

X. Fu, M. M. Cowee, R. H. Friedel, H. O. Funsten, S. P. Gary, G. B. Hospodarsky, C. Kletzing, W. Kurth, B. A. Larsen, K. Liu, E. A. MacDonald, K. Min, G. D. Reeves, R. M. Skoug, and D. Winske. Whistler anisotropy instabilities as the source of banded chorus: Van Allen Probes observations and particle-in-cell simulations. *Journal of Geophysical Research (Space Physics)*, 119:8288–8298, October 2014. doi: 10.1002/2014JA020364.

N. Furuya, Y. Omura, and D. Summers. Relativistic turning acceleration of radiation belt electrons by whistler mode chorus. *J. Geophys. Res.*, 113:A04224, April 2008. doi: 10.1029/2007JA012478.

C. Gabrielse, V. Angelopoulos, A. Runov, and D. L. Turner. Statistical characteristics of particle injections throughout the equatorial magnetotail. *J. Geophys. Res.*, 119:2512–2535, April 2014. doi: 10.1002/2013JA019638.

L. Gan, W. Li, Q. Ma, J. M. Albert, A. V. Artemyev, and J. Bortnik. Nonlinear Interactions Between Radiation Belt Electrons and Chorus Waves: Dependence on Wave Amplitude Modulation. *Geophys. Res. Lett.*, 47(4):e85987, February 2020a. doi: 10.1029/2019GL085987.

L. Gan, W. Li, Q. Ma, A. V. Artemyev, and J. M. Albert. Unraveling the Formation Mechanism for the Bursts of Electron Butterfly Distributions: Test Particle and

Quasilinear Simulations. *Geophys. Res. Lett.*, 47(21):e90749, November 2020b. doi: 10.1029/2020GL090749.

L. Gan, W. Li, Q. Ma, A. V. Artemyev, and J. M. Albert. Dependence of Nonlinear Effects on Whistler-Mode Wave Bandwidth and Amplitude: A Perspective From Diffusion Coefficients. *Journal of Geophysical Research (Space Physics)*, 127(5):e30063, May 2022a. doi: 10.1029/2021JA030063.

L. Gan, W. Li, Q. Ma, A. V. Artemyev, and J. M. Albert. Dependence of nonlinear effects on whistler-mode wave bandwidth and amplitude: A perspective from diffusion coefficients. *J. Geophys. Res.*, 127:e2021JA030063, 2022b. doi: 10.1029/2021JA030063.

Longzhi Gan, Anton Artemyev, Wen Li, Xiao-Jia Zhang, Qianli Ma, Didier Mourenas, Vassilis Angelopoulos, Ethan Tsai, and Colin Wilkins. Bursty energetic electron precipitation by high-order resonance with very-oblique whistler-mode waves. *Geophys. Res. Lett.*, 2023. doi: 10.1029/2022GL101920.

J. L. Gannon, X. Li, and D. Heynderickx. Pitch angle distribution analysis of radiation belt electrons based on Combined Release and Radiation Effects Satellite Medium Electrons A data. *J. Geophys. Res.*, 112:A05212, May 2007. doi: 10.1029/2005JA011565.

N. Yu Ganushkina, I. Dandouras, Y. Y. Shprits, and J. Cao. Locations of boundaries of outer and inner radiation belts as observed by Cluster and Double Star. *Journal of Geophysical Research: Space Physics*, 116(A9), 2011. ISSN 2156-2202. doi: 10.1029/2010JA016376. URL https://onlinelibrary.wiley.com/doi/abs/10.1029/2010JA016376. _eprint: https://onlinelibrary.wiley.com/doi/pdf/10.1029/2010JA016376.

R. Gendrin. Le guidage des whistlers par le champ magnetique. *Plan. Sp. Sci.*, 5:274, August 1961. doi: 10.1016/0032-0633(61)90096-4.

S. A. Glauert and R. B. Horne. Calculation of pitch angle and energy diffusion coefficients with the PADIE code. *J. Geophys. Res.*, 110:A04206, April 2005. doi: 10.1029/2004JA010851.

Veronika S. Grach, Anton V. Artemyev, Andrei G. Demekhov, Xiao-Jia Zhang, Jacob Bortnik, Vassilis Angelopoulos, Rumi Nakamura, Ethan Tsai, Colin Wilkins, and Owen W. Roberts. Relativistic Electron Precipitation by EMIC Waves: Importance of Nonlinear Resonant Effects. *Geophys. Res. Lett.*, 49(17):e99994, September 2022a. doi: 10.1029/2022GL099994.

Veronika S. Grach, Anton V. Artemyev, Andrei G. Demekhov, Xiao-Jia Zhang, Jacob Bortnik, Vassilis Angelopoulos, Rumi Nakamura, Ethan Tsai, Colin Wilkins, and Owen W. Roberts. Relativistic Electron Precipitation by EMIC Waves: Importance of Nonlinear Resonant Effects. *Geophys. Res. Lett.*, 49(17):e99994, September 2022b. doi: 10.1029/2022GL099994.

J. L. Green. Meped telescope data processing algorithm theoretical basis document, 2013.

M. Hanzelka and O. Santolík. Effects of Field-Aligned Cold Plasma Density Filaments on the Fine Structure of Chorus. *Geophys. Res. Lett.*, 49(24):e2022GL101654, December 2022. doi: 10.1029/2022GL101654.

Miroslav Hanzelka and Ondřej Santolík. Effects of Ducting on Whistler Mode Chorus or Exohiss in the Outer Radiation Belt. *Geophys. Res. Lett.*, 46(11):5735–5745, June 2019. doi: 10.1029/2019GL083115.

N. Haque, M. Spasojevic, O. Santolík, and U. S. Inan. Wave normal angles of magnetospheric chorus emissions observed on the Polar spacecraft. *J. Geophys. Res.*, 115:A00F07, April 2010. doi: 10.1029/2009JA014717.

M. Hayosh, D. L. Pasmanik, A. G. Demekhov, O. Santolík, M. Parrot, and E. E. Titova. Simultaneous observations of quasi-periodic ELF/VLF wave emissions and electron precipitation by DEMETER satellite: A case study. *Journal of Geophysical Research (Space Physics)*, 118(7):4523–4533, July 2013. doi: 10.1002/jgra.50179.

R. A. Helliwell. *Whistlers and Related Ionospheric Phenomena*. Stanford University Press, USA, 1965.

R. A. Helliwell. A theory of discrete VLF emissions from the magnetosphere. *J. Geophys. Res.*, 72:4773–4790, October 1967. doi: 10.1029/JZ072i019p04773.

A. T. Hendry, C. J. Rodger, and M. A. Clilverd. Evidence of sub-MeV EMIC-driven electron precipitation. *Geophys. Res. Lett.*, 44:1210–1218, February 2017. doi: 10.1002/2016GL071807.

Ryoko Hiraga and Yoshiharu Omura. Acceleration mechanism of radiation belt electrons through interaction with multi-subpacket chorus waves. *Earth, Planets, and Space*, 72(1): 21, February 2020. doi: 10.1186/s40623-020-1134-3.

R. B. Horne and R. M. Thorne. Relativistic electron acceleration and precipitation during resonant interactions with whistler-mode chorus. *Geophys. Res. Lett.*, 30(10):1527, May 2003. doi: 10.1029/2003GL016973.

R. B. Horne, R. M. Thorne, S. A. Glauert, J. M. Albert, N. P. Meredith, and R. R. Anderson. Timescale for radiation belt electron acceleration by whistler mode chorus waves. *J. Geophys. Res.*, 110:A03225, March 2005. doi: 10.1029/2004JA010811.

R. B. Horne, R. M. Thorne, S. A. Glauert, N. P. Meredith, D. Pokhotelov, and O. Santolík. Electron acceleration in the Van Allen radiation belts by fast magnetosonic waves. *Geophys. Res. Lett.*, 34:17107, September 2007. doi: 10.1029/2007GL030267.

R. B. Horne, S. A. Glauert, N. P. Meredith, D. Boscher, V. Maget, D. Heynderickx, and D. Pitchford. Space weather impacts on satellites and forecasting the Earth's electron radiation belts with SPACECAST. *Space Weather*, 11:169–186, April 2013. doi: 10.1002/swe.20023.

K. Hosokawa, Y. Miyoshi, M. Ozaki, S. I. Oyama, Y. Ogawa, S. Kurita, Y. Kasahara, Y. Kasaba, S. Yagitani, S. Matsuda, F. Tsuchiya, A. Kumamoto, R. Kataoka, K. Shiokawa, T. Raita, E. Turunen, T. Takashima, I. Shinohara, and R. Fujii. Multiple time-scale beats in aurora: precise orchestration via magnetospheric chorus waves. *Scientific Reports*, 10: 3380, February 2020. doi: 10.1038/s41598-020-59642-8.

Poorya Hosseini, Oleksiy Agapitov, Vijay Harid, and Mark Gołkowski. Evidence of Small Scale Plasma Irregularity Effects on Whistler Mode Chorus Propagation. *Geophys. Res. Lett.*, 48(5):e92850, March 2021. doi: 10.1029/2021GL092850.

Y.-K. Hsieh and Y. Omura. Nonlinear dynamics of electrons interacting with oblique whistler mode chorus in the magnetosphere. *J. Geophys. Res.*, 122:675–694, January 2017. doi: 10.1002/2016JA023255.

W. L. Imhof, J. B. Reagan, and E. E. Gaines. Fine-scale spatial structure in the pitch angle distributions of energetic particles near the midnight trapping boundary. *J. Geophys. Res.*, 82:5215–5221, November 1977. doi: 10.1029/JA082i032p05215.

Ning Kang and Jacob Bortnik. Structure of Energy Precipitation Induced by Superbolt-Lightning Generated Whistler Waves. *Geophys. Res. Lett.*, 49(5):e2022GL097770, March 2022. doi: 10.1029/2022GL097770.

Ning Kang, Jacob Bortnik, Xiaojia Zhang, Seth Claudepierre, and Xiaofei Shi. Relativistic Microburst Scale Size Induced by a Single Point-Source Chorus Element. *Geophys. Res. Lett.*, 49(23):e2022GL100841, December 2022. doi: 10.1029/2022GL100841.

Ning Kang, Jacob Bortnik, Xiaojia Zhang, Seth Claudepierre, and Xiaofei Shi. Relativistic microburst scale size induced by a single point-source chorus element. *Geophysical Research Letters*, 49(23):e2022GL100841, 2022. doi: https://doi.org/10.1029/2022GL100841. URL https://agupubs.onlinelibrary.wiley.com/doi/abs/10.1029/2022GL100841. e2022GL100841 2022GL100841.

V. I. Karpman. Nonlinear Effects in the ELF Waves Propagating along the Magnetic Field in the Magnetosphere. *Space Sci. Rev.*, 16:361–388, September 1974. doi: 10.1007/BF00171564.

V. I. Karpman and R. N. Kaufman. Whistler wave propagation in density ducts. *Journal of Plasma Physics*, 27(2):225–238, April 1982. doi: 10.1017/S0022377800026556.

V. I. Karpman and D. R. Shklyar. Particle precipitation caused by a single whistler-mode wave injected into the magnetosphere. *Plan. Sp. Sci.*, 25:395–403, April 1977. doi: 10.1016/0032-0633(77)90055-1.

V. I. Karpman, J. N. Istomin, and D. R. Shklyar. Nonlinear theory of a quasi-monochromatic whistler mode packet in inhomogeneous plasma. *Plasma Physics*, 16:685–703, August 1974. doi: 10.1088/0032-1028/16/8/001.

S. Kasahara, Y. Miyoshi, S. Yokota, Y. Kasahara, S. Matsuda, A. Kumamoto, A. Matsuoka, Y. Kazama, H. U. Frey, V. Angelopoulos, S. Kurita, K. Keika, K. Seki, and I. Shinohara. Pulsating aurora from electron scattering by chorus waves. *Nature*, 554:337–340, 2018a. doi: 10.1038/nature25505.

Satoshi Kasahara, Shoichiro Yokota, Takefumi Mitani, Kazushi Asamura, Masafumi Hirahara, Yasuko Shibano, and Takeshi Takashima. Medium-energy particle experiments-electron analyzer (MEP-e) for the exploration of energization and radiation in geospace (ERG) mission. *Earth, Planets, and Space*, 70(1):69, May 2018b. doi: 10.1186/s40623-018-0847-z.

Y. Katoh. A simulation study of the propagation of whistler-mode chorus in the Earth's inner magnetosphere. *Earth, Planets, and Space*, 66:6, December 2014. doi: 10.1186/1880-5981-66-6.

Y. Katoh and Y. Omura. Computer simulation of chorus wave generation in the Earth's inner magnetosphere. *Geophys. Res. Lett.*, 34:L03102, February 2007a. doi: 10.1029/2006GL028594.

Y. Katoh and Y. Omura. Relativistic particle acceleration in the process of whistler-mode chorus wave generation. *Geophys. Res. Lett.*, 34:L13102, July 2007b. doi: 10.1029/2007GL029758.

Y. Katoh, Y. Omura, and D. Summers. Rapid energization of radiation belt electrons

by nonlinear wave trapping. *Annales Geophysicae*, 26:3451–3456, November 2008. doi: 10.5194/angeo-26-3451-2008.

Yangguang Ke, Xinliang Gao, Quanming Lu, Xueyi Wang, and Shui Wang. Generation of rising-tone chorus in a two-dimensional mirror field by using the general curvilinear pic code. *J. Geophys. Res.*, 2017. ISSN 2169-9402. doi: 10.1002/2017JA024178. URL http://dx.doi.org/10.1002/2017JA024178.

Yangguang Ke, Lunjin Chen, Xinliang Gao, Quanming Lu, Xueyi Wang, Rui Chen, Huayue Chen, and Shui Wang. Whistler Mode Waves Trapped by Density Irregularities in the Earth's Magnetosphere. *Geophys. Res. Lett.*, 48(7):e92305, April 2021. doi: 10.1029/2020GL092305.

Yangguang Ke, Xinliang Gao, Quanming Lu, Xueyi Wang, Rui Chen, Huayue Chen, and Shui Wang. Deformation of Electron Distributions Due to Landau Trapping by the Whistler-Mode Wave. *Geophys. Res. Lett.*, 49(3):e96428, February 2022. doi: 10.1029/2021GL096428.

C. F Kennel. Low-Frequency Whistler Mode. *Physics of Fluids*, 9:2190–2202, November 1966. doi: 10.1063/1.1761588.

C. F. Kennel and F. Engelmann. Velocity Space Diffusion from Weak Plasma Turbulence in a Magnetic Field. *Physics of Fluids*, 9:2377–2388, November 1966. doi: 10.1063/1.1761629.

C. F. Kennel and H. E. Petschek. Limit on Stably Trapped Particle Fluxes. *J. Geophys. Res.*, 71:1–28, January 1966.

G. V. Khazanov, A. Glocer, and E. W. Himwich. Magnetosphere-ionosphere energy interchange in the electron diffuse aurora. *Journal of Geophysical Research (Space Physics)*, 119(1):171–184, Jan 2014. doi: 10.1002/2013JA019325.

G. V. Khazanov, R. M. Robinson, E. Zesta, D. G. Sibeck, M. Chu, and G. A. Grubbs. Impact of Precipitating Electrons and Magnetosphere-Ionosphere Coupling Processes on

Ionospheric Conductance. *Space Weather*, 16(7):829–837, July 2018. doi: 10.1029/2018SW001837.

M. Kitahara and Y. Katoh. Anomalous Trapping of Low Pitch Angle Electrons by Coherent Whistler Mode Waves. *J. Geophys. Res.*, 124(7):5568–5583, Jul 2019. doi: 10.1029/2019JA026493.

N. Kitamura, T. Amano, Y. Omura, S. A. Boardsen, D. J. Gershman, Y. Miyoshi, M. Kitahara, Y. Katoh, H. Kojima, S. Nakamura, M. Shoji, Y. Saito, S. Yokota, B. L. Giles, W. R. Paterson, C. J. Pollock, A. C. Barrie, D. G. Skeberdis, S. Kreisler, O. Le Contel, C. T. Russell, R. J. Strangeway, P. A. Lindqvist, R. E. Ergun, R. B. Torbert, and J. L. Burch. Direct observations of energy transfer from resonant electrons to whistler-mode waves in magnetosheath of Earth. *Nature Communications*, 13:6259, October 2022. doi: 10.1038/s41467-022-33604-2.

Zhenyu Kong, Xinliang Gao, Huayue Chen, Quanming Lu, Rui Chen, Yangguang Ke, and Shui Wang. The Correlation Between Whistler Mode Waves and Electron Beam-Like Distribution: Test Particle Simulations and THEMIS Observations. *Journal of Geophysical Research (Space Physics)*, 126(11):e29834, November 2021. doi: 10.1029/2021JA029834.

Y. Kubota and Y. Omura. Nonlinear Dynamics of Radiation Belt Electrons Interacting With Chorus Emissions Localized in Longitude. *Journal of Geophysical Research (Space Physics)*, 123:4835–4857, June 2018. doi: 10.1029/2017JA025050.

W. S. Kurth. Continuum radiation in planetary magnetospheres. In H. O. Rucker, S. J. Bauer, and M. L. Kaiser, editors, *Planetary Radio Emissions III*, page 329, 1992.

Mai Mai Lam, Richard B Horne, Nigel P Meredith, Sarah A Glauert, Tracy Moffat-Griffin, and Janet C Green. Origin of energetic electron precipitation¿ 30 kev into the atmosphere. *Journal of Geophysical Research: Space Physics*, 115(A4), 2010.

Remi Lam, Alvaro Sanchez-Gonzalez, Matthew Willson, Peter Wirnsberger, Meire Fortunato, Ferran Alet, Suman Ravuri, Timo Ewalds, Zach Eaton-Rosen, Weihua Hu, Alexan-

der Merose, Stephan Hoyer, George Holland, Oriol Vinyals, Jacklynn Stott, Alexander Pritzel, Shakir Mohamed, and Peter Battaglia. Learning skillful medium-range global weather forecasting. *Science*, December 2023. doi: 10.1126/science.adi2336. URL https://www.science.org/doi/10.1126/science.adi2336. Publisher: American Association for the Advancement of Science.

O. Le Contel, A. Roux, P. Robert, C. Coillot, A. Bouabdellah, B. de La Porte, D. Alison, S. Ruocco, V. Angelopoulos, K. Bromund, C. C. Chaston, C. Cully, H. U. Auster, K. H. Glassmeier, W. Baumjohann, C. W. Carlson, J. P. McFadden, and D. Larson. First Results of the THEMIS Search Coil Magnetometers. *Space Sci. Rev.*, 141:509–534, December 2008. doi: 10.1007/s11214-008-9371-y.

O. Le Contel, A. Roux, C. Jacquey, P. Robert, M. Berthomier, T. Chust, B. Grison, V. Angelopoulos, D. Sibeck, C. C. Chaston, C. M. Cully, B. Ergun, K.-H. Glassmeier, U. Auster, J. McFadden, C. Carlson, D. Larson, J. W. Bonnell, S. Mende, C. T. Russell, E. Donovan, I. Mann, and H. Singer. Quasi-parallel whistler mode waves observed by THEMIS during near-earth dipolarizations. *Annales Geophysicae*, 27:2259–2275, June 2009. doi: 10.5194/angeo-27-2259-2009.

O. Le Contel, P. Leroy, A. Roux, C. Coillot, D. Alison, A. Bouabdellah, L. Mirioni, L. Meslier, A. Galic, M. C. Vassal, R. B. Torbert, J. Needell, D. Rau, I. Dors, R. E. Ergun, J. Westfall, D. Summers, J. Wallace, W. Magnes, A. Valavanoglou, G. Olsson, M. Chutter, J. Macri, S. Myers, S. Turco, J. Nolin, D. Bodet, K. Rowe, M. Tanguy, and B. de la Porte. The Search-Coil Magnetometer for MMS. *Space Sci. Rev.*, 199:257–282, March 2016a. doi: 10.1007/s11214-014-0096-9.

O. Le Contel, A. Retinò, H. Breuillard, L. Mirioni, P. Robert, A. Chasapis, B. Lavraud, T. Chust, L. Rezeau, F. D. Wilder, D. B. Graham, M. R. Argall, D. J. Gershman, P.-A. Lindqvist, Y. V. Khotyaintsev, G. Marklund, R. E. Ergun, K. A. Goodrich, J. L. Burch, R. B. Torbert, J. Needell, M. Chutter, D. Rau, I. Dors, C. T. Russell, W. Magnes, R. J. Strangeway, K. R. Bromund, H. K. Leinweber, F. Plaschke, D. Fischer, B. J. Anderson,

G. Le, T. E. Moore, C. J. Pollock, B. L. Giles, J. C. Dorelli, L. Avanov, and Y. Saito. Whistler mode waves and Hall fields detected by MMS during a dayside magnetopause crossing. *Geophys. Res. Lett.*, 43:5943–5952, June 2016b. doi: 10.1002/2016GL068968.

D. Le Queau and A. Roux. Quasi-monochromatic wave-particle interactions in magnetospheric plasmas. *Solar Physics*, 111:59–80, March 1987. doi: 10.1007/BF00145441.

I. Lerche. Quasilinear Theory of Resonant Diffusion in a Magneto-Active, Relativistic Plasma. *Physics of Fluids*, 11, August 1968.

J. Li, J. Bortnik, L. Xie, Z. Pu, L. Chen, B. Ni, X. Tao, R. M. Thorne, S. Fu, Z. Yao, and R. Guo. Comparison of formulas for resonant interactions between energetic electrons and oblique whistler-mode waves. *Physics of Plasmas*, 22(5):052902, May 2015a. doi: 10.1063/1.4914852.

W. Li and M. K. Hudson. Earth's Van Allen Radiation Belts: From Discovery to the Van Allen Probes Era. *Journal of Geophysical Research (Space Physics)*, 124(11):8319–8351, Nov 2019. doi: 10.1029/2018JA025940.

W. Li, R. M. Thorne, V. Angelopoulos, J. Bortnik, C. M. Cully, B. Ni, O. LeContel, A. Roux, U. Auster, and W. Magnes. Global distribution of whistler-mode chorus waves observed on the THEMIS spacecraft. *Geophys. Res. Lett.*, 36:L09104, May 2009. doi: 10.1029/2009GL037595.

W. Li, R. M. Thorne, J. Bortnik, Y. Nishimura, V. Angelopoulos, L. Chen, J. P. McFadden, and J. W. Bonnell. Global distributions of suprathermal electrons observed on THEMIS and potential mechanisms for access into the plasmasphere. *J. Geophys. Res.*, 115:A00J10, December 2010a. doi: 10.1029/2010JA015687.

W. Li, R. M. Thorne, Y. Nishimura, J. Bortnik, V. Angelopoulos, J. P. McFadden, D. E. Larson, J. W. Bonnell, O. Le Contel, A. Roux, and U. Auster. THEMIS analysis of observed equatorial electron distributions responsible for the chorus excitation. *J. Geophys. Res.*, 115:A00F11, June 2010b. doi: 10.1029/2009JA014845.

W. Li, J. Bortnik, R. M. Thorne, and V. Angelopoulos. Global distribution of wave amplitudes and wave normal angles of chorus waves using THEMIS wave observations. *J. Geophys. Res.*, 116:A12205, December 2011a. doi: 10.1029/2011JA017035.

W. Li, R. M. Thorne, J. Bortnik, Y. Y. Shprits, Y. Nishimura, V. Angelopoulos, C. Chaston, O. Le Contel, and J. W. Bonnell. Typical properties of rising and falling tone chorus waves. *Geophys. Res. Lett.*, 38:L14103, July 2011b. doi: 10.1029/2011GL047925.

W. Li, B. Ni, R. M. Thorne, J. Bortnik, J. C. Green, C. A. Kletzing, W. S. Kurth, and G. B. Hospodarsky. Constructing the global distribution of chorus wave intensity using measurements of electrons by the POES satellites and waves by the Van Allen Probes. *Geophys. Res. Lett.*, 40:4526–4532, September 2013. doi: 10.1002/grl.50920.

W. Li, D. Mourenas, A. Artemyev, O. Agapitov, J. Bortnik, J. Albert, R. M. Thorne, B. Ni, C. A. Kletzing, W. S. Kurth, and G. B. Hospodarsky. Evidence of stronger pitch angle scattering loss caused by oblique whistler-mode waves as compared with quasi-parallel waves. *Geophys. Res. Lett.*, 41:6063–6070, 2014a. doi: 10.1002/2014GL061260.

W. Li, R. M. Thorne, Q. Ma, B. Ni, J. Bortnik, D. N. Baker, H. E. Spence, G. D. Reeves, S. G. Kanekal, J. C. Green, C. A. Kletzing, W. S. Kurth, G. B. Hospodarsky, J. B. Blake, J. F. Fennell, and S. G. Claudepierre. Radiation belt electron acceleration by chorus waves during the 17 March 2013 storm. *J. Geophys. Res.*, 119:4681–4693, June 2014b. doi: 10.1002/2014JA019945.

W. Li, R. M. Thorne, J. Bortnik, D. N. Baker, G. D. Reeves, S. G. Kanekal, H. E. Spence, and J. C. Green. Solar wind conditions leading to efficient radiation belt electron acceleration: A superposed epoch analysis. *Geophys. Res. Lett.*, 42:6906–6915, September 2015b. doi: 10.1002/2015GL065342.

W. Li, D. Mourenas, A. V. Artemyev, J. Bortnik, R. M. Thorne, C. A. Kletzing, W. S. Kurth, G. B. Hospodarsky, G. D. Reeves, H. O. Funsten, and H. E. Spence. Unraveling

the excitation mechanisms of highly oblique lower band chorus waves. *Geophys. Res. Lett.*, 43:8867–8875, September 2016a. doi: 10.1002/2016GL070386.

W. Li, O. Santolík, J. Bortnik, R. M. Thorne, C. A. Kletzing, W. S. Kurth, and G. B. Hospodarsky. New chorus wave properties near the equator from Van Allen Probes wave observations. *Geophys. Res. Lett.*, 43:4725–4735, May 2016b. doi: 10.1002/2016GL068780.

Wen Li, Q. Ma, X. C. Shen, X. J. Zhang, B. H. Mauk, G. Clark, F. Allegrini, W. S. Kurth, G. B. Hospodarsky, V. Hue, G. R. Gladstone, T. K. Greathouse, and S. J. Bolton. Quantification of Diffuse Auroral Electron Precipitation Driven by Whistler Mode Waves at Jupiter. *Geophys. Res. Lett.*, 48(19):e95457, October 2021. doi: 10.1029/2021GL095457.

M. D. Looper, J. B. Blake, and R. A. Mewaldt. Response of the inner radiation belt to the violent Sun-Earth connection events of October-November 2003. *Geophys. Res. Lett.*, 32 (3):L03S06, January 2005. doi: 10.1029/2004GL021502.

K. R. Lorentzen, J. B. Blake, U. S. Inan, and J. Bortnik. Observations of relativistic electron microbursts in association with VLF chorus. *J. Geophys. Res.*, 106(A4):6017–6028, April 2001. doi: 10.1029/2000JA003018.

L. R. Lyons and R. M. Thorne. Equilibrium structure of radiation belt electrons. *J. Geophys. Res.*, 78:2142–2149, May 1973. doi: 10.1029/JA078i013p02142.

L. R. Lyons and D. J. Williams. *Quantitative aspects of magnetospheric physics.* 1984.

L. R. Lyons, R. M. Thorne, and C. F. Kennel. Pitch-angle diffusion of radiation belt electrons within the plasmasphere. *J. Geophys. Res.*, 77:3455–3474, 1972. doi: 10.1029/JA077i019p03455.

Q. Ma, B. Ni, X. Tao, and R. M. Thorne. Evolution of the plasma sheet electron pitch angle distribution by whistler-mode chorus waves in non-dipole magnetic fields. *Annales Geophysicae*, 30:751–760, April 2012. doi: 10.5194/angeo-30-751-2012.

Q. Ma, W. Li, R. M. Thorne, B. Ni, C. A. Kletzing, W. S. Kurth, G. B. Hospodarsky, G. D. Reeves, M. G. Henderson, H. E. Spence, D. N. Baker, J. B. Blake, J. F. Fennell, S. G. Claudepierre, and V. Angelopoulos. Modeling inward diffusion and slow decay of energetic electrons in the Earth's outer radiation belt. *Geophys. Res. Lett.*, 42:987–995, February 2015. doi: 10.1002/2014GL062977.

Q. Ma, W. Li, R. M. Thorne, J. Bortnik, G. D. Reeves, C. A. Kletzing, W. S. Kurth, G. B. Hospodarsky, H. E. Spence, D. N. Baker, J. B. Blake, J. F. Fennell, S. G. Claudepierre, and V. Angelopoulos. Characteristic energy range of electron scattering due to plasmaspheric hiss. *J. Geophys. Res.*, 121:11, December 2016. doi: 10.1002/2016JA023311.

Q. Ma, A. V. Artemyev, D. Mourenas, W. Li, R. M. Thorne, C. A. Kletzing, W. S. Kurth, G. B. Hospodarsky, G. D. Reeves, H. E. Spence, and J. Wygant. Very Oblique Whistler Mode Propagation in the Radiation Belts: Effects of Hot Plasma and Landau Damping. *Geophys. Res. Lett.*, 44(24):12,057–12,066, December 2017. doi: 10.1002/2017GL075892.

Q. Ma, W. Li, J. Bortnik, R. M. Thorne, X. Chu, L. G. Ozeke, G. D. Reeves, C. A. Kletzing, W. S. Kurth, G. B. Hospodarsky, M. J. Engebretson, H. E. Spence, D. N. Baker, J. B. Blake, J. F. Fennell, and S. G. Claudepierre. Quantitative Evaluation of Radial Diffusion and Local Acceleration Processes During GEM Challenge Events. *Journal of Geophysical Research (Space Physics)*, 123(3):1938–1952, March 2018. doi: 10.1002/2017JA025114.

Q. Ma, W. Gu, S. G. Claudepierre, W. Li, J. Bortnik, M. Hua, and X. C. Shen. Electron Scattering by Very-Low-Frequency and Low-Frequency Waves From Ground Transmitters in the Earth's Inner Radiation Belt and Slot Region. *Journal of Geophysical Research (Space Physics)*, 127(6):e30349, June 2022. doi: 10.1029/2022JA030349.

D. M. Malaspina, A. Ukhorskiy, X. Chu, and J. Wygant. A Census of Plasma Waves and Structures Associated With an Injection Front in the Inner Magnetosphere. *J. Geophys. Res.*, 123:2566–2587, April 2018. doi: 10.1002/2017JA025005.

David M. Malaspina, Allison N. Jaynes, George Hospodarsky, Jacob Bortnik, Robert E.

Ergun, and John Wygant. Statistical properties of low-frequency plasmaspheric hiss. *Journal of Geophysical Research (Space Physics)*, 122(8):8340–8352, August 2017. doi: 10.1002/2017JA024328.

R. A. Marshall and J. Bortnik. Pitch Angle Dependence of Energetic Electron Precipitation: Energy Deposition, Backscatter, and the Bounce Loss Cone. *J. Geophys. Res.*, 123: 2412–2423, 2018. doi: 10.1002/2017JA024873.

Claudia Martinez-Calderon, Kazuo Shiokawa, Yoshizumi Miyoshi, Mitsunori Ozaki, Ian Schofield, and Martin Connors. Statistical study of ELF/VLF emissions at subauroral latitudes in Athabasca, Canada. *Journal of Geophysical Research (Space Physics)*, 120 (10):8455–8469, October 2015. doi: 10.1002/2015JA021347.

Claudia Martinez-Calderon, Kazuo Shiokawa, Yoshizumi Miyoshi, Kunihiro Keika, Mitsunori Ozaki, Ian Schofield, Martin Connors, Craig Kletzing, Miroslav Hanzelka, Ondrej Santolík, and William S. Kurth. ELF/VLF wave propagation at subauroral latitudes: Conjugate observation between the ground and Van Allen Probes A. *Journal of Geophysical Research (Space Physics)*, 121(6):5384–5393, June 2016. doi: 10.1002/2015JA022264.

Claudia Martinez-Calderon, Yuto Katoh, Jyrki Manninen, Yoshiya Kasahara, Shoya Matsuda, Atsushi Kumamoto, Fuminori Tsuchiya, Ayako Matsuoka, Masafumi Shoji, Mariko Teramoto, Iku Shinohara, Kazuo Shiokawa, and Yoshizumi Miyoshi. Conjugate Observations of Dayside and Nightside VLF Chorus and QP Emissions Between Arase (ERG) and Kannuslehto, Finland. *Journal of Geophysical Research (Space Physics)*, 125(1):e26663, January 2020. doi: 10.1029/2019JA026663.

B. H. Mauk, N. J. Fox, S. G. Kanekal, R. L. Kessel, D. G. Sibeck, and A. Ukhorskiy. Science Objectives and Rationale for the Radiation Belt Storm Probes Mission. *Space Sci. Rev.*, 179:3–27, November 2013. doi: 10.1007/s11214-012-9908-y.

A. S. Maxworth and M. Golkowski. Magnetospheric whistler mode ray tracing in a warm background plasma with finite electron and ion temperature. *J. Geophys. Res.*, 122(7):

7323–7335, 2017. ISSN 2169-9402. doi: 10.1002/2016JA023546. URL http://dx.doi.org/10.1002/2016JA023546.

J. P. McFadden, C. W. Carlson, D. Larson, M. Ludlam, R. Abiad, B. Elliott, P. Turin, M. Marckwordt, and V. Angelopoulos. The THEMIS ESA Plasma Instrument and In-flight Calibration. *Space Sci. Rev.*, 141:277–302, December 2008. doi: 10.1007/s11214-008-9440-2.

V. F. Melnikov and L. V. Filatov. Conditions for Whistler Generation by Nonthermal Electrons in Flare Loops. *Geomagnetism and Aeronomy*, 60(8):1126–1131, December 2020. doi: 10.1134/S0016793220080150.

J. D. Menietti, T. F. Averkamp, W. S. Kurth, M. Imai, J. B. Faden, G. B. Hospodarsky, O. Santolik, G. Clark, F. Allegrini, S. S. Elliott, A. H. Sulaiman, and S. J. Bolton. Analysis of Whistler-Mode and Z-Mode Emission in the Juno Primary Mission. *Journal of Geophysical Research (Space Physics)*, 126(11):e29885, November 2021. doi: 10.1029/2021JA029885.

N. P. Meredith, R. B. Horne, and R. R. Anderson. Substorm dependence of chorus amplitudes: Implications for the acceleration of electrons to relativistic energies. *J. Geophys. Res.*, 106:13165–13178, July 2001. doi: 10.1029/2000JA900156.

N. P. Meredith, R. B. Horne, R. H. A. Iles, R. M. Thorne, D. Heynderickx, and R. R. Anderson. Outer zone relativistic electron acceleration associated with substorm-enhanced whistler mode chorus. *J. Geophys. Res.*, 107:1144, July 2002. doi: 10.1029/2001JA900146.

N. P. Meredith, R. B. Horne, R. M. Thorne, and R. R. Anderson. Favored regions for chorus-driven electron acceleration to relativistic energies in the Earth's outer radiation belt. *Geophys. Res. Lett.*, 30(16):1871, August 2003. doi: 10.1029/2003GL017698.

N. P. Meredith, R. B. Horne, A. Sicard-Piet, D. Boscher, K. H. Yearby, W. Li, and R. M. Thorne. Global model of lower band and upper band chorus from multiple satellite observations. *J. Geophys. Res.*, 117:A10225, October 2012. doi: 10.1029/2012JA017978.

N. P. Meredith, R. B. Horne, X.-C. Shen, W. Li, and J. Bortnik. Global model of whistler mode chorus in the near-equatorial region ($|\lambda_m| < 18°$). *Geophys. Res. Lett.*, 47: e2020GL087311, 2020. doi: 10.1029/2020GL087311.

A. Micera, A. N. Zhukov, R. A. López, M. E. Innocenti, M. Lazar, E. Boella, and G. Lapenta. Particle-in-cell Simulation of Whistler Heat-flux Instabilities in the Solar Wind: Heat-flux Regulation and Electron Halo Formation. *Astrophys. J. Lett.*, 903(1):L23, November 2020. doi: 10.3847/2041-8213/abc0e8.

R. M. Millan and D. N. Baker. Acceleration of Particles to High Energies in Earth's Radiation Belts. *Space Sci. Rev.*, 173:103–131, November 2012. doi: 10.1007/s11214-012-9941-x.

R. M. Millan and R. M. Thorne. Review of radiation belt relativistic electron losses. *Journal of Atmospheric and Solar-Terrestrial Physics*, 69:362–377, March 2007. doi: 10.1016/j.jastp.2006.06.019.

Robyn Millan, Thomas Sotirelis, Aleksandr Ukhorskiy, Wen Li, John Sample, Leslie Woodger, and Arlo Johnson. The Relativistic Electron Atmospheric Loss (REAL) CubeSat. In *42nd COSPAR Scientific Assembly*, volume 42, pages PRBEM.2–3–18, July 2018.

K. Min, K. Liu, and W. Li. Signatures of electron Landau resonant interactions with chorus waves from THEMIS observations. *J. Geophys. Res.*, 119:5551–5560, July 2014. doi: 10.1002/2014JA019903.

Y. Miyoshi, Y. Kasaba, I. Shinohara, T. Takashima, K. Asamura, H. Matsumoto, N. Higashio, T. Mitani, S. Kasahara, S. Yokota, S. Wang, Y. Kazama, Y. Kasahara, S. Yagitani, A. Matsuoka, H. Kojima, Y. Katoh, K. Shiokawa, K. Seki, M. Fujimoto, T. Ono, and ERG project Group. Geospace exploration project: Arase (ERG). In *Journal of Physics Conference Series*, volume 869 of *Journal of Physics Conference Series*, page 012095, June 2017. doi: 10.1088/1742-6596/869/1/012095.

Y. Miyoshi, S. Saito, S. Kurita, K. Asamura, K. Hosokawa, T. Sakanoi, T. Mitani, Y. Ogawa, S. Oyama, F. Tsuchiya, S. L. Jones, A. N. Jaynes, and J. B. Blake. Relativistic Electron

Microbursts as High-Energy Tail of Pulsating Aurora Electrons. *Geophys. Res. Lett.*, 47 (21):e90360, November 2020. doi: 10.1029/2020GL090360.

Y. Miyoshi, S. Hosokawa, S.-I. Kurita, Y. Oyama, S. Ogawa, I. Saito, A. Shinohara, E. Kero, P. T. Turunen, S. Verronen, S. Kasahara, T. Yokota, T. Mitani, N. Takashima, Y. Higashio, S. Kasahara, F. Masuda, A. Tsuchiya, A. Kumamoto, T. Matsuoka, K. Hori, M. Keika, M. Shoji, S. Teramoto, C. Imajo, Jun, S., and Nakamura. Penetration of MeV electrons into the mesosphere accompanying pulsating aurorae. *Scientific Reports*, 11:13724, 2021. doi: 10.1038/s41598-021-92611-3.

D. Mourenas and J.-F. Ripoll. Analytical estimates of quasi-linear diffusion coefficients and electron lifetimes in the inner radiation belt. *J. Geophys. Res.*, 117:A01204, 2012. doi: 10.1029/2011JA016985.

D. Mourenas, A. Artemyev, O. Agapitov, and V. Krasnoselskikh. Acceleration of radiation belts electrons by oblique chorus waves. *J. Geophys. Res.*, 117:A10212, October 2012a. doi: 10.1029/2012JA018041.

D. Mourenas, A. V. Artemyev, J.-F. Ripoll, O. V. Agapitov, and V. V. Krasnoselskikh. Timescales for electron quasi-linear diffusion by parallel and oblique lower-band Chorus waves. *J. Geophys. Res.*, 117:A06234, 2012b. doi: 10.1029/2012JA017717.

D. Mourenas, A. V. Artemyev, O. V. Agapitov, and V. Krasnoselskikh. Consequences of geomagnetic activity on energization and loss of radiation belt electrons by oblique chorus waves. *J. Geophys. Res.*, 119:2775–2796, April 2014a. doi: 10.1002/2013JA019674.

D. Mourenas, A. V. Artemyev, O. V. Agapitov, V. Krasnoselskikh, and W. Li. Approximate analytical solutions for the trapped electron distribution due to quasi-linear diffusion by whistler mode waves. *J. Geophys. Res.*, 119:9962–9977, December 2014b. doi: 10.1002/2014JA020443.

D. Mourenas, A. V. Artemyev, O. V. Agapitov, V. Krasnoselskikh, and F. S. Mozer. Very

oblique whistler generation by low-energy electron streams. *J. Geophys. Res.*, 120:3665–3683, 2015. doi: 10.1002/2015JA021135.

D. Mourenas, A. V. Artemyev, O. V. Agapitov, F. S. Mozer, and V. V. Krasnoselskikh. Equatorial electron loss by double resonance with oblique and parallel intense chorus waves. *J. Geophys. Res.*, 121:4498–4517, May 2016. doi: 10.1002/2015JA022223.

D. Mourenas, Q. Ma, A. V. Artemyev, and W. Li. Scaling laws for the inner structure of the radiation belts. *Geophys. Res. Lett.*, 44:3009–3018, April 2017. doi: 10.1002/2017GL072987.

D. Mourenas, X.-J. Zhang, A. V. Artemyev, V. Angelopoulos, R. M. Thorne, J. Bortnik, A. I. Neishtadt, and A. A. Vasiliev. Electron Nonlinear Resonant Interaction With Short and Intense Parallel Chorus Wave Packets. *J. Geophys. Res.*, 123:4979–4999, June 2018. doi: 10.1029/2018JA025417.

D. Mourenas, A. V. Artemyev, X. J. Zhang, V. Angelopoulos, E. Tsai, and C. Wilkins. Electron Lifetimes and Diffusion Rates Inferred From ELFIN Measurements at Low Altitude: First Results. *Journal of Geophysical Research (Space Physics)*, 126(11):e29757, November 2021. doi: 10.1029/2021JA029757.

D. Mourenas, A. V. Artemyev, X. J. Zhang, and V. Angelopoulos. Extreme Energy Spectra of Relativistic Electron Flux in the Outer Radiation Belt. *Journal of Geophysical Research (Space Physics)*, 127(11):e2022JA031038, November 2022a. doi: 10.1029/2022JA031038.

D. Mourenas, X. J. Zhang, D. Nunn, A. V. Artemyev, V. Angelopoulos, E. Tsai, and C. Wilkins. Short Chorus Wave Packets: Generation Within Chorus Elements, Statistics, and Consequences on Energetic Electron Precipitation. *Journal of Geophysical Research (Space Physics)*, 127(5):e30310, May 2022b. doi: 10.1029/2022JA030310.

D. Mourenas, A. V. Artemyev, X. J. Zhang, and V. Angelopoulos. Upper Limit on Outer Radiation Belt Electron Flux Based on Dynamical Equilibrium. *Journal of Geophysical Research (Space Physics)*, 128(8):e2023JA031676, August 2023. doi: 10.1029/2023JA031676.

F. S. Mozer, O. Agapitov, A. Artemyev, J. F. Drake, V. Krasnoselskikh, S. Lejosne, and I. Vasko. Time domain structures: What and where they are, what they do, and how they are made. *Geophys. Res. Lett.*, 42:3627–3638, 2015. doi: 10.1002/2015GL063946.

B. Ni, R. M. Thorne, Y. Y. Shprits, and J. Bortnik. Resonant scattering of plasma sheet electrons by whistler-mode chorus: Contribution to diffuse auroral precipitation. *Geophys. Res. Lett.*, 35:L11106, June 2008. doi: 10.1029/2008GL034032.

B. Ni, R. M. Thorne, N. P. Meredith, Y. Y. Shprits, and R. B. Horne. Diffuse auroral scattering by whistler mode chorus waves: Dependence on wave normal angle distribution. *J. Geophys. Res.*, 116:A10207, October 2011. doi: 10.1029/2011JA016517.

B. Ni, W. Li, R. M. Thorne, J. Bortnik, J. C. Green, C. A. Kletzing, W. S. Kurth, G. B. Hospodarsky, and M. Soria-Santacruz Pich. A novel technique to construct the global distribution of whistler mode chorus wave intensity using low-altitude POES electron data. *J. Geophys. Res.*, 119:5685–5699, July 2014. doi: 10.1002/2014JA019935.

B. Ni, R. M. Thorne, X. Zhang, J. Bortnik, Z. Pu, L. Xie, Z.-j. Hu, D. Han, R. Shi, C. Zhou, and X. Gu. Origins of the Earth's Diffuse Auroral Precipitation. *Space Sci. Rev.*, 200: 205–259, April 2016. doi: 10.1007/s11214-016-0234-7.

Y. Nishimura, J. Bortnik, W. Li, R. M. Thorne, L. R. Lyons, V. Angelopoulos, S. B. Mende, J. W. Bonnell, O. Le Contel, C. Cully, R. Ergun, and U. Auster. Identifying the Driver of Pulsating Aurora. *Science*, 330:81–84, October 2010. doi: 10.1126/science.1193186.

Yukitoshi Nishimura, Marc R. Lessard, Yuto Katoh, Yoshizumi Miyoshi, Eric Grono, Noora Partamies, Nithin Sivadas, Keisuke Hosokawa, Mizuki Fukizawa, Marilia Samara, Robert G. Michell, Ryuho Kataoka, Takeshi Sakanoi, Daniel K. Whiter, Shin-ichiro Oyama, Yasunobu Ogawa, and Satoshi Kurita. Diffuse and Pulsating Aurora. *Space Sci. Rev.*, 216(1):4, January 2020. doi: 10.1007/s11214-019-0629-3.

D. Nunn. Wave-particle interactions in electrostatic waves in an inhomogeneous medium. *Journal of Plasma Physics*, 6:291, October 1971. doi: 10.1017/S0022377800006061.

D. Nunn, X. J. Zhang, D. Mourenas, and A. V. Artemyev. Generation of Realistic Short Chorus Wave Packets. *Geophys. Res. Lett.*, 48(7):e92178, April 2021. doi: 10.1029/2020GL092178.

T. P. O'Brien and M. B. Moldwin. Empirical plasmapause models from magnetic indices. *Geophys. Res. Lett.*, 30:1152, February 2003. doi: 10.1029/2002GL016007.

T. P. O'Brien, M. D. Looper, and J. B. Blake. Quantification of relativistic electron microburst losses during the GEM storms. *Geophys. Res. Lett.*, 31(4):L04802, February 2004. doi: 10.1029/2003GL018621.

M. Oka, F. Otsuka, S. Matsukiyo, III Wilson, L. B., M. R. Argall, T. Amano, T. D. Phan, M. Hoshino, O. Le Contel, D. J. Gershman, J. L. Burch, R. B. Torbert, J. C. Dorelli, B. L. Giles, R. E. Ergun, C. T. Russell, and P. A. Lindqvist. Electron Scattering by Low-frequency Whistler Waves at Earth's Bow Shock. *Astrophys. J.*, 886(1):53, November 2019. doi: 10.3847/1538-4357/ab4a81.

L. Olifer, I. R. Mann, A. J. Boyd, L. G. Ozeke, and D. Choi. On the Role of Last Closed Drift Shell Dynamics in Driving Fast Losses and Van Allen Radiation Belt Extinction. *J. Geophys. Res.*, 123:3692–3703, May 2018. doi: 10.1029/2018JA025190.

Y. Omura, N. Furuya, and D. Summers. Relativistic turning acceleration of resonant electrons by coherent whistler mode waves in a dipole magnetic field. *J. Geophys. Res.*, 112: A06236, June 2007. doi: 10.1029/2006JA012243.

Y. Omura, Y. Katoh, and D. Summers. Theory and simulation of the generation of whistler-mode chorus. *J. Geophys. Res.*, 113:A04223, April 2008. doi: 10.1029/2007JA012622.

Y. Omura, Y. Miyashita, M. Yoshikawa, D. Summers, M. Hikishima, Y. Ebihara, and Y. Kubota. Formation process of relativistic electron flux through interaction with chorus emissions in the Earth's inner magnetosphere. *J. Geophys. Res.*, 120:9545–9562, November 2015. doi: 10.1002/2015JA021563.

K. G. Orlova and Y. Y. Shprits. On the bounce-averaging of scattering rates and the calculation of bounce period. *Physics of Plasmas*, 18(9):092904, September 2011. doi: 10.1063/1.3638137.

D. L. Pasmanik and V. Y. Trakhtengerts. Dispersion properties of ducted whistlers, generated by lightning discharge. *Annales Geophysicae*, 23(4):1433–1439, June 2005. doi: 10.5194/angeo-23-1433-2005.

Christopher Rackauckas and Qing Nie. Differentialequations.jl–a performant and feature-rich ecosystem for solving differential equations in julia. *Journal of Open Research Software*, 5(1), 2017.

G. T. Roberg-Clark, O. Agapitov, J. F. Drake, and M. Swisdak. Scattering of Energetic Electrons by Heat-flux-driven Whistlers in Flares. *Astrophys. J.*, 887(2):190, December 2019. doi: 10.3847/1538-4357/ab5114.

A. Runov, V. Angelopoulos, C. Gabrielse, J. Liu, D. L. Turner, and X.-Z. Zhou. Average thermodynamic and spectral properties of plasma in and around dipolarizing flux bundles. *J. Geophys. Res.*, 120:4369–4383, June 2015. doi: 10.1002/2015JA021166.

C. T. Russell, B. J. Anderson, W. Baumjohann, K. R. Bromund, D. Dearborn, D. Fischer, G. Le, H. K. Leinweber, D. Leneman, W. Magnes, J. D. Means, M. B. Moldwin, R. Nakamura, D. Pierce, F. Plaschke, K. M. Rowe, J. A. Slavin, R. J. Strangeway, R. Torbert, C. Hagen, I. Jernej, A. Valavanoglou, and I. Richter. The Magnetospheric Multiscale Magnetometers. *Space Sci. Rev.*, 199:189–256, March 2016. doi: 10.1007/s11214-014-0057-3.

R. Z. Sagdeev and V. D. Shafranov. On the Instability of a Plasma with an Anisotropic Distribution of Velocities in a Magnetic Field. *Soviet Phys. JETP*, 12(1):130–132, 1961.

Hirobumi Saito, Masafumi Hirahara, Takahide Mizuno, Seisuke Fukuda, Yousuke Fukushima, Kazushi Asamura, Hiroyuki Nagamatsu, Koji Tanaka, Yoshitsugu Sone, Nobukatsu Okuizumi, Makoto Mita, Masatoshi Uno, Yoshimitsu Yanagawa, Takuya Takahara, Ryosuke Kaneda, Takashi Honma, Takeshi Sakanoi, Akira Miura, Toshinori Ikenaga,

Keita Ogawa, and Yasunari Masumoto. Small satellite reimei for auroral observations. *Acta Astronautica*, 69(7):499–513, 2011. ISSN 0094-5765. doi: https://doi.org/10.1016/j.actaastro.2011.05.007. URL https://www.sciencedirect.com/science/article/pii/S0094576511001366.

O. Santolík, D. A. Gurnett, J. S. Pickett, M. Parrot, and N. Cornilleau-Wehrlin. Spatio-temporal structure of storm-time chorus. *J. Geophys. Res.*, 108:1278, July 2003. doi: 10.1029/2002JA009791.

O. Santolík, D. A. Gurnett, J. S. Pickett, J. Chum, and N. Cornilleau-Wehrlin. Oblique propagation of whistler mode waves in the chorus source region. *J. Geophys. Res.*, 114: A00F03, December 2009. doi: 10.1029/2009JA014586.

O. Santolík, C. A. Kletzing, W. S. Kurth, G. B. Hospodarsky, and S. R. Bounds. Fine structure of large-amplitude chorus wave packets. *Geophys. Res. Lett.*, 41:293–299, January 2014a. doi: 10.1002/2013GL058889.

O. Santolík, E. Macúšová, I. Kolmašová, N. Cornilleau-Wehrlin, and Y. Conchy. Propagation of lower-band whistler-mode waves in the outer Van Allen belt: Systematic analysis of 11 years of multi-component data from the Cluster spacecraft. *Geophys. Res. Lett.*, 41: 2729–2737, April 2014b. doi: 10.1002/2014GL059815.

K. Sauer, K. Baumgaerte, and R. D. Sydora. Gap formation around $\omega_e/2$ and generation of low-band whistler waves by landau-resonant electrons in the magnetosphere: Predictions from dispersion theory. *Earth and Planetary Physics*, 4:138, 2020. ISSN 2096-3955. doi: 10.26464/epp2020020. URL http://eppcgs.xml-journal.net//article/id/3c6a82bf-66b3-436e-94ce-bc744f2e3c29.

M. Schulz and L. J. Lanzerotti. *Particle diffusion in the radiation belts*. Springer, New York, 1974.

V. A. Sergeev, E. M. Sazhina, N. A. Tsyganenko, J. A. Lundblad, and F. Soraas. Pitch-angle scattering of energetic protons in the magnetotail current sheet as the dominant source of

their isotropic precipitation into the nightside ionosphere. *Plan. Sp. Sci.*, 31:1147–1155, October 1983. doi: 10.1016/0032-0633(83)90103-4.

V. A. Sergeev, M. Malkov, and K. Mursula. Testing the isotropic boundary algorithm method to evaluate the magnetic field configuration in the tail. *J. Geophys. Res.*, 98(A5): 7609–7620, May 1993. doi: 10.1029/92JA02587.

B. W. Sheeley, M. B. Moldwin, H. K. Rassoul, and R. R. Anderson. An empirical plasmasphere and trough density model: CRRES observations. *J. Geophys. Res.*, 106:25631–25642, November 2001. doi: 10.1029/2000JA000286.

Xiao-Chen Shen, Wen Li, Luisa Capannolo, Qianli Ma, Murong Qin, Anton V. Artemyev, Vassilis Angelopoulos, Xiao-Jia Zhang, and Sheng Huang. Modulation of Energetic Electron Precipitation Driven by Three Types of Whistler Mode Waves. *Geophys. Res. Lett.*, 50(8):e2022GL101682, April 2023a. doi: 10.1029/2022GL101682.

Yangyang Shen, Lunjin Chen, Xiao-Jia Zhang, Anton Artemyev, Vassilis Angelopoulos, Christopher M. Cully, H. Gordon James, Andrew W. Yau, Andrew D. Howarth, Jacob Bortnik, Jiashu Wu, Sheng Tian, Michael D. Hartinger, Martin Connors, and Richard B. Horne. Conjugate Observation of Magnetospheric Chorus Propagating to the Ionosphere by Ducting. *Geophys. Res. Lett.*, 48(23):e95933, December 2021. doi: 10.1029/2021GL095933.

Yangyang Shen, Anton V. Artemyev, Qianli Ma, Xiao-Jia Zhang, Didier Mourenas, Ethan Tsai, Colin Wilkins, Jiashu Wu, and Vassilis Angelopoulos. Inner Belt Wisp Precipitation Measured by ELFIN: Regimes of Energetic Electron Scattering by VLF Transmitter Waves. *Journal of Geophysical Research (Space Physics)*, 127(11):e2022JA030968, November 2022a. doi: 10.1029/2022JA030968.

Yangyang Shen, Anton V. Artemyev, Xiao-Jia Zhang, Vassilis Angelopoulos, Ivan Vasko, Drew Turner, Ethan Tsai, Colin Wilkins, James M. Weygand, Christopher T. Russell, Robert E. Ergun, and Barbara L. Giles. Tens to Hundreds of keV Electron Precipitation

Driven by Kinetic Alfvén Waves During an Electron Injection. *Journal of Geophysical Research (Space Physics)*, 127(8):e30360, August 2022b. doi: 10.1029/2022JA030360.

Yangyang Shen, Anton V. Artemyev, Xiao-Jia Zhang, Ying Zou, Vassilis Angelopoulos, Ivan Vasko, Andrei Runov, Ethan Tsai, and Colin Wilkins. Contribution of Kinetic Alfvén Waves to Energetic Electron Precipitation From the Plasma Sheet During a Substorm. *Journal of Geophysical Research (Space Physics)*, 128(4):e2023JA031350, April 2023b. doi: 10.1029/2023JA031350.

Run Shi, Danny Summers, Binbin Ni, Joseph F. Fennell, J. Bernard Blake, Harlan E. Spence, and Geoffrey D. Reeves. Survey of radiation belt energetic electron pitch angle distributions based on the Van Allen Probes MagEIS measurements. *Journal of Geophysical Research (Space Physics)*, 121(2):1078–1090, February 2016. doi: 10.1002/2015JA021724.

Xiaofei Shi, Terry Z. Liu, Vassilis Angelopoulos, and Xiao-Jia Zhang. Whistler Mode Waves in the Compressional Boundary of Foreshock Transients. *Journal of Geophysical Research (Space Physics)*, 125(8):e27758, August 2020. doi: 10.1029/2019JA027758.

Xiaofei Shi, Xiao-Jia Zhang, Anton Artemyev, Vassilis Angelopoulos, Michael D. Hartinger, Ethan Tsai, and Colin Wilkins. On the Role of ULF Waves in the Spatial and Temporal Periodicity of Energetic Electron Precipitation. *Journal of Geophysical Research (Space Physics)*, 127(12):e2022JA030932, December 2022. doi: 10.1029/2022JA030932.

D. R. Shklyar. Stochastic motion of relativistic particles in the field of a monochromatic wave. *Sov. Phys. JETP*, 53:1197–1192, 1981.

D. R. Shklyar and H. Matsumoto. Oblique Whistler-Mode Waves in the Inhomogeneous Magnetospheric Plasma: Resonant Interactions with Energetic Charged Particles. *Surveys in Geophysics*, 30:55–104, April 2009. doi: 10.1007/s10712-009-9061-7.

David R. Shklyar. A Theory of Interaction Between Relativistic Electrons and Magnetospherically Reflected Whistlers. *Journal of Geophysical Research (Space Physics)*, 126(2): e28799, February 2021. doi: 10.1029/2020JA028799.

Y. Y. Shprits and B. Ni. Dependence of the quasi-linear scattering rates on the wave normal distribution of chorus waves. *J. Geophys. Res.*, 114:A11205, November 2009. doi: 10.1029/2009JA014223.

Y. Y. Shprits, R. M. Thorne, R. Friedel, G. D. Reeves, J. Fennell, D. N. Baker, and S. G. Kanekal. Outward radial diffusion driven by losses at magnetopause. *J. Geophys. Res.*, 111:A11214, November 2006a. doi: 10.1029/2006JA011657.

Y. Y. Shprits, R. M. Thorne, R. B. Horne, and D. Summers. Bounce-averaged diffusion coefficients for field-aligned chorus waves. *J. Geophys. Res.*, 111:A10225, October 2006b. doi: 10.1029/2006JA011725.

Y. Y. Shprits, S. R. Elkington, N. P. Meredith, and D. A. Subbotin. Review of modeling of losses and sources of relativistic electrons in the outer radiation belt I: Radial transport. *Journal of Atmospheric and Solar-Terrestrial Physics*, 70:1679–1693, November 2008a. doi: 10.1016/j.jastp.2008.06.008.

Y. Y. Shprits, D. A. Subbotin, N. P. Meredith, and S. R. Elkington. Review of modeling of losses and sources of relativistic electrons in the outer radiation belt II: Local acceleration and loss. *Journal of Atmospheric and Solar-Terrestrial Physics*, 70:1694–1713, November 2008b. doi: 10.1016/j.jastp.2008.06.014.

Mykhaylo Shumko, Drew L. Turner, T. P. O'Brien, Seth G. Claudepierre, John Sample, D. P. Hartley, Joseph Fennel, J. Bernard Blake, Matina Gkioulidou, and Donald G. Mitchell. Evidence of Microbursts Observed Near the Equatorial Plane in the Outer Van Allen Radiation Belt. *Geophys. Res. Lett.*, 45(16):8044–8053, August 2018. doi: 10.1029/2018GL078451.

Laura E. Simms, Mark J. Engebretson, Mark A. Clilverd, and Craig J. Rodger. Ground-Based Observations of VLF Waves as a Proxy for Satellite Observations: Development of Models Including the Influence of Solar Illumination and Geomagnetic Disturbance

Levels. *Journal of Geophysical Research (Space Physics)*, 124(4):2682–2696, April 2019. doi: 10.1029/2018JA026407.

M. I. Sitnov, G. K. Stephens, N. A. Tsyganenko, Y. Miyashita, V. G. Merkin, T. Motoba, S. Ohtani, and K. J. Genestreti. Signatures of Nonideal Plasma Evolution During Substorms Obtained by Mining Multimission Magnetometer Data. *Journal of Geophysical Research (Space Physics)*, 124(11):8427–8456, Nov 2019. doi: 10.1029/2019JA027037.

B. U. Ö. Sonnerup and L. J. Cahill, Jr. Explorer 12 observations of the magnetopause current layer. *J. Geophys. Res.*, 73:1757, March 1968. doi: 10.1029/JA073i005p01757.

G. K. Stephens, M. I. Sitnov, H. Korth, N. A. Tsyganenko, S. Ohtani, M. Gkioulidou, and A. Y. Ukhorskiy. Global Empirical Picture of Magnetospheric Substorms Inferred From Multimission Magnetometer Data. *Journal of Geophysical Research (Space Physics)*, 124 (2):1085–1110, Feb 2019. doi: 10.1029/2018JA025843.

T. H. Stix. *The Theory of Plasma Waves*. 1962.

L. R. O. Storey. An Investigation of Whistling Atmospherics. *Philosophical Transactions of the Royal Society of London Series A*, 246(908):113–141, Jul 1953. doi: 10.1098/rsta.1953.0011.

Anatoly V. Streltsov and Miles T. Bengtson. Observations and Modeling of Whistler Mode Waves in the Magnetospheric Density Ducts. *Journal of Geophysical Research (Space Physics)*, 125(10):e28398, October 2020. doi: 10.1029/2020JA028398.

D. Summers and B. Ni. Effects of latitudinal distributions of particle density and wave power on cyclotron resonant diffusion rates of radiation belt electrons. *Earth, Planets, and Space*, 60:763–771, July 2008.

D. Summers, C. Ma, N. P. Meredith, R. B. Horne, R. M. Thorne, and R. R. Anderson. Modeling outer-zone relativistic electron response to whistler-mode chorus activity during substorms. *Journal of Atmospheric and Solar-Terrestrial Physics*, 66:133–146, January 2004. doi: 10.1016/j.jastp.2003.09.013.

D. Summers, B. Ni, and N. P. Meredith. Timescales for radiation belt electron acceleration and loss due to resonant wave-particle interactions: 2. Evaluation for VLF chorus, ELF hiss, and electromagnetic ion cyclotron waves. *J. Geophys. Res.*, 112:A04207, April 2007a. doi: 10.1029/2006JA011993.

D. Summers, B. Ni, and N. P. Meredith. Timescales for radiation belt electron acceleration and loss due to resonant wave-particle interactions: 1. Theory. *J. Geophys. Res.*, 112: A04206, April 2007b. doi: 10.1029/2006JA011801.

X. Tao and J. Bortnik. Nonlinear interactions between relativistic radiation belt electrons and oblique whistler mode waves. *Nonlinear Processes in Geophysics*, 17:599–604, October 2010. doi: 10.5194/npg-17-599-2010.

X. Tao, R. M. Thorne, W. Li, B. Ni, N. P. Meredith, and R. B. Horne. Evolution of electron pitch angle distributions following injection from the plasma sheet. *J. Geophys. Res.*, 116: A04229, April 2011. doi: 10.1029/2010JA016245.

X. Tao, J. Bortnik, J. M. Albert, and R. M. Thorne. Comparison of bounce-averaged quasi-linear diffusion coefficients for parallel propagating whistler mode waves with test particle simulations. *J. Geophys. Res.*, 117:A10205, October 2012a. doi: 10.1029/2012JA017931.

X. Tao, J. Bortnik, R. M. Thorne, J. M. Albert, and W. Li. Effects of amplitude modulation on nonlinear interactions between electrons and chorus waves. *Geophys. Res. Lett.*, 39: L06102, March 2012b. doi: 10.1029/2012GL051202.

X. Tao, J. Bortnik, J. M. Albert, R. M. Thorne, and W. Li. The importance of amplitude modulation in nonlinear interactions between electrons and large amplitude whistler waves. *Journal of Atmospheric and Solar-Terrestrial Physics*, 99:67–72, July 2013. doi: 10.1016/j.jastp.2012.05.012.

Xin Tao, Fulvio Zonca, and Liu Chen. Identify the nonlinear wave-particle interaction regime in rising tone chorus generation. *Geophys. Res. Lett.*, 44(8):3441–3446, 2017. ISSN 1944-8007. doi: 10.1002/2017GL072624. URL http://dx.doi.org/10.1002/2017GL072624.

R. M. Thorne. The importance of energetic particle precipitation on the chemical composition of the middle atmosphere. *Pure and Applied Geophysics*, 118(1):128–151, March 1980. doi: 10.1007/BF01586448.

R. M. Thorne. Radiation belt dynamics: The importance of wave-particle interactions. *Geophys. Res. Lett.*, 372:L22107, November 2010. doi: 10.1029/2010GL044990.

R. M. Thorne, T. P. O'Brien, Y. Y. Shprits, D. Summers, and R. B. Horne. Timescale for MeV electron microburst loss during geomagnetic storms. *J. Geophys. Res.*, 110:A09202, September 2005. doi: 10.1029/2004JA010882.

R. M. Thorne, B. Ni, X. Tao, R. B. Horne, and N. P. Meredith. Scattering by chorus waves as the dominant cause of diffuse auroral precipitation. *Nature*, 467:943–946, October 2010. doi: 10.1038/nature09467.

R. M. Thorne, W. Li, B. Ni, Q. Ma, J. Bortnik, L. Chen, D. N. Baker, H. E. Spence, G. D. Reeves, M. G. Henderson, C. A. Kletzing, W. S. Kurth, G. B. Hospodarsky, J. B. Blake, J. F. Fennell, S. G. Claudepierre, and S. G. Kanekal. Rapid local acceleration of relativistic radiation-belt electrons by magnetospheric chorus. *Nature*, 504:411–414, December 2013. doi: 10.1038/nature12889.

Richard M. Thorne, Jacob Bortnik, Wen Li, and Qianli Ma. *Wave–Particle Interactions in the Earth's Magnetosphere*, chapter 6, pages 93–108. American Geophysical Union (AGU), 2021. ISBN 9781119815624. doi: https://doi.org/10.1002/9781119815624.ch6.

E. E. Titova, B. V. Kozelov, A. G. Demekhov, J. Manninen, O. Santolík, C. A. Kletzing, and G. Reeves. Identification of the source of quasi-periodic VLF emissions using ground-based and Van Allen Probes satellite observations. *Geophys. Res. Lett.*, 2015. doi: 10.1002/2015GL064911.

E. E. Titova, A. G. Demekhov, J. Manninen, D. L. Pasmanik, and A. V. Larchenko. Localization of the sources of narrow-band noise VLF emissions in the range 4-10 kHz from

simultaneous ground-based and Van Allen Probes satellite observations. *Geomagnetism and Aeronomy*, 57(6):706–718, November 2017. doi: 10.1134/S0016793217060135.

Yuguang Tong, Ivan Y. Vasko, Anton V. Artemyev, Stuart D. Bale, and Forrest S. Mozer. Statistical Study of Whistler Waves in the Solar Wind at 1 au. *Astrophys. J.*, 878(1):41, Jun 2019. doi: 10.3847/1538-4357/ab1f05.

V. Y. Trakhtengerts and M. J. Rycroft. *Whistler and Alfvén Mode Cyclotron Masers in Space*. Cambridge University Press, 2008.

Ethan Tsai. Particle tracing code for energetic electrons interacting with whistler-mode waves, June 2023. URL https://doi.org/10.5281/zenodo.8083874. Software.

Ethan Tsai. Particle tracing code for energetic electrons interacting with whistler-mode waves, January 2024. URL https://doi.org/10.5281/zenodo.10554701.

Ethan Tsai, Anton Artemyev, Xiao-Jia Zhang, and Vassilis Angelopoulos. Relativistic Electron Precipitation Driven by Nonlinear Resonance With Whistler-Mode Waves. *Journal of Geophysical Research (Space Physics)*, 127(5):e30338, May 2022. doi: 10.1029/2022JA030338.

Ethan Tsai, Anton Artemyev, Vassilis Angelopoulos, and Xiao-Jia Zhang. Investigating Whistler-Mode Wave Intensity Along Field Lines Using Electron Precipitation Measurements. *Journal of Geophysical Research (Space Physics)*, 128(8):e2023JA031578, August 2023. doi: 10.1029/2023JA031578.

Ethan Tsai, Anton V Artemyev, Qianli Ma, Didier Mourenas, Oleksiy Agapitov, Xiao-Jia Zhang, and Vassilis Angelopoulos. Key factors determining nightside energetic electron losses driven by whistler-mode waves. December 2023. doi: 10.22541/au.170216582.29158404/v1.

B. T. Tsurutani and E. J. Smith. Postmidnight chorus: A substorm phenomenon. *J. Geophys. Res.*, 79:118–127, January 1974. doi: 10.1029/JA079i001p00118.

B. T. Tsurutani, B. J. Falkowski, O. P. Verkhoglyadova, J. S. Pickett, O. Santolík, and G. S. Lakhina. Quasi-coherent chorus properties: 1. Implications for wave-particle interactions. *J. Geophys. Res.*, 116:A09210, September 2011. doi: 10.1029/2010JA016237.

Bruce T. Tsurutani, Rui Chen, Xinliang Gao, Quanming Lu, Jolene S. Pickett, Gurbax S. Lakhina, Abhijit Sen, Rajkumar Hajra, Sang A. Park, and Barbara J. Falkowski. Lower-Band "Monochromatic" Chorus Riser Subelement/Wave Packet Observations. *Journal of Geophysical Research (Space Physics)*, 125(10):e28090, October 2020. doi: 10.1029/2020JA028090.

N. A. Tsyganenko. A magnetospheric magnetic field model with a warped tail current sheet. *Plan. Sp. Sci.*, 37:5–20, January 1989. doi: 10.1016/0032-0633(89)90066-4.

N. A. Tsyganenko. Modeling the Earth's magnetospheric magnetic field confined within a realistic magnetopause. *J. Geophys. Res.*, 100:5599–5612, April 1995. doi: 10.1029/94JA03193.

N. A. Tsyganenko and M. I. Sitnov. Modeling the dynamics of the inner magnetosphere during strong geomagnetic storms. *J. Geophys. Res.*, 110:A03208, March 2005. doi: 10.1029/2004JA010798.

D. L. Turner, V. Angelopoulos, W. Li, J. Bortnik, B. Ni, Q. Ma, R. M. Thorne, S. K. Morley, M. G. Henderson, G. D. Reeves, M. Usanova, I. R. Mann, S. G. Claudepierre, J. B. Blake, D. N. Baker, C.-L. Huang, H. Spence, W. Kurth, C. Kletzing, and J. V. Rodriguez. Competing source and loss mechanisms due to wave-particle interactions in Earth's outer radiation belt during the 30 September to 3 October 2012 geomagnetic storm. *J. Geophys. Res.*, 119:1960–1979, March 2014. doi: 10.1002/2014JA019770.

D. L. Turner, J. F. Fennell, J. B. Blake, J. H. Clemmons, B. H. Mauk, I. J. Cohen, A. N. Jaynes, J. V. Craft, F. D. Wilder, D. N. Baker, G. D. Reeves, D. J. Gershman, L. A. Avanov, J. C. Dorelli, B. L. Giles, C. J. Pollock, D. Schmid, R. Nakamura, R. J. Strangeway, C. T. Russell, A. V. Artemyev, A. Runov, V. Angelopoulos, H. E. Spence, R. B.

Torbert, and J. L. Burch. Energy limits of electron acceleration in the plasma sheet during substorms: A case study with the magnetospheric multiscale (mms) mission. *Geophys. Res. Lett.*, 43(15):7785–7794, 2016. ISSN 1944-8007. doi: 10.1002/2016GL069691. URL http://dx.doi.org/10.1002/2016GL069691.

Esa Turunen, Antti Kero, Pekka T Verronen, Yoshizumi Miyoshi, Shin-Ichiro Oyama, and Shinji Saito. Mesospheric ozone destruction by high-energy electron precipitation associated with pulsating aurora. *Journal of Geophysical Research: Atmospheres*, 121(19): 11–852, 2016.

D. Vainchtein, X. J. Zhang, A. V. Artemyev, D. Mourenas, V. Angelopoulos, and R. M. Thorne. Evolution of Electron Distribution Driven by Nonlinear Resonances With Intense Field-Aligned Chorus Waves. *Journal of Geophysical Research (Space Physics)*, 123(10): 8149–8169, October 2018. doi: 10.1029/2018JA025654.

J. A. Van Allen and L. A. Frank. Radiation Around the Earth to a Radial Distance of 107,400 km. *Nature*, 183:430–434, February 1959. doi: 10.1038/183430a0.

I. Y. Vasko, O. V. Agapitov, F. S. Mozer, A. V. Artemyev, J. F. Drake, and I. V. Kuzichev. Electron holes in the outer radiation belt: Characteristics and their role in electron energization. *J. Geophys. Res.*, 122:120–135, January 2017a. doi: 10.1002/2016JA023083.

I. Y. Vasko, O. V. Agapitov, F. S. Mozer, J. W. Bonnell, A. V. Artemyev, V. V. Krasnoselskikh, G. Reeves, and G. Hospodarsky. Electron-acoustic solitons and double layers in the inner magnetosphere. *Geophys. Res. Lett.*, 44:4575–4583, May 2017b. doi: 10.1002/2017GL074026.

A. A. Vedenov, E.P. Velikhov, and R.Z. Sagdeev. Quasilinear theory of plasma oscillations. *Nuclear Fusion Suppl.*, 2:465–475, 1962.

Olga P. Verkhoglyadova, Bruce T. Tsurutani, and Gurbax S. Lakhina. Properties of obliquely propagating chorus. *Journal of Geophysical Research (Space Physics)*, 115(1):A00F19, September 2010. doi: 10.1029/2009JA014809.

S. N. Vernov and A. E. Chudakov. Investigations of Cosmic Radiation and of the Terrestrial Corpuscular Radiation by Means of Rockets and Satellites. *Soviet Physics Uspekhi*, 3(2):230, February 1960. ISSN 0038-5670. doi: 10.1070/PU1960v003n02ABEH003269. URL https://iopscience.iop.org/article/10.1070/PU1960v003n02ABEH003269/meta. Publisher: IOP Publishing.

Brian M. Walsh, Arthur J. Hull, Oleksiy Agapitov, Forrest S. Mozer, and Haimeng Li. A census of magnetospheric electrons from several ev to 30 kev. *Journal of Geophysical Research: Space Physics*, 125(5):e2019JA027577, 2020. doi: 10.1029/2019JA027577. URL https://agupubs.onlinelibrary.wiley.com/doi/abs/10.1029/2019JA027577. e2019JA027577 10.1029/2019JA027577.

Dedong Wang and Yuri Y. Shprits. On How High-Latitude Chorus Waves Tip the Balance Between Acceleration and Loss of Relativistic Electrons. *Geophys. Res. Lett.*, 46(14): 7945–7954, July 2019. doi: 10.1029/2019GL082681.

Dedong Wang, Yuri Y. Shprits, Irina S. Zhelavskaya, Oleksiy V. Agapitov, Alexander Y. Drozdov, and Nikita A. Aseev. Analytical Chorus Wave Model Derived from Van Allen Probe Observations. *Journal of Geophysical Research (Space Physics)*, 124(2):1063–1084, Feb 2019. doi: 10.1029/2018JA026183.

Shan Wang, Naoki Bessho, Daniel B. Graham, Olivier Le Contel, Frederick D. Wilder, Yuri V. Khotyaintsev, Kevin J. Genestreti, Benoit Lavraud, Seung Choi, and James L. Burch. Whistler Waves Associated With Electron Beams in Magnetopause Reconnection Diffusion Regions. *Journal of Geophysical Research (Space Physics)*, 127(9):e30882, September 2022. doi: 10.1029/2022JA030882.

C. E. J. Watt, A. W. Degeling, and R. Rankin. Constructing the frequency and wave normal distribution of whistler-mode wave power. *J. Geophys. Res.*, 118:1984–1991, May 2013. doi: 10.1002/jgra.50231.

C. Wilkins, V. Angelopoulos, A. Runov, A. Artemyev, X. J. Zhang, J. Liu, and E. Tsai. Sta-

tistical Characteristics of the Electron Isotropy Boundary. *Journal of Geophysical Research (Space Physics)*, 128(10):e2023JA031774, October 2023. doi: 10.1029/2023JA031774.

L. B. Wilson, A. Koval, A. Szabo, A. Breneman, C. A. Cattell, K. Goetz, P. J. Kellogg, K. Kersten, J. C. Kasper, B. A. Maruca, and M. Pulupa. Electromagnetic waves and electron anisotropies downstream of supercritical interplanetary shocks. *J. Geophys. Res.*, 118:5–16, January 2013. doi: 10.1029/2012JA018167.

L. B. Wilson, III, C. A. Cattell, P. J. Kellogg, J. R. Wygant, K. Goetz, A. Breneman, and K. Kersten. The properties of large amplitude whistler mode waves in the magnetosphere: Propagation and relationship with geomagnetic activity. *Geophys. Res. Lett.*, 38:L17107, September 2011. doi: 10.1029/2011GL048671.

Z. Xiang, W. Tu, B. Ni, M. G. Henderson, and X. Cao. A Statistical Survey of Radiation Belt Dropouts Observed by Van Allen Probes. *Geophys. Res. Lett.*, 45:8035–8043, August 2018. doi: 10.1029/2018GL078907.

Wei Xu, Robert A Marshall, Hilde Nesse Tyssøy, and Xiaohua Fang. A generalized method for calculating atmospheric ionization by energetic electron precipitation. *Journal of Geophysical Research: Space Physics*, 125(11):e2020JA028482, 2020.

Dabin Xue, Jian Yang, Zhizhao Liu, and Shiwei Yu. Examining the Economic Costs of the 2003 Halloween Storm Effects on the North Hemisphere Aviation Using Flight Data in 2019. *Space Weather*, 21(3):e2022SW003381, March 2023. doi: 10.1029/2022SW003381.

A. G. Yahnin, T. A. Yahnina, N. V. Semenova, B. B. Gvozdevsky, and A. B. Pashin. Relativistic electron precipitation as seen by NOAA POES. *Journal of Geophysical Research (Space Physics)*, 121(9):8286–8299, September 2016. doi: 10.1002/2016JA022765.

A. G. Yahnin, T. A. Yahnina, T. Raita, and J. Manninen. Ground pulsation magnetometer observations conjugated with relativistic electron precipitation. *Journal of Geophysical Research (Space Physics)*, 122(9):9169–9182, September 2017. doi: 10.1002/2017JA024249.

K. H. Yearby, M. A. Balikhin, Y. V. Khotyaintsev, S. N. Walker, V. V. Krasnoselskikh, H. S. C. K. Alleyne, and O. Agapitov. Ducted propagation of chorus waves: Cluster observations. *Annales Geophysicae*, 29:1629–1634, September 2011. doi: 10.5194/angeo-29-1629-2011.

X. Zhang, V. Angelopoulos, A. V. Artemyev, and J. Liu. Whistler and Electron Firehose Instability Control of Electron Distributions in and Around Dipolarizing Flux Bundles. *Geophys. Res. Lett.*, 45:9380–9389, September 2018a. doi: 10.1029/2018GL079613.

X. J. Zhang, R. Thorne, A. Artemyev, D. Mourenas, V. Angelopoulos, J. Bortnik, C. A. Kletzing, W. S. Kurth, and G. B. Hospodarsky. Properties of Intense Field-Aligned Lower-Band Chorus Waves: Implications for Nonlinear Wave-Particle Interactions. *Journal of Geophysical Research (Space Physics)*, 123(7):5379–5393, July 2018b. doi: 10.1029/2018JA025390.

X. J. Zhang, D. Mourenas, A. V. Artemyev, V. Angelopoulos, J. Bortnik, R. M. Thorne, W. S. Kurth, C. A. Kletzing, and G. B. Hospodarsky. Nonlinear Electron Interaction With Intense Chorus Waves: Statistics of Occurrence Rates. *Geophys. Res. Lett.*, 46(13):7182–7190, July 2019a. doi: 10.1029/2019GL083833.

X. J. Zhang, O. Agapitov, A. V. Artemyev, D. Mourenas, V. Angelopoulos, W. S. Kurth, J. W. Bonnell, and G. B. Hospodarsky. Phase Decoherence Within Intense Chorus Wave Packets Constrains the Efficiency of Nonlinear Resonant Electron Acceleration. *Geophys. Res. Lett.*, 47(20):e89807, October 2020a. doi: 10.1029/2020GL089807.

X. J. Zhang, D. Mourenas, A. V. Artemyev, V. Angelopoulos, W. S. Kurth, C. A. Kletzing, and G. B. Hospodarsky. Rapid Frequency Variations Within Intense Chorus Wave Packets. *Geophys. Res. Lett.*, 47(15):e88853, August 2020b. doi: 10.1029/2020GL088853.

X. J. Zhang, A. G. Demekhov, Y. Katoh, D. Nunn, X. Tao, D. Mourenas, Y. Omura, A. V. Artemyev, and V. Angelopoulos. Fine Structure of Chorus Wave Packets: Comparison

Between Observations and Wave Generation Models. *Journal of Geophysical Research (Space Physics)*, 126(8):e29330, August 2021. doi: 10.1029/2021JA029330.

X.-J. Zhang, V. Angelopoulos, D. Mourenas, A. V. Artemyev, E. Tsai, and C. Wilkins. Characteristics of Electron Microburst Precipitation Based on High-Resolution ELFIN Measurements. *J. Geophys. Res.*, 127(5):e2022JA030509, 2022a. doi: 10.1029/2022JA030509.

Xiao-Jia Zhang, Vassilis Angelopoulos, Didier Mourenas, Anton Artemyev, Ethan Tsai, and Colin Wilkins. Characteristics of Electron Microburst Precipitation Based on High-Resolution ELFIN Measurements. *Journal of Geophysical Research (Space Physics)*, 127 (5):e30509, May 2022b. doi: 10.1029/2022JA030509.

Xiao-Jia Zhang, Anton Artemyev, Vassilis Angelopoulos, Ethan Tsai, Colin Wilkins, Satoshi Kasahara, Didier Mourenas, Shoichiro Yokota, Kunihiro Keika, Tomoaki Hori, Yoshizumi Miyoshi, Iku Shinohara, and Ayako Matsuoka. Superfast precipitation of energetic electrons in the radiation belts of the Earth. *Nature Communications*, 13:1611, March 2022c. doi: 10.1038/s41467-022-29291-8.

Xiao-Jia Zhang, Vassilis Angelopoulos, Anton Artemyev, Didier Mourenas, Oleksiy Agapitov, Ethan Tsai, and Colin Wilkins. Temporal Scales of Electron Precipitation Driven by Whistler-Mode Waves. *Journal of Geophysical Research (Space Physics)*, 128(1): e2022JA031087, January 2023. doi: 10.1029/2022JA031087.

Xu Zhang, V. Angelopoulos, A. V. Artemyev, and Jiang Liu. Energy Transport by Whistler Waves Around Dipolarizing Flux Bundles. *Geophys. Res. Lett.*, 46(21):11,718–11,727, November 2019b. doi: 10.1029/2019GL084226.

Z. H. Zhong, M. Zhou, D. B. Graham, Yu. V. Khotyaintsev, Y. F. Wu, O. Le Contel, H. M. Li, X. Tao, R. X. Tang, and X. H. Deng. Evidence for Whistler Waves Propagating Into the Electron Diffusion Region of Collisionless Magnetic Reconnection. *Geophys. Res. Lett.*, 49(7):e97387, April 2022. doi: 10.1029/2021GL097387.